

**Towards GHz Detection:
Transition Metal Dichalcogenides
for Ultrafast Photodetection**

Dissertation

der Mathematisch-Naturwissenschaftlichen Fakultät
der Eberhard Karls Universität Tübingen
zur Erlangung des Grades eines
Doktors der Naturwissenschaften
(Dr. rer. nat.)

vorgelegt von
Fabian Strauß
aus Bad Dürkheim

Tübingen
2024

Gedruckt mit Genehmigung der Mathematisch-Naturwissenschaftlichen Fakultät der
Eberhard Karls Universität Tübingen.

Tag der mündlichen Qualifikation:

25.09.2024

Dekan:

Prof. Dr. Thilo Stehle

1. Berichterstatter:

Prof. Dr. Marcus Scheele

2. Berichterstatterin:

Prof. Dr. Monika Fleischer

3. Berichterstatter:

Prof. Dr. Andrey Turchanin

This dissertation has been completed in the group of Prof. Dr. Marcus Scheele at the Institute of Physical and Theoretical Chemistry of the Eberhard Karls University of Tübingen between February 2021 and March 2024.

©Fabian Strauß, 2024

‘There are no accidents.’
– Master Oogway –

Abstract

Transition metal dichalcogenides (TMDCs) are layered materials with extraordinary properties for optoelectronics like high carrier mobilities and large extinction coefficients. They are applicable as mono- or multilayers, in combination with other 2D materials, affordable, and they are compatible with silicon technology. Those properties render them ideal candidates for fast and sensitive next-generation photodetectors. However, the simultaneous optimization of detectivity / responsivity and speed is not possible, as the long carrier lifetimes necessary for a high sensitivity are unfavourable for a fast detection. Recent research has primarily focused on increasing the responsivity with astonishing results, whereas improvements, of the response times have been challenging for pure TMDCs with the exception of more complicated device architectures involving graphene and sophisticated photonics. The objective of this thesis is the development of procedures that enable a GHz response of pure TMDC photodetectors which is still pending to date.

This cumulative dissertation is based on three research papers and one comprehensive review showing the systematic reduction in the response time of TMDC photodetectors as well as questioning existing practices in converting the temporal response of a detector into the bandwidth.

Firstly, the common practice of approximating the optoelectrical bandwidth, instead of measuring it directly, is discussed with respect to detectors based on emerging nanomaterials. Here, a commercial silicon p-i-n-photodetector is used as reference, and its measured or approximated bandwidth is compared to detectors based on TMDCs as well as two kind of quantum dot (QD) detectors. The study shows tremendous differences depending on the chosen method up to a factor of 3000. The main conclusion of this study is that comparisons of the photoresponse of different materials should only be made with data acquired with the same method to avoid possible demerits of the approximation.

Secondly, the influence of the electrical interface by contacting the edges of MoS₂ crystals is examined and compared to commonly used top contacts. This work shows that edge contacts offer unique advantages for the speed of photodetectors based on the different in-plane and out-of-plane carrier behaviour in 2D materials, such as TMDCs. With a facile step of plasma etching, the edge of MoS₂ is unravelled. This accelerated the photoresponse, especially the fall time, by more than one order of magnitude. To further verify the influence of the Schottky barrier and the geometry, the influence of different metals contacting different facets of the crystals was demonstrated. The fastest device obtained in this study exceeded a bandwidth of 18 MHz.

The third publication analyzes the systemic reduction of the photoresistance of WSe₂ devices by increasing the saturation of absorption. In order to study this in a configurable environment, the irradiance of the laser is controlled with a confocal laser microscope setup. By lowering the photoresistance within the material, the device limiting RC time is lowered as well and consequently the detectors are accelerated. Subsequently, the device's electrode structure is optimized to decrease the capacitance and thus reduce the RC time further. By combining both strategies, WSe₂ detectors reach 230 MHz, which is the limitation of the measurement setup utilized, as confirmed by a commercial photodiode. In addition to the examination of bulk crystals of WSe₂, an investigation of a bilayer flake has shown similar

fast responses only limited by the lower absorption due to the short path length. Especially in comparison to the very slow MoS₂ mono- and bilayers, this is a promising finding towards ultrafast and atomically thin TMDC photodetectors.

Finally, additional contributions to other publications in the field of time-resolved photocurrent measurements are highlighted as well as an extended perspective for a future direction of this work is given. The outlook encompasses the combination of TMDC photodetectors with plasmonics as well as the time-resolved examination of layered materials within Fabry-Pérot microcavities and the bulk photovoltaic effect.

In summary, this thesis provides experimental pathways for the acceleration of TMDC based photodetectors by combining simple fabrication routes with guidelines to reduce the RC-limitation in such devices.

Zusammenfassung

Übergangsmetall-Dichalcogenide (TMDCs) sind Schichtmaterialien mit außergewöhnlichen Eigenschaften für optoelektronische Anwendungen. Sie weisen hohe Ladungsträgerbeweglichkeiten und große Extinktionskoeffizienten auf. Zusätzlich können TMDCs als Mono- oder Multilag und in Kombination mit anderen 2D-Materialien verwendet werden. Sie sind mit der bestehenden Siliziumtechnologie kompatibel und darüber hinaus zu einem erschwinglichen Preis erhältlich. Diese Eigenschaften machen sie zu idealen Kandidaten für den Einsatz als schnelles und responsives Material in Photodetektoren der nächsten Generation. Eine gleichzeitige Optimierung von Detektivität und Geschwindigkeit ist jedoch nicht ohne weiteres möglich, da die für eine hohe Empfindlichkeit erforderlichen langen Ladungsträgerlebenszeiten eine schnelle Detektion unmöglich machen. Die jüngste Forschung konzentrierte sich in erster Linie auf die Steigerung der Empfindlichkeit und erzielte dabei erstaunliche Ergebnisse. Die Verbesserung der schnellen Ansprechzeiten des reinen Materials stellt eine Herausforderung dar, und Erfolge scheinen nur mit komplexen Bauelementarchitekturen unter Einbeziehung von Graphen und hochentwickelter Photonik möglich. Insbesondere eine Schaltbarkeit der reinen TMDC-Photodetektoren im Gigahertz-Bereich ist noch nicht vollbracht und steht daher im Vordergrund dieser Arbeit.

Diese kumulative Dissertation basiert auf drei Forschungspublikationen und einem umfassenden Review, welche die systematische Verkürzung der Ansprechzeit von TMDC-Photodetektoren aufzeigen und bestehende Verfahren zur Umwandlung der zeitlichen Antwort eines Detektors in eine frequenzbasierte Bandbreite in Frage stellen.

Zunächst wird die gängige Praxis diskutiert, die optoelektrische Bandbreite von nanomaterial-basierten Detektoren zu nähern, anstatt sie direkt zu messen. Hier werden ein handelsüblicher p-i-n-Silizium-Photodetektor als Referenz sowie Detektoren auf der Basis von TMDCs und zwei Arten von Quantenpunkten (QDs) verglichen. Die Studie zeigt enorme Unterschiede in der bestimmten Bandbreite auf. Diese Unterschiede können je nach gewählter Methode um einen Faktor von bis zu 3000 variieren. Vergleiche zwischen verschiedenen Arbeiten und innerhalb einer Arbeit sollten sich daher auf Messungen beschränken, die mit derselben Methode durchgeführt wurden, um mögliche Nachteile der Näherungsformel zu vermeiden.

Der nächste Schritt ist die Untersuchung des Einflusses der elektrischen Kontaktierung der Kanten von MoS₂-Kristallen und der Vergleich mit der üblicherweise verwendeten Kontaktierung der Oberseite. Diese Arbeit zeigt, dass Kantenkontakte einzigartige Vorteile für die Geschwindigkeit von Photodetektoren bieten, die auf dem unterschiedlichen Verhalten von Ladungsträgern in und außerhalb der Ebene in 2D-Materialien wie TMDCs beruhen. Durch einen einfachen Schritt des Plasmaätzens wird die Kante von MoS₂ freigelegt, was einen direkten Zugang zu den Schichten ermöglicht. Das Ergebnis war eine Beschleunigung der Antwortzeit, insbesondere der Abfallzeit, um mehr als eine Größenordnung. Um den Einfluss der Schottky-Barriere und der Kontaktgeometrie weiter zu verifizieren, wird der Einfluss verschiedener Metalle, die verschiedene Facetten der Kristalle kontaktieren, demonstriert. Der schnellste in dieser Publikation fabrizierte und untersuchte Detektor erreichte eine Bandbreite von über 18 MHz.

In der dritten Veröffentlichung wird die systematische Verringerung des Photo-

widerstands von WSe_2 -Bauelementen durch Erhöhung der Absorptionssättigung analysiert. Um dies in einer konfigurierbaren Umgebung zu untersuchen, wird die Bestrahlungsstärke des Lasers mit einem konfokalen Lasermikroskop-Setup gesteuert. Die Verringerung des Photowiderstands im Material hat auch eine Verringerung der RC-Zeit des Bauelements zur Folge, was zu einer Beschleunigung des Detektors führt. Anschließend wird die Elektrodenstruktur des Bauelements optimiert, um zusätzlich die Kapazität zu verringern und damit eine weitere Reduktion der RC-Zeit zu erreichen. Kombiniert man beide Strategien, erreichen die WSe_2 -Detektoren Bandbreiten von 230 MHz, die Grenze des verwendeten Messaufbaus. Eine Bestätigung der Messaufbaulimitierung erfolgte mit Hilfe einer kommerziellen Photodiode. Folglich liegt die tatsächliche Bandbreite der Komponenten über diesen 230 MHz, und die tatsächliche Grenze der WSe_2 -Detektoren bleibt zu bestimmen. Neben der Untersuchung von WSe_2 -Bulkkristallen hat die Untersuchung eines zweilagigen Kristalls ähnlich schnelle Ansprechzeiten gezeigt, die nur durch die geringere Absorption aufgrund der geringeren Anzahl von Schichten begrenzt sind. Vor allem im Vergleich zu den sehr langsamen MoS_2 -Mono- und Doppellagen ist dies ein vielversprechender Befund in Richtung ultraschneller und gleichzeitig atomar dünner TMDC-Photodetektoren.

Abschließend werden weitere Beiträge zu anderen Publikationen im Bereich der zeitaufgelösten Photostrommessung hervorgehoben sowie ein erweiterter Ausblick auf eine zukünftige Ausrichtung dieser Arbeit gegeben. Der Ausblick umfasst die Kombination von TMDC-Photodetektoren mit plasmonischen Strukturen sowie die zeitaufgelöste Untersuchung von Schichtmaterialien in Fabry-Pérot-Mikrokavitäten und den Bulk-Photovoltaik-Effekt.

Zusammenfassend zeigt diese Arbeit experimentelle Wege zur Beschleunigung von TMDC-basierten Photodetektoren durch die Kombination einfacher Herstellungsrouten mit Richtlinien zur Reduzierung der RC-Limitierung auf.

Contents

Abstract	I
Zusammenfassung	III
1 Introduction	1
1.1 Motivation	1
1.2 Objective	3
1.3 Outline	3
2 Theoretical & Scientific Fundamentals	6
2.1 Photodetection	6
2.1.1 Mechanisms of Detection	8
2.1.1.1 Photoconductive Effect	8
2.1.1.2 Photogating Effect	11
2.1.1.3 Photovoltaic Effect	12
2.1.2 Metal-Semiconductor Interface	13
2.1.2.1 Ohmic Contact	13
2.1.2.2 Schottky Contact	14
2.1.2.3 Fermi Level Pinning and Charge Injection at a Schottky Contact	15
2.1.2.4 Device Architecture	16
2.1.3 Key Performance Parameters	17
2.2 Transition Metal Dichalcogenides	20
2.2.1 From 3D to 0D	20
2.2.2 Properties of TMDCs	22
2.2.2.1 Mono- vs. Multilayer for Fast Photodetection	24
2.2.3 What Makes a Good (TMDC) Photodetector?	24
2.3 Investigation of (Opto-) Electronic Properties	29
2.3.1 Conductivity Measurements	29
2.3.2 Time-Resolved Photocurrent Measurements	29
2.3.2.1 General Setup Considerations	29
2.3.2.2 Extrinsic Measurements	30
2.3.2.3 Intrinsic Measurements	32
2.3.3 Confocal Microscopy	33
2.4 Microfabrication Techniques	35
2.4.1 Mechanical Exfoliation	35
2.4.2 Optical Lithography	35
2.4.3 Electron Beam Lithography	37
2.4.4 Characterization Methods	37
3 Pitfalls in Determining the Electrical Bandwidth of Nonideal Nanomaterials for Photodetection	38
3.1 Abstract	39
3.2 Introduction	39
3.3 Experimental Section	40
3.4 Results & Discussion	41
3.4.1 Commercial photodiode	41
3.4.2 Photodiodes based on nanostructured materials	42

3.5	Conclusion	45
4	Edge Contacts accelerate the Response of MoS₂ Photodetectors	46
4.1	Abstract	47
4.2	Introduction	47
4.3	Experimental Section	48
4.3.1	Fabrication	48
4.3.2	Transient photoresponse	48
4.4	Results and discussion	49
4.4.1	Steady state photoresponse of edge and top contacted MoS ₂	49
4.4.2	Non-steady state photoresponse of edge and top contacted MoS ₂	52
4.5	Conclusions	53
4.6	Supplementary Information	54
5	A simple 230 MHz Photodetector Based on Exfoliated WSe₂ Multilayers	60
5.1	Abstract	61
5.2	Introduction	61
5.3	Experimental section	62
5.3.1	Fabrication	62
5.3.2	Transient photoresponse	62
5.4	Results and Discussion	62
5.4.1	Reduction of the photoresistance	62
5.4.2	Reduction of the capacitance	64
5.4.3	Reduction of the flake thickness to bilayers	66
5.5	Summary and Conclusion	67
5.6	Supplementary Information	68
6	Key Results of Further Projects	77
6.1	Substrate Effects on the Bandwidth of CdSe Quantum Dot Photodetectors	77
6.2	Substrate effects on the speed limiting factor of WSe ₂ photodetectors	79
6.3	Sub-nanosecond Intrinsic Response Time of PbS Nanocrystal IR-Photodetectors	81
7	Outlook	83
7.1	Measurement Setup 2.0	84
7.2	Bulk Photovoltaic Effect	85
7.3	Optical Cavities	88
7.3.1	Theoretical Background	88
7.3.2	Optical Cavities for Fast Photodetectors	90
7.4	Plasmonics	92
7.4.1	Theoretical Background	92
7.4.2	Plasmonics in Photodetectors	95
8	Summary & Conclusion	98
	Appendix	101
	List of Abbreviations & Symbols	103
	List of Figures	108

List of Tables & Boxes	109
Bibliography	110
List of Publications & Scholarly Contributions	141
Declaration of Contribution	144
Acknowledgements	146

1 Introduction

Our era can be described as the ‘silicon age’.¹ The influence of silicon on the semiconductor industry, electronics and our technological world is massive. It is everywhere in our everyday life e.g. transistors in smartphones, solar cells on the roofs and photodetectors in sensors.^{2,3} But inevitable quantum physical effects start to limit the further development of silicon for future applications.⁴ So, the next generation of technology and materials for the growing demand of energy saving, cheap, safe and fast technology must emerge. Since the discovery of graphene in 2004, the focus of research has shifted among others towards quantum-restrained materials, such as quantum dots and layered materials, respectively 2D materials in the limiting case of a monolayer.

1.1 Motivation

The class of layered materials has a variety of representatives that cover the whole spectrum from insulating to metallic properties. Some commonly used members are hexagonal boron nitride (hBN), graphene, black phosphorous and the transition metal dichalcogenides MoS₂ and WSe₂. Thereby, hBN serves as an insulator,⁵ black phosphorous,⁶ MoS₂ and WSe₂⁷ are semiconducting and graphene⁸ is a semimetal. Using those layered materials in their pure form or in more complex combinations, devices like transistors,⁹ solar cells,¹⁰ chemical sensors,¹¹ light-emitting diodes¹² and photodetectors¹³ with impressive results have been realized.

Narrowing this huge research area down, the focus will be on photodetection based on layered materials, more specifically on TMDCs. Thus, these topics will be addressed in more detail in this work.

Applications of photodetectors nowadays span from night vision and thermal imaging over photography to the usage in telecommunication. Depending on the utilization, different demands are placed on the detector in terms of sensitivity, speed and spectral range.¹⁴ Within this work, the main objective will be on high-speed detectors.

In times of growing demand for digitalisation of everyday tasks such as online purchases and streaming of videos or business calls, the interface between glass fibers based on optical data transmission and on-chip transistors using electrical signals is becoming increasingly meaningful. Record optical transmission technology exceeds 200 Tb/s in a single core over 13 km distance,¹⁵ whereas record transistors at low temperatures provide switching speeds of 0.8 THz.¹⁶ To keep up with the other technologies, photodetectors have to become faster, so the overall data transmission can be accelerated as well.

Especially the wavelength of transmission is a selection criterion and determines the suitability of a material. In optical communication several transmission windows can be found in the near-infrared (NIR), known as the telecommunication windows.¹⁷ The location is among others based on the least attenuation of optimized optical fibers. Technological breakthroughs of LED efficiency in the last two decades open up a complete new field - visible light communication (VLC). Since light-emitting diodes (LEDs) are current-driven semiconductors, fast light switching is possible offering illumination and fast data transfer simultaneously.^{18,19} Additionally, the visible spectrum is less susceptible to interference with existing radio systems, offering higher security possibilities and many applications, e.g.

in vehicular communication on the street.²⁰ Transmission records of the light sources already exceed 100 Gb/s,²¹ which in turn makes clear: Fast photodetectors are needed.

In search of fast detectors the material choice is a crucial step towards high-performance devices and their possible applications. Within the class of 2D materials, graphene holds great promise for high-speed detection. Already in 2009 it has demonstrated bandwidths of tens of gigahertz,²² and in 2010 a 16 GHz bandwidth RC-limited detector has been built, showing the potential of graphene.²³ The major drawback of pure graphene is a high dark current owing to its zero bandgap as well as low absorption (<2.3%) due to its atomic thickness.⁸ On the other hand, its semimetal nature enables graphene to absorb broad regions of light, expanding the absorbed spectrum in devices from the infrared to the ultraviolet.²⁴

Black phosphorous (BP), a group V-based 2D material on the contrary is a semiconductor with a small direct bandgap ranging from 0.35 to 2.0 eV depending on the number of layers, offering NIR absorption with high mobilities but significantly lower dark currents compared to graphene.²⁵ First examinations of the time-resolved photoresponse have shown response times of about 1 ms towards 940 nm excitation, respectively 3 kHz bandwidth.²⁶ A more sophisticated device based on a silicon waveguide and control over the photocurrent generation mechanism by a gate, shows a 3 GHz bandwidth limited by the RC time of device and setup.²⁷ However, BP suffers from degradation in ambient conditions through water and oxides.⁶ Due to this heavy degradation encapsulation of the BP is always needed as protection, thereby complicating the fabrication.

In the last decade photodetecting devices based on transition metal dichalcogenides gained more prominence. Especially the sulfides and selenides of molybdenum and tungsten receive a lot of attention due to their semiconducting nature, enormous stability at ambient conditions, fascinating optoelectronic properties and possibilities for combination with other materials.²⁸ This renders them ideal candidates for photodetectors (PDs). A lot of work on TMDC PDs focuses rather on responsivity than on speed.²⁹ On the other hand, projects studying the acceleration of TMDC detectors usually employ complex device architectures based on pn junctions, photonic circuits, incorporation of graphene or combination with quantum dots for functionality separation.²⁹ In pursuit of a more simple device architecture, photodetectors employing pure TMDCs are of interest. But until today, the speed of pure TMDC devices remains relatively slow. The theoretical limit of the material can be studied with intrinsic PD measurements and hence give hints about the lower limit of the response time. For TMDCs this has revealed picosecond response times for the pure material.^{30,31} This emphasises that material limits are not yet in reach with actual devices, and photodetectors based on pure TMDCs can be further accelerated to reach their full potential.

For that reason, this work tries to close the gap between the theoretically possible material speed and the device speed based on pure MoS₂ and WSe₂ PDs with a simple device architecture.

1.2 Objective

The optimization of photodetection has two aspects - detector speed as well as detector energy efficiency and sensitivity. Next-generation materials like quantum dots and layered materials provide the platform to employ modifications on the material level and on the device level to achieve such improvement.

The objective of this work is accelerating the speed of detectors based on transition metal dichalcogenides. MoS₂ and WSe₂ are chosen as showcase materials with the ulterior motive to develop accelerating methods that are applicable to layered materials in general. The initial goal for the device speed is the gigahertz regime, to close the gap to the current CPU (central processing unit) operating speed of <6 GHz.³² In addition, the energy needed per switching event should be low, ideally below 1 fJ/bit, and compatibility with the existing silicon based techniques is of advantage for an easier implementation.

In this context, this thesis attempts to answer the overarching question: *How to reach the limit of devices based on pure MoS₂ or WSe₂ without sacrificing a simple and cost-effective fabrication?*

1.3 Outline

This thesis is structured as outlined graphically below in Figure 1.1. Significant portions of the chapters detailed below are the basis for a comprehensive review article published in *Accounts of Chemical Research*.³³

Chapter 2 ‘Theoretical & Scientific Fundamentals’ provides a brief insight into the most important scientific background needed for this work. The material class of TMDCs is presented as well as the basic concepts of photodetection and corresponding figures of merit with a focus on detector speed. Furthermore, the used methods for data acquirement are shown and the fabrication methods are discussed in short.

Chapter 3 addresses the drawbacks and risks of using the approximation $f_{3dB} = 0.35/t_{rise}$ to convert experimental risetimes into bandwidths without performing a Fourier transformation. This chapter is based on the publication ‘Pitfalls in Determining the Electrical Bandwidth of Nonideal Nanomaterials for Photodetection’, published in *The Journal of Physical Chemistry C*.³⁴

In Chapter 4, edge contacts for TMDCs are investigated and compared to their commonly used counterparts towards their influence on the detector speed. They reveal accelerations of the response speed by more than one order of magnitude, up to a bandwidth of 18 MHz. This chapter is based on the publication ‘Edge Contacts accelerate the Response of MoS₂ Photodetectors’, published in *Nanoscale Advances*.³⁵

Chapter 5 further accelerates TMDC photodetectors up to at least 230 MHz bandwidth by systematically reducing the RC time of the device. To achieve this, the photoresistance is decreased by increasing the irradiance in a controlled manner with a confocal microscope while simultaneously decreasing the capacitance by electrode optimization. This chapter is based on the publication ‘A simple 230 MHz Photodetector Based on Exfoliated WSe₂ Multilayers’, published in *RSC Applied Interfaces*.³⁶

Chapter 6 presents other work with the author of this thesis, published within the scope of photodetection with nanomaterials. Namely, ‘Substrate Effects on the Bandwidth of CdSe Quantum Dot Photodetectors’, published in *ACS Applied Materials & Interfaces*,³⁷ ‘Substrate effects on the speed limiting factor of WSe₂ photodetectors’ published in *Physical Chemistry Chemical Physics*³⁸ and ‘Sub-nanosecond Intrinsic Response Time of PbS Nanocrystal IR-Photodetectors’ published in *Nano Letters*³⁹ are briefly summarized and the most important conclusions highlighted.

The Chapter 7 ‘Outlook’ shows future directions and how this work could be developed further with a focus on plasmonics, optical cavities and the bulk photovoltaic effect as well as a short description on the requirements of a measurement setup needed to resolve the faster detectors.

Chapter 8 ‘Summary & Conclusion’ gives a comprehensive summary of this theses.

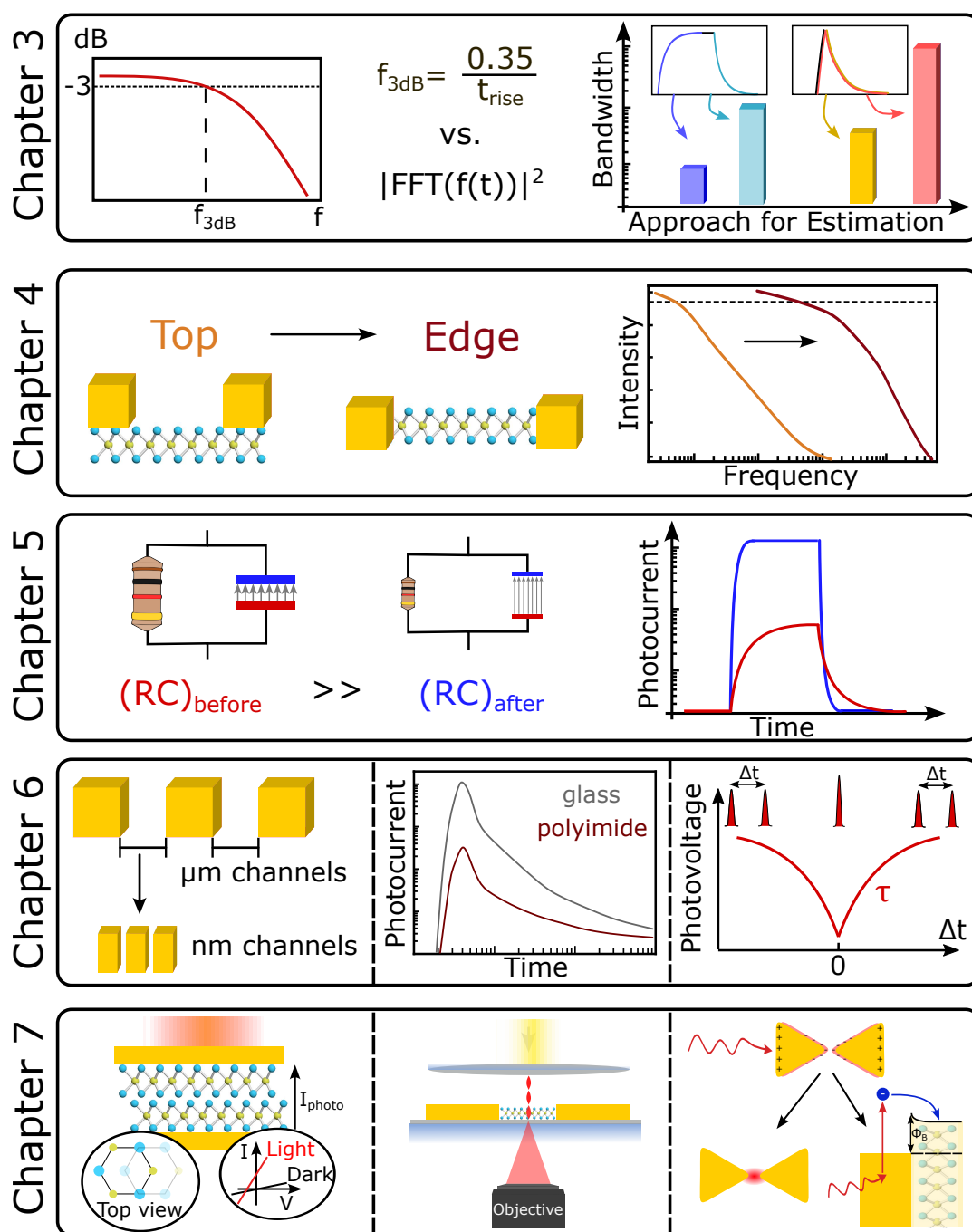


Figure 1.1. Graphical outline of this thesis. **Chapter 3:** ‘Pitfalls in Determining the Electrical Bandwidth of Nonideal Nanomaterials for Photodetection’. **Chapter 4:** ‘Edge Contacts accelerate the Response of MoS₂ Photodetectors’. **Chapter 5:** ‘A simple 230 MHz Photodetector Based on Exfoliated WSe₂ Multilayers’. **Chapter 6:** ‘Key results of further Projects’ including the major findings with respect to this thesis of the following three publications: ‘Substrate Effects on the Bandwidth of CdSe Quantum Dot Photodetectors’, ‘Substrate effects on the speed limiting factor of WSe₂ photodetectors’, and ‘Sub-nanosecond Intrinsic Response Time of PbS Nanocrystal IR-Photodetectors’. **Chapter 7:** ‘Outlook’ providing an extensive outlook on the bulk photovoltaic effect, optical cavities and plasmonics. Images of Chapter 7 are adapted with permission from Ref.³³ Copyright 2024 American Chemical Society.

2 Theoretical & Scientific Fundamentals

In this chapter the basics of photodetection and associated mechanisms as well as the metal-semiconductor interface and the respective figures of merit for photodetection are presented. Then, the material class of TMDCs will be briefly discussed in general and with respect to advantages of mono- and multilayer devices - everything with a focus towards high-speed detection. To be able to put this work into a broader context a literature overview of existing devices is shown. Afterwards, the methods used for acquiring the data in this work will be detailed as well as the fabrication techniques needed for detector production.

2.1 Photodetection

The fundamental principle of photodetection is the conversion of an incoming photon into an electrical signal. Photodetectors (PDs) can be divided into two principal groups: thermal and photoelectric detectors.^{40,41} Thermal detectors rely either on a non-uniform heating induced temperature gradient generating a photocurrent, or on a homogeneous temperature change altering the resistivity of the material. Those effects are called photo-thermoelectric and photo-bolometric effect.^{7,42,43} They are considered relatively slow, based on the required time for the temperature change and thus are generally not very suitable for fast photodetection.^{40,42} On the other hand, PDs relying on electron-hole separation are capable of providing high-speed detectors, depending on the configuration, and are thus discussed in more detail in the following.

There are two forms of photoeffect, the *external* photoeffect involving photogenerated electrons escaping the material by photoelectric emission^{40,44} and the *internal* photoeffect, leading to a photocurrent within the material. In order to create an electron-hole pair, a so-called exciton, the optical band gap E_{opt} of a semiconductor has to be overcome⁴⁵⁻⁴⁷

$$h\nu = \hbar\omega \geq E_{opt} \quad (2.1)$$

with the (reduced) Planck constant (\hbar) h and ν the frequency / ω the angular frequency of the incoming light. From there, the as-formed exciton is bound by Coulomb attractions with an exciton binding energy E_B .^{45,48} Before the carriers can contribute to a possible photocurrent, this energy has to be overcome and the resulting necessary energy is called the electrical bandgap $E_G = E_{opt} + E_B$, see Figure 2.1a.⁴⁵ If the exciton is bound strongly, for example in ionic crystals, the electron and hole are in close proximity, possibly even in the same unit cell. They are referred to as Frenkel-excitons.^{46,48} In inorganic semiconductors, the dielectric screening is usually high enough to extend the distance between the hole and the electron over several unit cells. They are then referred to as Wannier-Mott-excitons.^{46,48} For those excitons, the excitonic binding energy can be calculated similar to the hydrogen atom with an analogue of the effective Rydberg constant to^{41,46,48-50}

$$E_B^{(n)} = \frac{Me^4}{2\hbar^2(4\pi\epsilon_0\epsilon_r)^2} * \frac{1}{n^2}. \quad (2.2)$$

In this equation, M is the reduced exciton mass,⁴⁶ e the elementary charge, ϵ_0 the vacuum permittivity, ϵ_r the dielectric constant of the material and n the energy state into which the

electron is excited. Consequently, the ‘atom radius’ of the exciton can be defined, again in analogy to the hydrogen atom, to the Bohr exciton radius a_{exc} ^{46,50,51}

$$a_{exc}^{(n)} = n^2 \frac{4\pi\hbar^2\epsilon_r\epsilon_0}{Me^2}, \quad (2.3)$$

giving a measure of the spatial extension of an electron-hole-pair.

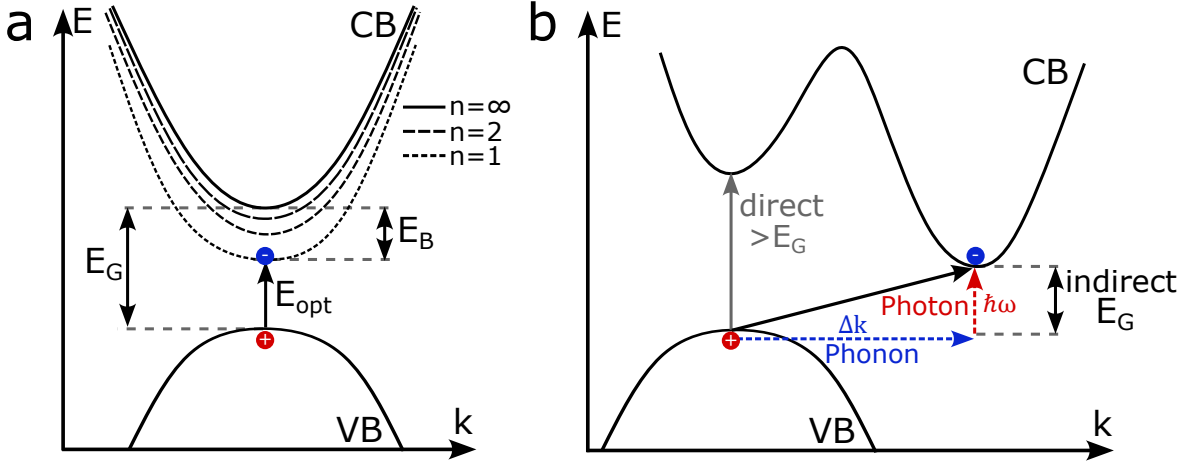


Figure 2.1. a) Energy levels in k -space for a direct band gap semiconductor with the excitonic energy levels sketched with dashed lines. b) Energy levels of an indirect band gap semiconductor with the higher direct energy band gap indicated in grey. The required photon and phonon with their respective energy $\hbar\omega$ and momentum change Δk are indicated with dashed lines. The electron and hole, forming the exciton, are shown in blue and red.

Besides the concept of the binding energy, Figure 2.1 also shows the difference between direct and indirect band gaps in semiconductors. If the optical excitation alone is sufficient to create an exciton, then, the transition is called direct. On the other hand, if an additional change of momentum is needed, because the valence band (VB) maximum and conduction band (CB) minimum are slightly shifted in the k -space, the transition is referred to as indirect.⁴⁶ For indirect semiconductors, like shown in Figure 2.1b, a direct transition may also be possible with higher photon energies. The change of momentum Δk can be delivered by phonons, the oscillation of the lattice.^{46,48} Considering that the indirect excitation needs two steps simultaneously, a phonon and a photon, the transition is less likely in comparison to a direct one and thus, the absorption coefficient is lower.^{46,52}

Semiconductors are very versatile and so are their applications within detectors. The most popular types of PDs are photoconductors and photodiodes, but also more exotic combinations can be found.^{43,53} Within this chapter, the focus will first be on the mechanisms driving conductors and diodes. Second, the interface between metal and semiconductor will receive particular attention as well as typical device architectures, before the key performance parameters are discussed. Readers interested in PDs beyond the descriptions here, like avalanche diodes or phototransistors, are referred to more specialized literature provided elsewhere.^{41,43,53–56}

2.1.1 Mechanisms of Detection

The two main mechanisms driving PDs are the photoconductive and the photovoltaic effect. Within the photoconductive effect, the photogain mechanism is a special case altering the device performance with enormous influence on the response time.

2.1.1.1 Photoconductive Effect

The photoconductive (PC) effect is based on an increased conductivity and thus decreased resistance under illumination. The working principle is sketched in Figure 2.2. In the dark, under an applied bias V_{SD} , only a few carriers are able to flow between the two metal electrodes. This is called the dark current I_{dark} (Figure 2.2a). Once the device is illuminated with photons of energies higher than the band gap, cf. Equation (2.1), electron-hole pairs are generated and separated by the applied bias. In the energy level picture, this V_{SD} can be seen as an elevation of one side, leading to a difference in the energy, separating holes and electrons in opposite directions (Figure 2.2b). The current increase is called the photocurrent I_{photo} and can be seen in Figure 2.2c.^{7,40,41,57}

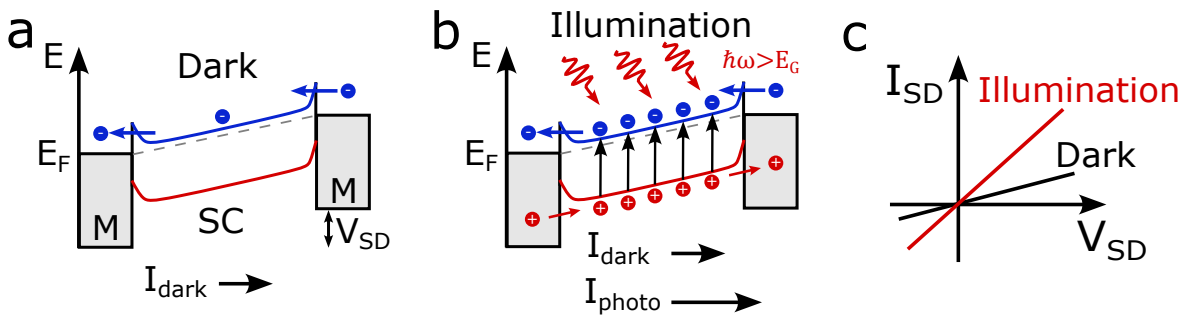


Figure 2.2. Photoconductive effect. **a)** Energy levels of a semiconductor (SC), contacted by two metals under a bias V_{SD} in the dark. **b)** Illumination leads to a photocurrent I_{photo} by separating the excitons with the applied bias. **c)** $I_{SD} - V_{SD}$ characteristic in the dark and under illumination. I_{SD} equals I_{dark} in the dark and I_{photo} under illumination, respectively. Figure similar to Ref.⁷

Although the number of holes and electrons is the same, the velocity of them towards the electrode can show large differences.^{43,58} The time it takes the carriers to transit from the original position of the generated exciton to the electrode is thus based on the mobility μ of the carriers, the channel length g and the applied bias:^{7,41,51}

$$t_{transit} = \frac{g^2}{\mu V_{SD}} \quad (2.4)$$

For different mobilities of the charge carriers, the faster carrier type (majority carriers), for TMDCs usually electrons, can pass the channel faster than the minority carriers (usually holes) and thus get reinjected at the opposite electrode to maintain charge neutrality. This continues until the minority carrier is extracted as well, or recombination takes place.^{40,41,58} A brief overview of the most common mechanisms of recombination can be found in Box 1.

Box 1: Recombination Mechanisms

The most common recombination mechanisms are sketched in Figure 2.3. Band gap recombination is a radiative decay path, occurring at high carrier concentrations and results in the emission of a photon.⁵⁹ Other processes are mainly non-radiative, meaning they transfer their energy either to the lattice via phonons or towards a third particle in the case of Auger recombination, which requires high carrier concentrations.⁶⁰ Induced by (deep) traps within the band gap, Shockley-Read-Hall (SRH) recombination can take place.⁶¹ Here, a carrier has to be inside such a localized interband state. Those states are not close to the band edges in thermal equilibrium as trap states, instead they are deep within the gap. The energy of the transition into this state can either be dissipated by transfer to phonons or by emission of a photon.⁵⁹ At the particle surface a lot of trap states occur, e.g. due to an unsaturated surface, which can facilitate recombination.⁶²

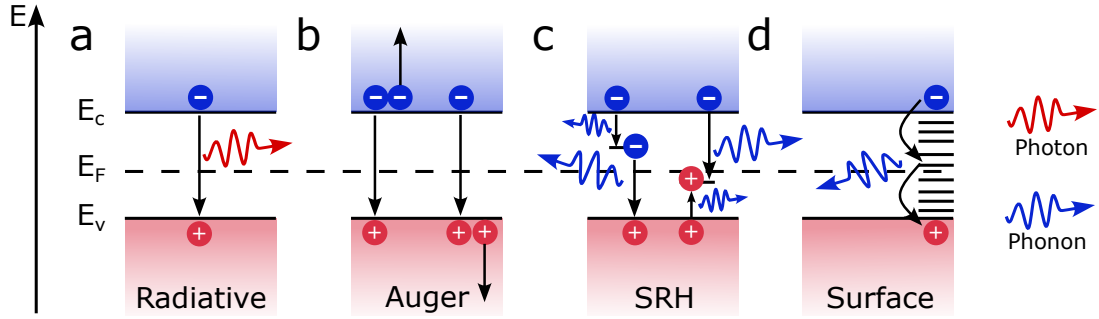


Figure 2.3. a) Radiative decay by band gap recombination. b) Auger recombination occurs for high charge carrier concentrations and requires a third particle on which the excessive energy is transferred. c) Shockley-Read-Hall (SRH), or trap-assisted recombination requires traps within the band gap in which either electrons or holes can be caught. From there they can either get re-excited into the CB or VB or can recombine. This process can also happen radiatively, shown here only non-radiatively. d) Surface recombination occurs in trap states at the surface due to defects or insufficient surface saturation.

Based on the lifetime of the minority carriers t_{life} and the transit time of the majority carriers, a factor can be determined, how often the average electron can transverse the channel before it recombines. This is called gain (G) and can be calculated by the ratio of the two magnitudes^{7, 40, 41}

$$G = \frac{t_{life}}{t_{transit}} = \frac{t_{life} \mu V_{SD}}{L^2} \quad (2.5)$$

Hence, a large deviation between the mobility of the electron and the hole as well as a small channel length and a long lifetime increase the gain. This is closely related to the photogating effect, discussed in more detail in the next section.

Making use of the PC effect in the simplest possible device, an ohmic photoconductor, puts another time influence onto the detector: the RC time. The product of resistance R and capacitance C is omnipresent in electric components, delaying the temporal response.^{40, 52} Further information of the origin can be found in Box 2. To examine or calculate the RC time (experimentally), the resistance has to be determined as well as the capacitance. For

the simple case of a plate capacitor consisting of two parallel plates with an area A and a distance d , the capacitance is

$$C = \frac{\epsilon_r \epsilon_0 A}{d}. \quad (2.6)$$

Furthermore, it is crucial to also account for the parasitic capacitance of the circuitry used for the measurement as well as for the (load) resistance of the setup.⁶³

Box 2: Charging of a Capacitor

Electrical circuits suffer from time delay - the input is not directly transferred into the output. Based on the model-circuit of a resistance in series with a capacitor, see Figure 2.4, this RC delay can be calculated.⁶⁴

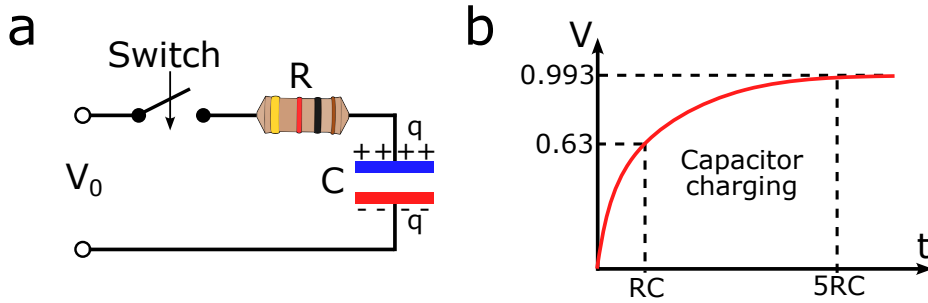


Figure 2.4. a) Sketch of an RC circuit with a switch to start charging of the capacitor. b) Voltage increase at the capacitor over time.

To charge the empty capacitor C in series with the resistance R , the switch has to be closed at time $t = 0$. The charge Q on the capacitor is dependent on the capacitance and the voltage, thus $Q(t) = C * V(t)$. According to Ohm's law, the charging current can be calculated to⁶⁴

$$I(t) = \frac{V_0 - V(t)}{R} = \frac{V_0}{R} - \frac{Q(t)}{RC} \quad (2.7)$$

Since the current is defined as the number of charges transported through a cross section in a given time $I(t) = dQ/dt$, differentiating the equation above yields⁶⁴

$$\frac{dI}{dt} = -\frac{1}{RC} * I(t). \quad (2.8)$$

Integrating back with $I(0) = I_0$ gives the end result for the current and the voltage⁶⁴

$$I(t) = I_0 * e^{-t/(RC)} \quad (2.9)$$

$$V(t) = V_0 \left(1 - e^{-t/(RC)}\right) \quad (2.10)$$

Figure 2.4b shows the time dependency for the charging voltage of a capacitor. After the RC time constant τ_{RC} , $1 - 1/e = 63\%$ of the capacitor is charged. A common approximation for the time to reach steady-state condition is after five times the RC constant, when the charging level of the capacitor is 99.3% .

2.1.1.2 Photogating Effect

Photogating (PG) can be seen as a special case of the PC effect, since the gain is determined in the same way and detectors based on PC and PG need a bias voltage to work.^{7,58} The difference between them is the trap concentration, shown for shallow hole traps close to the valence band in Figure 2.5. They can be distinguished within transistor measurements, requiring an additional gate of silicon and dielectric to influence the charge carrier concentration in the active material. Within those, an $I_{SD}-V_G$ characteristic reveals that the PG results in a horizontal shift, as the trapped carriers act as an additional gate, whereas the PC effect results in a purely vertical one, see Figure 2.5c.⁷ The effect of this gating can be described like an electric field-effect in a transistor, shifting the Fermi level E_F , thereby inducing more electrons in the channel. In contrast to the PC effect, one carrier type is trapped (in an idealized case) completely, consequently prolonging the lifetime.⁴⁰ It has to be stressed, that realistic photoconductors are often a mixture of PC and PG effects and a clear distinction is often impossible.^{58,65}

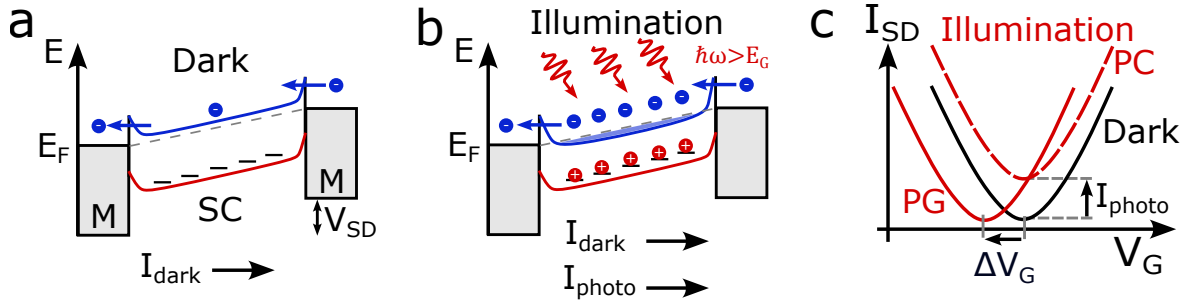


Figure 2.5. Photogating effect. **a)** Energy levels of a semiconductor (SC), contacted by two metals under a bias V_{SD} in the dark. The solid horizontal lines are trap states close to the valence band. **b)** Illumination leads to a photocurrent by separating the excitons with the applied bias. The trap states are filled with holes which act as a local gate, inducing more electrons within the channel. **c)** $I_{SD}-V_G$ characteristic in the dark and under illumination. The dashed line shows the behaviour for the PC scenario, the solid red line for the PG case. Figure similar to Ref.⁷

Depending on the material, screening and doping concentration, recombination lifetimes in the span from 10^{-13} s to many seconds have been reported.⁴⁰ So, incredibly high gain can be achieved, as the lifetime is increased. At the same time, this is directly limiting the temporal response, causing the detector to be slower. Via the temporal response characteristics, the different speeds can be used to try to distinguish between PC and PG.⁶⁵

To account for the trade-off of higher gain and prolonged lifetime vs. low gain and speed, the gain-bandwidth-product (GBP) is a useful measure. In a very simple approximation, which will be further specified later, the bandwidth is roughly the inverse of the time. More information on these key parameters of performance can be found in section 2.1.3. Using the GBP accounts for the trade-off and gives a measure of optimization for photodetectors acknowledging both, speed and gain. Thus, improving detectors should aim for maximising the GBP. Proposed devices which rely on gating induced by a photovoltage at a silicon quantum dot interface (photovoltage-FET) rather than the charge transport and traps within the quantum dot layer (photo-FET), have shown theoretical values of the GBP exceeding 10^{13} , which is higher than the typical 10^9 for photodiodes,

phototransistors and conductors.^{58,66,67} Since those gated devices rely on material junctions they are thus beyond the scope of this work and will not be further described.

2.1.1.3 Photovoltaic Effect

The previously shown mechanisms relied on an applied bias to separate the charge carriers. In contrast, the photovoltaic effect (PV) is based on an internal electric field for charge separation. The origin can be from two differently doped semiconductors forming a pn-junction or from a Schottky barrier occurring between a semiconductor and a metal.⁴⁶ Figure 2.6 shows a pn-junction between a p-type and an n-type semiconductor. They possess an excessive amount of holes or electrons, respectively, thus shifting the Fermi level accordingly. When brought in contact, a junction is formed by adjusting the Fermi energies of the semiconductors. Thus, an internal field is formed which can separate the charges within the so-called depletion region. The I-V characteristic of a pn-diode is given in Figure 2.6c.⁴⁶

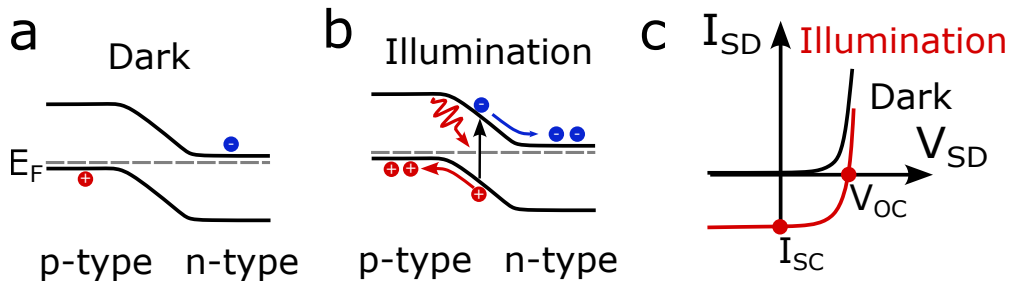


Figure 2.6. Photovoltaic effect. **a)** Energy levels of a p-type and an n-type semiconductor junction with an internal bias inside the depletion region in the dark. **b)** Illumination leads to a photocurrent by separating the excitons within the depletion region. **c)** $I_{SD} - V_{SD}$ characteristic in the dark and under illumination. The open-circuit voltage V_{OC} and the short-circuit current I_{SC} are marked.

Moreover, the forward source-drain current is exponentially depending on an externally applied voltage. In the reverse direction, the dark current is negligible since thermal energy is not enough to overcome the potential barrier of the junction. At some point, junction breakdown will occur and the current will increase tremendously.⁴¹ An open-circuit voltage V_{OC} will be generated for a non-closed circuit due to charge accumulation at the different ends. For no external bias applied, the internal field produces a photocurrent called the short-circuit current I_{SC} , which can be sufficient for photodetection.⁷ A diode based on a pn-junction cannot only convert photon energy into electrical energy, the principle of a solar cell, it can also be operated in either PV or PC mode.^{41,57} By using such a detector at no applied bias, it is operated in the PV mode, among other advantages benefiting from an exceptionally low dark current. On the other hand, operating in PC mode under reverse bias increases the speed of the diode by influencing the capacitance and increasing the strength and width of the electrical field in the depletion region.^{7,55} In contrast to the photoconductor, a photodiode is limited to a gain of maximal one, since no trap states are available within the depletion region.^{40,41,47}

Within this depleted region, the charge carriers experience the acceleration of the internal field, and the corresponding drift time would be calculated similarly to the transit time in

Equation (2.4). Outside of this region, the carriers diffuse until they are eventually reaching the depletion region or recombine.⁴¹ This diffusion length l is overcome in a timespan of⁶⁸

$$t_{diff} = \frac{l^2}{D} \quad (2.11)$$

depending on the diffusion coefficient D , and is limited by the slower carrier diffusion. The diffusion coefficient can be influenced with temperature T and the mobility, according to $D = \frac{\mu k_B T}{e}$, with k_B being the Boltzmann constant.⁴⁷ Since charge carriers in proximity to the depleted region can diffuse to the region at some point, they prolong the temporal response by generating a slow tail within the photocurrent. Hence, the depletion region should be maximized to minimize those diffusive reductions of the bandwidth, for example with p-i-n-detector architectures.⁵⁵ A more detailed comparison of the different diode types and their implications on the response time can be found in Ref.⁶⁹ Since the focus of this work is on single-material detectors, the interested reader is referred to elsewhere for more explanations and calculations on pn-diodes and other diodes relying on more than one active material.^{40,41,47,54,55,70} Instead, in the following section, the focus will be on diodes based on the Schottky junction at a metal-semiconductor interface.

2.1.2 Metal-Semiconductor Interface

Up to this point, the photodetection mechanisms have been introduced and all the effects have been ascribed to the active material. Besides the semiconductor properties, the interplay of semiconductor and metal at the electrode influences the contact type and thus the device type and performance as a whole.

2.1.2.1 Ohmic Contact

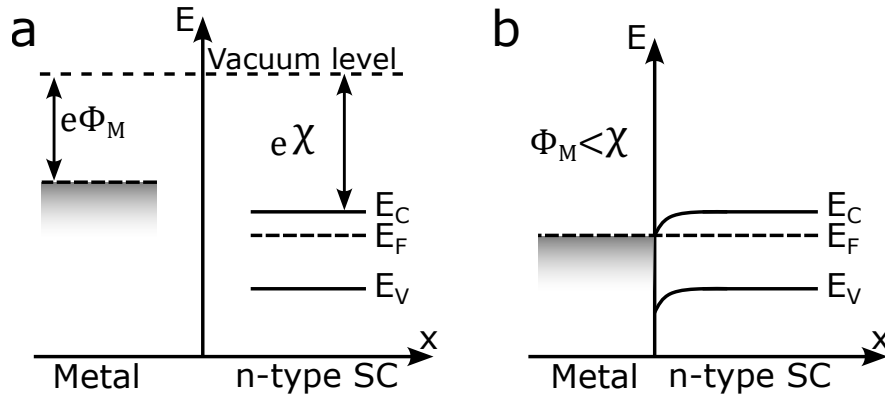


Figure 2.7. Formation of an Ohmic contact. Metal and n-type semiconductor **a)** before, and **b)** after contact. The work function of the metal Φ_M is smaller than the electron affinity χ of the semiconductor.

Determination of the contact type can be done by aligning the band diagram with the work function Φ_M of a metal and the electron affinity χ as well as Fermi level E_F of the semiconductor, see Figure 2.7a. When they are brought into contact, the Fermi levels of both materials will be brought into thermodynamic equilibrium, see Figure 2.7b. This leads

to a bending of the valence and conduction band of the semiconductor. Two cases have to be distinguished: $\Phi_M < \chi$ and $\Phi_M > \chi$. The former leads to an Ohmic contact and the latter to a Schottky junction.^{41,47,71}

This band bending could also be interpreted by the accumulation of electrons out of the metal within the semiconductor due to the higher electron affinity. The higher charge carrier concentration is equivalent to the conduction band approaching the Fermi level. For some applications Ohmic contacts are a necessity, like discussed before, photoconductors with high gain are dependent on them^{41,55} or the fabrication of integrated circuits.⁴⁷ Therefore, it is crucial to have control over the nature of the contact.

2.1.2.2 Schottky Contact

The other possibility, $\Phi_M > \chi$, can be seen in the band diagram in Figure 2.8. This time, after contact a rectifying potential barrier between semiconductor and metal is formed, called Schottky barrier. It can be estimated via the Schottky-Mott rule to^{41,71}

$$e\Phi_{SB} = e(\Phi_M - \chi). \quad (2.12)$$

This approximation may be invalidated for the case of 2D materials or materials with many interface states, where Fermi level pinning can take place, see section 2.1.2.3 for a more detailed description.⁷²

For electrons flowing from the semiconductor towards the electrode or vice versa, Φ_{SB} opposes a potential barrier which has to be overcome, see section 2.1.2.3 for charge injection mechanisms. By applying an additional external bias, the barrier height and width can be further in- or decreased. As the work function of the metal is higher than the electron affinity, when bringing them both in contact, free electrons flow into the metal and a so-called space charge region evolves within the semiconductor.⁴⁷ Thus, the metal semiconductor interface behaves similar to a pn-junction and an internal electric field is formed.

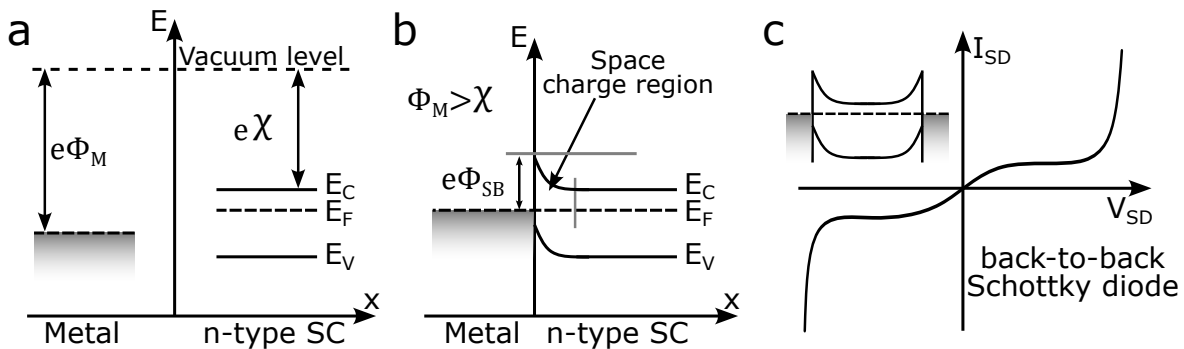


Figure 2.8. Formation of a Schottky junction. Metal and n-type semiconductor **a)** before, and **b)** after contact. The work function of the metal Φ_M is larger than the electron affinity χ of the semiconductor. **c)** I-V characteristic of a back-to-back Schottky diode.

Schottky diodes made of one metal-semiconductor interface are often used in high frequency application.^{40,41,47} But again, like for pn-junctions, the gain is limited to one. For p-type semiconductors which have holes as majority charge carriers, the formation of a

Schottky junction can be achieved in the opposite case, when $\Phi_M < \chi$.

In a typical, symmetrical photodetector architecture, see section 2.1.2.4, two Schottky contacts are employed, which leads to two junctions within the same device in a back-to-back arrangement, sometimes also called a MSM (metal-semiconductor-metal) photodiode.^{70,73-75} Thus, for every applied bias, one of the junctions is in reverse bias mode suppressing the dark current. By tuning the bias voltage, the depletion regions at the electrodes can be varied in their width, influencing the regime in which charge carriers are accelerated by the electric field.⁷⁵ A typical I-V characteristic of such a symmetric device can be seen in Figure 2.8c. For a small applied voltage the current flow looks similar to the Ohmic case (Figure 2.2c), before a saturation regime begins, which is terminated by the breakthrough voltage.⁷⁵

In summary, diodes have better prospects with regard to the dark current and the response speed, as their internal field is favourable for both. The major drawback for diodes is the limitation to a maximal gain of one, which on the other side explains their fast temporal response due to (nearly) no trapping prolonging the charge transport. On the other hand, photoconductors can have a gain much larger than one, by sacrificing their response time with a longer lifetime of the carriers. To control which device is built, the contacting is crucial, since Ohmic contacts are needed for pn-diodes and photoconductors while Schottky contacts are needed for Schottky diodes.

2.1.2.3 Fermi Level Pinning and Charge Injection at a Schottky Contact

The Schottky barrier model applied above considers idealized, defect free interfaces. Under real experimental conditions alloying of metals with the semiconductor or metal-induced gap states alter this idealized picture and consequently lead to a different contacting situation.⁷² Especially surface states are responsible for this effect, making nanoparticles with a high surface-to-volume ratio vulnerable.⁷⁶ In such situations, where the Schottky-Mott rule does not apply any more to calculate the barrier, Fermi level pinning (FLP) takes place. Thereby, the Fermi energy of the metal is pinned at a new level within the semiconductor called the charge neutrality level (CNL), see Figure 2.9a. In other words this could be described as the point above which the energy levels of a neutral surface would be empty, or the energy with the highest surface state density.⁷⁷ Additionally, a pinning factor can be introduced which is a number between one, ideal Schottky-Mott like behaviour, and zero, a strongly pinned interface.⁷⁸ This pinning factor gives a material-specific measure of how much the Schottky barrier may be influenced. For MoS₂ it can be as low as 0.11,⁷⁷ which thus shows, that the work function of the metal might have only little influence on the barrier height.

A deeper insight into FLP with a focus onto 2D materials is given in Ref.⁷⁸ One possibility to reduce FLP is the use of edge contacts, which will be further discussed in chapter 4.

Independent of whether the Fermi level is pinned or not, charges have to overcome the Schottky barrier. Figure 2.9b shows the different possibilities to overcome an idealized Schottky barrier from a metal to a semiconductor or vice versa. Based on the thermionic emission-diffusion theory, the current flow can be described. The dark current over a Schottky barrier is typically thermionic emission over Φ_{SB} .⁴¹

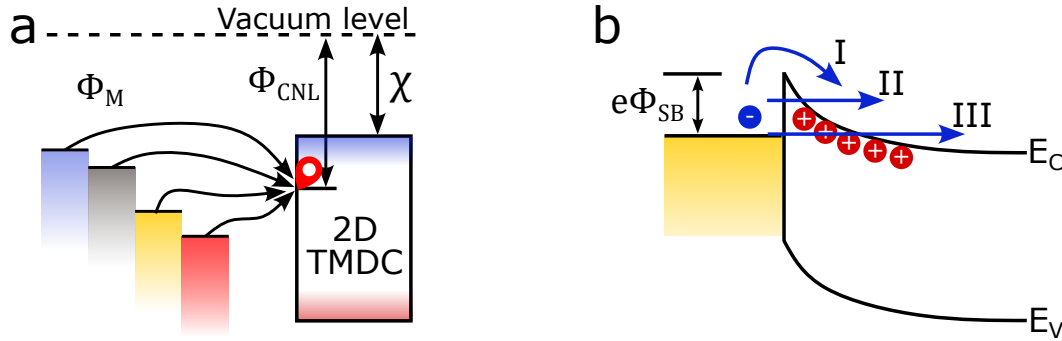


Figure 2.9. **a)** Fermi level pinning of different metals with work function Φ_M onto the charge neutrality level (CNL). Figure similar to Ref.⁷⁷ **b)** Charge injection from a metal to a semiconductor over a Schottky barrier Φ_{SB} . I) Thermionic emission, II) thermionic field emission and III) field emission.

For energies lower than the barrier, tunnelling through the barrier is possible, see II & III in Figure 2.9b. This requires either highly doped semiconductors to enable thermionic field emission (II), or large defect densities at the interface for field emission (III).^{72,79} The additional field dependency of the effects can give further clues, which processes, tunnelling or thermionic, are dominating. For low fields thermionic emission dominates, conversely for high fields tunnelling.⁸⁰

Using exactly these properties of charge injection, one method to determine the Schottky barrier height experimentally is by exposure of the barrier with light of different photon energies lower than the band gap of the semiconductor to trigger internal photoemission in the metal. Those processes are not very efficient with quantum efficiencies η of less than 1 %, but the following formula, called the Fowler-Nordheim equation has been found to describe the dependency between the photon energy $h\nu$ and the barrier height Φ_{SB} ^{41,81}

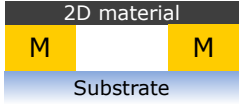
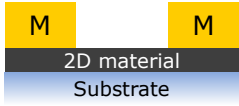
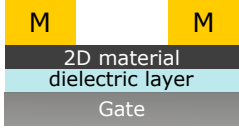
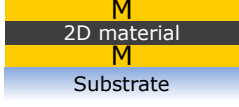
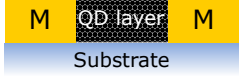
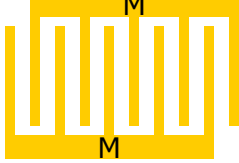
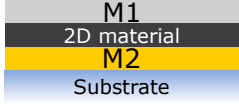
$$\eta = C_F \frac{(h\nu - e\Phi_{SB})^2}{h\nu} \quad (2.13)$$

with C_F being a device specific proportionality factor. By fitting this equation to the obtained measurements, the Schottky barrier can be approximated under certain limitations.⁸²

2.1.2.4 Device Architecture

The possibilities to design devices for photodetection seem almost unlimited. For nanoparticle systems and layered materials (2DM) there are a few types of device architecture that are very common, due to their simple fabrication and possibility to test QDs and 2DMs with them, see Table 1. They can be divided into lateral and vertical structures. Depending on the material, different demands are put on the fabrication process. If the active material is unstable under atmospheric conditions, all the electrode fabrication has to be done a priori, which is possible for bottom contacts like interdigitated electrodes (IDEs). For all the devices, the principle of Schottky or Ohmic contact can be applied and the performance of the device thus further altered. Additionally, combinations are possible like in a semi-vertical geometry contacting once from above and once from below with a lateral shift in between them.^{83,84}

Table 1. Commonly used device architectures for a simple fabrication of photodetectors based on QDs and layered / 2D materials (2DM). The (dis-) advantages are stated briefly as well as exemplary references using this geometry are given.

	Brief description & (dis-) advantages	Refs	Schematic
Bottom contacts for 2DM	Stamping of 2DM on finished electrode structure. + no lithography procedure for material – can induce cracks in 2DM ± no hybridization with electrode	35,38,85	
Top contacts	Electrodes fabricated onto 2DM + precise arrangement of electrode on flake – exposure to solvents & metallizing process	36,86	
Top contacts-bottom gate	Top contacts fabricated on gated substrate + more flexibility by gate voltage – excellent dielectric needed	87–89	
Vertical contacts	2DM / QDs sandwiched between electrodes + short channels in vertical direction – illumination through electrode	90–92	
Bottom contacts for QDs	Deposition of QD solution on finished electrode structure + Material within electrode area – particles needed in liquid phase	37,39,93	
Inter-digitated electrodes (IDE)	Special structure for lateral contacts + large area while maintaining short channel lengths + smaller capacitance ⁷⁵	37,70,94	
Asymmetric contacts	All devices can be build with two different electrode materials. + Built-in electrical field + new functionalities e.g. transparent top electrode for more light transmission – More elaborate fabrication	91,95,96	

For different material classes, different device architectures may have additional benefits or drawbacks which can be further exploited, see chapter 4.

2.1.3 Key Performance Parameters

Comparing the performance of different photodetectors is key in developing better devices. Therefore, various figures of merit are available, independent of the device geometry. In a rough classification for photodetectors, they can be divided into sensitivity and speed. A more detailed overview of the speed limiting times can be found in section 2.3.2. Additional

figures of merit as well as the description of the figures shown here can be found elsewhere.^{7, 24, 40, 41, 54, 97, 98}

Since the operation wavelength limits and / or determines the application of a PD, an important figure of merit is the spectral range of the detector, e.g. limited by the band gap. Thus, all the following figures of merit have to be taken as wavelength-dependent.⁴¹

Rise time. The rise time is a key parameter for this work, and single components of it have already been discussed in previous chapters. With respect to the gain in the context of photoconductors, the lifetime of charge carriers can put a limitation to it. For conductors as well as for diodes, the RC time and transit time can limit the speed and for non-depleted regions in detectors a diffusion time can further limit devices. In general, the response time is given as a rise time or fall time measuring the photocurrent increase from the 10 to 90 % of its final value. For diodes the formula is given as⁹⁹

$$t_{rise} = \sqrt{t_{diff}^2 + t_{drift}^2 + (2.2 * \tau_{RC})^2} \quad (2.14)$$

Since τ_{RC} is a time constant and gives only the 63 % value, see Box 2, it has to be multiplied with 2.2 to account for the difference.

3 dB bandwidth. Closely related to the temporal response is the bandwidth, the frequency-based speed measure. It determines the maximal operation frequency of detection at which two pulses can be distinguished. At this frequency the initial photocurrent has dropped to $\sqrt{0.5} \approx 70\%$ or the power spectrum to 50 %. After Fourier transforming a measured impulse response to the power spectrum $P(\omega)$, conversion to the dB scale is performed with the signal power under steady state conditions (P_1), and the 3 dB crossing can be determined.

$$P(\omega) = |FFT(f(t))|^2 \quad (2.15)$$

$$dB = 10 \log_{10}(P(\omega)/P_1) \quad (2.16)$$

An alternative way to obtain the bandwidth is the often-used approximation

$$f_{3dB} = 0.35/t_{rise} \quad (2.17)$$

However, this approximation can lead to large deviations compared to the much more precise power spectrum, when calculating the bandwidth. The correct determination of the bandwidth will be discussed in more detail in Chapter 3.

Gain-bandwidth-product. A measure independent of the gain-lifetime trade-off is the gain-bandwidth-product GBP. Using the GBP, a better comparison in this widespread area of detectors with different rise times and gain (G) can be achieved.²⁹

$$GBP = G * f_{3dB} \quad (2.18)$$

Going one step further is the normalization of the GBP by the dark current, which takes the sensitivity further into account.⁶⁶

Responsivity. The ratio of photocurrent I_{photo} generated per incident optical laser power P_{laser} ^{7,98}

$$\mathfrak{R} = \frac{I_{photo}}{P_{laser}} \quad (2.19)$$

is important to determine how much output can be expected and thus, how sensitive the detector is towards dim light. It has to be stressed that the responsivity \mathfrak{R} is a value that is highly dependent on the irradiance of the laser in photoconductors.⁵⁸ Hence, estimations of the responsivity at low laser power typically lead to high values. If the laser power needed for operation of the device is much higher, this can lead to an overestimation of \mathfrak{R} .

External quantum efficiency. A related measure for the sensitivity is the EQE, defined as the ratio of photocarriers generated within the material per number of incoming photons^{7,97}

$$EQE = \frac{I_{photo}}{e} * \frac{h\nu}{P_{laser}} = \mathfrak{R} \frac{h\nu}{e} \quad (2.20)$$

The EQE can be seen as a measure of gain, since an EQE higher than one means that per impinging photon more than one charge carrier is measured.⁷ If all photon losses by transmission or reflection at the detector are accounted for and only absorbed photons are used to calculate the quality of the detector, this figure of merit is called the internal QE.^{41,75}

ON / OFF ratio. Taking the dark current of a detector into consideration, the easiest measure is the division of the photo current by the dark current, resulting in the ON / OFF ratio. This value can give an overview of how good a photoresponse is expected to be distinguishable from the background. Besides the dark current, there are many other forms of noise which might suppress a good visibility of a photocurrent, like thermal noise, shot noise or frequency dependant 1/f noise.^{100,101} They can be regarded as noise levels on their own or in form of a noise equivalent power NEP. The NEP gives the minimal illumination power needed to get a signal-to-noise ratio of 1 at 1 Hz bandwidth.⁷

Specific detectivity. By now, the largely different detector sizes are not accounted for. The specific detectivity is an area- (A) and bandwidth- (f_{3dB}) independent measure of sensitivity considering the NEP of the device.⁴¹ Assuming the dark current I_{dark} dominates the noise within the detector it can be rewritten as^{98,102,103}

$$D^* = \frac{\sqrt{A}f_{3dB}}{NEP} = \frac{\mathfrak{R}\sqrt{A}}{\sqrt{2eI_{dark}}} \quad (2.21)$$

Switching energy. Another parameter depending on the bandwidth is the energy needed per individual switching event

$$E_{switch} = P_{laser}/f_{3dB} \quad (2.22)$$

In addition to the pitfalls in determining the bandwidth, other key parameters discussed here can be flawed as well. For measuring the sensitivity this is detailed in Ref.,¹⁰⁴ whereas more general problems like determining the device area are discussed in Ref.¹⁰¹

2.2 Transition Metal Dichalcogenides

Understanding the properties of nanomaterials requires understanding the basic principles of confinement. Thus, upon introducing TMDCs, quantum confinement is discussed briefly. Then, TMDCs are described phenomenologically with some characteristic optoelectronic features highlighted, before the pros and cons of mono- and multilayers with respect to photodetection are weighed up against each other. At last, the question ‘*What makes a good (TMDC) photodetector?*’ will give a short overview of strategies used within the scientific community as well as a comparison of literature photodetectors based on TMDCs.

2.2.1 From 3D to 0D

On the way from the bulk material to the individual atom, different dimensionalities are passed through, which exhibit a distinct change of behaviour in their optical and electronic properties due to their size and spatial confinement. Those dimensionalities can be defined by their level of confinement: the bulk or 3D material electronic and optical properties are the initial state. Reduction in only one spatial dimension leads to thin films, 2D materials, also referred to as quantum wells. Further confinement yields 1D materials, like quantum wires / nanotubes. If the material is confined in all three dimensions, a zero-dimensional quantum dot (QD) is reached. These dimensionalities are shown in the upper row in Figure 2.10.^{43,105} A good measure for confinement is the Bohr exciton radius (Equation (2.3)). Once a material is below this radius in at least one dimension, it is referred to as strongly confined.¹⁰⁵

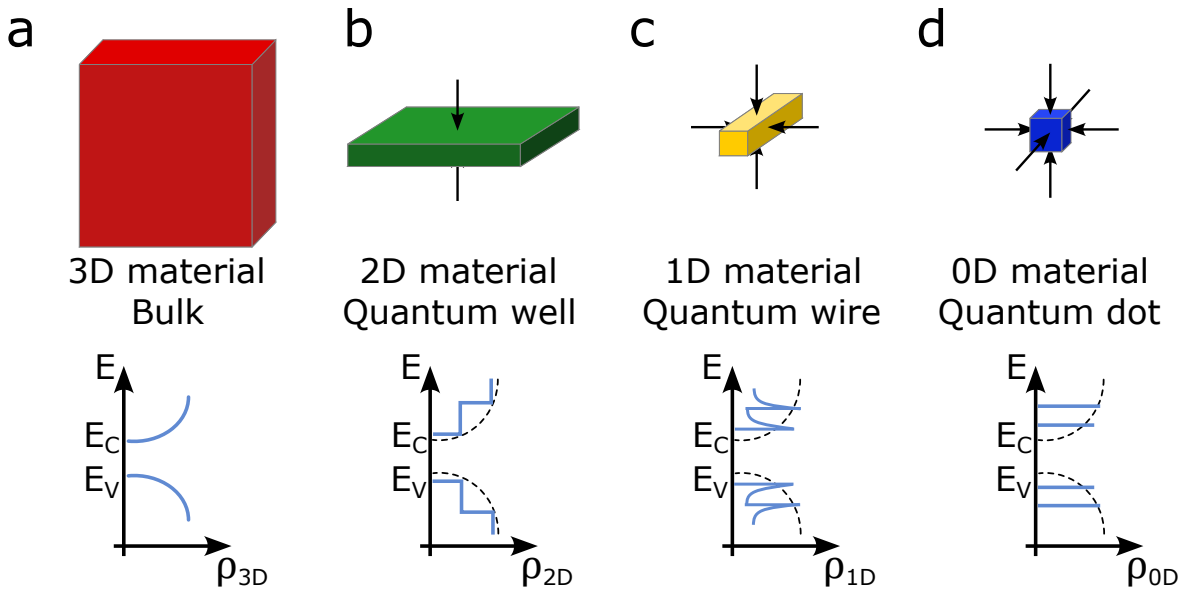


Figure 2.10. Illustration of confined dimensionality and density of states ρ_{nD} for a) 3D bulk, b) 2D quantum wells, c) 1D quantum wires, and d) 0D quantum dots.

The lower panels within Figure 2.10 show the density of states (DOS) $\rho_{\delta D}(E)$ for the free electron gas in 3D and the confined DOS in the lower dimensional materials.¹⁰⁶ Thereby, the DOS is a measure of the number of available states at a specific energy calculated by

deriving the number of (discrete) states per energy.⁴⁶ For a detailed derivation the interested reader is referred to elsewhere.^{46,105,106} The interesting key take aways for 2D and 0D systems is that the DOS is independent of the energy for 2D materials, while it exhibits a delta-function for QDs.¹⁰⁶ With this quantization of energies, the influence on optical and electronic properties evokes new possibilities and phenomena within those confined systems. Recalling Equation (2.2) for the binding energy, the dimensionality δ changes the energy of the n -th state according to^{49,107–109}

$$E_B^{(n)} = E_B * \frac{1}{\left(n + \frac{\delta-3}{2}\right)^2}. \quad (2.23)$$

Ignoring dielectric effects, the binding energy for $n = 1$ would thus be a factor of 4 larger in 2D materials in comparison to the bulk. Considering the change of the dielectric environment around the monolayer, those effects balance each other out, but still high binding energies of several hundred milli-electron volts can be observed.^{49,107}

With size (thickness for 2D materials) being a new degree of freedom influencing the electronic and optical properties, the quantum confinement effect (Figure 2.11) can be used to explain a size dependent band gap.¹⁰⁵ The largest band gap can be seen for a two energy level atom. Adding a second atom, a molecule is formed, in which the interacting orbitals can be described with the molecular orbit model. If now more and more atoms are added to the particle, the number of orbitals with slightly different energies increases more and more until at some point they are so dense they can be described as bands. In this process, the bandgap shrinks for larger particles until the bulk band gap is reached.¹⁰⁵ This is much more pronounced for QDs due to their confinement in three dimensions,⁴³ but also TMDCs and other 2D materials encounter an increasing band gap for thinner flakes.¹⁰⁷ From a different perspective, the quantum confinement can be seen as a limitation to Schrödinger's equation to the particle-in-a-box problem, in which the QD, the box which defines the confinement width, gets smaller and smaller, and thus the energy eigenvalues get more discrete.

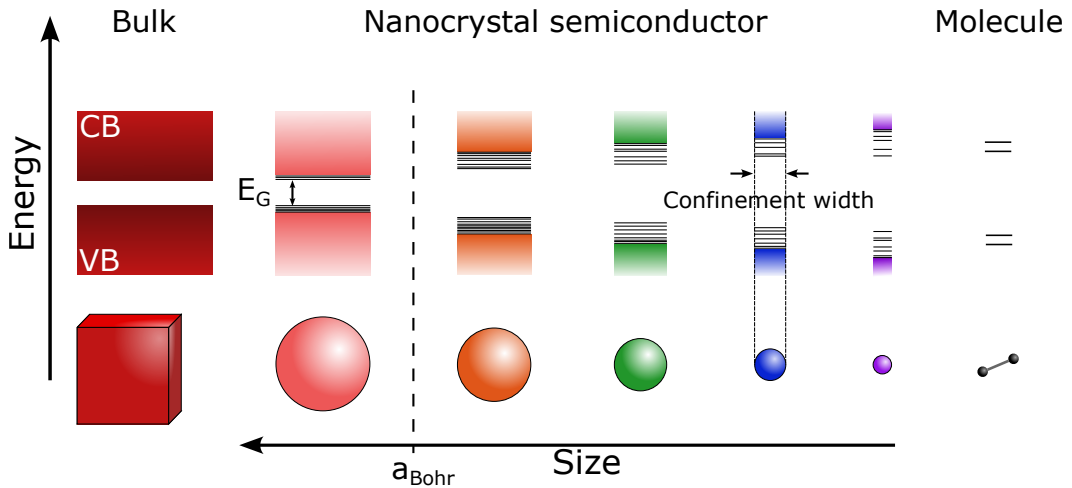


Figure 2.11. Quantum confinement effect of nanocrystal semiconductors showing the increasing bandgap E_G for decreasing particle size. The exciton Bohr radius a_{Bohr} marks the size below which strong confinement starts.

This work focusses on the photodetecting properties of 2D materials, namely TMDCs. Nevertheless, in Chapter 3 and 6 QDs are partially used as photodetection material. A very

brief overview as well as further literature about QDs is thus given in Box 3.

Box 3: Quantum Dots for Photodetection

A typical synthesis of QDs, e.g. lead sulfide (PbS), cadmium selenide (CdSe) or the wet-chemical synthesis of colloidal TMDCs includes long-chain organic molecules like oleic acid and oleylamine as surfactants.^{110–112} Thus, the interparticle distance between individual nanocrystals is rather long and electrical transport difficult. Therefore, short linker molecules with functional groups, like 1,2-ethanedithiol or hydrazine, are needed to couple the QDs, reduce the distance and enable better charge transport.^{110,113,114} The mobility in QD-based devices varies greatly, with most of them having a low mobility of around $10^{-3} \text{ cm}^2/(\text{Vs})$ (due to the above mentioned impact of initial synthesis), but there are also some with a mobility equal to or higher than that of (exfoliated) TMDC components.^{92,115} Nanocrystals have a high surface-to-volume ratio making them vulnerable to surface defects.¹¹⁶ In contrast to QDs, 2D materials have a huge surface as well but no dangling bonds on the surface protecting the material. At the same time, the highly unsaturated surface of QDs opens a chance for tailored surfaces, for instance by coupling them to organic semiconductors.¹¹⁷ Being confined in every direction, the quantum confinement effect is much more pronounced in QDs than in higher dimensional materials.¹¹¹

A promising field for QD based photodetectors is the near-infrared region where applications like night vision are currently based on exotic materials and detectors which need to be cooled, like HgCdTe-devices.^{43,115,118} Based on QDs high-speed detectors have been realised as well.^{119,120}

2.2.2 Properties of TMDCs

The multitude of scientific works covering TMDCs has begun after the discovery of graphene in 2004, although early reports of single layer MoS₂ date back as early as 1986.¹²¹ The general chemical formula for TMDCs is MX₂ (M: transition metal, X: chalcogen). Although there are approximately 40 different layered materials within this class, the most commonly used ones are the group-VI TMDCs, namely MoS₂, WS₂, WSe₂, MoSe₂ and MoTe₂.^{24,28,107} They can occur in different phases, most commonly a trigonal prismatic 2H-phase and an octahedral 1T-phase which may further relax into the thermodynamically more stable distorted 1T'-phase.¹⁰⁸ For MoS₂ for instance a rhombohedral 3R-phase exists as well naturally.¹⁰⁷ In those polymorphs (1T, 2H, 3R) the letter describes the symmetry and the number gives the amount of layers needed per unit cell to describe the phase completely.¹⁰⁷ By phase engineering, the different phases can be converted into each other.¹²²

The bonding situation inside TMDCs can be described with strong covalent intralayer bonds, in contrast to the weak van-der-Waals interlayer bonds at the dangling bond free surface.^{108,123} This makes the material highly mechanically stable within one layer. The layer-like structure of the material gives rise to new preparation techniques like mechanical exfoliation from a bulk crystal.¹²⁴ The further possibility of deterministic transfer onto a substrate sets the foundation for the examination of layer-dependent properties or heterostructures.¹²⁵ Alternatively to the mechanical cleavage, TMDCs can be grown by chemical vapour deposition (CVD) with increasingly high quality.¹²⁶

Apart from the structural features and manufacturing processes, the optical and electric properties of TMDCs are of great interest for research. Due to the rich variety of TMDCs, a lot of metallic and semiconducting phases have been identified with bandgaps from nearly zero (bulk PtSe_2 and PdSe_2) to more than 2 eV in single layer MoS_2 and WS_2 .²⁴ Examinations of layer-dependent properties have revealed a transition from an indirect to a direct band gap semiconductor from a bi- to a monolayer.^{123,127} This strongly influences the photoluminescence (PL) of the material. Layer-dependent emission shifts in the spectral position as well as the absolute PL intensity, which drops by orders of magnitudes beyond the single layer, can be observed.^{123,128,129} Similarly, the influence of the flake thickness causes different Raman shifts, which is together with PL measurements exploited to determine the thickness of flakes.¹³⁰ A complex exciton physics within those materials gives rise to interlayer excitons, bi-excitons as well as charged excitons, so-called trions, all three stable at room-temperature.²⁸ In addition, the Coulomb interactions with the surrounding dielectric may lead to renormalization of the band gap, altering the optical and total band gap.^{45,127,131} Usually, the manipulation of charge by gating or exciton generation is used to drive transistors or photodetectors. 2D materials also allow manipulation of the spin and the valley, which could be exploited to encode or process information in the future. For such technologies beyond the scope of this work, the interested reader is referred to the specialised literature.^{124,127,132–135}

All of the phenomenological properties mentioned above render TMDCs interesting for the next generation of device building blocks in transistors,^{9,136,137} LEDs,¹² advanced memory computing,¹³⁷ solar cells,¹⁰ as well as photodetectors, which are the focus of this work. An indicator for the prospect of a material for application can be the number of publications per year. For the keywords ‘TMDC’ or ‘TMD’ and ‘photodetector’ those numbers are given in Figure 2.12. Since 2010, the number of publications has nearly increased linearly up to more than 100 publications a year, containing those words alone in their title or abstract and nearly 3000 per year containing them in the full text. Thus, the topic is heavily examined by researchers around the world.

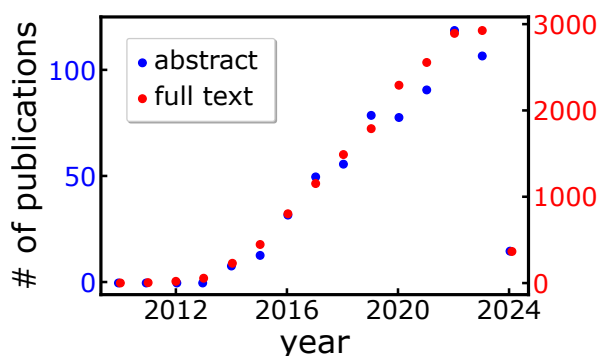


Figure 2.12. Number (#) of publications per year, containing the keywords ‘TMDC’ or ‘TMD’ and ‘photodetector’. Blue shows the numbers containing the keywords in the paper title or abstract and red if they appear within the whole paper. The data was acquired using the tool Dimensions.ai with the numbers as of 09.02.2024.

2.2.2.1 Mono- vs. Multilayer for Fast Photodetection

The question, whether mono- or multilayers are better can be straightforward, if the application relies on photoluminescence (PL). There, the PL decreases by orders of magnitude from the mono- to the bilayer, due to the direct to indirect semiconductor transition.^{128–130}

For photodetection, which relies on the absorption and the generation of charge carriers within the material, this question is not as easy to address. Direct optical transitions, like in monolayer TMDCs, are connected to a larger extinction coefficient than indirect ones.^{46,106} Additionally, intrinsic measurements (see section 2.3.2 for more information) of the material properties suggest that thinner flakes are faster. For MoTe₂ for instance, the response time from 35 nm thick flakes down to 2 nm flakes improved from almost 1 ns to 4 ps. This was attributed to the time the carrier needs from inside the bulk crystal, by out-of-plane drift and interlayer transfer, to get to the top electrode.¹³⁸ A similar behaviour was found for WSe₂.¹³⁹

Other factors, however, must be taken into account for the extrinsic photoresponse, as they may outweigh the inherent intrinsic benefits of monolayers. The longer optical path lengths in multilayers result in a stronger total absorbance and a corresponding increase in photocurrent. Additionally, the lifetimes of surface defects vary depending on the material and its thickness. In the case of MoS₂, a study on thickness dependence displayed extrinsic response times that were three orders of magnitude longer for monolayers than those of multilayers with a thickness of 10 nm. This was attributed to deep surface trap states, which become increasingly screened in the bulk.¹⁴⁰ This defect-related prolonged response time is referred to as persistent photocurrent.^{141,142}

Although intrinsic studies have shown greater potential for monolayers, for photodetectors, the defect related influence seem to dominate the response time. This opens up the question, whether a suitable monolayer with less defects could outcompete bulk flakes?

2.2.3 What Makes a Good (TMDC) Photodetector?

After discussing the basic mechanisms of photodetection and phenomenologically the (opto-) electronic properties of TMDCs, the question ‘*What makes a good (TMDC) photodetector?*’ needs to be addressed with respect to requirements applied in literature:¹⁴³

- **Speed:** operation in the GHz regime
- **Responsivity:** as high as possible, i.e. 1 A/W
- **Noise:** low dark current as indicator for low noise
- **Footprint:** small footprint of few μm^2
- **Compatibility:** CMOS compatible to be implemented in existing technology
- **Manufacturing costs:** preferably low and with simple architecture to enable upscaling of the process

With these requirements in mind, the approaches to solutions based on literature and the fundamentals of photodetection can be made.

Detector type. Based on the demands above, such a detector cannot be based on photogain as it prolongs the carrier lifetime by trapping.⁵⁸ Consequently a diode architecture has to be used and the external quantum efficiency should reach up to 100 % or alternatively, the maximal responsivity of 1 A/W.

Diffusion time. For diodes it is best to design the device in a way in which the

diffusion will play no role - e.g. by shortening the channel length below the width of the depletion region or by extending the depletion region in p-i-n-devices.^{91,102,144}

Mobility. For a fast transit time and a short diffusion time, a high mobility is of importance, since both correlate negatively: $t_{trans}, t_{diff} \sim 1/\mu$, see equations (2.4) and (2.11). In contrast to QDs with typical mobilities in the range of 10^{-5} – 10^{-2} cm²/Vs,⁹² TMDCs possess orders of magnitude higher mobilities around 10–100 cm²/Vs.^{98,103,136} This value is still orders of magnitude lower than for graphene with a predicted maximum of 40 000 cm²/Vs.¹³⁶ Thus, implementing TMDCs with graphene into vdW heterostructures is often done.¹³⁸ Since mobility is such an important parameter, a lot of the following techniques either lead to a better mobility or are depending on it.

Electrode material. A large influence on the contacting situation and thus another possibility to create a diode, aside pn-junctions, is the creation of a Schottky barrier. Closely related to the Schottky barrier formation is the electrode material which has consequently been shown to influence the response time and gain. Thereby, the higher Schottky barrier resulted in the faster device with less responsivity due to less gain and vice versa.¹⁴⁵

Dark current. Assuming only thermionic contributions to the dark current (compare section 2.1.2.3), the dark current is proportional to $I_{dark} \sim \exp(-e\Phi_{SB}/k_B T)$, respectively $I_{dark} \sim \exp(-E_G/2k_B T)$, assuming equal work function of the metal and electron affinity of the semiconductor and the Fermi level exactly in the middle of the bandgap.^{136,146} Thus, a sufficiently high Schottky barrier or band gap is needed to get a low dark current.

Resistance. The photoresistance determines the RC time of a device, thus a lower photoresistance can accelerate it. Thereby, it has to be pointed out that the total resistance R_T consists of a channel / sheet resistance R_{ch} and a contact resistance R_c . For a channel with width W and length L this sums up to $R_T W = R_{ch} L + 2R_c W$, assuming the identical contact resistance at both sides which might not be the case.¹⁴⁷ Thereby, the resistance has to include the width of the device, because the contact resistance depends on the contact area which can be approximated by the width. The channel resistance on the other hand scales with the length of the channel.¹⁴⁷ For 2D materials, the contact resistance can be greatly reduced with edge contacts.⁷² This will be discussed in more detail in Chapter 4 of this work.

Channel length. To further lower the resistance, the channel length can be shortened. For layered materials, vertical detectors create channel lengths only depending on the thickness of the flake.⁹¹ In the lateral dimension this requires advanced lithographic techniques like electron beam lithography, adhesion lithography or edge mediated shadow deposition.^{148–150} A positive side effect to the lower resistance is a much faster transit time, which is quadratically depending on the channel length, cf. Equation (2.4). For layered materials, the interlayer transfer time can further influence the device response time, see section 2.2.2.1, and thus favour one of the geometries over the other.

Simple design. Although implementing complex photonic structures like waveguides has been shown to produce fast detectors based on TMDCs,^{151,152} at the same time the grating needed for coupling makes the footprint large and scalability hard. Hence, a simple

structure, cf. section 2.1.2.4, should be aimed for.

Dielectric engineering. Altering the dielectric environment with so-called high- κ materials like Al_2O_3 or HfO_2 influences the exciton binding energy and can screen charge impurity scattering.^{133,153} Depending on the impurity level, different material combinations may be beneficial.¹⁵⁴ Thereby, not only top dielectrics for simultaneous passivation are of advantage, introducing a thin high- κ layer between the substrate and the material has shown to reduce charge traps and consequently improve the mobility as well.¹⁵⁵ The goal of implementing high- κ dielectrics is to reach the phonon-limited mobility of a material.¹⁵⁶

Interface roughness. Similar to a high dielectric constant, a prominent method is the use of hexagonal boron nitride as smooth substrate, reducing the roughness to get higher mobilities as well as a reduced doping and chemical reactivity.¹⁵⁷⁻¹⁵⁹ hBN can further be taken as isolation layer for gating.¹⁶⁰

Heterostructures. Besides the combination with isolating hBN, two different conducting layered materials, like graphene and TMDCs or p-type with n-type TMDCs can be combined as well. Thereby, faster or more sensitive detectors are achieved by creating pn-junctions or due to new emerging properties, like interlayer excitons below the band gap of the two materials extending the detection wavelength.¹⁶¹⁻¹⁶³ Alternatively to the combination of two 2DM, combining TMDCs with QDs which exhibit a high absorption coefficient, has been shown to increase or extend the responsivity into the near-infrared.¹⁶⁴ Apart from intensifying the photogating effect, other works tried doping to create vertical pn-junctions which showed increased responsivity.¹⁶⁵

Adsorbates. Adsorbates not only influence the mobility by charge impurity scattering,¹⁵⁶ furthermore, they can reduce the (persistent) photocurrent by acting as recombination centers.^{7,166,167} On the other hand, adsorbates can lead to minor carrier trapping which again increases the persistent photocurrent. To circumvent this, passivation with organic molecules has been shown to reduce the photogating.¹⁵³ Other works try to desorb adsorbates by annealing in vacuum which additionally enhances the electrical properties.^{133,150,158} Adsorbates have furthermore shown to also influence the dark current of PDs.³⁸ Alternatively, by using oxygen plasma, an atomically thin oxide layer has been shown to prevent adsorbed traps while improving the responsivity by 24 times.¹⁶⁸

Gating Gating is often used to influence the charge carrier density within the active channel. By using two separate gates, a pure material can be even turned into a homojunction by creating p-type and n-type areas.¹⁶⁰

All those methods are used to provide better TMDC devices. In order to reach the limit of the material-specific response time, the device speed has to overcome any form of transit-/ drift-, diffusion-, life- or RC time limitation. Assessing the rise time and bandwidth of a detector as well as its limiting mechanisms can be done by measuring the time-resolved photocurrent directly. Two principal kind of measurements have to be carefully distinguished from one another: extrinsic and intrinsic measurements. Those will be introduced in more detail in the next chapter. In short, the extrinsic photoresponse is measured to access the speed of the entire device. Thus, it is highly relevant for real

applications, whereas intrinsic measurements determine the material limit by measuring the lifetime circle of the charge carriers from creation of the exciton until recombination takes place. Thus, intrinsic response times display an upper limit which can only be achieved if all extrinsic decelerations like the RC-, transit- or diffusion time are optimized to be faster than recombination. From a different perspective, the intrinsic techniques allow measurements of the fastest processes inside a photodetector, whereas extrinsic measurements reveal the slowest process.

Furthermore, a high responsivity should be reached to measure with high sensitivity. To get an overview of the discussed solutions and where they put TMDC based photodetectors, the figures of merit responsivity and speed can be plotted for the devices. Figure 2.13 shows the responsivity and the corresponding response time of various devices found in literature. For greater clarity of the plot, the detailed data and linked sources can be found in Table 2 in the Appendix, which is why they are not marked directly in Figure 2.13.

The responsivity depends non-linearly on the laser power, which can lead to a high maximum responsivity at a low laser power. At higher laser power, often used for speed measurements, it might be significantly lower. To account for this, the graphic tries to take the responsivity at the same set of parameters such as laser power, which are used for the determination of the speed response. Otherwise, this could overestimate the responsivity. Accordingly, the values for \mathcal{R} may vary by orders of magnitude in comparison to those usually found in reviews showing such plots.

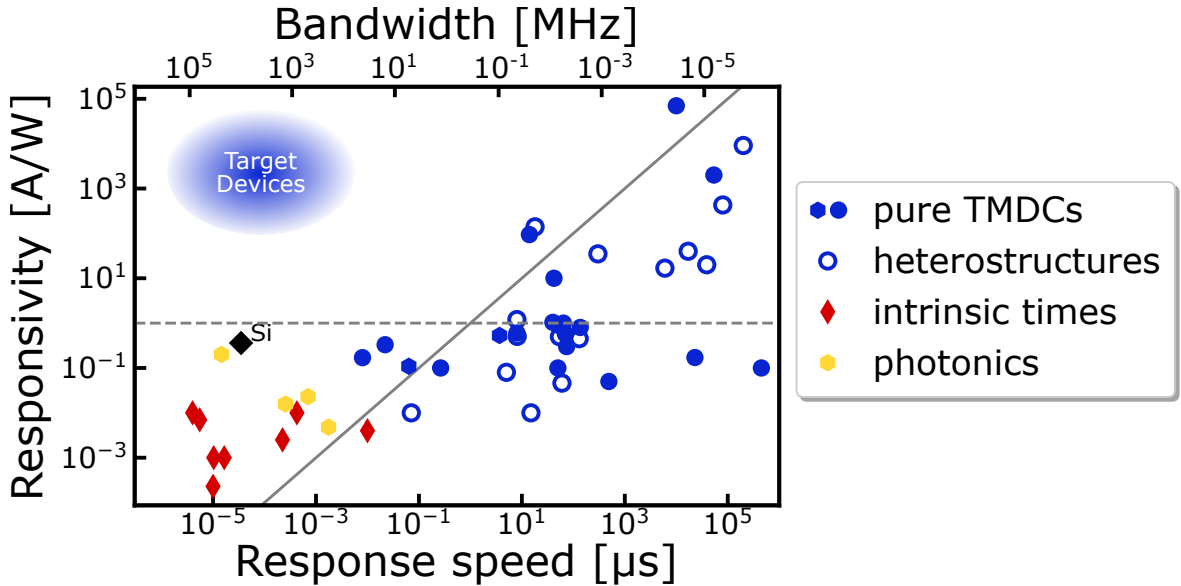


Figure 2.13. Overview of responsivity vs. speed for photodetectors from literature. The tables and corresponding sources can be found in the Appendix. The horizontal dashed line is the maximum responsivity for diodes. The solid grey line shows where $R/t = 1A/(W\mu s)$ which approximately correlates to a GBP of 10^6 . The bandwidth axis and the response speed axis are connected via Equation (2.17). The hexagonal blue and yellow markers are referred to the bandwidth, the red diamonds and blue circles to the response speed. A commercial silicon diode is given as reference.

Some studies measure the speed as a function of frequency and thus provide only the bandwidth. Such values are shown as hexagons whereas the time values are displayed as circles. Full circles depict pure material detectors and Schottky diodes or split-gate tuned homojunctions. Empty circles depict material-based heterojunctions between TMDCs and QDs, other TMDCs, BP or graphene. In yellow, detectors based on complex photonic structures are shown. The intrinsic response time constants are shown in red. Since for intrinsic measurements a responsivity is not always given for those values only the time is of relevance. Within this plot, the focus is on the fastest devices presented in literature, further data of slower devices can for example be found in similar plots in the following reviews.^{7, 29, 97, 98, 160, 162, 169–172}

Based on this literature comparison, it becomes obvious that only few extrinsically measured detectors based on TMDCs, without photonic integration, are faster than the microsecond regime. Furthermore, it has to be stressed that the direct comparison between intrinsic and extrinsic time is not possible without further ado and is made here to provide an imagination of the orders of magnitude which are left for improvements.

2.3 Investigation of (Opto-) Electronic Properties

Investigating the optoelectronic properties of TMDCs requires a measurement setup which enables illumination with light as well as electrical readout. The setup used is based on the work of Dr. Christine Schedel.⁶⁹ A detailed list of which measurement setup and devices are used for the examination is given in the respective part of each of the following chapters. Here, an overview of the important core issues of reliable optoelectronic measurements at high-speed is given, as well as a scheme of the measurement setup.

2.3.1 Conductivity Measurements

Measuring an electrical response or the conductivity of TMDCs requires the flake to be connected to metal pads which can then be connected to an external circuit via conducting, e.g. gold coated, tips, cf. Figure 2.14. By measuring the I-V characteristic the dark current and photo current magnitude can be extracted. Furthermore, the curve progression can give hints, whether the detector is a diode or a conductor, cf. Figures 2.8c, 2.6c and 2.2c for dark currents and I-V characteristics under illumination.

2.3.2 Time-Resolved Photocurrent Measurements

2.3.2.1 General Setup Considerations

The implementation of an experimental setup to measure time-resolved optoelectronic properties needs to consider both the sensitivity of the setup, as well as the bandwidth of the optical and electronic parts. In general, the least possible number of adapters and the shortest cable length is always desirable. Additionally, a Faraday cage surrounding the sample and tips is necessary to shield the sample from disturbing noise. To further minimize noise, the electrical circuit should be impedance matched to $50\ \Omega$. Thus, a probe station is often used for such experiments, with the additional possibility to cool the sample under vacuum down to 8 K or to measure in different environments like nitrogen or vacuum. A scheme of the setup is shown in Figure 2.14.

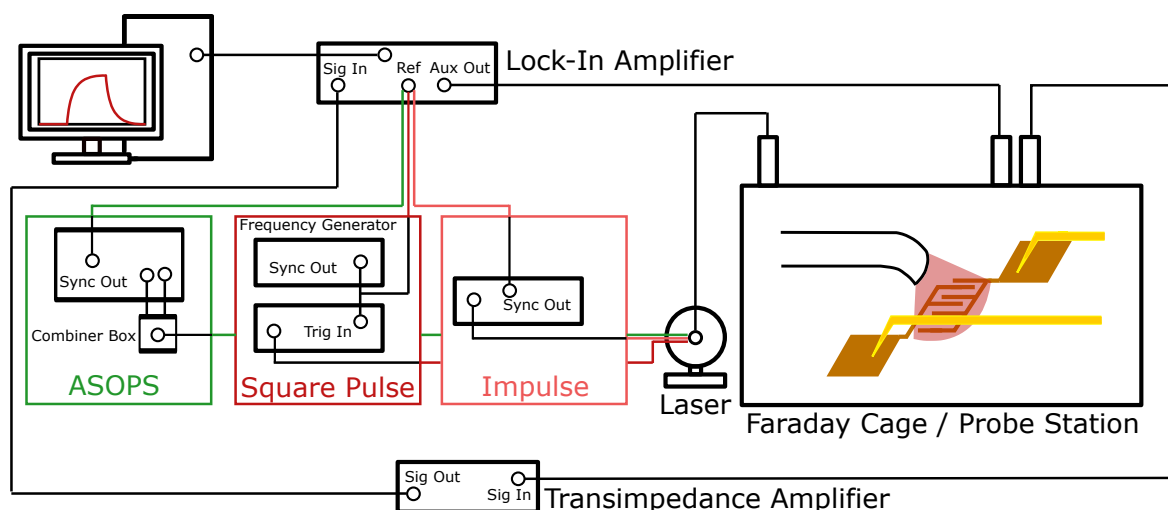


Figure 2.14. Sketch of the measurement setup used for the time-resolved optoelectronic measurements throughout this work. Adapted with permission from Ref.³⁷ Copyright 2021 American Chemical Society.

For measuring the extrinsic properties of a device with a square pulse or an impulse laser, the electrodes are connected to the external circuit inside the Faraday cage e.g. via tips. Before connecting to the measurement device, an oscilloscope or a lock-in amplifier (UHF Lock-In; Zurich Instruments used for the studies), a transimpedance amplifier (TIA) may be used to amplify the output current into a measurable signal. Hereby, the bandwidth of the cables, the TIA and the lock-in should be suitable for the sample speed. If the bandwidth is too low, then the high frequency signals get slowed down. If a bandpass filter is used e.g. from 10 kHz to 2 GHz, then slow signals may be even lost completely, and the results might get falsified. Also, the smallest bandwidth within the circuit limits the whole circuit to this bandwidth. A more detailed description of which instrument is used for which work can be found in the material and methods section of the publications in the following chapters.

For the measurement of the intrinsic times, only the laser is exchanged to the ASOPS laser system. The detuning frequency is provided to the lock-in system and the cables are connected as usual.

2.3.2.2 Extrinsic Measurements

Two different kinds of illumination styles are used in this work: square pulse illumination simulating steady state conditions and delta-function like impulse measurements simulating non-equilibrium conditions, or rather realistic conditions of optical transmission. A sketch of the two different illumination patterns can be seen in Figure 2.15.

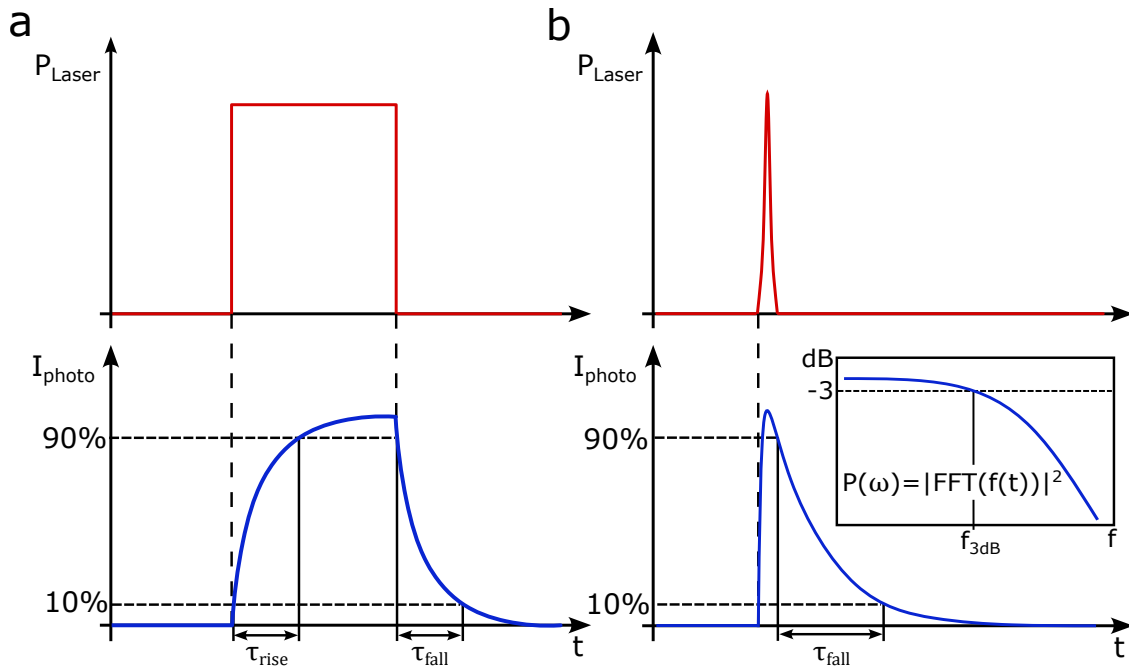


Figure 2.15. Scheme of a) square pulse and b) impulse illumination. The upper graph shows the laser power and the lower graph the idealized device response plotted against time. The 10 % and 90 % levels of the photocurrent are drawn with dashed lines to sketch the respective rise and fall times. The inset in b) shows the power spectrum in the dB-scale acquired by the given formula.

Depending on the illumination style used, different information can be obtained. Using square pulses, the steady state is simulated, meaning, the detector is saturated to the highest possible photocurrent. If trap states within the material enable photogating / persistent photocurrent, this becomes visible in these measurements, since traps typically take longer to be filled.^{58,141,142,173} Additionally, the square pulse offers examination of the rise and the fall time of a system either by measuring the time difference between the 10% and 90% photocurrent level or by (multi-) exponential fitting of the rising / falling flank.¹⁵³ Square pulse measurements are ideal to observe the influence of an altered photodetector e.g. by experimentally adjusting fabrication, active material or geometry towards their influence on the rise (fall) time. A short guide on how to determine the limiting mechanism is given in Box 4.

Box 4: Determination of the Speed Limiting Mechanism

Understanding the speed limiting mechanism is key in improving the response time of a photodetector. In the following, a short guide on how to determine the limiting mechanism is given.

RC time limitation. $t_{RC} = R * C$

A variation of the irradiance in a non-saturated system is the simplest way to observe an RC time limitation, since the photoresistance correlates positively with the response time. In addition, the time can be calculated or estimated via measuring or approximating the capacitance and the resistance. Equation (5.1) can be used for estimating the capacitance of IDEs, while the resistance can be measured.

Transit time limitation. $t_{transit} = L^2 / (\mu V_{SD})$

By changing the applied voltage, hints towards a transit time limitation which correlates negatively with the voltage can be obtained. If the mobility of the material is known, the transit time can be calculated to verify or reject the hypothesis of a transit time limitation. Changing the channel length is a possibility too, but this simultaneously alters the RC time and the diffusion time if non-depleted regions are present.

Diffusion time limitation. $t_{diff} = l^2 / D$

Diffusion is only present if there are non-depleted regions in the detector. So either by increasing the voltage in reverse diode direction, the depleted regions can be extended,⁴⁷ or by shrinking the channel size, the non-depleted regions can be diminished. Furthermore, if the calculation of transit and RC time is significantly faster than the rise time, exclusion process suggests diffusion limitation.

Lifetime limitation. t_{life}

Lastly, the lifetime and thus, gain, could limit the detector. This should be visible when calculating the gain or the EQE directly, since values larger than one are expected, assuming a moderately fast transit time.

For lateral detectors, the z-direction, in other words, the film thickness, is sometimes neglected. However, its implications on the above-mentioned times make it a crucial parameter in observing the time limiting mechanism.⁹²

For measurements with a deltafunction-like impulse (Figure 2.15b), the rise time is not significant, since it is solely depending on the laser pulse width and the measurement

system. The fall time can either be evaluated as usual to obtain the 90 % to 10 % fall time or the decay can be fitted with exponential and / or power law fits. For the latter, the initial decay usually represents the exponential recombination mechanism of the material and initial trapping of charge carriers. The slower tail is often dominated by trap states. Influenced by the number and depth of trap states this decay can for example follow a power law. Via Equation 2.15, the impulse measurement readily affords the 3 dB bandwidth via the power spectrum. This bandwidth has the highest relevance for application.

2.3.2.3 Intrinsic Measurements

Revealing the intrinsic temporal material limit is also a measure for the prospects of this material in a photodetector. On the contrary to extrinsic measurements, which rely on one single laser, to determine the intrinsic times, all-optical methods are required, such as the two-pulse coincidence (2PC) technique shown in Figure 2.16.

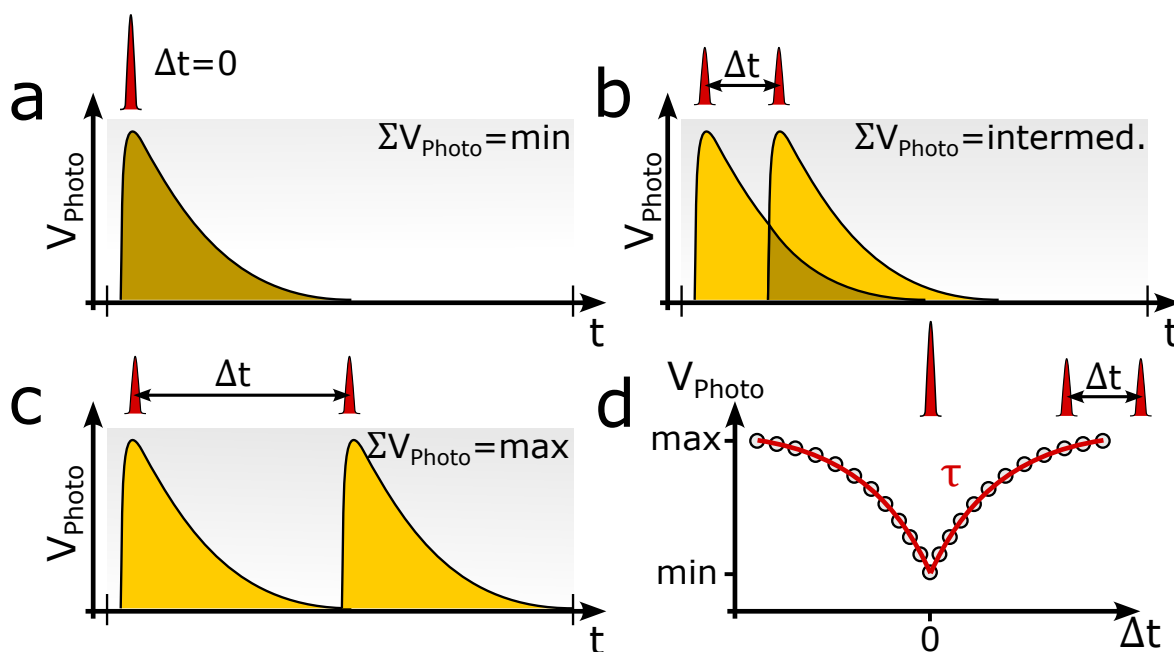


Figure 2.16. a) For no time delay Δt , the two pulses overlap completely and the photovoltage will thus be minimal, if the lasers saturate the system. b) With increasing delay time, the overlap between pump and probe laser decreases and the photovoltage will display an intermediate value. c) With large delays between the pump and probe laser, each laser will excite the sample completely, if the relaxation of each pulse is completed before the next laser coincides. The photovoltage is then maximal. The final graph, which will be measured, is sketched in d). The characteristic time constant τ of the exponential process can be extracted by fitting. Adapted with permission from Ref.³⁹ Copyright 2022 American Chemical Society.

A first laser pumps the material into the excited state. After a short delay time Δt , a second laser probes how many charge carriers can be re-excited. For small Δt the re-excitation rate is low, and the resulting signal small. With variation of the delay time, the intrinsic photoresponse can be reconstructed measurement point for measurement point and

the resulting signal be measured at every point in time. Once the second laser can re-excite all charge carriers, the signal gets to its maximal value. All the measured data points for the different delay times are plotted in one graph and the time constant can be extracted by fitting of the data. For this principle to work properly, the saturation of the sample is crucial, otherwise a coinciding pulse or a small delay time would result in twice the photocurrent, and they could not be distinguished from two separate pulses with large delay. The saturation thus puts a limit on the depth of the resulting graph of 50 % in an idealized system which is completely saturated by the first pulse.

The obtained time constant τ_{in} resembles the entire lifetime of the carrier:

$$\tau_{in}^{-1} = (\tau_d + \tau_s)^{-1} + \tau_r^{-1} \quad (2.24)$$

with τ_d and τ_s , the charge carrier drift time and transfer time, respectively. Thereby, the drift time constant is similar to the drift / transit time discussed before and the transfer time resembles a charge transfer e.g. between two materials or two layers in the case of TMDCs. τ_r is the recombination time of the charge carriers. Typical values of τ_{in} vary from several picoseconds to hundreds of nanoseconds.¹⁷⁴ The accessible time window of the 2PC method is defined by the largest possible delay time of the correlated pulses. At the lower end, the pulse width of the laser limits the resolution. Consequently, a temporal resolution down to tens of femtoseconds is possible.

Conventionally, the 2PC, also called photocurrent autocorrelation technique, relies on splitting a laser beam and delaying one of the resulting beams with a mechanical delay line before recombination of the then cross-polarized beams by a translation stage. For each delay time created by the delay line, one photocurrent is measured and the correlation is thus reconstructed point by point. A more sophisticated method of achieving the same result is by asynchronous optical sampling (ASOPS). The working principle of ASOPS is similar, but a detuned repetition frequency δf of the pump laser relative to the probe laser is used to form a pump-probe delay. When the first pulses coincide, the difference in repetition frequency Δf creates a successive offset for the subsequent pulses as a delay time. The delay time window displayed in the end is determined by the repetition frequency of the laser as $1/f_{rep}$ and amounts to $1/100\text{ MHz}=10\text{ ns}$ for the one available in this work (Chapter 6). The scan resolution Δt_0 , assuming a deltafunction-like pulse, is determined by the offset frequency and the repetition rate f_{rep} as³⁹

$$\Delta t_0 = \frac{\Delta f}{f_{rep} * (f_{rep} + \Delta f)} \sim \frac{\Delta f}{f_{rep}^2}. \quad (2.25)$$

This equals 10 fs for a detuning frequency of 100 Hz, which can subsequently become worse by the pulse width. The advantage of using ASOPS over the delay line is the time efficiency and elimination of mechanical vibrations in the delay mirrors. The acquisition time in ‘real time’ is just $1/\Delta f$, which would be 10 ms for $\Delta f = 100\text{ Hz}$. Additionally, the time window covered by ASOPS, is much larger in comparison to typical literature time windows in the picoseconds up to 250 ps^{30,138,175} and rarely nanoseconds.^{176,177} A drawback can be jitter and the limitation to one laser wavelength within one ASOPS laser system.

2.3.3 Confocal Microscopy

Confocal microscopy is a commonly used technique in life science to improve image quality by cutting of a lot of disturbing out-of-focus information with a pinhole. For imaging

purposes it offers a vastly improved z-resolution and by scanning, images can be reconstructed that offer much higher resolution than in conventional widefield microscopy.⁶⁴ Those advantages are not equally beneficial for characterizing photodetectors as for high-resolution imaging and are therefore not described in detail here, the interested reader is referred to the following Refs.^{64,178,179}

The key take away of confocal microscopy for this work is the improved spatial resolution. In an optimized setup, the illuminated area is only limited by the diffraction limit and the observed area can be approximated by a so-called Airy disk. The minimal size of the focused light is limited by the wavelength λ and the numerical aperture (NA) of the objective used. The diameter D can be calculated according to $D_{Airy} = 1.22 * \lambda / NA$.^{64,180} Thus, the irradiance, the radiant flux per surface area, can be enhanced drastically when reducing the size of the illuminated area by confocal microscopy. A drawback of this method is the reduced intensity of the laser beam due to the blocking of light which is off-center by the pinhole. A sketch of the confocal microscope used in the course of this work can be found in Figure SI5.15.

2.4 Microfabrication Techniques

The field of microfabrication enables building devices like transistors or photodetectors with precise electrode geometries, defined material thicknesses and highly-customizable samples as well as commercialized mass productions of computer chips or similar integrated circuits. The seemingly endless possibilities and methods are beyond the scope of this work and the interested reader is referred to elsewhere.^{181–185} In this section, the methods for fabricating the devices used in this work are briefly introduced and explained.

2.4.1 Mechanical Exfoliation

For this work, the TMDC crystals are mechanically cleaved from bulk following the deterministic transfer method.¹²⁵ In short, an optical microscope equipped with a transfer stage for micrometer precise control of the three axes is needed for this procedure. The TMDC (MoS_2 or WSe_2) is cleaved once with a sticky scotch tape. From there, the flakes are transferred to polydimethylsiloxane (PDMS) on which a suitable flake for stamping can be determined with the microscope. Hereby, it is important to mention that this process is statistical and parameters like the peel-off speed of the adhesive tape may influence the procedure. Once a flake with a suitable morphology is found, the PDMS stamp is pressed onto the final substrate at the position of interest. After a few minutes, the stamp is slowly and carefully peeled-off and in the ideal case, the transfer is complete.

2.4.2 Optical Lithography

For microfabrication it is crucial to minimize contamination sources and thus, if possible, all the steps should be done in a clean room environment.

The cleaned and HMDS (hexamethyl disilazane) functionalized glass substrates either with or without TMDC flake on them are the basic substrate used throughout this work. Thereby, the HMDS is necessary as adhesion agent between the photoresist and glass substrate. The multi-step process of lithography is schematically illustrated in Figure 2.17. First, an UV-sensitive photoresist is spin-coated onto the substrate. By adjusting the rotation parameters, the thickness can be controlled. Subsequent soft baking is used for curing of the resist. In the next step, the resist is selectively exposed to UV radiation to alter its solubility. Therefore, two different kind of resists have to be distinguished: negative and positive resist. For positive resists, the exposed parts become better soluble in a subsequent development step. Conversely, negative resists polymerize and thus become insoluble at the exposed parts, whereas the unexposed parts retain their solubility.¹⁸¹

The selective exposure is conventionally achieved with a mask, displaying the pattern which has to be transferred into the resist.^{181,184} Instead of using such a mask-based technology to control the light, a pixel array of mirrors can be used instead of selective exposure of the resist using a so-called maskless aligner.¹⁸⁶ This combines two advantages for the deterministic fabrication of electrodes exactly on top of a TMDC. On the one hand, the flake can be specifically targeted and positioned with the included microscope. On the other hand, the electrode design can be tailored to the flake and is not rigid and fixed like in a mask, where each design needs an extra mask.¹⁸⁶ Following the exposure is the development of the structure by dissolving the better soluble parts of the resist.

After development, the shown lithographic scheme can be extended by an additional step of reactive ion etching (RIE) with the patterned resist being an etching mask for the underlying substrate. Inside a chamber, radicals and ions are accelerated by an external field towards the sample and a mixture of selective etching due to the used plasma, like O_2 or SF_6 , and physical ion bombardment takes place.¹⁸¹ Within this work, this process is used to selectively etch TMDCs at the positions of the electrodes, leading to edge contacts, cf. Chapter 4.

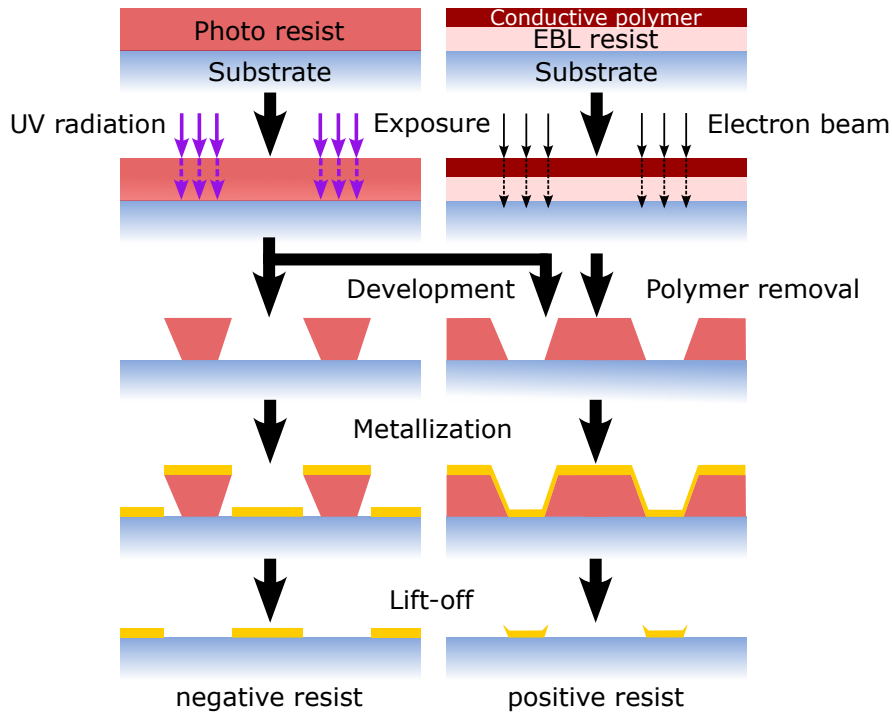


Figure 2.17. Scheme of optical and electron beam lithography for positive and negative resist based on the fabrication performed in this work.

Independent of whether RIE was utilized or not, next, the sample is metallized with the desired material in an evaporation machine. This is either done by thermal evaporation until the material evaporates and condensates on the substrate surface or by electron beam evaporation, in which the material is bombarded with electrons until it evaporates.¹⁸⁴ Usually an adhesion layer of e.g. titanium is needed for gold to better stick to the substrate.¹⁸¹ Lastly, in the lift-off the residual resist is dissolved and with it the metal which is not in direct contact with the sample surface. Consequently, only the electrode structure remains and the samples are ready to be characterized. Although the features of negative and positive resist are exaggeratedly drawn in Figure 2.17, negative resist often exhibits some undercut see step 4 in Figure 2.17, due to the exposure of the parts that remain.¹⁸¹ Thus, in the lift-off they tend to form smoother edges than positive resist structures, which suffer from small spikes which could influence the stamping process for bottom contacts.

2.4.3 Electron Beam Lithography

Electron beam lithography (EBL) has the same basic principle as optical lithography, cf. Figure 2.17. By switching from a UV light source to an electron beam with much shorter wavelength, the resolution can be drastically improved, depending on the scanning electron microscope (SEM) down to a few tens of nanometer or less.¹⁸⁴ For close packed structures, proximity effects induced by the scattering of the electrons inside the material can limit the resolution and have to be corrected for.^{182,184} During exposure with electrons, the resist is charged and at some point, this negative charge would deflect the incoming electron beam and worsen the resolution. To account for this, either a thin conductive layer is deposited underneath the resist, which would short-circuit electronic measurements later on, or a conductive polymer layer is spin-coated on top to prevent charging.¹⁸² This conductive layer has to be removed before the development of the electron-sensitive resist. Since this process takes long due to the scanning with high resolution, positive electron beam resist is used.¹⁸²

2.4.4 Characterization Methods

Accompanying the time-resolved photocurrent investigations of TMDCs are other methods to determine experimental parameters like electrode spacing or thickness of the flakes.

Profilometry. A common method to determine the surface topography is profilometry. Herein, a diamond stylus presses with a defined force onto the sample and is then moved linearly across its surface.¹⁸⁷ The obtained profile can be used to determine a flake height.

Scanning electron microscopy. For size features below the diffraction limit of visible light, an SEM is used due to its nanometer resolution. Thereby, either lateral structures can be resolved with great detail or by tilting the sample a cross section, and thus a height profile can be observed and measured.

Photoluminescence. Having distinct PL features that vary with thickness and from material to material, analysing the emission of TMDCs is a great tool to distinguish atomically thin flakes (one to three layers) with only minimal changes in their height profile.¹³⁰

3 Pitfalls in Determining the Electrical Bandwidth of Nonideal Nanomaterials for Photodetection

Christine Schedel^{1,a}, Fabian Strauß^{1,2,a}, Marcus Scheele^{1,2,}*

¹ Institute for Physical and Theoretical Chemistry, University of Tübingen, 72076 Tübingen, Germany.

² Center for Light-Matter Interaction, Sensors and Analytics LISA+, University of Tübingen, 72076 Tübingen, Germany.

* Corresponding author

^a These authors contributed equally.

This chapter is based on the publication in *The Journal of Physical Chemistry C*.

3.1 Abstract

The electrical 3 dB bandwidth is regularly used as a measure for the response speed of a photodetector and is estimated via various approaches in literature, ranging from direct measurements to gauged values via approximations. Great care must be taken when comparing these 3 dB bandwidths, since approximations are only strictly valid for ideal circuits. This paper demonstrates that, for typical photodetectors based on new emerging nanostructured materials, namely quantum dots and transition metal dichalcogenides, the bandwidth can deviate up to 10^3 depending on the chosen approach for the bandwidth specification.

3.2 Introduction

For the development of new materials and devices for time-resolved (opto-) electronics, the analysis in the time- or frequency-domain is a pivotal task. Nearly a hundred years ago, a first connection between those two domains was established by K upfm uller's uncertainty principle,¹⁸⁸ which laid the foundation for connecting the electrical bandwidth to the time-response in telecommunication. In data transmission and receiving, the bandwidth is a crucial measure for the maximum frequency of device operation under which two data points can still be distinguished. Traditionally, the 3 dB bandwidth is taken, which is the frequency at which the power of the response has decreased to fifty percent.^{111,189} The main approaches for determining the electrical 3 dB bandwidth of a photodetector are either direct measurements in the frequency domain^{27,190} or measuring the time-resolved photocurrent vs. varying laser repetition rates.^{66,191–193} If only one repetition rate is chosen, the impulse photoresponse ($f(t)$) is regularly used to calculate the power spectrum ($P(\omega)$) via fast Fourier transformation (FFT):^{68,194–202}

$$P(\omega) = |FFT(f(t))|^2 \quad (3.1)$$

Upon normalization against the power under steady state conditions (P_1), the electrical bandwidth is obtained according to $dB = 10 \log_{10}(P(\omega)/P_1)$.

Another, more convenient approach involves the analysis of the response time (τ) or the rise-time (t_{rise}) obtained by time-resolved square pulse-^{66,192,203} or sinusoidal-^{203–205} illumination of the device. However, these techniques require a conversion formula to approximate the 3 dB bandwidth f_{3dB} , and by far the most commonly used one is:^{22,190–192,203,206–212}

$$f_{3dB} = 0.159/\tau = 0.35/t_{rise} \quad (3.2)$$

We stress that this approximation only holds true for ideal circuits consisting of an RC-device behaving like a first order pole low-pass filter.^{213,214} Other approximations used range from $f_{3dB} = 1/t_{rise}$ ^{215–217} up to $f_{3dB} = 2.2/t_{rise}$.²¹⁸ In addition, Equation (3.2) is also applied to infer the 3 dB bandwidth from the impulse response of a material by inserting the fall time in place of the rise time into Equation (3.2).²¹⁹

In light of the growing attention devoted to nanomaterials and their photodetecting properties,^{220,221} we note that the above-mentioned approximations are frequently applied, although many nanostructured photodetectors are far from representing ideal circuits and the required first order pole low-pass filter characteristics. This is likely to introduce inconsistencies in the reported 3 dB bandwidths with potentially misleading conclusions for the comparison of studies that apply different methodologies for determining f_{3dB} . The purpose of this work is to evaluate the magnitude of the deviations in f_{3dB} for typical nanomaterials when the ideal circuit approximation is applied compared to the exact

bandwidth determinations outlined above. Specifically, we investigate a commercial silicon p-i-n photodiode for reference, two detectors based on quantum dots (QDs) and two devices made from the transition metal dichalcogenides (TMDCs) MoS₂ and WSe₂. The QD detectors are iodide-capped CdSe QDs crosslinked with the organic dye zinc β -tetraaminophthalocyanine, (hereafter referred to as CdSe/I-/Zn4APc) as well as PbS QDs crosslinked with ethane-1,2-dithiol (PbS/EDT). We use square-pulse measurements for the steady-state and impulse excitation for the non-steady state response. From the latter, we determine f_{3dB} according to Equation (3.1). We compare this value to the approximated bandwidths according to Formula (3.2).

3.3 Experimental Section

Detectors. The commercially available photodiode BPW 34 (expected rise time: 20 ns for 5 V reverse bias, 50 Ω load resistance) by Osram Opto Semiconductors²²² was investigated. For the PbS/EDT photodetector the particles were synthesized after a route of Weidman et al.²²³ and the ligand exchange was performed according to Luther et al.¹¹³ The films were prepared on a glass substrate with interdigitated electrodes (4 nm Ti / 20 nm Au, 2.5 $\mu\text{m} \times 1$ cm, finger width 20 μm , film height) as reported elsewhere.³⁹ In short: 7.5 ml oleylamine and 0.04 g sulfur were heated to 120 $^{\circ}\text{C}$ for 20 min in an oil bath under nitrogen atmosphere before allowed to cool back to room temperature while maintaining the nitrogen flow. For the lead solution 7.5 ml oleylamine and 2.5g PbCl₂ were degassed for 10 min at a Schlenk line (150 mTorr) before heating under oxygen exclusion to 120 $^{\circ}\text{C}$. The flask temperature was held at 120 $^{\circ}\text{C}$ while 2.25 ml of the previously prepared sulfur solution was injected. Then the reaction was quenched after 6 min by putting the flask into a water bath and adding 20 ml cold hexane, yielding 6 nm sized PbS quantum dots. Device preparation was done in a nitrogen filled glovebox by covering a glass substrate with 75 μl of the PbS hexane solution and spin coating after 30 s for 30 s with a speed of 20 rps. Then, 150 μl EDT acetonitrile solution (5 mM) was added and again spin coated with the same parameters after 30 s. 150 μl acetonitrile were added and after 30 s spin coated (30 s, 20 rps). All three steps were repeated twice, before the device was put under vacuum for half an hour. The film thickness amounted to approximately 50 nm. The detector was examined under vacuum.

For the CdSe/I-/Zn4APc devices, 4.5 ± 0.4 nm sized CdSe QDs were synthesized according to Sayevich et al.²²⁴ In short, 176.0 mg CdO, 8.0 g trioctylphosphine oxide, 8.0 g hexadecylamine, 2.2 mL oleic acid, and 45.8 mL 1-octadecene were kept under vacuum ($\sim 10^3$ mbar) for 2 h and were heated to 300 $^{\circ}\text{C}$ under nitrogen afterwards. A clear solution was formed, then the temperature was reduced and held at 275 $^{\circ}\text{C}$ for 30 min. A solution of 126.0 mg Se in 4 mL trioctylphosphine, 4 mL trioctylphosphine, and 4 mL 1-octadecene was injected into the reaction mixture, then the temperature was increased to 280 $^{\circ}\text{C}$ and kept there for 45 min. Afterwards, the reaction was quenched by a sudden cooling with cold water. The QDs were purified by precipitation with ethanol (twice) and acetone (twice) and redispersed in hexane. For the ligand exchange with iodide, 0.84 mL of a 60.5 mg/mL CdSe solution in hexane was stirred over night with 300 μL of a 1 M solution of NH₄I in N-methylformamide and 2.7 mL acetone. The mixture was centrifuged, washed with acetone, and redispersed in 400 μL N-methylformamide. Subsequently, the CdSe/I-/Zn4APc films were prepared as reported elsewhere.²²⁵ In short, 45 μL of an 88 μM QD solution in N-methylformamide and 65 μL of a saturated Zn4APc solution in DMSO were deposited on a glass substrate with interdigitated electrodes on top (4 nm Ti / 20 nm Au, 350 nm \times 10 mm, finger width 80 nm). After film formation over-night, excess solvent

was spun-off the substrate, the film was washed with acetonitrile to get rid of unbound Zn4APc, and the film was annealed at 190 °C for 30 min. The film was inhomogeneous with up to 3.5 μm thickness, as reported elsewhere.³⁷ The detector was examined under vacuum.

The WSe₂ transition metal dichalcogenide detectors were prepared as reported elsewhere³⁸ using scotch tape exfoliation of TMDC flakes onto lithographically fabricated electrodes (WSe₂: 2 nm Ti / 10 nm Au, MoS₂: 4 nm Ti / 20 nm Au, 5 μm \times 80 μm , finger width 10 μm , flake thickness WSe₂: 30 nm, flake thickness MoS₂: 110 nm). In contrast, the MoS₂ detectors were fabricated by exfoliating the TMDC first before performing lithography onto the flakes. Prior to evaporation of the electrode material, the flake was etched with a mixture of O₂/SF₆ plasma (100 W, 25 % O₂ / 75 % SF₆, 50 mTorr, 15 s) to get an edge-on contact.^{226,227} Both TMDC detectors were prepared onto glass substrates and examined under atmosphere.

Transient photoresponse. The time-resolved photocurrent measurements were carried out at room temperature in a Lake Shore Cryotronics probe station CRX-6.5K. Steady state photoelectric response was measured using square pulse illumination of the photodetectors. A fast switchable laser driver (FSL500, PicoQuant) was used, operated with a Hewlett Packard 33120A arbitrary waveform generator at 100 Hz. The 635 nm laser diode has a laser rise time of < 0.5 ns and an optical output power of \leq 12 mW. The impulse photoresponse of the photodetectors was examined with a picosecond pulsed laser driver (Taiko PDL M1, PicoQuant), using a 636 nm laser head with a pulse width of < 500 ps. For 100 kHz repetition rate, 22 μW average optical power was chosen for the nanostructured detectors. The given laser powers were reduced by inefficient coupling into the optical fiber, scattering, decollimation of the beam and due to the different detector sizes, an unfocused beam was used with the laser spot usually being larger than the detector area under study. The photodetector electrodes were contacted with 50 Ω matched tungsten probes and 40 GHz coaxial cables chosen as short as possible. For the homebuilt detectors, the current was preamplified with a FEMTO DHPA-100 current amplifier. The photocurrent of all devices was measured with a Zurich Instruments UHFLI lock-in amplifier with a Periodic Waveform Analyzer Function, which averaged the signal from 2 G samples. All signals were background corrected. The maximum time resolution amounts to 600 MHz, which is the signal input limitation of the lock-in amplifier. For the QD devices the Fourier transform was done after applying zero-padding to mimic a 12.5 kHz measurement for the CdSe and a 250 Hz for the PbS device in order to determine the 3 dB bandwidth.

3.4 Results & Discussion

3.4.1 Commercial photodiode

The normalized photoresponses of the commercially available silicon p-i-n photodiode *BPW 34* by Osram Opto Semiconductors are shown in Figure 3.1. The photoelectric response towards a 635 nm 3 MHz square pulse illumination with 100 ns pulse width under 5 V reverse bias and with a 50 Ω load resistance is given in Figure 3.1a. Steady state photocurrent is reached and a rise time (10 – 90 %) of 23.8 ns is determined. This matches the rise time of approx. 20 ns given in the data sheet of the diode.²²² We approximate f_{3dB} with 14.7 MHz according to Equation (3.2). The response of the detector towards 636 nm 3 MHz impulse illumination is depicted in the inset of Figure 3.1b, and the bandwidth spectrum is calculated according to Equation (3.1), shown in Figure 3.1b. A 3 dB bandwidth of 18.0 MHz can be

specified. With the fall time of the impulse response used as an estimate for the rise time of the square pulse response, a bandwidth of 20.7 MHz is expected. The bandwidths determined by the three approaches match closely, indicating a near-ideal circuit, and the diode can be specified with a bandwidth of roughly 17.8 ± 3 MHz. All bandwidth values are depicted in Figure 3.1.

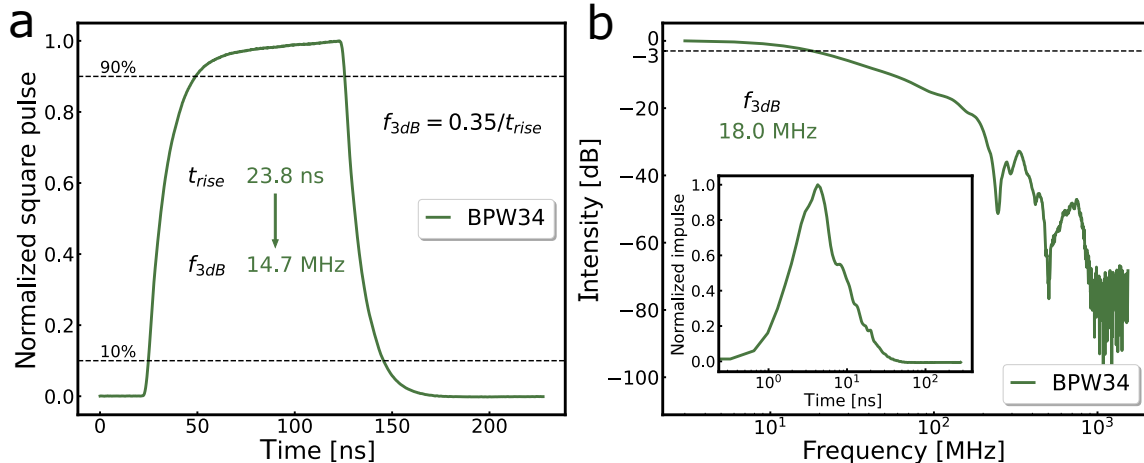


Figure 3.1. a) Normalized photoresponse of a BPW 34 photodiode towards a 635 nm 3 MHz square pulse laser. b) Fourier transformed photoresponse of the same diode towards a 636 nm 3 MHz impulse laser. Inset: normalized impulse photoresponse.

3.4.2 Photodiodes based on nanostructured materials

The channel lengths for the nanostructured photodetectors are 5 μm for PbS/EDT, 350 nm for CdSe/I-/Zn4APc, 15 μm for MoS₂ and 5 μm for WSe₂. While we used bottom electrodes for the QD detectors, we exploited both bottom face-on and edge-on electrode geometries for the TMDC based detectors, to enable a better transfer of the charge carriers to the electrode.⁷² We worked under low electric fields of 0.40 kV/cm and 0.67 kV/cm for the WSe₂, MoS₂ detectors, respectively, to avoid breakdown of the devices. For the more stable PbS/EDT and CdSe/I-/Zn4APc devices, we applied 5.00 kV/cm, 85.7 kV/cm, respectively. We measured the QD devices under vacuum due to their susceptibility to oxygen and the more inert TMDC devices under atmosphere. A detailed description of the photodetector preparation is given in the section Materials and Methods. Thus, the choice of nanostructured devices investigated here reflects a large variety of different materials, electrode geometries, preparation procedures, and measurement conditions. The photoresponses of the four different nanostructured detectors are given in Figure 3.2, with the measurements performed on QD systems shown in Figures 3.2a (square pulse), 3.2b (impulse), and on TMDCs shown in Figures 3.2c (square pulse), 3.2d (impulse).

For the PbS/EDT device, we find a rise time of 4.9 μs which translates into a 71.7 kHz 3 dB bandwidth using Equation (3.2). Compared with the result of 1.1 kHz determined via Fourier transformation of the data in Figure 3.2b, this seventy-fold difference highlights the poor applicability of the first order pole low-pass filter approximation in this case. Similarly, the CdSe/I-/Zn4APc exhibits a rise time of 61.5 μs , which corresponds to an approximated 5.7 kHz bandwidth. In contrast, the bandwidth determined via Fourier transformation is five

times larger with 28.8 kHz. We note that using the impulse fall time for the approximation via Equation (3.2) agrees perfectly with the result after Fourier transformation for PbS/EDT (1.1 kHz), but with 18.0 MHz it deviates by almost three orders of magnitude for CdSe/I-/Zn4APc.

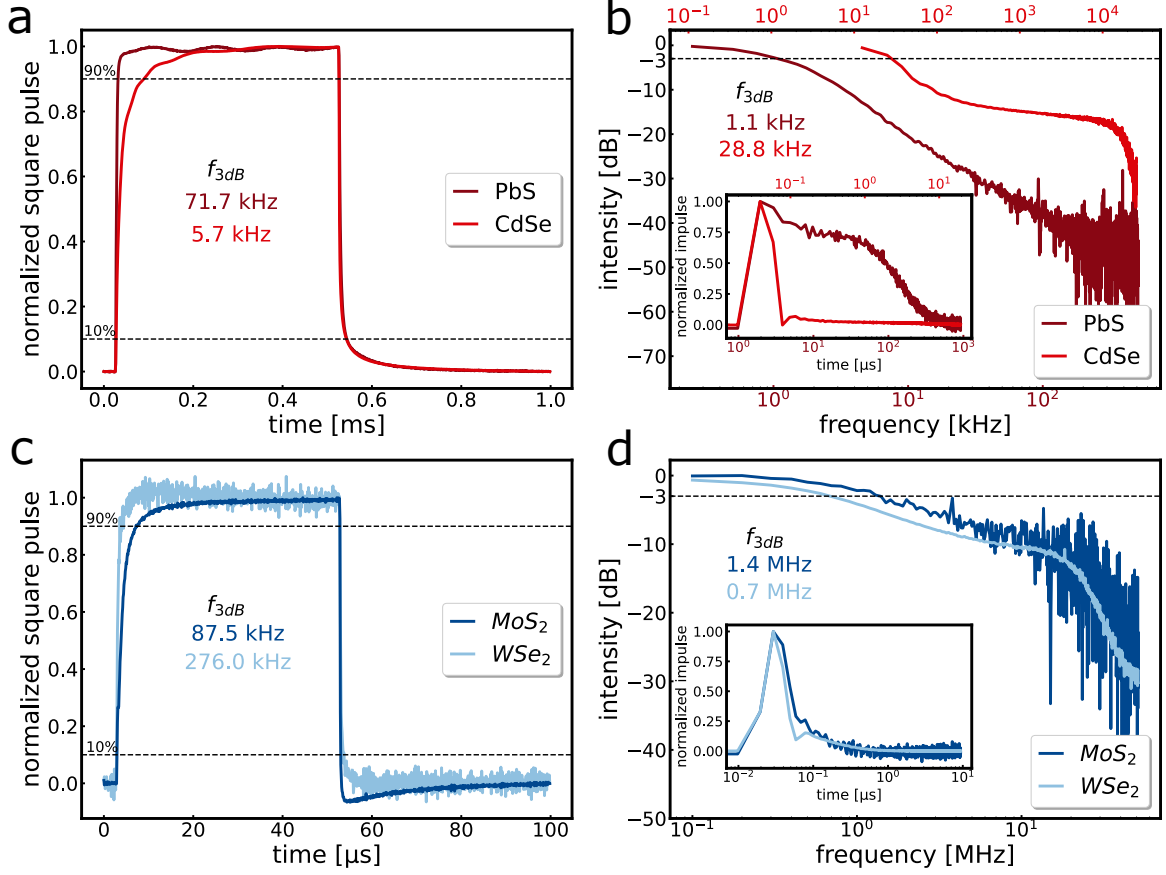


Figure 3.2. a) Normalized photoresponses of the four photodetectors towards both, square pulse illumination (a, c) and impulse illumination (b, d), giving the bandwidth spectrum. The two QD systems are shown in a) towards a 635 nm 1 kHz square pulse laser and in b) with the bandwidth spectrum determined via Fourier transformation of the photoresponse of the QDs towards a 636 nm impulse laser with 50 kHz (CdSe) and 1 kHz (PbS) laser repetition rate. The responses of the TMDC systems are shown in c) towards a 635 nm 10 kHz square pulse illumination and in d) together with the bandwidth spectrum for a 636 nm 100 kHz impulse illumination.

For MoS₂, the approximated bandwidth is 87.5 kHz (Figure 3.2c), which compares to 1.4 MHz upon Fourier transform of the impulse photoresponse (Figure 3.2d). Likewise, the approximated bandwidth of the WSe₂ device is 276.0 kHz, compared to 0.7 MHz after Fourier transform of the impulse response. When utilizing the impulse response fall time in Equation (3.2), the bandwidths are estimated with 3.6 MHz for both devices. All bandwidths estimated with Equation (3.2) or the Fourier transformation of the impulse, Equation (3.1), are shown in Figure 3.3 for easy comparability.

While the analysis of the commercial photodiode (representing a near-ideal circuit)

verifies that all four approaches for determining the 3 dB bandwidth utilized here can lead to good agreement, significant differences are observed for the nanostructured devices. The largest deviations arise for the CdSe detector with a factor of 3×10^3 . The PbS detector and the MoS₂ detector show deviations of around 65 and 40, respectively, and for the WSe₂ device, still a factor of 10 is detectable. We argue that the bandwidth determined via Fourier transformation of the impulse response gives the most accurate result, since it uses a complete signal as basis for the calculation without any approximation. It is evident that the approximation in Equation (3.2) can lead to drastic over- and underestimations of the 3 dB bandwidth without a clear trend.

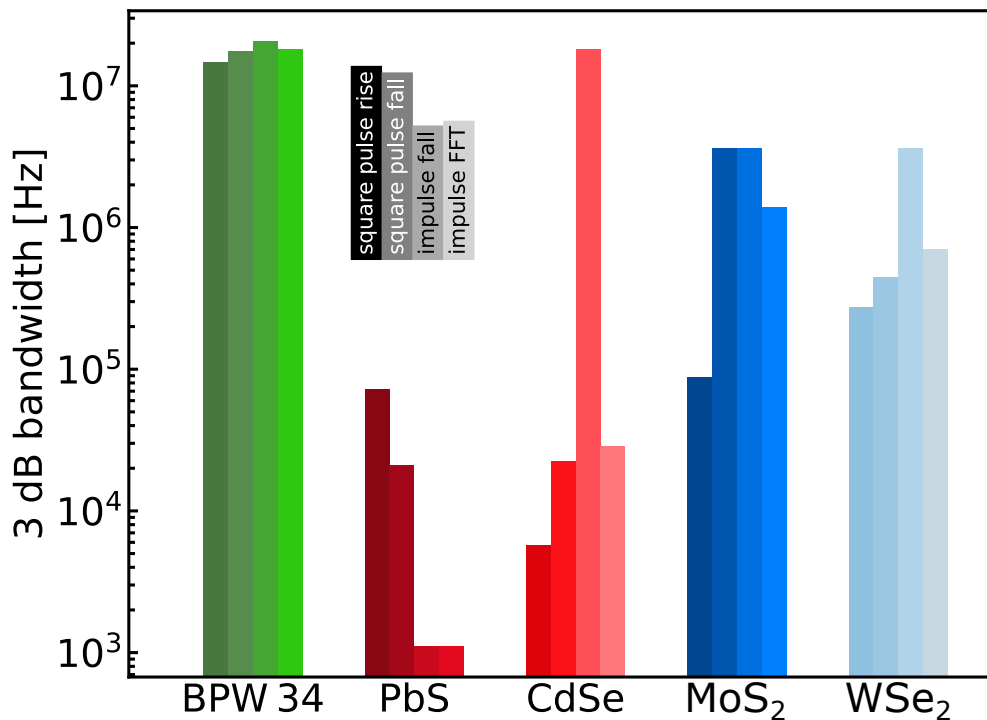


Figure 3.3. Overview of all bandwidths derived with either Equation (3.2): $f_{3dB} = 0.35/t$ using the respective square pulse rise / fall time or the impulse fall time or the bandwidth estimated using the Fourier transformation of the impulse response with Equation (3.1).

We note that the 3 dB bandwidth can depend on the illumination intensity,^{218,228} which needs to be considered as an alternative explanation for the different results obtained from the square pulse vs. the impulse data. However, two observations speak against a dominant contribution of this dependence: I) We find no significant deviations for the commercial p-i-n photodiode despite using two different laser sources. II) Even the results obtained from the impulse photoresponse with the same illumination intensity yield largely different values as demonstrated for the CdSe/I-/Zn4APc detector, where the deviation amounts to a factor of 625. These large deviations in the 3 dB bandwidth of one and the same photodetector highlight that care must be taken when comparing 3 dB bandwidths of different devices specified via different approaches. We suggest to primarily compare the bandwidth values detected with the identical approach.

3.5 Conclusion

We apply four related methods to determine the electrical 3 dB bandwidth of photodetectors based on CdSe or PbS nanocrystals, MoS₂ or WSe₂ nanoflakes as well as a commercially available photodiode for reference. While we find similar results with all four methods for the commercial, ideal photodiode, the derived 3 dB bandwidths for the nanostructured, non-ideal photodetectors differ by up to 10³ depending on the applied method/approximation. These discrepancies need to be taken into account when comparing non-ideal photodetectors – such as most devices based on nanoparticles - with existing data. We recommend comparing only bandwidths obtained with the same method.

4 Edge Contacts accelerate the Response of MoS₂ Photodetectors

Fabian Strauß^{a,b}, Christine Schedel^a, Marcus Scheele^{a,b,}*

^a Institute for Physical and Theoretical Chemistry, University of Tübingen, 72076 Tübingen, Germany.

^b Center for Light-Matter Interaction, Sensors and Analytics LISA+, University of Tübingen, 72076 Tübingen, Germany.

* Corresponding author

This chapter is based on the publication in *Nanoscale Advances*.

4.1 Abstract

We use a facile plasma etching process to define contacts with an embedded edge geometry for multilayer MoS_2 photodetectors. Compared to the conventional top contact geometry, the detector response time is accelerated by more than an order of magnitude by this action. We attribute this improvement to the higher in-plane mobility and direct contacting of the individual MoS_2 layers in the edge geometry. With this method, we demonstrate electrical 3 dB bandwidths of up to 18 MHz which is one of the highest values reported for pure MoS_2 photodetectors. We anticipate that this approach should also be applicable to other layered materials, guiding a way to faster next-generation photodetectors.

4.2 Introduction

The rise of 2D materials in optoelectronics has led to remarkable research results in recent years, from ultra-thin transistors^{9,85} to single-layer light-emitting diodes¹² and novel photodetectors.^{229,230} For the latter, two properties are of particular interest: device responsivity and device speed. For high frequency applications, silicon and InGaAs are the most advanced materials today,¹⁶⁹ but they are starting to reach physical limits. A possible alternative is found in layered materials. The intrinsic photoresponse of these layered materials such as graphene or transition metal dichalcogenides (TMDCs) has revealed response times in the picosecond regime.³⁰ This intrinsic response is a measure for the pure, material-specific photoresponse and defines an upper limit for an ideal photodetector, in which the speed is solely limited by the active material. However, in most devices the actual speed is furthermore affected by extrinsic properties related to the device geometry, such as the RC- or transit time. Pure TMDC devices exhibit typical response times ranging from milliseconds^{98,172} to seconds,^{98,172,231} with a few fast devices in the microsecond range^{30,94,98,140,172} and even less in the sub-microsecond regime.⁹⁰ Many methods have been used in the search for ultrafast photodetectors based on nanomaterials: chemical doping,²³² heterojunction implementation,^{233,234} photonic waveguide integration,²³⁵ and small channel lengths,^{37,91} to name a few. In addition, parameters such as the choice of substrate,^{37,38} interface roughness,²³⁶ electrode material,^{145,159,231} and geometry^{90,237,238} or environment^{39,239} must be considered each time.

Traditionally, top contacts above, or bottom contacts below the active material are used for nanomaterial photodetectors. More advanced structures can also be built by a vertical arrangement of electrodes and desired material.^{90,91} In addition, layered materials can be contacted at the edge of the flake.^{72,240} Thereby, instead of touching the surface of the layered material, cf. Figure 4.1a, the edge of a flake is uncovered, for example with etching,^{240,241} and the electrodes are evaporated on the edge of the material, cf. Figure 4.1b.

An SEM-image of an etched flake showing the exposed edge of a MoS_2 flake can be seen in Figure 4.1c and Figure SI4.2. These one-dimensional edge contacts have attracted much attention in recent years. They are being investigated for their reduced transfer length,^{242,243} lower contact resistance,^{72,244–246} better control of the Schottky barrier,^{247,248} higher capability of charge injection^{248,249} or Fermi level depinning,^{72,241,247} to name a few examples. However, to our knowledge, the effect of edge contacts on the response time properties of TMDC photodetectors is still unknown.

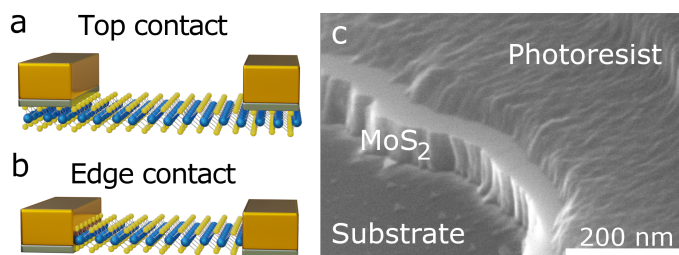


Figure 4.1. Schematic of an **a)** top contacted and **b)** edge contacted MoS_2 crystal. **c)** SEM image of an etched MoS_2 flake.

In this work, we investigate the difference between edge electrodes and conventional top electrodes and their influence on the response speed of pure MoS_2 photodetectors. The MoS_2 flakes studied here were exfoliated using a standard scotch tape / PDMS exfoliation method.²⁴⁰ They are between 50 and 200 nm thick, see Figure SI4.1e, and can thus be considered bulk crystals where the height no longer affects the properties.¹⁴⁰ We show that the electrode geometry of the device – edge electrodes instead of top contacts – accelerate the decay time by at least an order of magnitude. Primarily, we have studied the steady state photoresponse towards a 635 nm square pulse with some additional non-steady state measurements towards a 636 nm impulse laser. By using these techniques, pure MoS_2 devices can be realized with one of the highest recorded bandwidths of more than 18 MHz. We hypothesize that this geometry should be particularly advantageous for TMDCs in view of the much more efficient in-plane transport compared to transport across several van-der-Waals layers.

4.3 Experimental Section

4.3.1 Fabrication

MoS_2 detectors were fabricated by exfoliating TMDC flakes with scotch tape onto cleaned glass substrates functionalized with HMDS. For the bottom contacts, the flakes were stamped directly onto lithographically fabricated electrodes ($2.5\text{-}20\ \mu\text{m} \times 80\ \mu\text{m}$). For all other electrode geometries, optical lithography was performed directly on the flakes using a maskless aligner (μMLA Heidelberg Instruments). For the edge contacts, an additional plasma etching step is performed before vapor deposition of the electrode material. The platelets were etched with a mixture of O_2/SF_6 plasma (100 W, 25% O_2 / 75% SF_6 , 50 mTorr, 20 s). The electrode material, e.g., 4 nm Ti and 20 nm Au, was evaporated at a pressure of $< 2 \times 10^{-6}$ mbar. The detectors were examined under atmospheric conditions.

For the Ti: Au top contacts as well as the Au edge electrodes, 4 nm Ti and 20 nm Au were evaporated. For the Ti edge contacts, 2 nm Ti and 4 nm Au or only 25 nm Ti were evaporated. Since they have shown similar behavior, their data is shown jointly. The Au bottom contacts are made of 4 nm Ti and 20 nm Au and the Ti bottom contacts of 25 nm Ti.

4.3.2 Transient photoresponse

Time-resolved photocurrent measurements were performed at room temperature in a Lake Shore Cryotronics CRX-6.5K probe station. Square pulse illumination of the photodetectors was used to measure the steady state photoelectric response. For this, a

fast-switching laser driver (FSL500, PicoQuant), driven by a Hewlett Packard 33120A arbitrary waveform generator was used. The 635 nm laser diode has an optical output power of ≤ 12 mW and a laser rise time of < 0.5 ns. The non-steady state photoresponse of the detectors was investigated with a picosecond pulsed laser driver (Taiko PDL M1, PicoQuant) utilizing a 636 nm laser head with a pulse width < 500 ps. For a repetition rate of 100 kHz, an average optical power of $22 \mu\text{W}$ was chosen. The laser powers were further reduced due to decollimation of the beam, inefficient coupling into the optical fiber and scattering. An unfocused beam was used with a laser spot larger than the detector area.

50Ω matched tungsten probes and 40 GHz coaxial cables as short as possible were used to contact the detector with the external circuit. A transimpedance amplifier (FEMTO DHPKA-100) was used to preamplify the current before measuring with a Zurich Instruments UHFLLI lock-in amplifier with a Periodic Waveform Analyzer function averaging the signal from 2 G samples. Before further analysis, the signals were background corrected. The bandwidth of the lock-in amplifier is 600 MHz which is further reduced to 14-200 MHz by the variable gain transimpedance amplifier.

For some contacts, the Fourier transform of 100 kHz measurements was performed after applying zero padding to mimic a 25 kHz measurement and determine the 3 dB bandwidth.

4.4 Results and discussion

4.4.1 Steady state photoresponse of edge and top contacted MoS₂

Square pulse laser measurements determine the rise time to reach steady state as well as the corresponding fall time. This allows investigating the influence of changing the electrode geometry and / or the contacting metal for both parameters, which we used to study the effect of an edge contact compared to titanium:gold top electrodes (Ti:Au top). For further information and a scheme of the measurement setup used, the interested reader is referred to our previous work.³⁷

The edge geometry is either fabricated with the same ratio of Ti:Au (Au edge) or with the inverted ratio of titanium and gold (Ti edge), referring to the predominant contacting metal. See Figure SI4.3 for the fabrication process. Typical square pulse responses of these three geometries are shown in Figure 4.2a.

The fall time accelerates tremendously for the edge geometry, while the rise time accelerates only slightly. We attribute this result predominantly to the geometry but note that the metal also plays an important role. The significance of each effect can be seen in Figure 4.2b, which shows the box-and-whisker plots across all 10 kHz square pulse measurements for all investigated Ti:Au top and Ti and Au edge contact flakes (4 Ti:Au top, 8 Au edge, 5 Ti edge contacts; 18 Ti:Au top, 74 Au edge, 46 Ti edge measurements). Thereby, the box includes all values from the first to the third quartile, while the whiskers span to the value maximal 1.5 times the box size away. Every value exceeding this range is displayed as an outlier. Again, the rise time does not show much improvement in the median values, although some contacts display much faster rise times for the edge contact compared to the top contacts. In contrast, the fall time shows a massive acceleration for the edge contacts, an improvement of at least a factor of eleven for the mean value compared to the top contacts. This uneven acceleration can be attributed to the multiple mechanisms that play a role in the rise time compared to the fall time, like generation of electron-hole pairs. The large spread in the Au edge data is caused by the slightly bigger sample size, a pronounced persistent photocurrent effect for especially higher bias

voltages,¹⁴² cf. Figure SI4.4, and the specific challenges of the fabrication of edge contacts: As can be seen in Figure 4.1c, the etched flank is bolt upright, but it has a slight tendency to be tilted either inwards or outwards, thereby changing the contact angle for the edge electrodes and thus the quality of the contact. To further improve the edge contact in the future, more dedicated procedures like the etching process by Cheng et al.²⁴² may be beneficial, which has the benefit to produce edge contacts with greater reliability and control over the environment.

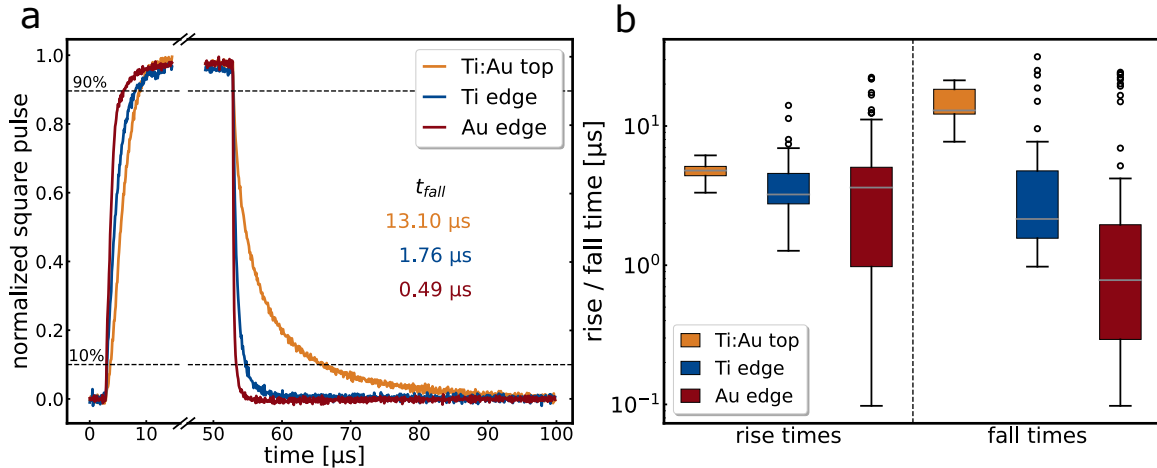


Figure 4.2. **a)** Normalized square pulse response of a top contact (ochre), a titanium edge contact (blue) and a gold edge contact (red). All measurements performed with a 635 nm square pulse laser with 10 kHz repetition rate, 15 μm channel length, 0.1 V bias applied. **b)** box-and-whisker-plots of all 10 kHz, 635 nm square pulse measurements for each electrode configuration. The left half displays the rise times, and the right half the fall times. Measurements of 18 Ti:Au top, 74 Au edge, 46 Ti edge measurements contacts are included at various bias voltages between -1 and 1 V.

We attribute the accelerated response times to the improved contacting method. Conventional top contacts with vapor deposited electrodes have many defects and hybridization in the first layers,²⁵⁰ eliminating the van der Waals gap between the electrode and TMDC. Underneath, however, are many more layers with vdW gaps and thus tunnelling barriers that must be overcome to inject a charge carrier into the electrode. In the geometry of the edge electrodes, (nearly) all layers are contacted and charge transport to the contact occurs in the plane of the MoS_2 crystal, which has much higher mobilities.²⁵¹ This greatly enhances the carrier injection.⁷² Moreover, the edge contacts may form covalent bonds with the dangling bonds of the TMDCs,⁷² which further improve charge transport.

In addition to the different electrode geometry, the contacting metal has also been shown to have an impact on device speed. To quantify this influence, MoS_2 flakes were investigated in a bottom electrode geometry with either titanium or gold as contact material (see Figure 4.3a).

In addition, an analysis was performed by patterning the same flake twice so that some channels were contacted with the Ti:Au top electrodes and others with Au top electrodes

only (see Figure 4.3b). Both sets of experiments show the same trend already observed in the edge contact experiments, namely an acceleration of the rise and fall times with gold as the contact metal. However, the mean value of all Ti edge contacts is still faster than the best top contacts, demonstrating that the contact geometry remains an important factor for the overall response speed of the MoS_2 photodetectors.

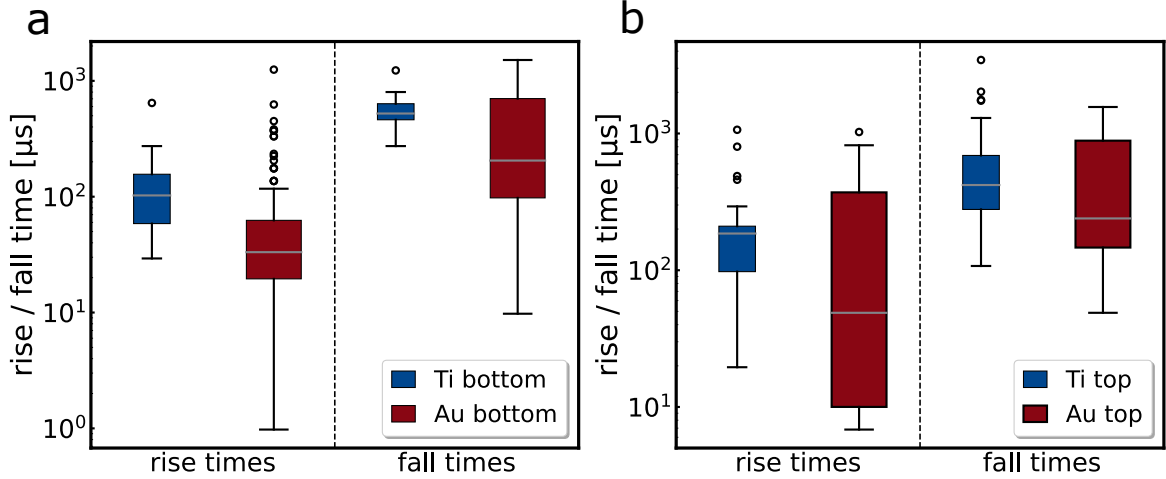


Figure 4.3. Box-and-whisker plots of rise and fall times of MoS_2 flakes contacted with either titanium (blue) or gold (red). **a)** bottom electrode geometry, **b)** top electrodes where the different channels on the same flake are contacted with titanium or gold. All measurements are carried-out with a 635 nm laser and a repetition rate of 100 Hz.

The influence of the contacting metal on the electrical or optoelectrical behaviour of materials is not new and has been detailed for instance in the work of Jain et al.²⁵² Nevertheless, it is often discussed only in terms of contact resistance or dark currents, cf. Figure SI4.5, but rarely in terms of response times. For TMDCs, a study by Zhang et al.¹⁴⁵ already investigated the rise time effects of palladium and titanium contacts on WSe_2 . The authors explained the faster response for titanium with a higher Schottky barrier. In the case of Au, Ti, and MoS_2 , the respective work functions are about 5.4 eV,²⁵³ 4.3 eV,²⁵⁴ and 3.9 eV²⁵⁵ for the edge facet of MoS_2 or 5.4 eV²⁵⁶ for the top facet. Thus, regarding the titanium gold comparison, the higher Schottky barrier is expected for Au contacts, which are shown to be faster in the experiments.²⁴⁹ Furthermore, in a comparison of Au with the corresponding work functions of MoS_2 , again, the higher Schottky barrier is found for the faster contact geometry – edge contacts, cf. Figure SI4.6. A detailed analysis of the work functions in the different contact geometries shown here is beyond the scope of this work and would require surface tunnelling spectroscopy or similar methods.

With respect to the limiting mechanism of edge and top contact we performed measurements at different voltages which could provide hints towards a transit time limitation. Additional measurements with different channel lengths in the range from 2.5 μm to 20 μm could give further information on either a transit time limited mechanism or an RC-time limit in case of no voltage dependency. Both, voltage, and channel length variation do not show any trend, cf. Figure SI4.7 and SI4.8, thereby a limiting mechanism cannot be determined. Further distinctions towards an RC-limitation would require impedance measurements.

In summary, MoS_2 detectors can be accelerated enormously by using edge contacts in comparison to top contacts, cf. Ti:Au top and Ti edge in Figure 4.2a. An additional tuning by using an appropriate electrode metal as already announced in literature can further help to accelerate the detector especially in the fall times, as shown by using Au edge electrodes.

4.4.2 Non-steady state photoresponse of edge and top contacted MoS_2

The investigation with a delta-shaped laser pulse mimics the data transmission in optical fibres and is therefore of relevance to determine the bandwidth of the device. For this purpose, the impulse response ($f(t)$) must be Fourier transformed (FFT) to obtain the power spectrum ($P(\omega)$): $P(\omega) = |FFT(f(t))|^2$. After normalization with the steady-state power (P_1), the bandwidth spectrum can be converted to $\text{dB} = 10\log_{10}(P(\omega)/P_1)$. The 3 dB bandwidth is then a measure of the frequency at which the power of the signal drops to half its value.

Most flakes have relatively little signal, so it is not possible to determine the impulse photoresponse for each bias voltage and channel. Thus, no further information about the limiting mechanism can be obtained, only a representative trend, which can be seen in Figure 4.4.

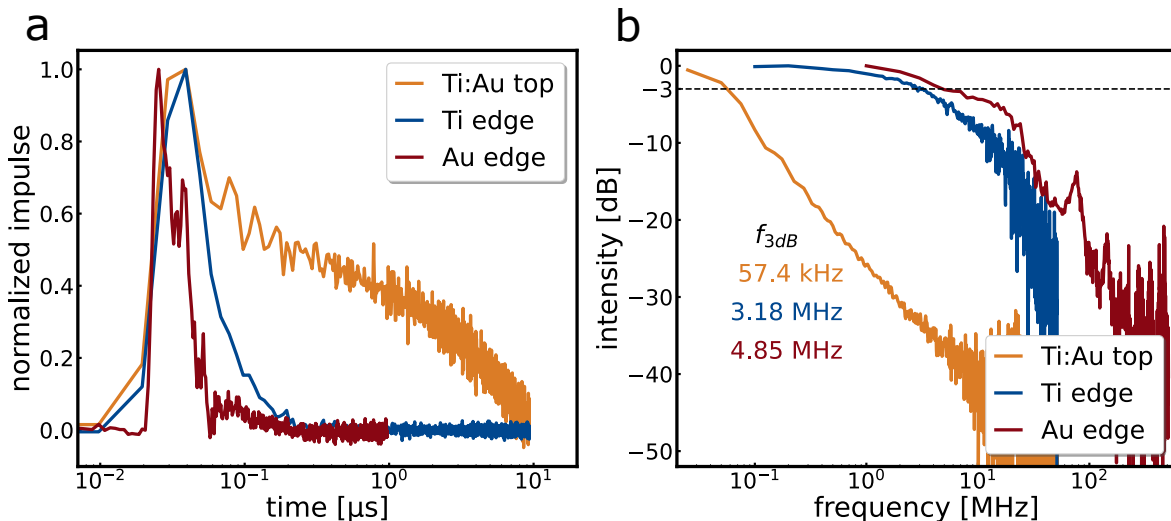


Figure 4.4. **a)** Normalized impulse photoresponse of a Ti:Au top (ochre), a titanium edge (blue) and a gold edge (red) contacted MoS_2 device towards a 636 nm pulsed laser. Measured are $10 \mu\text{m}$ contacts under a 1 V bias with either 100 kHz for the Ti edge and Ti:Au top device or 1 MHz for the Au edge device. **b)** Fourier transformed impulse response to determine the 3 dB bandwidth of the device. For the top contact zero-padding is performed to mimic a quasi 25 kHz measurement.

Figure 4.4a shows exemplary impulse responses of the three types of detectors investigated and Figure 4.4b the corresponding bandwidth spectra obtained by fast Fourier transform. As with the steady-state measurements, the trend shows the acceleration of the bandwidth when using edge contacts by a factor of more than 80 times for the example shown. The fastest device response exceeding a bandwidth of 18 MHz can be seen in Figure SI4.9.

4.5 Conclusions

In summary, we have demonstrated the accelerating effect of edge contacts for the response of MoS_2 photodetectors compared to the conventionally used top contacts. This improvement is caused by the better charge carrier injection into the electrodes due to the higher in-plane mobility compared to the out-of-plane mobility of TMDCs. In addition, the contacting metal and the associated Schottky barrier play an important role: for MoS_2 , gold leads to faster rise and fall times than titanium. By combining these two effects, we have built photodetectors with a bandwidth as high as 18 MHz, which, to the best of our knowledge, surpasses all neat MoS_2 photodetectors developed so far. We believe that the implementation of edge contacts in photodetectors made of 2D materials has great potential due to their scalability and simplicity.

4.6 Supplementary Information

Light microscopy images and flake height

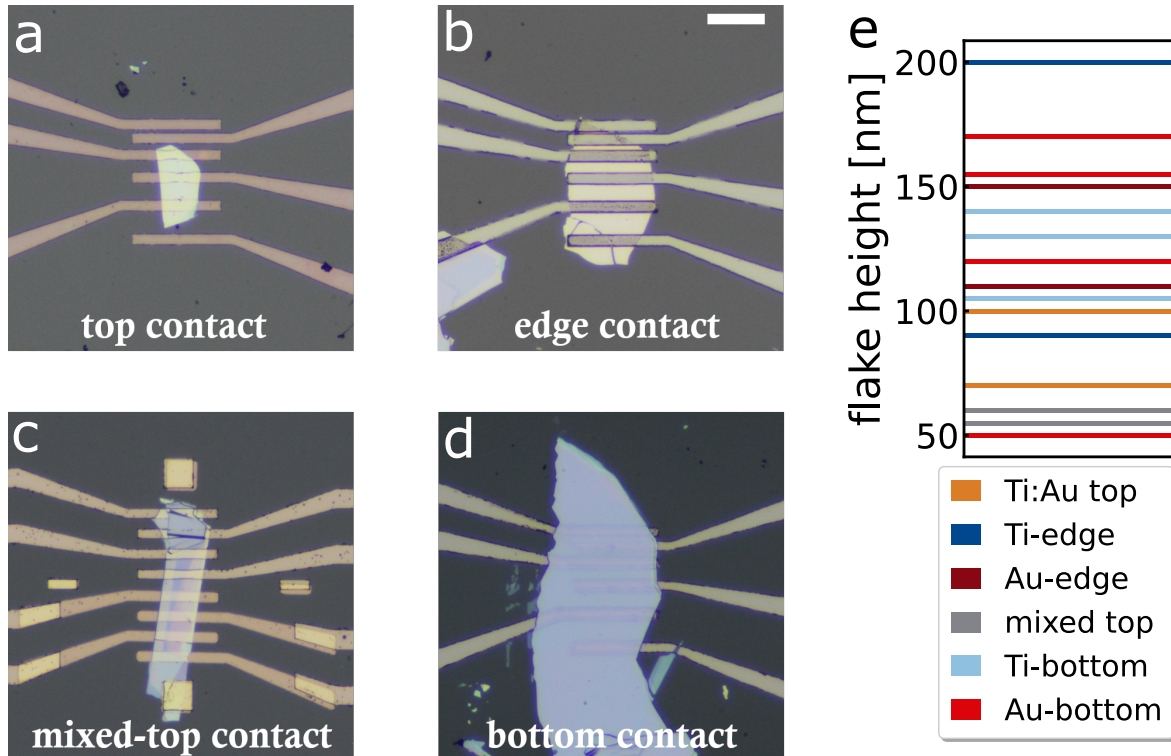


Figure SI4.1. Light microscopy images of MoS_2 flakes with different electrode styles: **a)** top contact; **b)** edge contact; **c)** mixed top contact; **d)** bottom contact. **e)** Flake height for every examined flake, measured with a profilometer (*Dektak XT*). The thickness ranges from 50 nm to 200 nm. The scale bar is 50 μm .

SEM-images of an etched flake

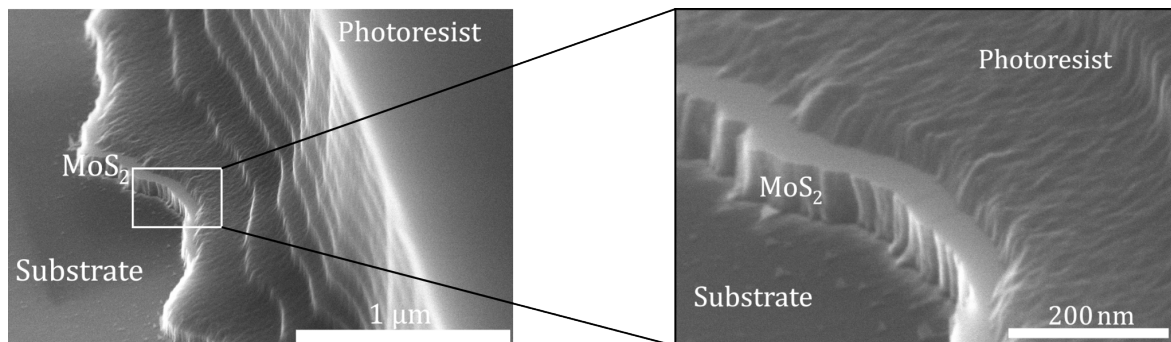


Figure SI4.2. SEM images of an etched MoS_2 flake. **a)** Overview with visible resist flank, **b)** zoomed in image of the marked spot in a). The height of this particular flake is approximately 70 nm.

Lithographic process for fabricating edge contacts

For bottom contacts, the lithography is done prior to the exfoliation. For top contacts, the fabrication is exactly the same as in Figure SI4.3, only the etching part (Figure SI4.3c) is left out.

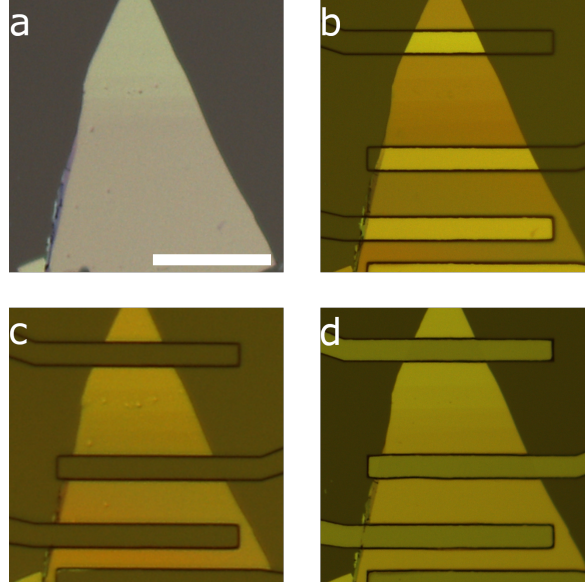


Figure SI4.3. Fabrication process of an edge contact: **a)** exfoliated flake on a glass substrate; **b)** patterned electrodes after photolithography and resist development; **c)** flake after O₂/SF₆ plasma etching; **d)** flake after evaporation of the electrodes. The scale bar is 50 μm.

Edge contacts are obtained by following the lithographic steps depicted in Figure SI4.3. The mixed top contacts are fabricated in two lithographic processes: In the first one, the upper four electrode fingers, cf. Figure SI4.1c, are made as well as the leads with 4 nm Ti and 20 nm Au. After lift-off, the lithography is repeated and the lower four electrodes consisting of 25 nm Au are evaporated without a wetting layer of titanium.

Persistent photocurrents in MoS_2 flakes

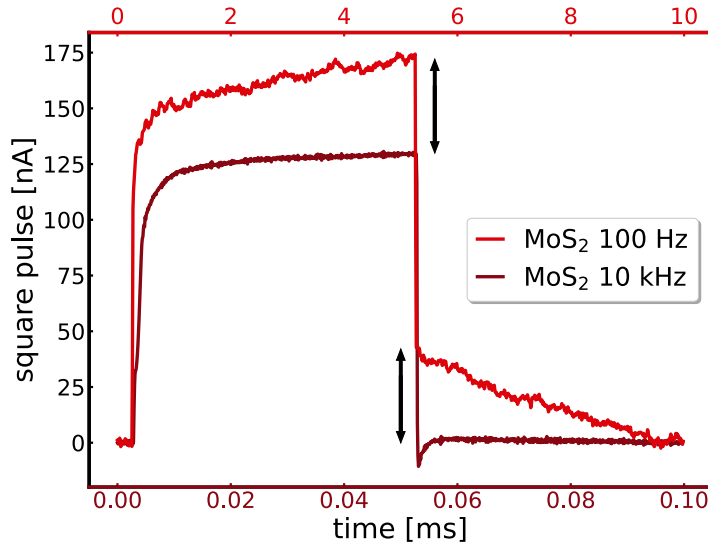


Figure SI4.4. 635 nm square pulse measurements of a $20\ \mu\text{m}$ Au edge contact under 1 V bias. Bright red shows the measurement with a laser repetition rate of 100 Hz and dark red with 10 kHz. The two black arrows are equally long, indicating the height difference caused by the slow parts in the rise and fall time for the 100 Hz measurement.

For measurements at 100 Hz, a persistent photocurrent is sometimes observable, more pronounced for higher voltages. This can be seen in a step increase and decrease of the rise and fall time respectively, followed by a slow and steady increase / decrease, cf. Figure SI4.4 bright red curve. These two effects can be attributed to the fast photoconductive and the slower photogating effect. Di Bartolomeo et al.¹⁴² examined that the slower photogating relies on deeper traps which yield very long response times, but require a longer exposure to be filled. Thus, this behaviour can be suppressed when switching to higher repetition rates like 10 kHz, showing only the relevant photoconductive component.

I-V characteristics

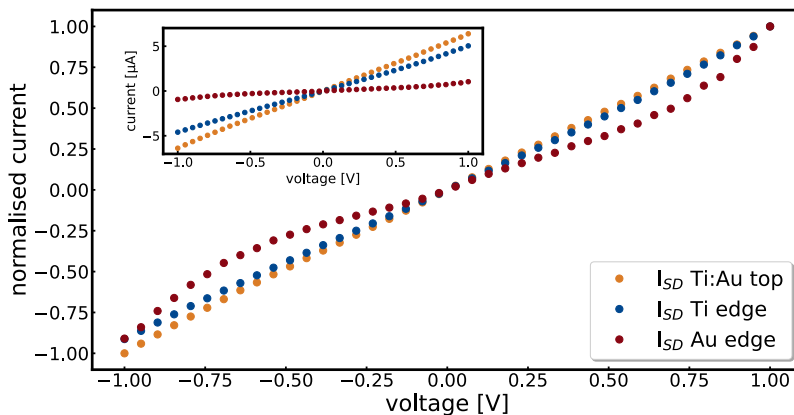


Figure SI4.5. Normalized I-V characteristics of a Ti:Au top (ochre), a Ti edge (blue) and a Au edge (red) contacted flake without illumination. Measurements made on $10\ \mu\text{m}$ contacts from 1 to 1 V. The inset shows the absolute current values. The slope can be translated into resistances of $161\ \text{k}\Omega$, $218\ \text{k}\Omega$ and $1.46\ \text{M}\Omega$ respectively.

The I-V characteristic shows the same trend observed in literature: for a titanium contacting, either top or edge, there is an (nearly) ohmic behaviour, whereas for a gold contacting the curves tend to differ due to the higher Schottky barrier. The dark currents are generally rather high, due to the bulk MoS₂ flakes.

Band diagram of an Au top and an Au edge contact

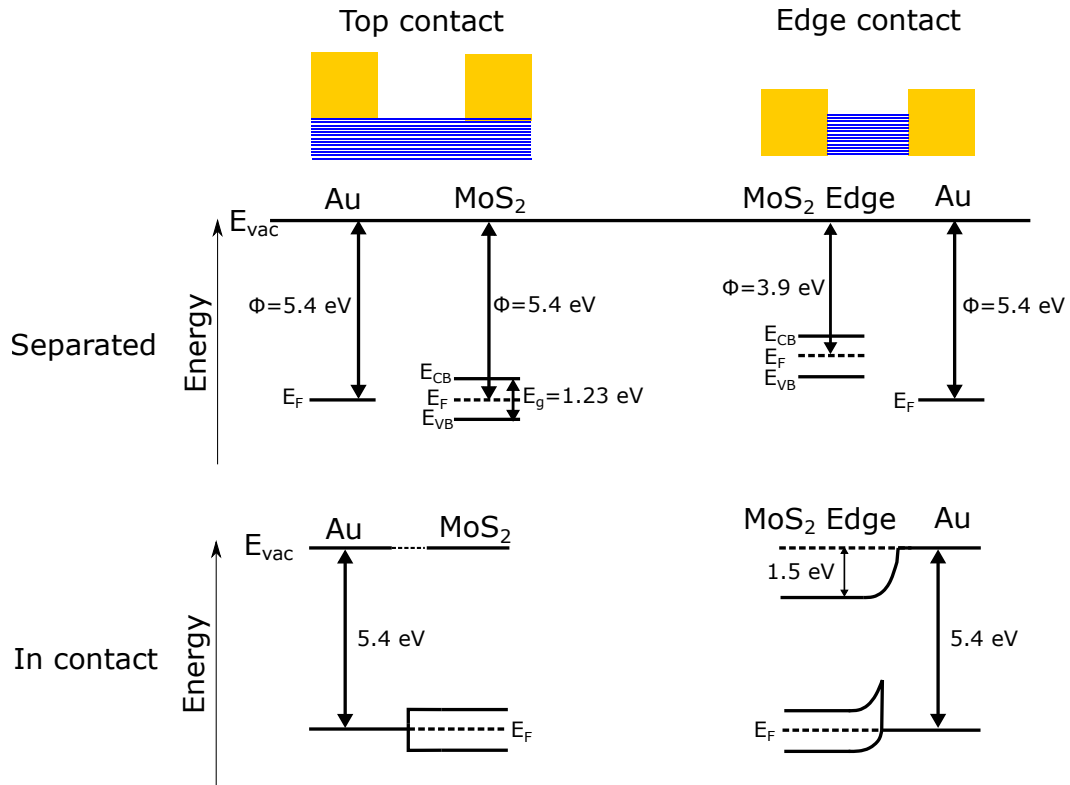


Figure SI4.6. Band diagrams for an idealized top contact (left) and edge contact (right). The upper half shows all the work functions extracted from literature.^{253–256} At the bottom, an idealized model of the materials brought into contact can be seen.

The band diagram in Figure SI4.6 shows an idealized model of a top and an edge contact consisting of gold and MoS₂. Thereby, it is important to use the appropriate MoS₂ work function, depending on the electrode geometry. When contacting the edge, a larger Schottky barrier arises than when contacting from the top. It is important to emphasise, that those literature values may differ in reality, depending on the nature of the semiconductor (n- or p-type or intrinsic), the exact work function of Au and stress, strain, defects or any order form of imperfection in the MoS₂ flake, to name just a few examples. Additionally, metallization at the edge contact might occur, altering the band model.²⁴¹

Rise / fall time vs. channel length and voltage

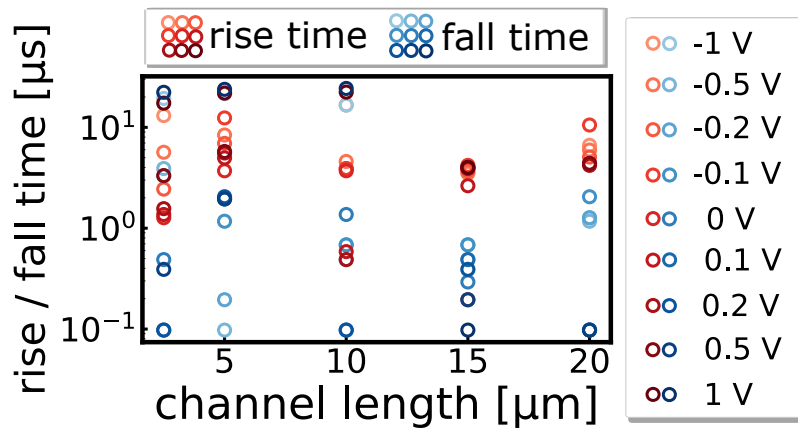


Figure SI4.7. Rise times (red) and fall times (blue) of 10 kHz measurements of an Au edge contact plotted vs. the channel length. The different shades resemble the different biases applied.

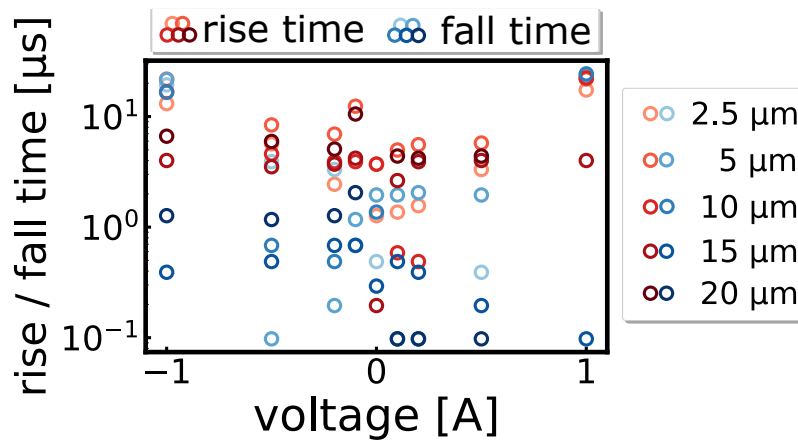


Figure SI4.8. Rise times (red) and fall times (blue) of 10 kHz measurements of an Au edge contact plotted vs. the bias voltage. The different shades resemble the different channel lengths of the electrodes.

There is no clear trend visible towards the applied voltage or channel length. Therefore, we cannot further determine the speed limiting mechanism of the MoS_2 flakes.

Impulse response and bandwidth of the fastest device

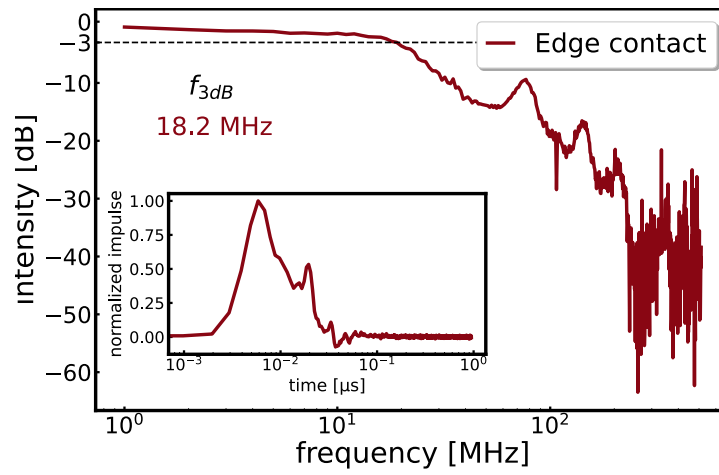


Figure SI4.9. Bandwidth of fastest MoS₂ photodetector fabricated. The inset shows the impulse response of a 10 μm channel with 0.5 V applied bias of an Au edge contacted device towards a 636 nm laser operated at 1 MHz repetition rate. The graph shows the Fourier transformation of the impulse response.

5 A simple 230 MHz Photodetector Based on Exfoliated WSe₂ Multilayers

Fabian Strauß^{1,2,a}, Pia Kohlschreiber^{1,2,a}, Jakob Keck^{1,2}, Patrick Michel^{1,2}, Jonas Hiller¹, Alfred J. Meixner^{1,2}, Marcus Scheele^{1,2,}*

¹ Institute for Physical and Theoretical Chemistry, University of Tübingen, 72076 Tübingen, Germany.

² Center for Light-Matter Interaction, Sensors and Analytics LISA+, University of Tübingen, 72076 Tübingen, Germany.

* Corresponding author

^a These authors contributed equally.

This chapter is based on the publication in *RSC Applied Interfaces*.

5.1 Abstract

We demonstrate 230 MHz photodetection and a switching energy of merely 27 fJ by using WSe₂ multilayers and a very simple device architecture. This improvement over previous, slower WSe₂ devices is enabled by systematically reducing the RC constant of the devices through decreasing the photoresistance as well as the capacitance. In contrast to MoS₂, reducing the WSe₂ thickness toward monolayers only weakly decreases the response time, highlighting that ultrafast photodetection is also possible with atomically thin WSe₂. Our work provides new insights into the temporal limits of pure transition metal dichalcogenide photodetectors and suggests that Gigahertz photodetection with these materials should be feasible.

5.2 Introduction

Next generation photodetectors have to meet several requirements to overcome the current limitations of silicon-based devices.^{24,169,257} They must be cheap, reliable in fabrication and exhibit low power consumption, for which high speed and low dark currents are essential.^{24,29} Transition metal dichalcogenides (TMDCs) are promising in this regard,^{24,169,257} especially since the increasing quality of flakes produced via chemical vapor deposition is closing the gap to the excellent properties of mechanically exfoliated ones, allowing reliable and relatively inexpensive production.^{258–260} However, achieving high switching speeds toward Gigahertz photodetection remains challenging, in particular without compromising the responsivity too much. This is resembled by the gain-bandwidth product accounting for the necessity for a high gain/responsivity to have a long lifetime and thus a low bandwidth.^{29,160,257,261} The intrinsic response, i.e., the pure material-based upper limit for photodetection without limitations such as the RC time of the device, has been shown to be in the picosecond regime.^{30,31,139} In contrast, for the application-relevant extrinsic response time, most reports have revealed response times of milliseconds to microseconds.^{98,159,160,172,203,262–267} Some groups report nanosecond response times,^{35,90,102,171} and in the combination with highly advanced photonic circuits, even faster detectors are possible.^{268–270} The problem with such sophisticated fabrication techniques remains the scalability. Furthermore, many approaches are based on TMDC heterostructures^{31,265,271} or combinations of TMDCs with other materials,²⁷² i.e., hBN,^{159,160,265} graphene^{266,267} or quantum dots,^{273,274} which in turn complicates fabrication.²⁴

In this work, we study highly simple TMDC photodetectors, comprising only exfoliated multilayers or bilayers of pure WSe₂ and gold top-contacts. We show that multilayer devices are RC-limited and that reducing their photo resistance as well as the device capacitance affords a response time below 2 ns and an electrical bandwidth in excess of 230 MHz, which is unprecedented for pure TMDC photodetectors to our knowledge. The devices are operated at zero bias, leading to a switching energy of only 27 fJ/bit, highlighting the potential of TMDC photodetectors for low-power optical communication. We find response times < 20 ns for bilayers, indicating that the deleterious persistent photocurrent known for MoS₂ mono- and bilayers is not an issue for WSe₂.

5.3 Experimental section

5.3.1 Fabrication

WSe₂ photodetectors were fabricated following a standard scotch tape exfoliation technique¹²⁵ onto HMDS-functionalised glass substrates. Multilayer devices show thicknesses between 5 and 32 nm. Once exfoliated, the contacts were patterned using optical photolithography with a maskless aligner (μ MLA, Heidelberg Instruments). For geometries with channel lengths of less than 2 μ m, the electrodes were written using electron beam lithography (JEOL JSM-6500F). The metal contacts were evaporated with a thickness of 2.5 nm titanium followed by 10 nm of gold at a pressure of $<2 \times 10^{-6}$ mbar. The storage and examination were performed under atmospheric conditions.

5.3.2 Transient photoresponse

The transient photoresponse was analysed using two different setups. First, at a Lake Shore Cryotronics CRX-6.5K probe station, described in more detail in our previous work,³⁷ and second, on a custom built confocal microscope to enable diffraction limited illumination,²⁷⁵ cf. Figure SI5.15 for more details. In short, laser illumination was carried out with either a square pulse laser (635 nm) switched on and off by a Hewlett Packard 33120A arbitrary waveform generator triggering a FSL500, PicoQuant laser driver to record the steady state response. To measure the impulse response of the sample a pulsed laser, emitting pulses with a pulse length < 500 ps at a repetition rate of 1 MHz (average output power 81 μ W, 636 nm) controlled by a Taiko PDL M1 (PicoQuant) driver. The square pulse laser had a nominal laser rise/ fall time of less than 0.5 ns and an output power of approximately 2 mW at the fibre end face. The laser power was further reduced due to coupling losses from fibre to fibre in the case of the probe station setup or via coupling through pinholes, reflection in mirrors and beam splitters when coupled with the confocal microscope. The dark current and ON/OFF electrical measurements were performed with a Keithley instruments 2636B source meter. For the time-resolved measurements, a Zurich Instruments UHF Lock-In amplifier was used with a Periodic Waveform Analyzer function averaging over 2 G samples in combination with a transimpedance amplifier (FEMTO DHPA-100) when necessary. The electrode pads were connected with 50 Ω matched tungsten probes and coaxial cables with bandwidths exceeding 1 GHz at the probe station. At the confocal setup, gold plated probe tips and triaxial probe holders (79-8000-T-03 Micromanipulator) were used to make contact beneath a custom build Faraday cage. For connection between the triaxial cables and the BNC-input at the lock-in amplifier a triax(F)-to-BNC(M) connector (Pomona) was used, however, the manufacturer's bandwidth specifications were not provided. The bandwidths of the other devices are 600 MHz for the lock-in amplifier and 175 MHz for the transimpedance amplifier at an amplification of 10^3 .

5.4 Results and Discussion

5.4.1 Reduction of the photoresistance

Steady state and non-steady state measurements were performed to characterise the switching behaviour of photodetectors. Typical illumination in literature ranges from minimal laser powers in the nW and sub-nW regime up to irradiances of more than 10 kW/cm².^{90, 159, 160, 203, 262–267, 271, 272, 276, 277} We begin by examining the photoresponse of a bulk WSe₂ flake, Figure 5.1c, under wide field illumination with an unfocussed laser beam

illuminating an area of about 1.5 mm^2 under ambient conditions. (See Figure SI5.1 and SI5.2 for the dark current and optical microscopy images, “flake 1”.) Typical steady state and non-steady-state responses are shown in Figure 5.1a (blue) and Figure 5.1b (blue), respectively, which are consistent with our previous studies on WSe₂.³⁸ As the response time depends among other things on the photoresistance of the sample, we increased the irradiance per area by repeating the same measurements within a confocal microscope using a diffraction-limited focussed laser beam. Considering the reduction of the illuminated area as well as coupling losses at pinholes and beam splitters, this increases the irradiance from roughly 0.4 to 400 W/cm^2 . Additionally, the illumination position can be precisely controlled in the confocal setup and the intensity can be varied by neutral density filters. By maximising the illumination intensity per area, the photoresistance in the steady state measurements decreases by a factor of 23, from $82.7 \text{ M}\Omega$ to $3.6 \text{ M}\Omega$, leading to the greatly reduced response time (measured with current amplifier) as shown in red in Figure 5.1a. This behaviour indicates an RC-limitation of the device.

The impulse response ($f(t)$) is fast Fourier transformed (FFT) to obtain the power spectrum ($P(\omega)$): $P(\omega) = |FFT(f(t))|^2$. After conversion to the dB scale, via $dB = 10 \log_{10}(P(\omega)/P_1)$ with the steady state power P_1 , the 3 dB bandwidth, i.e., the frequency at which the power drops to half its value can be read out.³⁴ Comparing the two values for the unfocussed and focussed measurement again reflects the factor 23, the dependence on the photoresistance, and supports the hypothesis of RC-limitation. The non-normalised square pulse measurements can be seen in Figure SI5.4. ON/OFF measurements performed with the same sample after six months (Figure SI5.3) reveal ratios $> 10^4$ and long-term stability under ambient conditions.

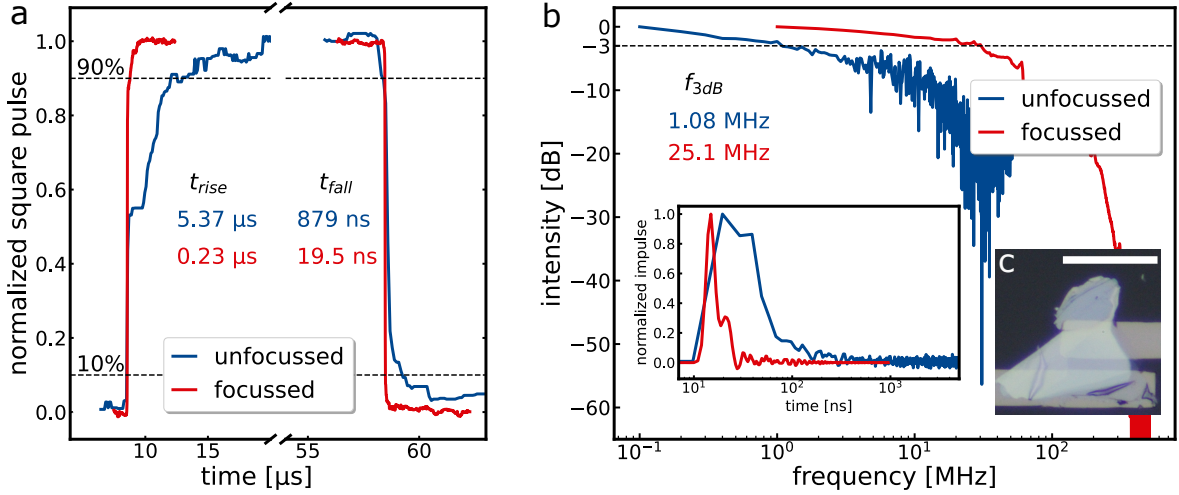


Figure 5.1. a) Square pulse measurements of the same WSe₂ flake characterised with an unfocussed (blue) and focussed (red) 635 nm laser illumination and 0.5 V bias. The unfocussed measurement is conducted at 10 kHz, whereas the focussed one has a repetition rate of 100 kHz. The red trace is split and shifted horizontally to match the unfocussed curve for better visibility. The irradiance is 0.4 W/cm^2 (unfocussed) over the whole channel and approximately 200 W/cm^2 (focussed), with only a fraction of the channel width illuminated. b) Power spectra of the 636 nm impulse laser with 100 kHz (blue) and 1 MHz (red). The inset shows the measurements in real-time. c) Light microscopy images of the WSe₂ flake fabricated with optical lithography. The scalebar is $20 \mu\text{m}$.

To determine the influence of the photoresistance onto the response time, the device was measured under different illumination intensities and positions of the laser focus on the sample. All measurements obtained in this way for the same device are summarized in Figure 5.2. If the hypothesis of an RC-limitation is correct, the slope of the linear fit to this data should resemble the capacitance of the device. The expected capacitance is obtained following Nabetl et al.:²⁷⁸

$$C = L(N - 1)\epsilon_0(1 + \epsilon_r)\frac{K(k)}{K(k')} \quad (5.1)$$

with the channel width $L = 25 \mu\text{m}$, the number of fingers $N = 2$, the vacuum permittivity (ϵ_0), the dielectric constant of WSe₂ ($\epsilon_r = 20$, as in our previous studies³⁹) and $K(k)$ being the complete first order elliptical integral with $k = \cos\left(\frac{\pi}{2}\left(1 - \frac{w}{w+g}\right)\right)$ and $k' = \sqrt{1 - k^2}$. The width w of the electrodes is $10 \mu\text{m}$ in the optical lithography structure and the gap g between the two electrodes is $2.5 \mu\text{m}$. This leads to a calculated capacitance of 7.6 fF . Multiplying by a factor of 2.2 which accounts for the 10 to 90 % rise/fall time values affords the black line in Figure 5.2, which provides a reasonable fit to the experimental data, thus strongly supporting the hypothesis of RC-limitation.

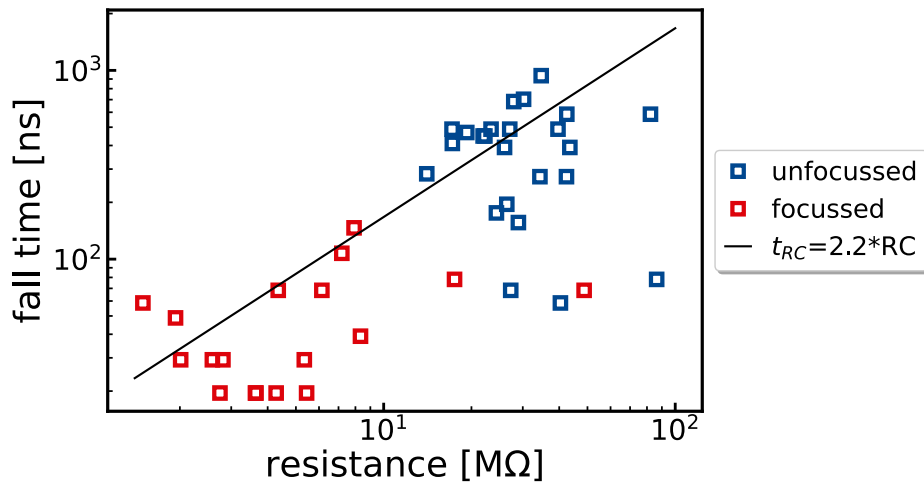


Figure 5.2. Fall time vs. photo resistance for all voltages. The data was obtained from various measurements performed at different dates, laser intensities and positions on an optical lithography processed flake. The black line represents the calculated RC-limited fall time using the estimated capacitance of 7.6 fF for the used geometry, according to $t_{RC} = 2.2 * RC$.

5.4.2 Reduction of the capacitance

We now aim to further increase the speed of photodetection with multilayer WSe₂ by reducing the device dimensions and, thus, the capacitance. With reference to the parameters in the formula for the capacitance by Nabetl et al., we reduce the electrode width (w) from 10 to $1 \mu\text{m}$, the channel length (g) from 2.5 to $1 \mu\text{m}$, and the channel width (L) from $25 \mu\text{m}$ to $20 \mu\text{m}$, see Figure SI5.5 for a scheme of the geometrical parameters. This decreases the expected capacitance from 7.6 fF to 4 fF .

An image of this new device based on a multilayered WSe₂ bulk flake is shown in Figure SI5.1b (“flake 2”) and the dark current as well as the ON/OFF ratios are displayed

in Figure SI5.6-SI5.8. At zero bias and $2\ \mu\text{W}$ illumination at 635 nm we find a photocurrent higher than 20 nA, as shown in Figure SI5.8, hinting at the presence of a built-in electric field presumably either due to slight height differences of the flake within the channel²⁷⁹ or to altered electric contacting of the electrodes as a result of the electron beam evaporation process.²⁵⁰ Figure 5.3 displays the non-steady state response and power spectrum of the new device (red curve) with a fall time $< 2\ \text{ns}$ and a 3 dB bandwidth of 230 MHz. For comparison, the photo response curve of the previous device from Figure 5.1 is also displayed (blue curve) to illustrate the effect of the reduced capacitance. In addition, we measure the power spectrum of a commercial photodiode with a nominal fall time of 200 ps (ochre curve) and expected 3 dB bandwidth of 1.75 GHz to find essentially the same 230 MHz cut-off as with the improved WSe₂ device. This strongly suggests that the measurements are limited by the setup, presumably due to the applied cables, connectors, the 600 MHz low pass filter within the lock-in amplifier, and that the true speed of the improved WSe₂ device might be even faster. Further evidence for such limitations is found in the periodic wiggles in the non-steady state response and the resulting noisy power spectrum, which can be attributed to reflections inside the cables as detailed in the SI, Figure SI5.13.

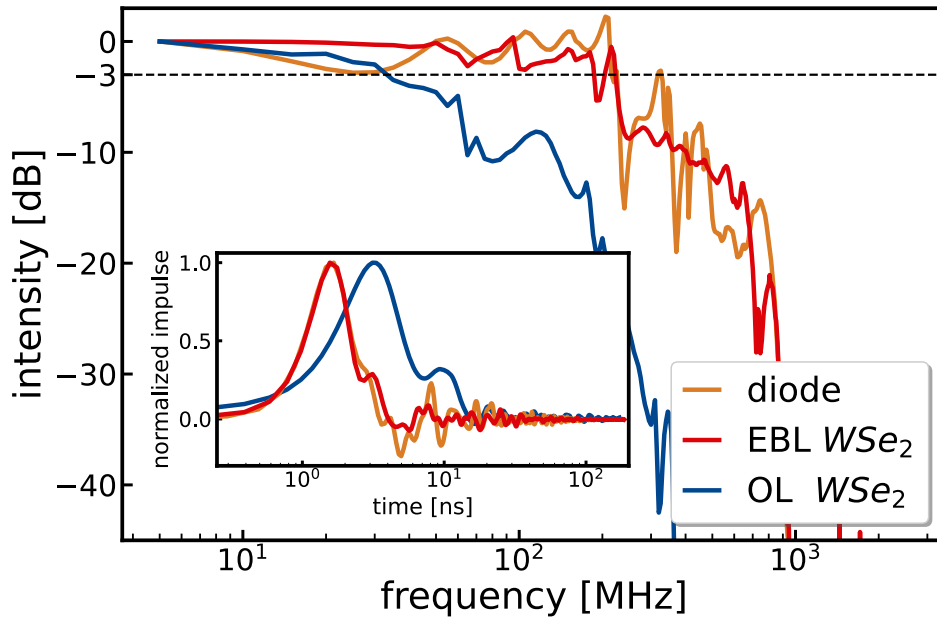


Figure 5.3. Power spectrum of a commercial photodiode (ochre) and an EBL fabricated WSe₂ flake (red) in comparison with an optical lithography WSe₂ flake (blue). The inset shows the impulse measurements in real-time. Both measurements were performed with a 636 nm pulsed laser excitation at 5 MHz. For the WSe₂ detector a bias voltage of 0.5 V is applied, for the diode 5 V in reverse bias direction. Irradiance for the measurements approximately $400\ \text{W}/\text{cm}^2$. Measurements of the diode and the EBL WSe₂ flake were performed without transimpedance amplifier.

We note that neither changing the bias between 0 to 0.5 V (Figure SI5.9) nor altering the laser intensity with optical density filters between 0.08 and 0.54 (Figure SI5.14) has a significant effect on the 3 dB bandwidth, again suggesting that all of these measurements fall into the setup limit. In principle, further reduction of the channel length below $1\ \mu\text{m}$

(Figure SI5.11) and channel width to decrease the resistance and capacitance, respectively, could be easily implemented with standard electron beam lithography. For instance, an easily feasible reduction of the channel width from 20 μm to 1 μm would decrease the capacitance by a factor of 20, cf. Figure SI5.10. However, we neglect such further optimisations at this point due to the speed-limitations of our setup.

For low-power optical communication, the switching energy is an important device parameter. For a measurement with zero bias, there is no additional energy cost for the applied voltage and the switching energy amounts to < 27 fJ/bit upon dividing a typical incident laser power of 6.25 μW by the (setup limited) 230 MHz bandwidth. Using a square pulse laser with comparable output power (2 μW) and irradiance (100 W/cm²), we calculate the responsivity of the device under typical operating conditions of 50 mA/W using the ON/OFF characteristics in Figure SI5.7. We note a strong power-dependence of the responsivity with quickly declining values at higher powers in line with earlier reports.^{90,271} Under the assumption that the dark current dominates the noise, we calculate the specific detectivity according to:¹⁰² $D^* = (\mathfrak{R} * \sqrt{A}) / \sqrt{2q * I_{dark}} = 3.9 * 10^{10}$ Jones, with 50 mA/W for the responsivity, an area A of 20 μm^2 , the electron charge q and a dark current of 1 pA. We obtain the external quantum efficiency as $EQE = (\mathfrak{R} * h\nu) / q$ with the responsivity, Planck's constant, the frequency and the electron charge respectively. With a responsivity of 50 mA/W at a wavelength of 636 nm this yields a value of approximately 10% which is in good agreement with earlier reports.⁹⁰

5.4.3 Reduction of the flake thickness to bilayers

For some photonic applications, it is desirable to decrease the thickness of TMDC devices from multilayers to bi- or even monolayers, e.g. to increase the photoluminescence quantum yield.²⁵⁹ However, for the most widely studied TMDC, MoS₂, Tang et al. have revealed that the speed of photodetection decreases by several orders of magnitude when approaching bi- or monolayer thickness.¹⁴⁰ This is the result of persistent photocurrents²⁸⁰ due to interface trap states²⁶¹ which are very prominent in atomically thin MoS₂ and provide a serious drawback for optical communication with MoS₂ photodetectors. To assess whether similar drawbacks exist for WSe₂, we have fabricated an ultra-thin WSe₂ device using the same geometries as for the 230 MHz multilayer photodetector (see Figure SI5.1c). Figure 5.4a shows a luminescence map of the flake with the respective spectra shown in Figure 5.4b. Positions 1 and 2 show the characteristic emission peak of WSe₂ monolayers at approximately 750 nm, whereas the others show the less intense and red-shifted bilayer emission.¹³⁰ Based on the luminescence, the scattering in Figure 5.4c and the optical image (Figure SI5.1c), we reconstructed the position of the mono- and the bilayer as marked in Figure 5.4c. From this, we infer that this photodetector consists exclusively of mono- and bilayers of WSe₂ within the channel. While a reliable power spectrum cannot be obtained due to the relatively weak absorption and photocurrent signal, we obtain a fall time of 19 ns in response to a square pulse (Figure 5.4d), demonstrating that the speed of WSe₂ photodetectors is much more robust against surface trap states, in stark contrast to MoS₂. We attribute the remaining speed difference compared to our champion multilayer WSe₂ device to the higher photoresistance due to the weaker absorption, which increases the RC time.

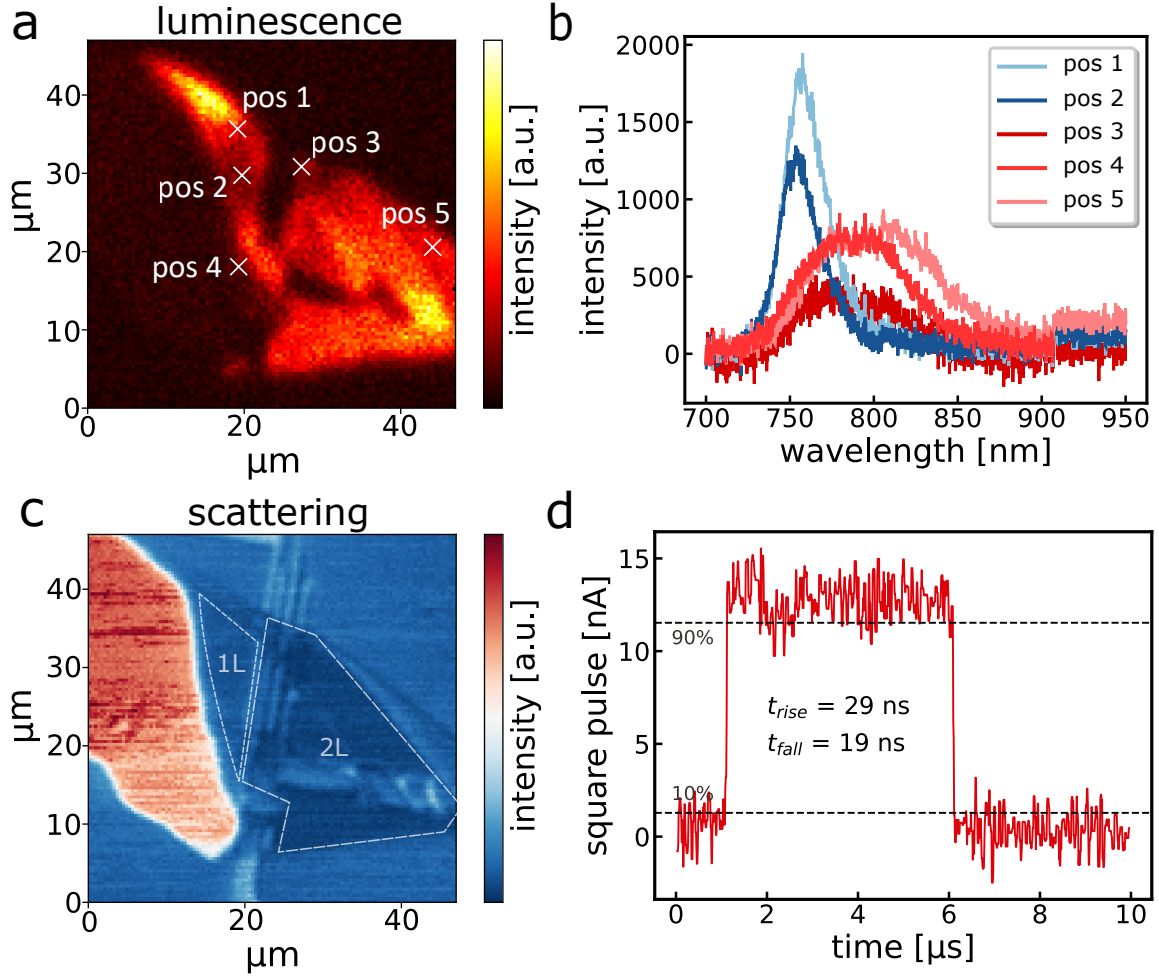


Figure 5.4. a) Luminescence scan of a mono-/bilayer WSe₂ flake. b) Representative spectra recorded at the positions marked in a). c) scattering image of the same flake. d) steady state measurement with a 635 nm square pulse laser driven at 100 kHz at a confocal setup at a bilayer WSe₂ flake.

5.5 Summary and Conclusion

We have systematically reduced the response speed of RC-limited, multilayered, pure WSe₂ photodetectors toward a record-high 3 dB bandwidth of 230 MHz. We have shown that optical switching with this device can be carried out at zero bias, requiring just 27 fJ per switching event. Reducing the detector thickness to mono- and bilayers of WSe₂ only weakly decreases the response speed, rendering WSe₂ advantageous over MoS₂ for fast optical communication. Further miniaturizations of the device geometry have the potential for Gigahertz photodetection with such easily fabricated WSe₂ photodetectors which exhibit long-term stability under ambient conditions.

5.6 Supplementary Information

Light microscopy images and height profile of the flakes 1 - 4

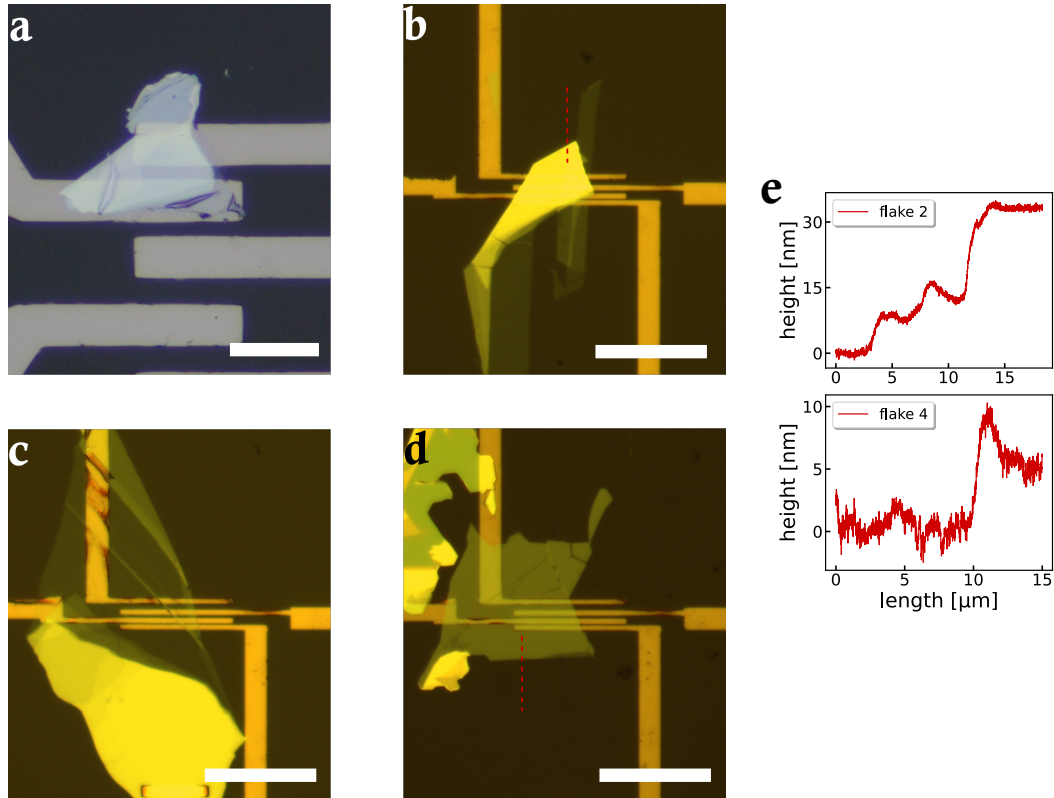


Figure SI5.1. Light microscopy images of the WSe₂ flakes measured for this work. **a)** shows the flake 1 which was fabricated with optical lithography. Flakes 2-4 are fabricated via electron beam lithography and shown in **b)-d)**. The scalebar is 20 μm in each image. **e)** shows the height profile of flake 2 (b) and flake 4 (d). The lines, where the thickness were measured are shown as dashed lines in the microscopy images. Profiles are measured at a Bruker DektakXT.

This figure shows the thicknesses of the measured flakes. Flake 1, shown in (a) has a thickness between flake 2 (32 nm) and flake 4 (5 nm), shown in SI5.1e, as can be seen in the microscopy images. Flake 3 is further characterised with luminescence spectra, see Figure 5.4. It consists of a monolayer region, cf. positions 4 and 5 in Figure 5.4, and a bilayer region, including the electrodes.

Dark current flake 1

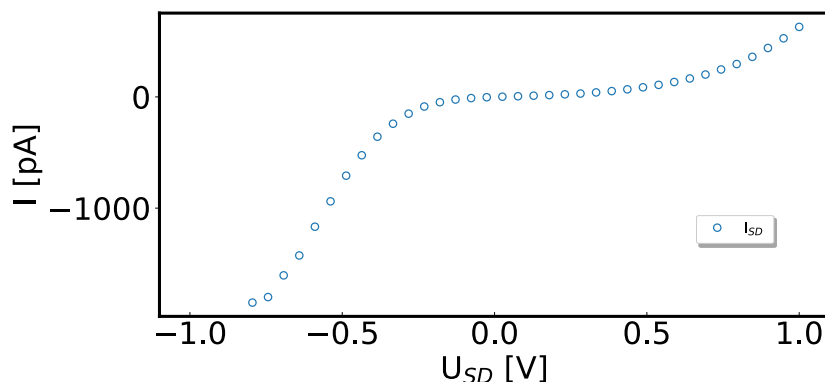


Figure SI5.2. Dark current of flake 1 from -1 to $+1$ V. The IV-curve shows a non-ohmic behaviour, typical for WSe₂.

In addition to the non-ohmic behaviour, the flake shows a slight asymmetry which can be caused by different heights.²⁷⁹

ON/OFF ratio of flake 1

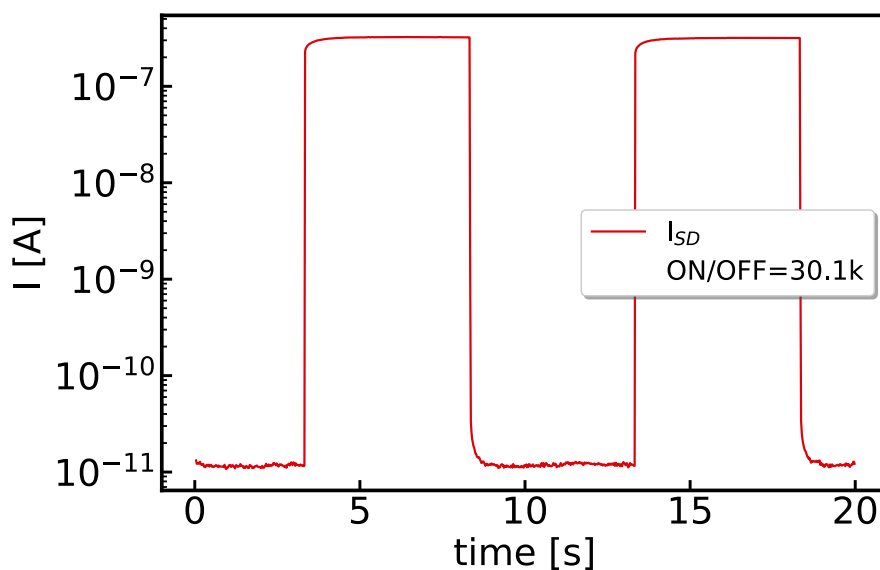


Figure SI5.3. ON/OFF ratio for flake 1 with 200 mV bias applied and 31 μ W illumination power with a 635 nm laser driven at 0.1 Hz. With a widefield lens the whole channel was illuminated evenly.

The ON/OFF ratio exceeded the measurement range of the Keithley 2636B. Therefore, the lower values were set from e-10 to e-11, to reflect the enormous ON/OFF ratio more accurately. Compared to Figure SI5.2, the dark currents at 200 mV bias are still lower than displayed here.

Square pulse measurements – current height

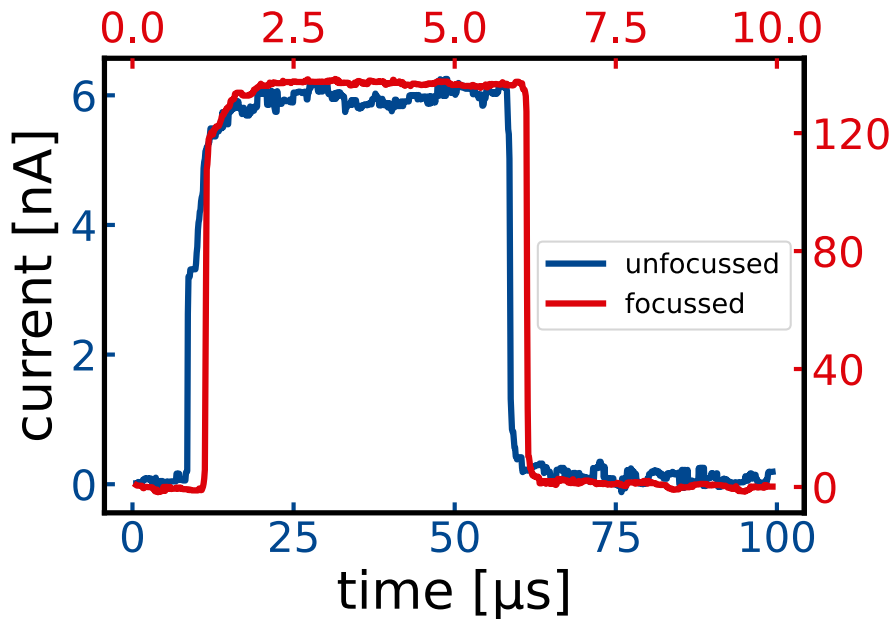


Figure SI5.4. Here, the exact same measurements like in Figure 5.1a are shown without normalization. The left y-axis and the lower x-axis correspond to the 10 kHz measurement without a focus. The red axis belongs to the 100 kHz measurement of the same flake under illumination. Irradiances are 0.4 W/cm^2 for the unfocussed measurement and 400 W/cm^2 for the focussed one.

Scheme of geometrical terminology

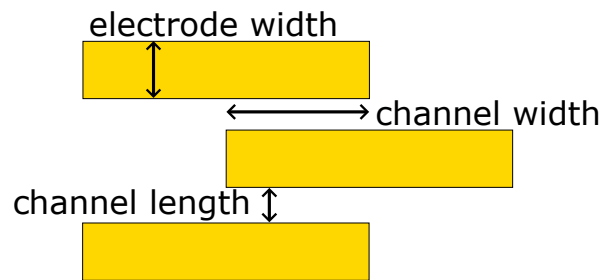


Figure SI5.5. Scheme of the contact geometry with specification of the used geometrical terminology.

Dark current flake 2

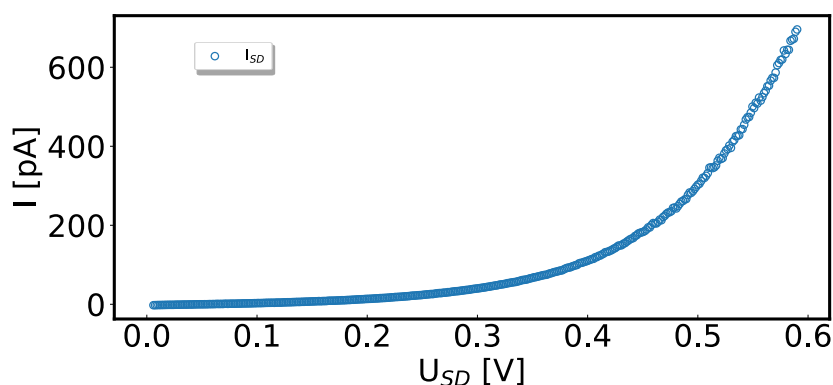


Figure SI5.6. Dark current of flake 2 from 0 to 0.6 V. The IV-curve shows a similar behaviour like before for flake 1.

ON/OFF ratio of flake 2

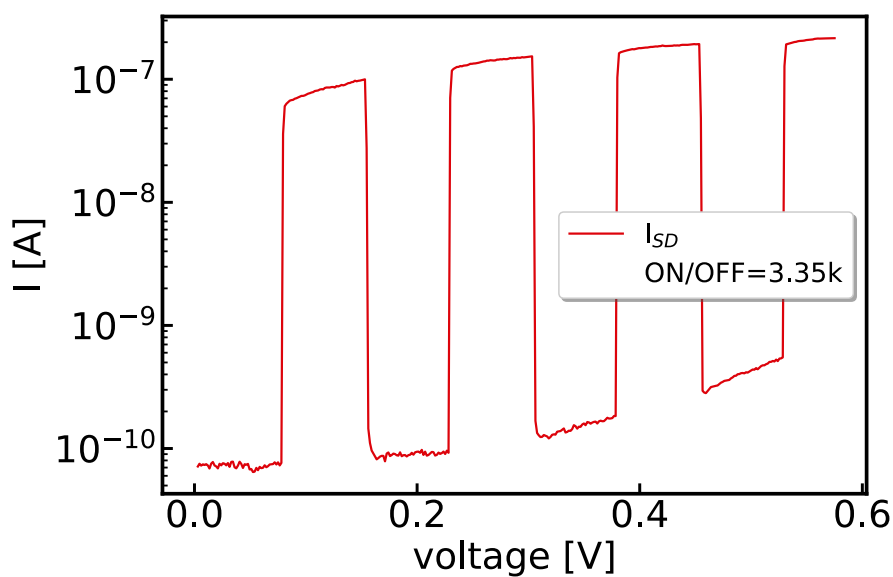


Figure SI5.7. ON/OFF ratio for flake 2 with a sweeping bias from 0 V to 0.6 V applied and $2 \mu\text{W}$ illumination power with a 635 nm laser driven at 0.1 Hz.

Figure SI5.7 shows the same dark current behaviour as before seen for Figure SI5.6. At the same time, the light current is increasing with higher voltage, but not as steep as the dark current. Thus, the ON/OFF ratio is shrinking for higher applied voltages and the displayed ON/OFF is the maximal ratio obtained.

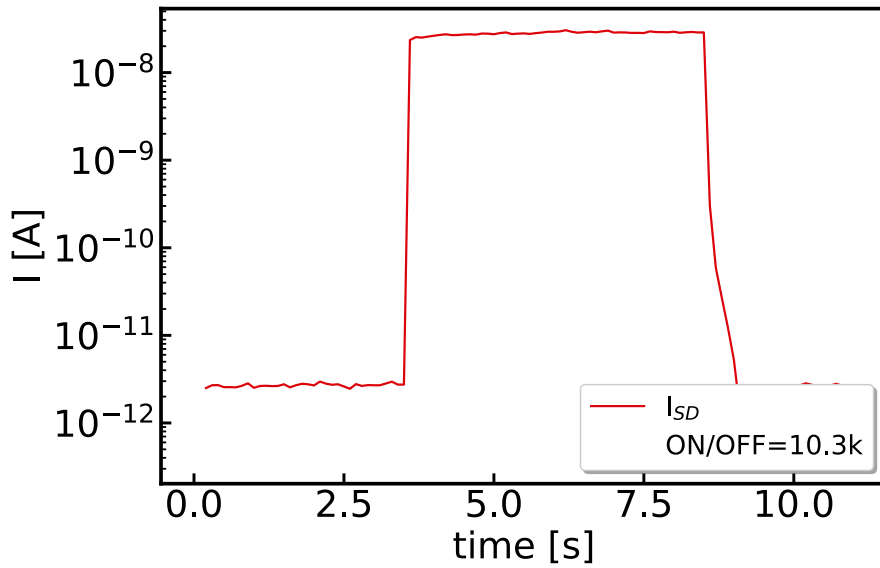


Figure SI5.8. ON/OFF ratio for flake 2 with a bias of 0 V and 2 μ W illumination power with a 635 nm laser driven at 0.1 Hz. The focus size was approximately 2 μ m.

Variation of bias for flake 2

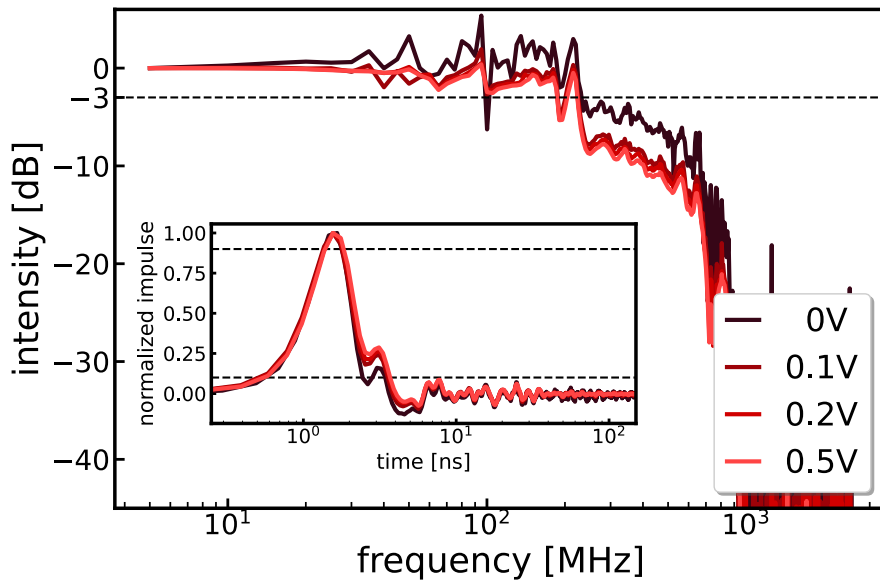


Figure SI5.9. Influence of different applied bias voltages for flake 2 on the power spectrum. The 636 nm impulse laser was driven at 5 MHz repetition frequency.

In Figure SI5.9 the voltage is varied to check for a transit limitation of the 1 μ m channel of flake 2. Since no difference between 0.1 V and 0.5 V is visible, no transit limitation is detectable at least within the 230 MHz setup limitation. The theoretical transit time can be estimated with: $t_{trans} = d^2/\mu U = \frac{(1 \mu\text{m})^2}{100 \text{ cm}^2/\text{Vs} * 0.1\text{V}} = 1 \text{ ns}$. Thereby, even the lowest voltage already yields a transit time of 1 ns with a moderate mobility estimated from few layer flakes.²⁵⁹ Accordingly, higher voltages would only be even faster than this time.

Simulated Capacity

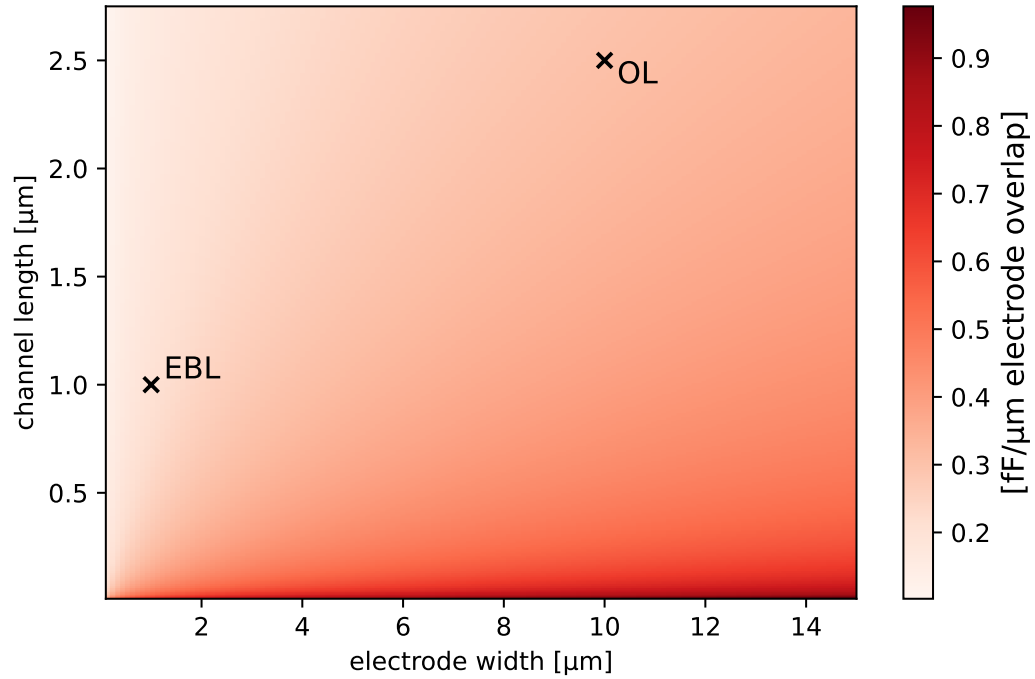


Figure SI5.10. Capacitance simulated for a variation of electrode width w and channel length g according to $C = L(N - 1)\epsilon_0(1 + \epsilon_r)\frac{K(k)}{K(k')}$ with $k = \cos\left(\frac{\pi}{2}\left(1 - \frac{w}{w+g}\right)\right)$ and $k' = \sqrt{1 - k^2}$. ϵ_r is set to 20, N to 2 and L is set to $1\ \mu\text{m}$. The crosses indicate the capacitances for the different lithographic approaches optical lithography (OL) and electron beam lithography (EBL).

Figure SI5.10 shows the calculated capacitance in fF per μm electrode overlap. For the $L = 25\ \mu\text{m}$ used in optical lithography and $L = 20\ \mu\text{m}$ used in electron beam lithography in this work, the capacitance is 7.6 fF and 4 fF respectively. The trends that can be seen follow the intuition, that the capacitance increases for larger electrode widths, longer channel widths and shorter channel lengths, cf. Figure SI5.5 for clarification of the geometry.

Channel length and photo resistance vs. fall time for flake 3 and 4

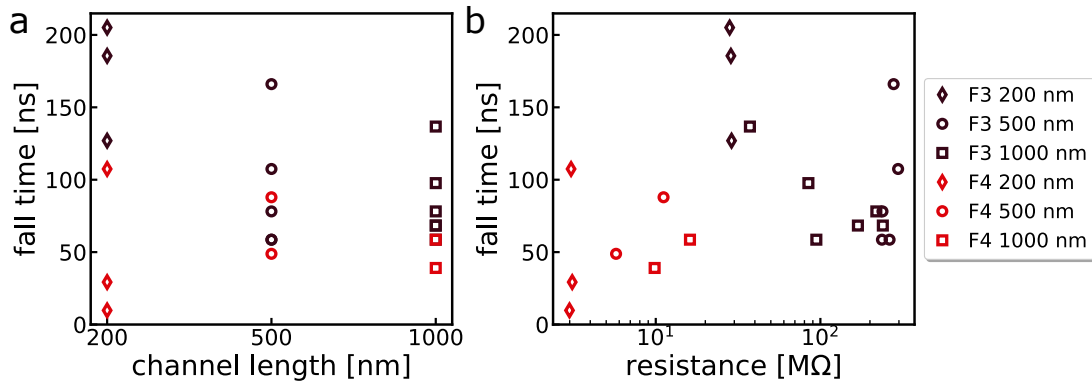


Figure SI5.11. a) channel length plotted versus fall time for the bilayer flake, flake 3 and the few layer flake, flake 4. b) the same measurements of a) are plotted in a resistance – fall time plot. All measurements are performed with a square pulse laser driven with 100 kHz and a laser power of $5.25 \mu\text{W}$. The bias voltages are 1 V for $1 \mu\text{m}$ channels, 0.5 V for 500 nm and 0.2 V for 200 nm channels.

Figure SI5.11 shows the variation of the channel length for the bilayer and the few layer flake. The idea behind a shortening of the electrode gap is again an acceleration of the detector due to the decrease of resistance, due to less material³⁷ and a shortening of the transit time.²⁹ For the two flakes shown here, it can be seen, that the shortening shows an ambiguous trend and the main limiting mechanism for the steady state measurements still seems to be the photoresistance, as can be seen in Figure SI5.10.

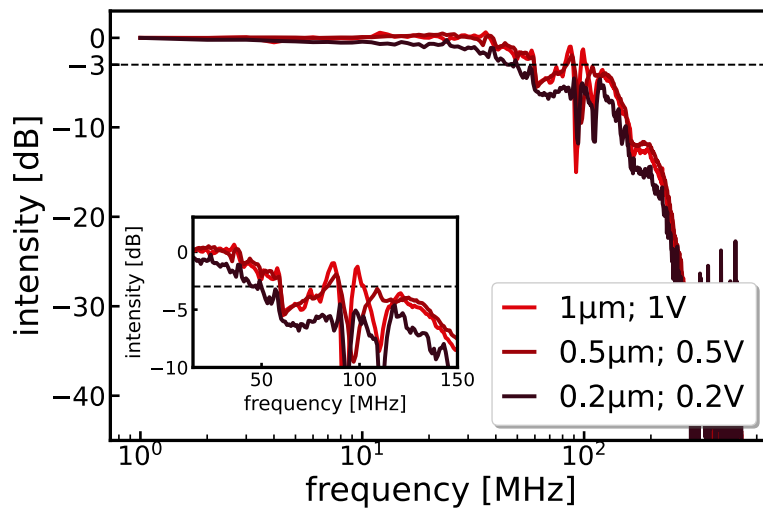


Figure SI5.12. Influence of the channel length on the power spectra of 1 MHz 636 nm laser measurements of flake 4. The bias is adjusted to get similar electric fields in the different channels.

The power spectrum tends to show a decreased bandwidth for the 200 nm channel. But all the bandwidths are close to the limit of our setup and thus too noisy, to observe a solid trend.

Cable reflections and influence on the Bandwidth

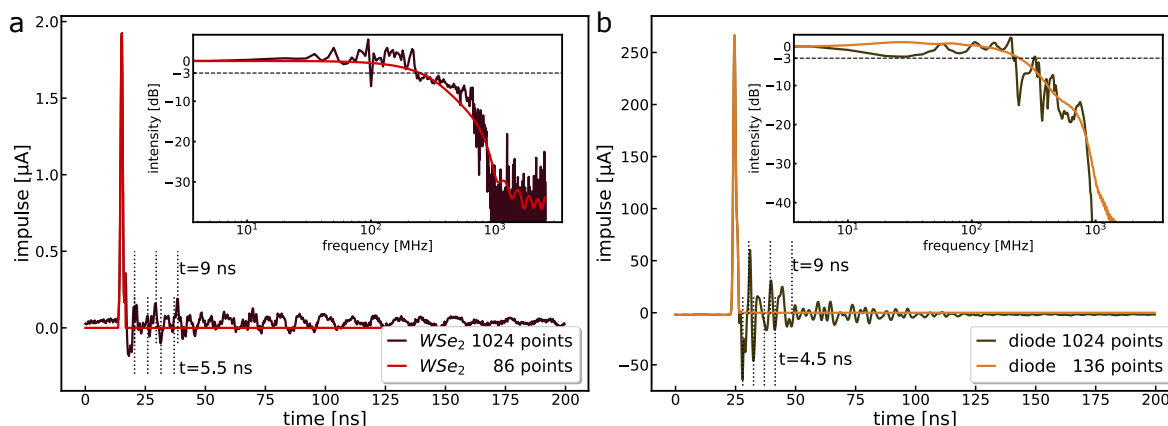


Figure SI5.13. Impulse and Fourier transformed impulse measurements for **a)** a WSe₂ sample (flake 2; 0 V) and **b)** a commercial Photodiode FDS015 (Thorlabs) with 200 ps nominal fall time. The dashed lines mark periodicities found in the time regime.

The impulse response decays very fast to zero followed by periodic signals. If the period of those signals is taken and multiplied with $2/3$ times the speed of light c , which approximately is the speed of charges inside the cables, it can be attributed to reflections in the cables with a cable length of about $9 \text{ ns} * 2/3 * c = 1.8 \text{ m}$ which roughly agrees with the length of the cable we have used (1.7 m). If the periodic signal following the delta pulse is set zero, then the power spectrum loses the spikes observed at frequencies larger than 40 MHz. Thereby, the frequency limit of our setup can be estimated to be between 230 and 240 MHz from the measurement of the commercial diode with a nominal bandwidth of 1.75 GHz.

Variation of the illumination intensity for flake 2

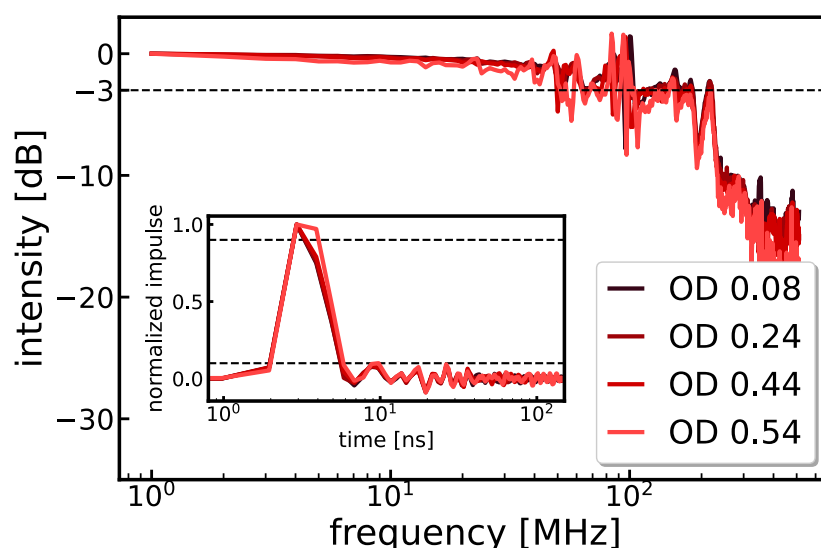


Figure SI5.14. Power spectra and impulse responses for 1 MHz 636 nm measurements of flake 2 for varied OD filters to alter the laser intensity to check for a RC-limitation.

By varying the irradiation onto the sample, an RC-limitation can be excluded or shown,

since the RC-time is a limiting factor. In combination with Figure SI5.9, the variation of the transit time, the limiting extrinsic mechanisms for a photodetector can be observed. Here, no influence of the photoresistance onto the response speed can be observed, thus the detector is either not RC-limited or the setup limit hides any dependencies.

Scheme of the custom built confocal microscope

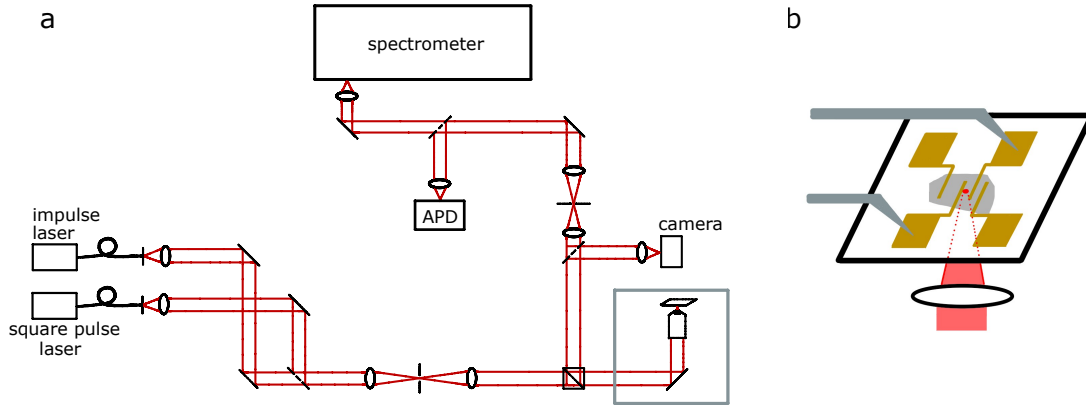


Figure SI5.15. a) Sketch of the confocal setup used for the focussed experiments. The part inside the grey box is rotated out of the plane and shown in more detail in b).

Figure SI5.15 shows the free beam setup. In more detail: The laser beam diameter is expanded by a telescope containing a 30 μm pinhole. The light is focused onto the sample through a Spindler und Hoyer 20x NA 0,5 objective after passing through an 50/50 non polarizing beam-splitter. For spectra collection and confocal imaging, the emission light is collected via the beam-splitter and sent through the detection telescope with an inserted 100 μm pinhole. The signal is collected on a ProEM+ 512B eXcelon camera attached to a Princeton Instruments Acton SP-2-500i spectrometer and a PerkinElmer optoelectronics SPCM AQR-13 (APD) respectively.

The minimal focal spot size can be estimated by the diameter of the Airy disc as follows:

$$D_{Airy} = 1.22 \frac{\lambda}{NA} = 1.22 \frac{636nm}{0.5} = 1.55\mu m$$

6 Key Results of Further Projects

During the work on this thesis, contributions to other publications within the framework of fast photodetection were made. This section summarises the key results of those publications, with a focus on the author's contribution and its relevance to the objective of this thesis.

6.1 Substrate Effects on the Bandwidth of CdSe Quantum Dot Photodetectors

Christine Schedel, Fabian Strauß, Krishan Kumar, Andre Maier, Kai M. Wurst, Patrick Michel & Marcus Scheele

The related article for the following chapter can be found in *ACS Applied Materials & Interfaces*.

The results of this study can be divided into the determination of the substrate influence onto the bandwidth of CdSe/I-/Zn4APc QDs and into the improvement of the detector limiting RC time. The change from glass to polyimide substrates accelerates the bandwidth of the detectors from 67 kHz to 85 kHz. This can be explained by the slow multiple trapping events within the particles, which are more pronounced on glass substrates.

The RC-limitation of the particles and ways to improve it are more interesting from the perspective of this work. First of all, the work emphasises again that the *photoresistance* not the resistance in the dark must be considered, when calculating or approximating the RC time.

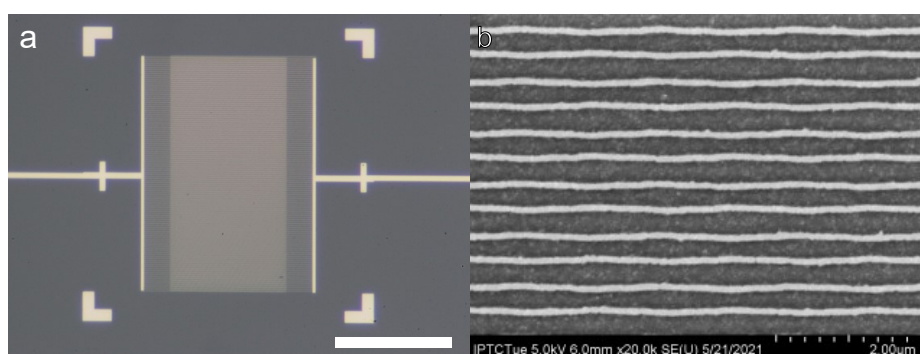


Figure 6.1. a) Light micrograph of the complete interdigitated electrode structure with channel length of 350 nm and width of 10 mm. Scalebar: 40 μm b) SEM image of electrode fingers with 350 nm gaps. Reprinted with permission from Ref.³⁷ Copyright 2021 American Chemical Society.

The strategy deployed to overcome or at least reduce the RC-limitation is shrinking of the channel length. Indeed, the reduction in the number of hopping events between QDs leads to a decrease in overall resistance. In pursuit of this strategy the channel length is shrunk from $2.5\ \mu\text{m}$ - $20\ \mu\text{m}$ down to $350\ \text{nm}$ by electron beam lithography, cf. Figure 6.1 for an exemplary device.

For a comparison between the new electrode geometries ('glass nm') and the previous devices with μm channels ('glass μm ') the rise times are plotted against the photoresistance, see Figure 6.2.

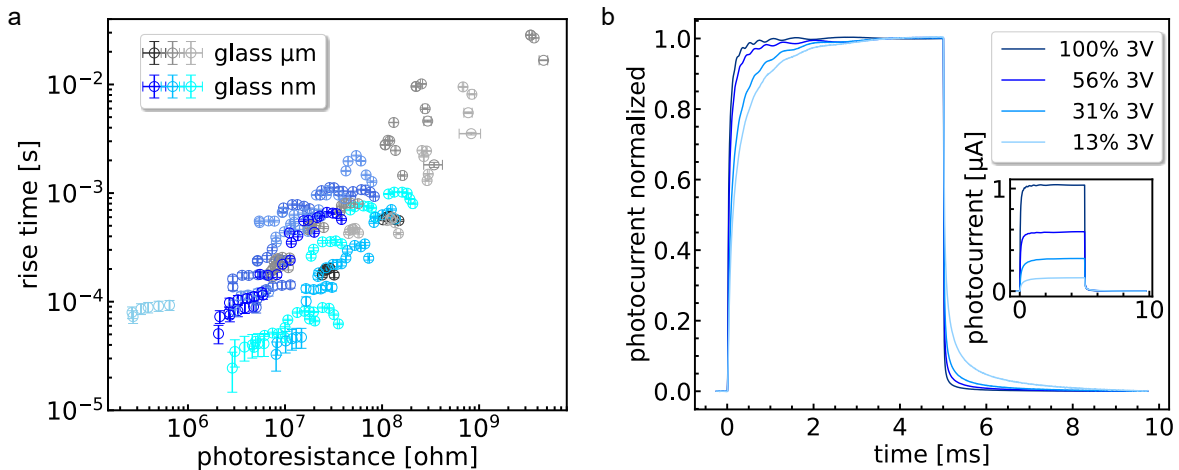


Figure 6.2. **a)** rise time plotted against photoresistance R_{illum} , for nm (blue) and μm (grey) channel lengths of CdSe photodetectors. **b)** 635 nm square pulse measurements at 100 Hz repetition rate for one representative nm device with varying illumination power. Reprinted with permission from Ref.³⁷ Copyright 2021 American Chemical Society.

Figure 6.2a reveals a trend of faster rise times with lower photoresistance emphasising the RC-limitation, as well as the success of the channel reduction strategy for faster detectors. To further verify that the RC-limitation is still persisting in the nm geometry devices, Figure 6.2b shows the laser power-dependent rise and fall time of the photodetector. A decrease in irradiance on the detector results in a higher photoresistance and in increased RC time.

The fastest devices in this work have a rise time of $24\ \mu\text{s}$.

6.2 Substrate effects on the speed limiting factor of WSe₂ photodetectors

Christine Schedel, Fabian Strauß, Pia Kohlschreiber, Olympia Geladari, Alfred J. Meixner & Marcus Scheele

The article related to this chapter can be found in *Physical Chemistry Chemical Physics*.

In a photodetector, the performance is affected by everything that surrounds or comes into contact with the active material. Often neglected is the substrate. To illustrate the significance of the substrate material on which the TMDC is deposited, the focus of this study was on the surface roughness and the dielectric constant.

In the limit of a monolayer's atomic thickness, surface roughness has a particularly strong influence on carrier scattering. This is because an uneven surface strongly enhances scattering. But even in the bulk crystal case, the first layers, and consequently the whole crystal are affected. In this study, bulk WSe₂ is measured on glass and polyimide with a surface roughness of 5.5 ± 0.7 nm and 30.7 ± 11.6 nm, respectively. On the rougher polyimide the dark currents are two orders of magnitude lower compared to the smoother glass, see Figure 6.3. This is presumably caused by the surface roughness.

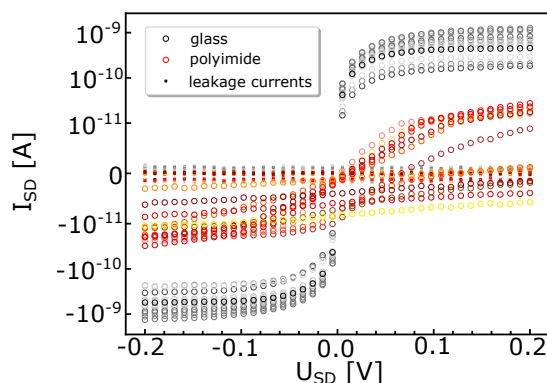


Figure 6.3. Dark currents of WSe₂ photodetectors on glass (grey) and polyimide (orange). Reprinted from Ref.³⁸ with permission from the PCCP Owner Societies.

Additionally, the absolute values of the photoresponse are lower on polyimide, increasing the RC time and the expected response speed at first sight. A popular prevention is the insertion of hBN as atomically thin and smooth protection layer between substrate and TMDC. Another benefit is the improved charge carrier mobility at the cost of a more complicated fabrication.¹⁵⁸

Besides the surface roughness, the substrate influence also extends to the dielectric constant. The study reveals an altered response time and mechanism on the two different substrate materials employed. The dielectric constant of glass (4.5 - 8)²⁸¹ induces stronger screening than on polyimide (dielectric constant 3.7)²⁸² for the TMDC detectors. The polyimide detectors are RC-limited and faster than the respective WSe₂ glass detectors which are limited before they could reach their RC time (Figure 6.4). The higher dielectric

screening presumably induces a shortened depletion layer and the glass detectors can be accelerated in non-steady state measurements to a maximal bandwidth of 2.6 MHz.

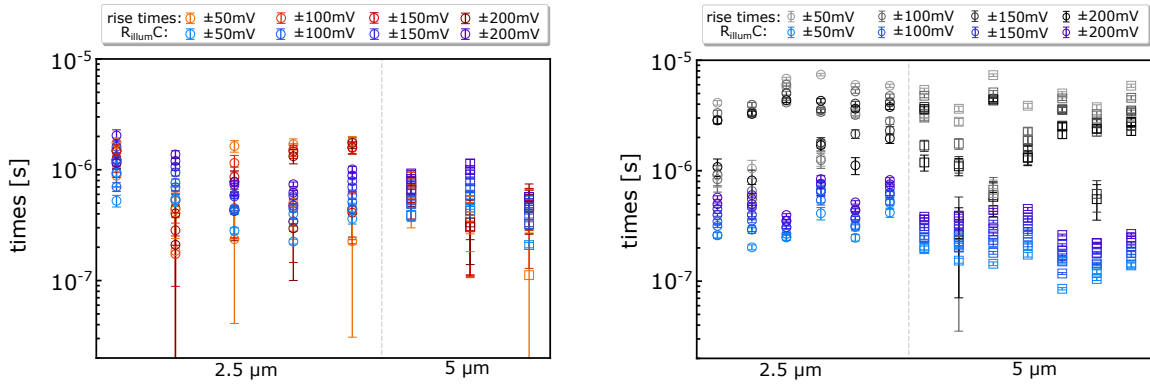


Figure 6.4. Measured rise times for WSe₂ detectors on a) glass and b) polyimide substrates. In blue, the calculated $R_{\text{illum}}C$ time is given. On the x-axis all measured contacts are listed with their respective channel length. Reprinted from Ref.³⁸ with permission from the PCCP Owner Societies.

6.3 Sub-nanosecond Intrinsic Response Time of PbS Nanocrystal IR-Photodetectors

Andre Maier, Fabian Strauß, Pia Kohlschreiber, Christine Schedel, Kai Braun & Marcus Scheele

The related article for the following chapter can be found in *Nano Letters*.

In contrast to the other projects presented here, this article focuses on intrinsic measurements and determines the material response time of PbS QDs with 1,2-ethanedithiol (EDT). Although the material differs from TMDCs, the concept presented here, particularly the differences between extrinsic and intrinsic, are a good example of device and material response.

The study shows intrinsic response times τ of $1 \text{ ns} \pm 0.1 \text{ ns}$ after fitting the exponential decay. This can be roughly translated into a bandwidth of 0.55 GHz using the approximation $f_{3dB} = 0.55/\tau$.²² To determine the recombination mechanism defining this time, different measurement parameters have to be varied. In summary, the observed acceleration is correlated with higher laser power, and no significant differences were found for applying a gate voltage, changing the temperature, or the channel length. These results strongly suggest that trap-assisted Auger recombination is the dominant mechanism. Equation (2.24) suggests that a drift- or transfer-limitation may be a factor. However, calculating the drift via the mobility yields a time on the order of milliseconds which is not visible on this short time scale.

Additionally, the influence of the surrounding atmosphere shows a deceleration of the recombination time under vacuum and an acceleration after air exposure, highlighting once more the importance of the measurement conditions also for material response times, cf. Figure 6.5a.

Another noteworthy point of this study is the comparison between the intrinsic and the extrinsic times. Upon square pulse illumination, the extrinsic rise time showed values of $3.5 \mu\text{s}$. This value may be limited by the RC time, which can be calculated to be approximately $8 \mu\text{s}$ for the detector. In contrast, the fall time towards the impulse laser shows fall times on the order of $300 \mu\text{s}$ which can be Fourier transformed into bandwidths around 1 kHz, see Figure 6.5b. Furthermore, higher voltages accelerate these times, indicating a transit time limitation.

The thus obtained deviation emphasises, for the showcase of PbS-EDT nanocrystals, the discrepancy between the detector speed (extrinsic response time) and the material speed (intrinsic response time) and why the values in literature are so widespread (Figure 6.5c). Theoretically, by changing and optimizing the detectors, speeds closer to the material response can be realised.

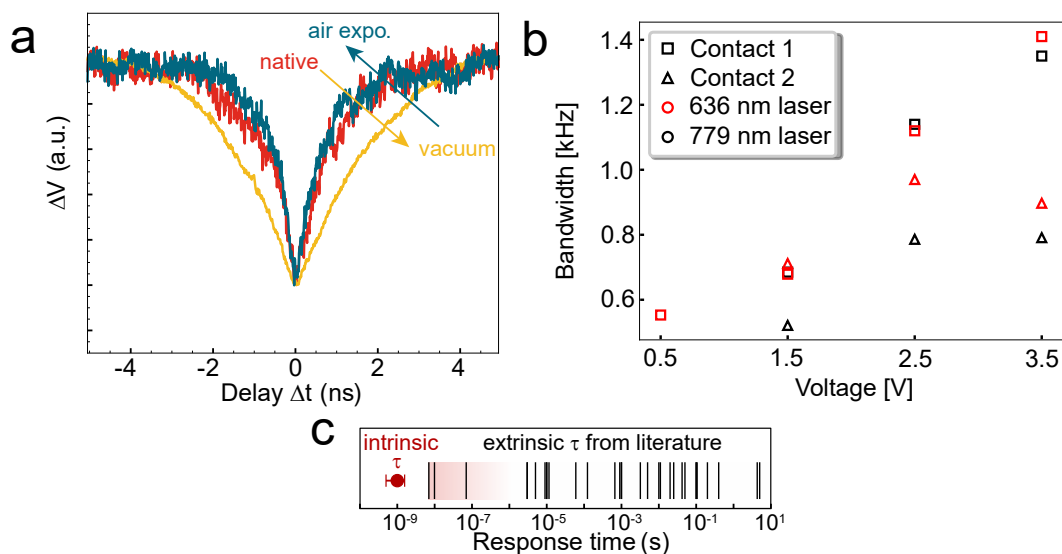


Figure 6.5. **a)** Normalized 2PC signal under different environments: under nitrogen (red), vacuum (yellow) and after 80 min air exposure, measured again under nitrogen (blue). All measurements were performed at room temperature with 1 V source drain voltage applied and an average laser power of 90 mW. **b)** Extrinsic bandwidths of the PbS-EDT QDs on two different devices excited with a 636 nm and a 779 nm laser with a repetition rate of 1 kHz. **c)** Comparison between the intrinsic time acquired in this study in comparison to several values for extrinsic times from literature.^{118,120,228,283} Reprinted with permission from Ref.³⁹ Copyright 2022 American Chemical Society.

7 Outlook

After evaluating different approaches for the acceleration of nanostructured photodetectors, this chapter provides an extended outlook on how this work could be continued. Thereby, the focus remains on pure material detectors renouncing heterostructures to create junctions in the detector.²³³ Especially intrinsic measurements show that approaches using TMDC heterostructures or the incorporation of graphene, either as electrodes, absorber or junction, are promising to speed-up the material response time, and the interested reader is referred directly to those articles found elsewhere.^{31,139,174} Another promising technique towards high-speed devices are waveguides.^{143,284} Existing examples show the feasibility of GHz bandwidths based on TMDCs, black phosphorous and graphene. While it overcomes the small interaction volume of a 2D material by a larger area size, the complex structuring and area needed makes scalability hard, thus, they are not discussed further in this outlook.^{151,152,213,285–287} Instead, the intention of this work is continued to further maximize the photodetecting speed of the pure TMDCs with scalable and easy-to-implement approaches. Once those implementations are understood and successful, the insights can be easily transferred towards more complicated material combinations.

In this spirit, the chapter first describes the required improvements for the measurement setup, on the one hand, to measure the true limit of the detectors described in Chapter 5 and on the other hand to measure the further improved detectors, which are expected to be faster.

Thereafter the bulk photovoltaic effect (BPVE) will be discussed. The BPVE is an anomalous effect based on materials with a broken inversion symmetry that gained more popularity recently due to more control over the 2D materials in fabrication. This effect promises not only to accelerate the detectors, but also to boost the responsivity at the same time.

Then, optical cavities are introduced to gain control over the exciton via coupling to photonic modes within such a cavity. By starting in a tunable cavity, the measurement will be much more complicated to begin with, but thus, optimal configuration for fixed cavities can be determined which then leads back to simpler experiments in the future.

Last but not least, the established field of plasmonics is briefly introduced with all the possibilities to enhance photodetectors with their ultrafast hot electrons and their well known field enhancement, which already revolutionized fields like Raman spectroscopy.

7.1 Measurement Setup 2.0

The current limitation of the setup used for the high-speed optoelectronic measurements is 230 MHz.³⁶ Starting from here, several consecutive steps have to be taken for reaching GHz regime measurements. First of all, the limitation imposed by the lock-in amplifier has to be reached by omitting the adapter needed from the 3 lug triaxial to BNC.²⁸⁸ This can be achieved by using different tips or exchanging the connector to the probe station respectively. Once the 600 MHz limit of the lock-in is reached, a new measuring instrument is necessary - an oscilloscope with bandwidths in the GHz regime.²⁸⁹ Additionally, new cables and a faster transimpedance amplifier (TIA) are needed, since both have a bandwidth of approximately 1-3 GHz.^{290,291} Since the BNC connector type is not suitable for higher frequencies, the connection has to be changed to SMA or similar cables which is a requirement for the oscilloscopes anyway.²⁹² For the TIA, the factor of amplification and the desired bandwidth range is the decisive factor in selection. Crucial for any decision is the principle that the smallest and largest 3 dB bandwidth of the setup determines which frequencies can be measured.

Despite the electronic improvements, which need to be done to detect faster photocurrents, the excitation can be optimised as well. The current laser systems used are approaching their temporal limits, thus a faster laser system with pulse widths below 100 ps would be a future benefit. Furthermore, being able to extend the feature of spectral flexibility, a super continuum laser providing excitation from 400 nm to NIR wavelengths, would be advantageous.²⁹³ With such a laser system, wavelength depending effects, such as cavities or plasmonics discussed in this chapter, could be exploited and examined even more.

7.2 Bulk Photovoltaic Effect

The use of extraordinary and anomalous effects is one way to continue applying pure materials without the necessity of creating heterostructures. The bulk photovoltaic effect (BPVE) is an exceptional example of using one material instead of a heterostructure.

Conventional photovoltaics is based on a pn-junction to separate the charges via an internal electric field created by the heterostructure, see Figure 7.1a.⁷ However, in non-centrosymmetric materials already the pure material can produce a photocurrent without any external field applied. This phenomenon is called the BPVE (Figure 7.1c).²⁹⁴ Describing the theoretical origin of the BPVE in detail is rather complex, reliant on second- and third order tensors describing e.g. the susceptibility and will thus be only done qualitatively in the following.²⁹⁵

Based on first experimental observations in the 1970s in ferroelectric oxides, a microscopic theory of the effect was proposed in 1982.^{296,297} This theory states that the effect is based on two distinguishable currents, the ballistic and the shift current.²⁹⁸ The quantum-mechanical shift current j_{sh} originates from electron shifts in real space following light-induced interband transitions, insensitive to scattering.^{298,299} This is sketched in Figure 7.1e, as the shift vector \bar{R} . In contrast, the ballistic current j_b originates from the asymmetric momentum distribution $\bar{\mu}$ related to kinetic processes within the material, like momentum relaxation in the fs regime.^{294,299} The thermalization of the non-thermalized carriers occurs within a transit length, called the free path length l_0 , around their excitation position back to the bottom of the conductive band, see Figure 7.1e.^{294,299} This ballistic current highly depends on scattering, making the exact theoretical prediction only possible with recent numerical calculations.²⁹⁵ Further distinctions could split the ballistic current into an additional injection current, appearing under circular polarized light.^{295,300} Comparing the I-V characteristics of conventional PV vs. BPV (Figure 7.1b,d), the latter can have an open-circuit voltage V_{OC} larger than the bandgap, if the carriers are collected within this l_0 .²⁹⁵ The importance of this free path length is mirrored in the necessity to collect charges within this regime to harvest the maximal photocurrent, otherwise the extracted current could display the dark current again, favouring small lateral channels or vertical stacks.³⁰¹

Due to those non-thermalized currents, there is a possibility to realize a photoelectric conversion efficiency beyond the Shockley-Queisser limit,³⁰² which gives the theoretical limit for (conventional) photovoltaic, making the BPVE also highly interesting in solar energy research.^{299,303,304}

The generation of the BPVE relies on the broken-inversion symmetries in non-centrosymmetric materials. Among them, ferroelectrics and piezoelectrics with spontaneous polarization are typical representative materials.^{305,306} However, it is also possible to observe the effect in centrosymmetric materials, when the inversion symmetry is broken at the edge or at a grain boundary.^{307,308} To generate the effect within the whole material, the usually used 2H-phases of semiconducting TMDCs are not suited. Instead, the symmetry has to be changed first, possibly by phase transitions into the distorted, semimetallic 1T' phase,³⁰⁹ or by so-called sliding ferroelectricity. The latter has been shown in MoS₂, MoSe₂, WS₂, and WSe₂ up to room temperature with low switching barriers beneficial for low energy and ultrafast application.³¹⁰ Realizing this rhombohedral (R)

stacking is either possible by the 3R-phases of TMDCs or by carefully aligning two monolayers, which usually leads to smaller domains caused by twist misalignments.³¹¹ The polarization and electric dipole moment formed is out-of-plane, leading to an interfacial charge transfer between the hybridized non-identical layers.³⁰⁶ Accomplishing non-centrosymmetry in TMDCs can also be done via strain engineering to maximize the photovoltage by approaching the two sides of a unit cell or electrical fields.^{294,312,313} More suitable for simple devices is the attempt to introduce (point) defects on purpose inside the material to break inversion symmetry.³¹⁴ Although it can be elaborate and complex to force TMDCs into a non-centrosymmetric phase, the benefit may be the possibility to retain the ferroelectricity down to the atomic scale, offering novel applications of the BPVE.³⁰⁶ Due to the dangling bond-free surface and, thus, large tolerance of interface states, the depolarization field of TMDCs is weak in comparison to conventional ferroelectric oxides. The depolarization field occurs at the interface by unscreened bound charges generating an electric field opposing the field of the polarization.^{305,315}

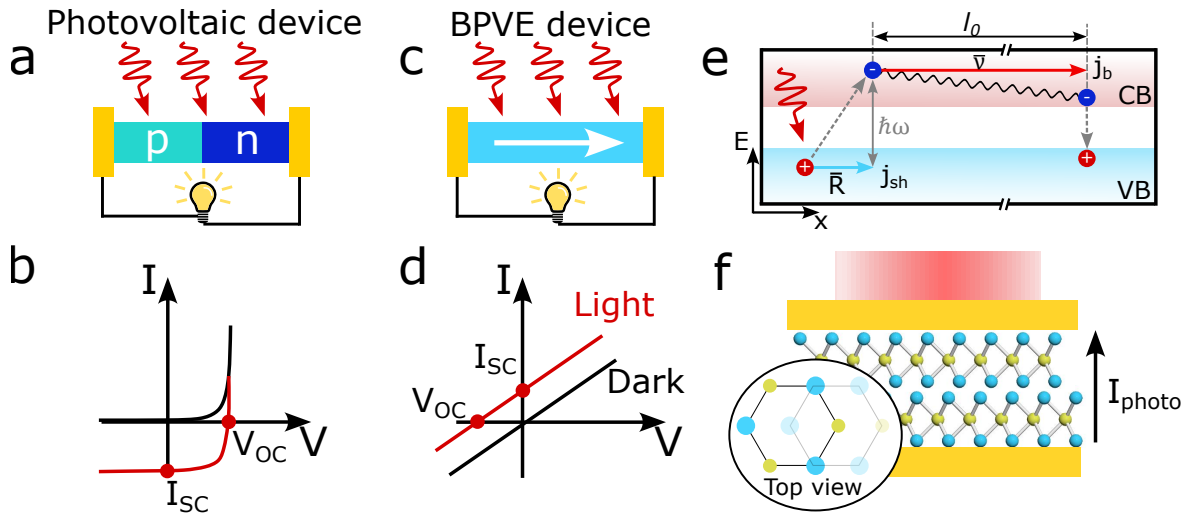


Figure 7.1. a) Scheme of a photovoltaic device based on a pn-junction. b) Exemplary I-V-curve of the device in a). c) Scheme of a bulk photovoltaic device with d) the corresponding I-V characteristic. Figures similar to Ref.³⁰⁹ e) Scheme of shift and ballistic current in a BPV device. Only optical excitation and recombination is sketched for simplicity. Horizontal axis displays the lattice x and vertical axis the energy. l_0 is the free path length of the excited hot electron. Figure similar to Ref.²⁹⁴ f) Scheme of a possible BPVE device based on non-centrosymmetric bilayer 3R-MoS₂ producing a photocurrent. Adapted from Ref.³³ Copyright 2024 American Chemical Society.

Verification of the successful implementation of broken symmetry can be done by non-invasive, all-optical measurements of the second harmonic generation (SHG).^{313,315,316} Thereby, the BPVE can be seen as the electrical counterpart of the SHG, thus measuring the SHG is no proof of the BPV behaviour, but a good indicator.³¹⁴ To further verify the ferroelectric properties, other techniques like surface tunnelling microscopy / spectroscopy or piezoresponse force microscopy have to be performed.³¹³ Based on the close relationship between SHG and BPV, implementing the same techniques which are used to increase the SHG in TMDCs³¹⁷ should give at least a correlation and hint in which direction the TMDCs can be boosted for the BPVE. Thus, methods like the charge-induced SHG,³¹⁸ or

injection of plasmonic hot electrons for ultrafast SHG³¹⁹ should also be possible to create a BPV current.³²⁰

Since the field of vdW-based BPVE is still evolving, further experiments are necessary to strengthen the understanding.²⁹⁵ Shedding more light onto the effect, like comprehension of the recombination mechanisms, demands intrinsic photocurrent measurements.¹⁷⁴ Nevertheless, some principal fabrication guidelines are already in place. First of all, larger shift currents are expected for materials with smaller band gaps.³¹² Concerning the device geometry, a channel parallel to the polarization and smaller than the free path length l_0 is needed. In-plane³²¹ and out-of-plane^{305,322} polarization thus dictates whether a planar or vertical detector is needed, cf. Figure 7.1f for a scheme of a vertical device. In addition, examinations with a tip-vertical geometry have shown the benefits of ferroelectrics over piezoelectrics due to the screening field surrounding the tip, which leads to band bending and impact ionization.²⁹⁹

First time-resolved photocurrent experiments have revealed ultra fast recombination mechanisms in vertical devices with graphene sandwiched 3R-MoS₂ down to 2 ps.³¹¹ Another study has found a responsivity and external quantum efficiency of up to 70 mA/W⁻¹ and 16 %, respectively.³⁰⁵ These initial results of the anomalous BPVE in TMDCs have shown a promising ultrafast photoresponse with high conversion efficiencies. Taking a step back and testing a simple detector without graphene electrodes would be necessary to determine the response of pure TMDCs. Either the 3R-phase could be taken directly, or defect engineering beyond PtSe₂³¹⁴ on the more typical TMDCs could be tried to produce a strong BPVE. As already mentioned before, testing the effects which induced an SHG in TMDCs is of interest as well. Thereby, especially the coupling with plasmonic structures is expected to be a promising approach.³¹⁹ Once a suitable material is established, a vertical detector design for the out-of-plane polarisation is suggested with the upper electrode consisting of a nanopyramid array,³²³ combining the already known benefits²⁹⁹ with possible plasmonic enhancement effects, which will be discussed later on in this chapter.

7.3 Optical Cavities

Confining the electromagnetic field via an optical resonator opens up the possibility of enhancing light-matter interaction.³²⁴ Before discussing some exemplary studies and applications, the theoretical background is briefly introduced. For a more detailed introduction and derivation of the equations described here, the reader is referred to elsewhere.³²⁵

7.3.1 Theoretical Background

An optical cavity can be formed by two plane-parallel mirrors with adjustable distance L_{cav} and reflectivity R , so light in between them is reflected back and forth, cf. Figure 7.2a. This particular example is the easiest way to describe an optical cavity and is also called a Fabry-Pérot resonator. Resonance is achieved when the phase matches during each passage, resulting in constructive interference:³²⁵

$$L_{cav} = \frac{m\lambda}{2n} \quad (7.1)$$

Thereby, m is an integer and n the refractive index of the medium inside the cavity. A photon is lost when it is transmitted through the mirror, called the photon decay rate of the cavity κ , which is resembled by the spectral width of the resonance $\Delta\omega$, see Figure 7.2a and b:³²⁵

$$\kappa \equiv \Delta\omega = \frac{c(1-R)}{nL_{cav}}, \quad (7.2)$$

with c being the speed of light. The quality factor Q of a cavity can be defined via the same $\Delta\omega$ as $Q = \omega/\Delta\omega$, which gives the deviation from a perfect cavity with no losses. It is therefore a good measure for comparing different cavities.³²⁶

Upon introducing a simple 2-level system into the cavity, such as an atom with the ability to absorb and emit photons, an additional non-resonant decay rate (γ) needs to be considered. This loss parameter accounts for off-axis and / or non-resonant emission of photons (Figure 7.2a). Furthermore, an atom-photon coupling parameter g_0 , determining the strength of interaction between the cavity and atom based on the interaction energy set by the electric dipole interaction, can be defined:³²⁵

$$g_0 = \left(\frac{\mu_{12}^2 \omega}{2\epsilon_0 \hbar V_0} \right)^{1/2} \quad (7.3)$$

It is influenced by the transition dipole moment μ_{12}^2 , the frequency of the light ω and the mode volume V . For more than one atom inside the cavity, g_0 scales with the square root of the number of atoms \sqrt{N} .^{325,327}

If the losses κ and γ are compared to the coupling, two different regimes can be determined: weak and strong coupling. If the interaction in the atom-cavity system merely influences the spontaneous emission rate, weak coupling is observed. However, if the frequency of the emitted photon is influenced, the interaction alters the energy levels responsible for emission, and strong coupling is achieved. Both models will be briefly described in the following.³²⁵

Weak coupling. In this regime, the photons are lost faster than they are reabsorbed by the atom, that is, $g_0 \ll \kappa, \gamma$, in which case the interaction can be described by perturbation

theory. The main effect, also called the ‘Purcell effect’,³²⁸ of the cavity is the suppression or enhancement of the emission rate W by influencing the density of states $g(\omega)$ by being *in-* or *off-*resonance with the atomic transition (Figure 7.2b) in accordance to Fermi’s golden rule:³²⁵

$$W = \frac{2\pi}{\hbar^2} |M_{12}|^2 g(\omega), \quad (7.4)$$

With the transition matrix element $M_{12} = \xi^2 \mu_{12}^2 E_{vac}^2$, the electric dipole interaction with ξ being the normalized dipole orientation factor. By comparing the transition in free space (W_{free}) with that in the cavity, W_{cav} , assuming exact resonance and dipoles oriented along the electric field, the Purcell factor $F_P W_{cav}/W_{free}$ is obtained:³²⁵

$$F_P = \frac{3Q(\lambda/n)^3}{4\pi^2 V_0} \quad (7.5)$$

For $F_P > 1$, one can expect enhanced emission, while $F_P < 1$ leads to suppressed emission.

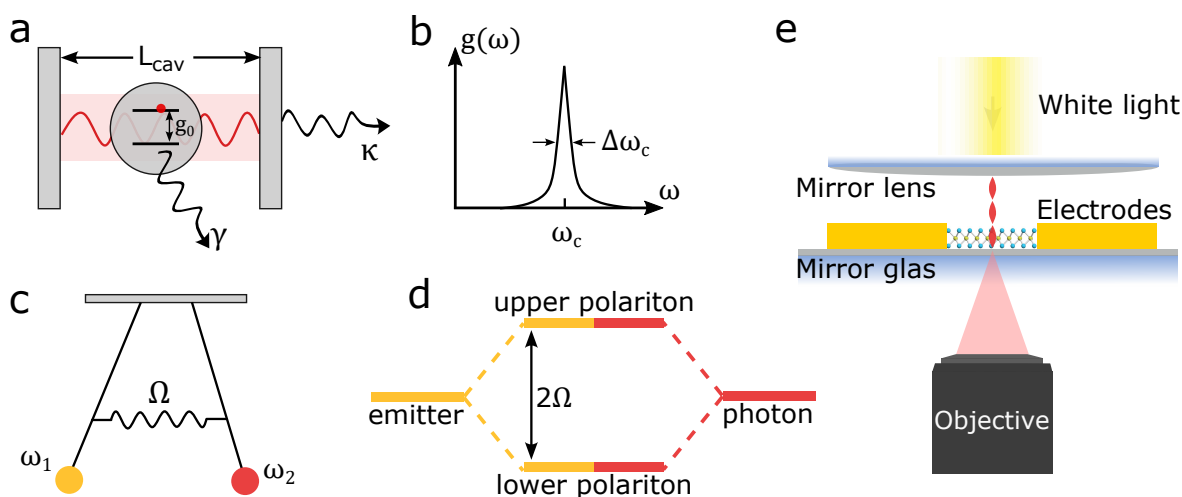


Figure 7.2. a) Scheme of a Fabry-Pérot resonator with a two-level atom inside. b) Density of states within a cavity. c) Pendulum analogy for strong coupling. d) Hybridization between photon and emitter into a lower and upper polariton under strong coupling. Figure similar to Ref.³²⁹ e) Scheme of an experimental setup allowing time-resolved photocurrent measurements simultaneously to cavity resonance tuning. Adapted from Ref.³³ Copyright 2024 American Chemical Society.

Strong coupling. If a photon is reabsorbed faster by the atom than lost by the cavity, that is, $g_0 \gg \kappa, \gamma$, the interaction between the cavity and atom is reversible and strong coupling is achieved. This can be described by the quantum mechanical Jaynes-Cummings Model³³⁰ which is in a rough approximation similar to the Rabi model, considering the interaction between only few photons and quantized light fields including the vacuum E-field. In a quasi-classical analogy, strong coupling can be understood as two coupled pendulums, with Ω being the coupling strength (Figure 7.2c). At the resonance of the oscillation, the system will then experience an energy transfer induced by the coupling, which appears as a spectral splitting into two polaritonic states:

$$\omega_{\pm} = \omega \pm \Omega, \quad (7.6)$$

around the resonance frequency, see Figure 7.2d.³²⁵ Briefly, the proportionalities for strong light-matter coupling can be described by:^{325,327}

$$\frac{g}{\gamma} \sim \sqrt{N}\mu \times \frac{Q}{\sqrt{V}} \quad (7.7)$$

Thus, higher coupling strengths can be achieved via tuning the material (increasing the number of emitters or the dipole strength), or the cavity (increasing the quality factor or reducing its volume).

7.3.2 Optical Cavities for Fast Photodetectors

Coupling with a cavity can be understood as light confinement in time and space.²⁸⁴ Thereby, a small cavity volume defines the confinement in space, and this is much more pronounced in plasmonic cavities.³³¹ However, higher quality factors are hard to achieve in light of the losses present in such plasmonic cavities.²⁸⁴ Optical cavities realized by Fabry-Pérot resonators, Bragg mirrors or whispering gallery modes on the other hand are able to achieve high quality factors,³²⁶ and thus are able to achieve a relatively long photon lifetime compared to the free space, which has to be paid attention to, especially for ultrafast applications.

Augmenting the photoluminescence and absorption (PL) by the Purcell effect in the weak coupling regime has been shown for a variety of 2D materials and cavities.^{332–335} Enhancing the absorption does not only increase the PL, but also affects the photocurrent. For example, a graphene-based photodetector inside a Bragg mirror has been shown to improve from 2.3% to 60% absorption which increased the photocurrent by a factor of approximately 20.³³⁶ Interestingly, for the experimental design the spacer layer between mirror and active material was found to be pivotal, since no spacer can lead to a worse absorption than no mirror at all.³³²

The relationship between the Purcell effect and the time-resolved photocurrent remains unclear so far. Since the weak coupling regime does not change the exciton dynamics,³³⁷ the effect of enhanced absorption and thus photocurrent could lead to a decreased RC time of the device. The suppression of the radiative decay paths promises to influence the material response time by leading to more charge carriers in non-radiative pathways. This might be only visible within intrinsic measurements, or if the influence on the response time is tremendous maybe even within extrinsic measurements.

First experiments with black phosphorous on a photonic crystal cavity / waveguide demonstrated a 36-fold enhancement of the responsivity in combination with a fast bandwidth of >1.42 GHz, thus showcasing the compatibility of cavities with high speeds.³³⁸

The strong coupling regime requires large exciton energies to be observable at room-temperature, for which TMDCs are an ideal platform.³³⁹ The realization of strong coupling for TMDCs has first been shown in 2014 with monolayer MoS₂.³⁴⁰ Since then, several reports with different coupling strength Ω have been published, not only for MoS₂.^{284,341,342} Being able to couple to a cavity, the resulting properties which are influenced by the coupling are of great interest, particularly with respect to charge transport and exciton transfer. For the Förster-like excitation-transfer it has been shown that the limitation of transfer lengths to a few nanometers is lifted upon introduction into a cavity.³⁴³ Further results on exciton conductance show a delocalization of the polaritonic

mode, overcoming disorder or imperfections.^{344,345} Experiments with organic semiconductors strongly coupled to a plasmonic cavity have shown increases of the conductivity by one order of magnitude caused by delocalizing the excitons via polaritons.³⁴⁶ Thereby, the influence on the conductivity has been demonstrated to depend on the Rabi splitting Ω , favouring higher splitting strengths. The examination of six-layer WS_2 within a Fabry-Pérot cavity has shown an increased electron mobility by a factor of 50, as well as a modulation of the Schottky barrier height up to 45 meV under resonance conditions.³⁴⁷ This shows further possibilities of tuning the photoresponse and device properties within a cavity. Theoretical considerations even predict superconductivity within TMDCs in cavities intensifying the importance of research in exciton-polariton coupled systems.³⁴⁸

Beyond the altered conductivity, early studies in organic semiconductors have shown strong coupling to increase the radiative rates and suppressing the slow, rate-limiting, non-radiative pathways,³⁴⁹ which could have promising impacts on TMDC based photodetectors.

Conducting time-resolved photocurrent measurements within an optical cavity requires a well-designed setup which will be shortly addressed here. An obvious prerequisite is a tunable cavity³⁵⁰ that allows the variation of the cavity resonance while measuring the photocurrent. This will give access to the relation between the optical effects described above and the (time-resolved) photocurrent, cf. Figure 7.2e. Once the effect of the cavity is clear, it is possible to implement the device in a fixed cavity with the desired resonance to enable scalability. Such an implementation of one or two fixed cavities simultaneously has been shown to i.e. bring new switchable detection in QDs based on the bias-dependent diffusion length,³⁵¹ or wavelength-dependent sensing based on the implemented resonance.³³⁶

In more detail, particular attention has to be directed to the material with regards to thickness and the Stokes shift. The emission rate decreases drastically for thicknesses above a monolayer due to the transition from direct to indirect semiconductor for most TMDCs.¹²⁹ Interestingly, thick TMDCs can be treated as a cavity by themselves which would complicate the system even more.³⁵² By choosing a material with a small Stokes shift, e.g. WS_2 , strong coupling gets more relevant due to the larger possibility of reabsorbing an emitted photon.³⁵³ As mentioned before, the cavity mirrors have to be highly reflective to provide a higher Q-factor, but at the same time they have to preserve some transmittance, otherwise no light can enter the cavity.³³⁶ In addition to the necessity of a spacer layer for an appropriate distance to the mirrors,³³² the layer has to be electrically insulating to allow accurate photocurrent measurements. A suitable process in this context is applying Al_2O_3 by atomic layer deposition.³⁵⁴ Last but not least, it is important to encapsulate the tips and the whole cavity within a Faraday cage to prevent external interference signals.

Following those guidelines, one can expect that reaching the weak and the strong coupling regime of a photodetector and a photonic microcavity will drastically change the speed and efficiency of the device.

7.4 Plasmonics

In the context of cavities, plasmonics have already been briefly introduced in the previous section.^{331,337,355–357} Within this section, the point of view will be shifted slightly away from the strong light-matter coupling and Rabi oscillations towards the subject of near-field enhancement and hot electrons inherent to plasmonic nanostructures, although this inevitably overlaps with optical cavities with respect to the polaritonic nature of the excitation.

Plasmonics offer a versatile and promising platform for the next generation of subwavelength and ultrafast optoelectronics, exceeding the diffraction limit of conventional optics as well as current delay time limitations and heat development in modern day electronics.³⁵⁸ After some theoretical basics of the subject, recent advances and future prospects of this field are given with respect to ultrafast photodetection. More detailed derivations of the formulas presented here can be found elsewhere.^{359,360}

7.4.1 Theoretical Background

In a simplified picture, plasmons can be described as the quantized oscillations of the free electron gas excited by an external electromagnetic wave. In this approximation of the *plasma model* according to Drude and Sommerfeld, the positively charged ion cores are taken as static and the electrons as a freely moving gas. This model collapses when it comes to interband transitions within the material. Other effects, like electron-electron interactions are accounted for by taking an effective optical mass m_e for each electron. Solving the equations of a damped, driven oscillator with an external electric field E with harmonic time dependence as well as damping of γ results in the dielectric function $\epsilon(\omega)$:^{359,360}

$$\epsilon(\omega) = 1 - \frac{\omega_p^2}{\omega^2 + i\gamma\omega} \quad (7.8)$$

with $\omega_p^2 = ne^2/\epsilon_0 m_e$, the so-called volume plasma frequency, which is characteristic for any conductor. The damping γ resembles a collision frequency inside the material on the order of 100 THz at room temperature. The complex dielectric function $\epsilon(\omega)$ can be split into a real and an imaginary part. Qualitatively, the real part has to be negative to enable plasmonics inside the material and the imaginary part, the absorption, should be as small as possible. Materials that fulfil this prerequisite are mostly conductive materials, specifically, noble metals. For gold i.e. the interband transitions occur above 2.5 eV and thus it is not suited for plasmonics in the UV, due to the large absorption loss in this part of the spectrum.^{359,360}

By solving Maxwell's equations for a conductor and a dielectric, surface plasmon polaritons (SPP) are obtained which propagate along the flat interface. To excite an SPP, special techniques like the aid of a prism or a grating are necessary to ensure energy and momentum matching.^{361,362} Estimations for the propagation length on gold interfaces yield 10 μm before the SPP is thermalized. For the penetration depths of the evanescent waves into the metal and the dielectric, 1/e decay lengths of 28 nm and 328 nm are achieved, respectively.³⁶⁰

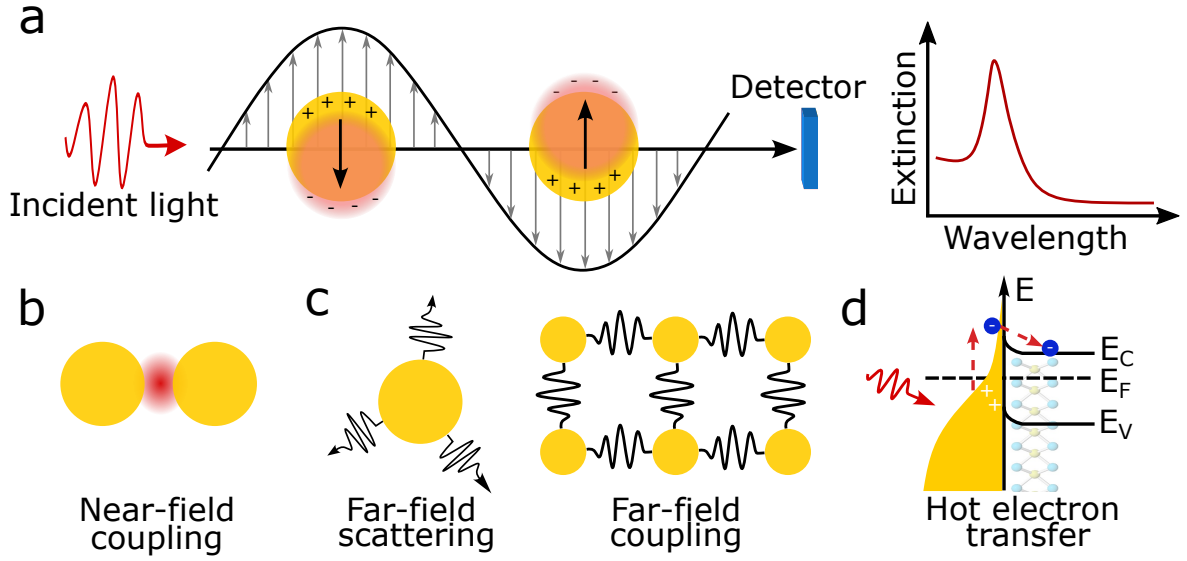


Figure 7.3. **a)** Excitation scheme of a localized surface plasmon resonance (LSPR) in a gold nanosphere. The displayed signal on the detector shows the spectral response. Figure similar to Ref.³⁶³ **b-d)** Processes after LSPR excitation in nanoparticles. **b)** Near-field coupling between two gold spheres in close proximity. The near-field enhancement is indicated in between them. **c)** Far-field scattering on the left for a single particle. Particles arranged in a proper lattice can couple their far-field radiation. **d)** Schematic hot electron transfer from a gold nanoparticle over a Schottky barrier to a TMDC semiconductor. Figure similar to Ref.³⁶⁴

Direct excitation of a plasmon is possible in small nanoparticles of size d , smaller than the excitation wavelength due to the curved surface, cf. Figure 7.3a. Thus, the phase of the harmonic electromagnetic wave is nearly constant over the whole particle. In this quasi-static approximation, the simplest solution is derived for spheres, but can also be calculated (numerically) for more complex shapes. Solving the Laplace equation $\nabla^2\Phi = 0$ to calculate the electric field, the equations evolving can be interpreted as a superposition of the external field and a dipole in the center of the particle. Introducing the polarizability α , the dipole moment can be written in the form of $p = \epsilon_0\epsilon_m\alpha E_0$, with the dipole moment p . Solving the equation more precisely yields:³⁵⁹

$$p = \epsilon_0\epsilon_m 4\pi a^3 \frac{\epsilon - \epsilon_m}{\epsilon + 2\epsilon_m} E_0, \quad (7.9)$$

from which it follows that α can be written as: $\alpha = 4\pi a^3 \frac{\epsilon - \epsilon_m}{\epsilon + 2\epsilon_m}$. Thereby, $4\pi a^3$ corresponds to a factor based on the geometry of a sphere with radius a . ϵ_0 and ϵ_m are the dielectric constants of the particle and the surrounding medium, respectively, and E_0 is the surrounding electric field. Apparently, α becomes resonant under the assumption of a nearly constant $\text{Im}[\epsilon]$ around the resonance under the so-called ‘Fröhlich condition’ $\text{Re}[\epsilon(\omega)] = -2\epsilon_m$. Particularly interesting for the application of plasmonic nanoparticles in optoelectronics is the scattering and absorption cross section C_{sca} & C_{abs} :³⁵⁹

$$C_{sca} = \frac{k^4}{6\pi} |\alpha|^2 = \frac{8\pi}{3} k^4 a^6 \left| \frac{\epsilon - \epsilon_m}{\epsilon + 2\epsilon_m} \right|^2 \quad (7.10)$$

$$C_{abs} = k \text{Im}[\alpha] = 4\pi k a^3 \text{Im} \left[\frac{\epsilon - \epsilon_m}{\epsilon + 2\epsilon_m} \right] \quad (7.11)$$

Those two equations show a dependence on the radius of the nanosphere of $C_{sca} \sim a^6$ and $C_{abs} \sim a^3$. For applications, this means that the scattering increases more strongly for increasing particle size, while for small particles absorption dominates over scattering. Furthermore, the cross section shows a direct connection between the resonance and absorption / scattering, which is enhanced at the resonance as well.³⁵⁹

Beyond the single particle resonance, collective plasmonic resonances can be observed between many particles. Two different forms are distinguished: near-field and far-field coupling. Thereby, the near-field coupling leads to spectral shifts and new hybrid modes distributed among the different particles (Figure 7.3b),³⁶⁵ whereas the far-field can lead to surface lattice resonances (SLR) in a well-designed periodic lattice, leading to a narrow spectral response.³⁶⁶ Thereby, the far-field scattering of each single particle has to be in phase with each other in order to be reinforced, see Figure 7.3c. In a very rough approximation (homogenous environment, perpendicular incidence), the first order diffraction is found when the resonance wavelength divided by the refractive index matches the lattice period.³⁶⁶

All discussed phenomena so far highlight the radiative decay paths of the plasmonic oscillation. Usually, the non-radiative pathways are regarded as loss. But the free carriers needed for energy conservation in small structures help to store the kinetic energy of the process and thus enable i.e. confinement of the light below the diffraction limit.³⁶⁷ They are considered hot carriers because they have reached energies which are significantly above thermal excitation.³⁶⁸ The timescales of those processes, depicted in more detail in Refs.,^{369–372} show nearly instantaneous excitation within few femtoseconds of the LSPR followed by damping which results in hot charge carrier generation, i.e. via Landau damping. Afterwards, carrier relaxation takes place either by the faster carrier-carrier scattering or by the slightly slower carrier-phonon scattering within 1 to 10 ps. Energy is subsequently dissipated as heat.³⁶⁹ A more detailed discussion of the different hot electron generation and transfer mechanisms is beyond this work and can be found elsewhere.^{367,369} Revisiting the Fowler equation (Equation (2.13)) for the internal photoemission of metals, the formula can be applied to describe the direct hot electron transfer.⁸¹ Experimental data suggests that this transfer occurs on the order of 100 fs or less.³⁷³ To better capture the plasmonic aspect and the influence of the plasmonic particles, Equation (2.13) can be expanded to a slightly modified version for the responsivity in dependence of the frequency ν ^{373,374}

$$\mathfrak{R}(\nu) = \left[C_f \frac{(h\nu - e\Phi_{SB})^n}{h\nu} \right] \alpha(\nu) \quad (7.12)$$

Thereby, the exponent n is usually 2 in metals and larger in semiconductors. The term $\alpha(\nu)$ describes the photon absorption of the plasmonic nanoparticle or structure. By tuning the plasmonic structure in size and structure, the hot electron generation can thus be further controlled and maximized e.g. with sharp structures like stars.^{370,375} The key take away of the hot electrons in plasmonics is the extraordinary timescale in the femtosecond regime during which the hot electron has to be transferred over the Schottky barrier onto a semiconductor in order to contribute to a photocurrent, see Figure 7.3d. Hereby, it has to be highlighted that the Schottky barrier limits the spectral detection rather than the bandgap of the semiconductor. Thus, spectral extension into the NIR can be achieved.^{370,376}

7.4.2 Plasmonics in Photodetectors

Combining plasmonics with photodetectors is no inherently new concept and has been subject to several reviews.^{143, 170, 364, 369, 370, 372, 377} Nevertheless, especially the perspective of plasmonics in combination with materials beyond graphene, like pure TMDCs, for fast photodetection is more scarcely described.

The two most suitable paths to tune photocurrent generation by plasmonics within TMDCs are either direct enhancement of the exciton generation process or injection of hot carriers produced in the plasmonic structure.³⁶⁴ The former has been shown to improve the photocurrent by factors spanning across three orders of magnitude, which will be detailed exemplarily below.

The simple approach of depositing AuNPs (NP) on a TMDC detector has led to a 3-fold enhancement of the photocurrent and a 2-fold PL enhancement with only less than 1% of the surface covered.³⁷⁸ This is achieved with the high absorption cross section of the NPs. Using a more sophisticated structure like a pyramid, combines the possibility of a large collection area at the base with a confinement of the light at one sharp tip.^{379, 380} This principle, which enables techniques like TERS, could also be used by combining a pyramid array³²³ as one of the electrodes of the detector with a TMDC flake. Going beyond the single particle, near-field enhancement between two structures can be exploited. A simple, yet efficient structure is the bow tie structure consisting of two triangles.³⁸¹ Arranging such a bow tie structure within an array of bow ties makes additional use of the far-field coupling and potential surface lattice resonances.³⁸² Although this example is not TMDC based, it is one of the rare examples showing an influence not only on the photocurrent with enhancements up to a factor of 30, but also an improved temporal response of a factor three to four in the millisecond regime.³⁸² Further exploiting the collective properties of several nanoparticles based on platinum has shown to enhance the photocurrent by three orders of magnitude.³⁷⁶ But again, the response speed remains nearly unchanged (~ 1 s).

Combining the advantages of plasmonic enhancement with the necessary electrodes needed to extract photocurrents leads to guided-mode resonance electrodes.³⁸³ For colloidal QDs they have shown 250-fold improvements in the responsivity, but again no influences on the time scale. The underlying effect is the accumulation of the electro magnetic field within the layer of the absorber. Such electrodes are arguably easier to implement in the near-infrared due to the larger feature size needed, but with EBL they are also applicable for the visible range. Additional advantage of such grating-based detectors in direct comparison to waveguides is the absence of additional coupling, which produces losses in waveguides.¹⁴³ Further possibilities of the grating / electrode approach lies in the design of asymmetric gaps offering new degrees of freedom.^{351, 384}

The common ground for all these photocurrent enhancements is the apparent signal amplification by the plasmonic field enhancement with an absence of improvements in the response time.³⁷⁷

In contrast to the pure field enhancement, utilizing hot electrons seems to be more promising for accelerating the temporal response. Purely plasmonic detectors rely on this principle and achieve bandwidths in the higher GHz regime.^{143, 287} For implementing a photodetector based on hot electrons, the whole process including the timescales has to be considered: First, generation of hot carriers following the plasmonic excitation. This takes

only several femtoseconds.³⁷¹ Second, the hot electrons have to move to the metal-semiconductor interface without losing the energy by scattering before the transport over the interface across the Schottky barrier can take place.³⁷⁰ The different possible pathways for the hot electron injection can be divided into a direct and an indirect transfer mechanism,³⁶⁹ which seem to be sensitive towards external influences like strain.³⁸⁵ Once injected, the electrons have to be extracted to result in a photocurrent. A detailed analysis on how to boost each of the steps can be found elsewhere.³⁷⁰

Experimental approaches of the hot carrier injection mechanism have revealed times of 143 fs between platinum and MoS₂.³⁸⁶ Besides a fast injection, a large efficiency is of high interest as well. An interesting approach toward further increasing the efficiency of the transfer process, despite decreasing the particle size,³⁸⁷ is the combination of a SPP with a LSP.³⁸⁸ Thereby, hot electron transfer within 40 fs from gold to MoS₂ with 1.65 % efficiency was shown, enhanced by the strong coupling of SPP and LSP. The suggested mechanism proposes that the non-radiative part of the SPP acts as a ‘recycle bin’ for the LSP radiative energy. Thus, not only coupling between plasmonics and the active material is relevant, also coupling of different plasmon types can be of great advantage. In this regard, the interaction between Fano resonances of a plasmonic grating with WS₂ has shown interactions in the femtosecond regime as well, showing the ultrafast injection of hot electrons also for SLRs.³⁸⁹ Thus, plasmonics provide ultrafast electrons to TMDCs, but what happens with them inside the TMDC? As shown before, most detectors operate at much longer timescales than femtoseconds. The study revealing 143 fs injection time also showed a prolonged lifetime in the TMDC exceeding 800 ps leading to an overall photoresponse of 10 μ s.³⁸⁶ Additionally, if the excitation wavelength is also absorbed by the TMDC, then the fraction of hot electrons may be small in comparison to the (slow) excitons in the material. A good workaround for the latter problem is the exploitation of sub-bandgap excitation in the NIR. A dedicated review to this can be found in Ref.¹⁷⁰

Combining hot electrons of gold electrodes which are excited by the evanescent field of a waveguide rather than by a LSP shows the general feasibility of this approach with bandwidths exceeding 1.37 GHz at telecommunication wavelengths for pure TMDCs.³⁹⁰ However, generally the device geometry and the material seems to be a limiting component as well.

Keeping all the various strategies and examples in mind, the following fabrication guidelines and ideas are proposed to continue the work of this thesis with plasmonics. Some questions will remain until experimental proof. Since the most examples in literature show (milli-)second detectors in combination with femtosecond plasmonics, the question is: If the operating time scales of a photodetector and plasmonics are close, will the near-field enhancement without hot electrons already have an impact? Furthermore, is it possible to harness hot electrons at above-bandgap-wavelengths and see an acceleration in the response or is it limited to below-bandgap-excitation?

For verification of the plasmonic influence onto the photodetector, either a before-after approach on the same flake or two channels, one without and one with a plasmonic structure, are necessary. The recommended starting point is a rather simple system and from there, more complexity to the plasmonic system can be added step by step. If EBL is not an option, a rather simple but yet effective first approach could be performed with a rapid annealing at elevated temperatures producing randomly distributed nano particles on the surface.¹⁵³ If the high temperatures pose a risk to the existing electrodes needed for

before-after measurements, alternative techniques like printing with gold ink could be tried.^{391,392} However, if EBL is a feasible option, a bow tie structure is proposed, since it combines sharp tips, preferable for hot electron generation,^{370,375} with a high near-field enhancement.³⁸¹ To further boost the hot electron generation in the plasmonic structure, platinum as plasmonic material could be tested, because each atom can contribute a variable amount of 1 to 5 electrons due to interband transitions, and it offers lower screening than gold.^{376,393} Specifically, one would expect a significantly different response near the plasmon resonance compared to off-resonance excitation as well as sub- vs. above-bandgap excitation of the TMDC. Interesting options to make use of both simultaneously could be either a system with two different SLRs in x and y or dual plasmonic particles with two resonances.^{394,395} With hindsight to the approach of coupled SPP and LSP,³⁸⁸ the bow ties could be arranged in an array to make use of the additional SLR or in Fisher patterns to extend the near-field coupling further.³⁹⁶ By introducing a high- κ layer like Al_2O_3 in between the active material and the plasmonic structure, the near-field enhancement could be separated from a potential hot electron transfer.³⁸² Additionally, benefits like defect saturation, mobility enhancement and dielectric effects could be employed by such methods as well as index engineering to boost the plasmonics.³⁹⁷⁻³⁹⁹ The downside would be a more complicated fabrication in which the electrodes and the plasmonic structure cannot be fabricated in one step. Once the plasmonic influence on the response speed is understood and the parameters altering the detector the most are clear, more precise guidelines for plasmonic TMDC photodetectors can be developed.

Although the three approaches, BPVE, cavities and plasmonics, seem to be different, combinations of them could be beneficial as hinted throughout the chapter. By employing the proposed techniques at least partially, a faster response speed as well as a higher responsivity is expected for pure TMDC devices.

8 Summary & Conclusion

To fully address the initial question ‘How to reach the limit of photodetectors based on pure MoS_2 and WSe_2 without sacrificing a simple and cost-effective fabrication?’ the findings of this work will be summarized and concluded in the following.

Initially, the practises for the electrical bandwidth determination of photodetectors are compared and discussed in Chapter 3. Especially, the pitfalls which might be encountered when working with nanostructured materials in contrast to commercialized photodiodes are highlighted. The analysis of two different QD systems, specifically PbS/EDT and CdSe/I/Zn4APc and two TMDCs, MoS_2 and WSe_2 , reveal deviations of up to 3×10^3 when applying the commonly used approximation $f_{3dB} = 0.35/t_{rise}$ instead of the Fourier transformation approach. Given these large deviations, the comparison of different bandwidths should be only done when acquired with the same method. These results have been published in *The Journal of Physical Chemistry C*, 126, 14011-14016 in 2022.

Secondly, after specifying the good practice when determining the response time / bandwidth, MoS_2 detectors are being investigated towards their speed of response. Accordingly, the electrode style to contact the flakes is varied and the influence on the rise and fall times examined. For TMDCs, the particular structure of separate layers offers new possibilities of making contact to the edge and, thus, to the individual layers directly. Conventionally used top electrodes contact the huge dangling bond-free surface of MoS_2 instead of the edge. By changing this, the fall times of MoS_2 photodetectors are accelerated by more than one order of magnitude, exceeding 18 MHz for the fastest device. Additionally, the influence of the contacting metal, gold and titanium, is examined as well. By changing the metal, the work function of the electrode is varied and, thus, the resulting Schottky barrier between metal and semiconductor influenced. Taking all these observations into account, the acceleration is explained by the higher in-plane carrier mobility accessible with the edge contacts, because no tunneling over the individual vdW layers has to be completed. Thus, the interlayer transfer time is irrelevant and the carriers can be extracted in parallel over the edges. Considering the Schottky barrier, the faster response times of gold in comparison with titanium can be explained by the larger barrier. The same barrier is also changed when contacting the face or the edge of a TMDC, thus contributing to the acceleration. Most important for the aspect of scalability is the fabrication, which is only expanded by one additional step of reactive ion etching. Consequently, the concept is expected to be applicable to all layered materials, demonstrating a simple and scalable route for future TMDC photodetectors. These results have been published in *Nanoscale Advances*, 5, 3494, in 2023. Details are given in Chapter 4.

During the previous studies, an important observation is the absence of saturation within the detectors. Additionally, the laser power is not enough to yield sufficient photocurrents within few layers of TMDCs for examination with the used measurement setup. Thus, by focussing the laser, the irradiance is increased and consequently a lower photoresistance is achieved as well as the possibility to investigate atomically thin flakes with high spacial resolution. This is realized by establishing the time-resolved photocurrent measurements within a home-built confocal microscope. As a result, the irradiance could be increased by a factor of up to a 1000. Hence, the photoresistance and subsequently the RC

time constant can be controlled directly. For this study, the model system chosen is WSe₂ due to the known limitation mechanism with the used device geometry from previous studies. Variation of the irradiance with e.g. optical filters, showed a direct correlation between response time and photoresistance, indicating an RC-limitation of around 30 MHz, which is further verified by calculating the capacitance. In a next step, the device geometry is altered to overcome the RC-limitation. This is possible due to the small focus spot, which enables a shrinking of the electrode geometry. Hence, the channel length is reduced to decrease the resistance further and the capacitance is optimized by shrinking the electrode dimensions. With this new geometry, fabricated with EBL, the bandwidth of the detectors exceeds the limit of the measurement setup of 0.23 GHz. Additional improvements, like optimising the device geometry further in terms of channel width and length, can be performed easily by EBL, once the setup is upgraded. With regards to energy consumption, a low switching energy of < 27 fJ/bit is calculated. For bilayer WSe₂, nearly the same speed is measured, presumably only limited by the larger photoresistance. Overall, increasing the saturation in TMDCs to decrease the omnipresent RC time is another universally applicable and simple concept for photodetectors to increase the speed towards their material limit. The results can be found in more detail in Chapter 5 and have been published in *RSC Applied Interfaces*, 1, 728-733 in 2024.

The additional projects described briefly within Chapter 6 show the possibility to reduce the RC time for CdSe photodetectors by reducing the channel length. This concept is later on reused for the acceleration of the WSe₂ detectors, described in the previous paragraph. The next project highlights the influence of the used substrate on the detector performance as well as the resulting change of the speed-limiting mechanism. The last project shows the discrepancy between intrinsic measurements and extrinsic photocurrent measurements for the example of PbS nanocrystals. The different projects are published in *ACS Applied Material & Interfaces*, 13, 47954-47961 in 2021, *Physical Chemistry Chemical Physics*, 24, 25383-25390 in 2022 and *Nano Letters* 22, 2809-2816 in 2022, respectively.

To conclude this work, the initial question is answered from four perspectives.

RC time reduction. The major step towards a response time reduction in this work is the reduction of the RC time. This can be achieved by reducing the resistance by increasing the absorption within the flakes, by reducing the channel length or by decreasing the contact resistance with edge contacts. None of those methods are complicating the fabrication process to hinder scalability. Additional methods like the combination with cavities or plasmonics, presented in the outlook or like high- κ dielectrics addressed in the fundamentals are expected to further accelerate the devices.

Mono- vs. multilayer. The question whether atomically thin monolayers or multilayer flakes are better for TMDC photodetectors has to be answered depending on the purpose. Although intrinsic measurements indicate the opposite, for now, if the detector speed is the top priority, then the increased absorption of the multilayer is of great benefit to guarantee a low RC time. If the detector also needs to satisfy other constraints like reduced vertical dimensions, then a mono- or bilayer of WSe₂ may be beneficial. For such a purpose the bulk photovoltaic effect described in the outlook may be an option in the future to satisfy both criteria simultaneously.

MoS₂ or WSe₂. Already for the measurements prior to the confocal setup without edge contacts for MoS₂, WSe₂ appeared to be faster for thick, bulk-like flakes. An additional advantage of WSe₂ over the MoS₂ crystals was the dark current which has been shown to

be several orders of magnitude lower in WSe_2 within this work. Approaching the monolayer limit, WSe_2 again showed a faster detector speed whereas MoS_2 suffered from slow and large persistent photocurrents induced by defects. If those defects can be cured, thin layers of MoS_2 are expected to be faster as well, but for now it is outperformed by WSe_2 .

Intrinsic and extrinsic photocurrent measurements. Reaching the limit of a device implies approaching the intrinsic response time. For the two examined TMDCs, the intrinsic times given in literature reach from nanoseconds down to few picoseconds, depending on the publication. The fastest devices here have shown response times down to at least $2\text{ ns} / 230\text{ MHz}$, presumably faster. Hence, a gap of maximal three orders of magnitude remains to be overcome if the boundaries are taken conservatively. Figure 8.1 displays the performance of the devices examined in this work within the devices published in literature as well as the intrinsic response times. Once, the setup is extended into the GHz regime, a clearer picture of the extrinsic / intrinsic difference can be drawn.

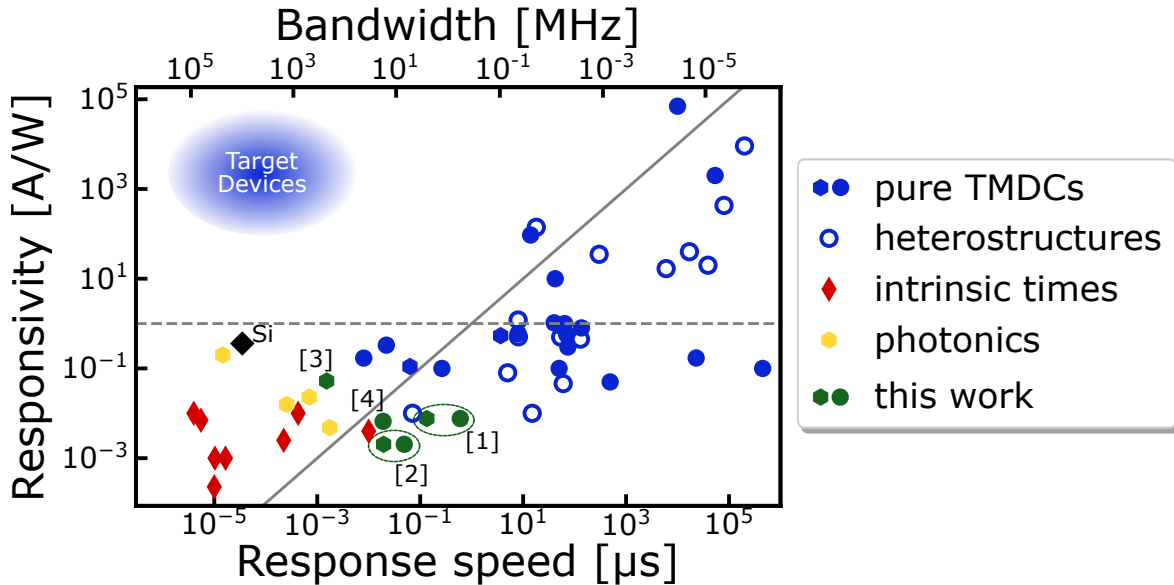


Figure 8.1. Overview of responsivity vs. speed for photodetectors from literature in combination with the figures of merit obtained for the detectors within this work. Details can be found in Table 2 in the Appendix. Data from this work: [1]³⁸ multilayer WSe_2 , [2]³⁵ edge contacted multilayer MoS_2 , [3]³⁶ multilayer and [4]³⁶ bilayer WSe_2 under focussed illumination.

For now, the routes to systematically reduce the device response times have shown photodetectors among the fastest based on pure TMDCs without photonic integration in literature, cf. Figure 8.1. Furthermore, the exploration of the full effect of the single measures for increasing the response time described here, as well as their combination, was hindered by the current setup limit. Giving these points and the concepts presented in the outlook of this work, it is expected that they can close the gap between the device response time towards the material response time. Consequently, TMDCs are envisioned to be more than capable of becoming the next generation of photodetectors, beyond the era of silicon.

Appendix

Table 2. Detailed data of the responsivity \mathfrak{R} vs. response speed t_{rise} plot in Figure 2.13 and 8.1. Responsivities with * are estimated values based on the laser power used.

Material	λ_{Laser} [nm]	\mathfrak{R} [A/W]	t_{rise} / t_{fall} [μ s]	f_{3dB} [MHz]	Ref.
MoS ₂	635	7×10^4	$10^4 / 10^4$	-	165
MoS ₂ /SnSe ₂	500	9.1×10^3	$2 \times 10^5 / 6 \times 10^5$	-	400
WSe ₂	852	2×10^3	$5.3 \times 10^4 / -$	-	401
MoS ₂	561	880	$4 \times 10^6 / 9 \times 10^6$	-	231
MoS ₂ /ZnPc	532	430	$8 \times 10^4 / 8 \times 10^4$	-	402
MoSe ₂ /WSe ₂	650	140	18 / 16	-	403
WSe ₂	532	94	14 / -	-	160
MoS ₂ /WSe ₂	532	40*	1.7×10^4	-	89
MoS ₂ /MA ₃ Bi ₂ Br ₉	530	35*	300 / 300	-	404
MoS ₂ /WS ₂	532	20*	$3.9 \times 10^4 / 4.7 \times 10^4$	-	405
MoS ₂ /Perovskite	637	16.8	$6 \times 10^3 / 4 \times 10^3$	-	167
MoS ₂	555	10	42 / -	-	140
WSe ₂ /PtS ₂	635	1.2	8 / 9	-	83
MoS ₂	532	1.04	40 / 50	-	406
MoS ₂	637	1	64 / 51	-	91
MoSe ₂	520	0.89	52 / 62	-	168
WSe ₂	633	0.8	136 / 39	-	407
WSe ₂	740	0.6	<8 / <8	-	159
MoS ₂	532	0.57	70 / 110	-	94
MoTe ₂ /MoS ₂	638	0.55	- / -	>0.1	84
WS ₂	635	0.51	$4.1 \times 10^6 / 4.4 \times 10^6$	-	86
PtSe ₂ /CdTe	780	0.51	8.1 / >43.6	0.0062	408
MoS ₂ /Gr/WSe ₂	637	0.5	53.6 / 30.3	-	409
MoS ₂ /Gr	632.8	0.45*	130 / -	-	95
MoTe ₂	980	0.33	0.022 / 0.024	-	171
PtS ₂	830	0.3	74 / 101	-	88
WSe ₂	550	0.171	< 2.3×10^4 / -	-	145
WSe ₂	450	0.17	0.008 / 0.02	22	171
MoS ₂	640	0.11	- / -	5.5	90

APPENDIX

Material	λ_{Laser} [nm]	\mathfrak{R} [A/W]	t_{rise} / t_{fall} [μ s]	f_{3dB} [MHz]	Ref.
WSe ₂	637	0.1	50 / 20	-	264
WS ₂	532	0.1*	$4.5 \times 10^5 / 6 \times 10^4$	-	410
WSe ₂	450	0.1	0.264 / 0.552	1.9	102
WSe ₂ /ReSe ₂	532	0.08*	5 / 5	-	163
MoSe ₂	520	0.05*	490 / 495	-	411
MoTe ₂ /MoS ₂	637	0.046	60 / 25	-	96
MoS ₂ /BP	1550	0.01*	15 / 70	-	87
PtSe ₂ /Perovskite	808	0.01*	0.071 / 0.056	2	412
Photonic integration					
MoTe ₂ /Gr	1300	0.2	- / -	2.4×10^4	270
MoTe ₂	1300	0.023	- / -	500	152
MoS ₂	1550	0.0157	- / -	$>1.37 \times 10^3$	390
MoTe ₂	1160	0.0048	- / -	>200	151
Si	850	0.36	$3.5 \times 10^{-5} / 2 \times 10^{-4}$	-	413
Detectors of this work					
WSe ₂	636	0.05	- / -	>230	36
WSe ₂	636	0.0075*	- / -	2.6	38
WSe ₂	635	0.0075*	1 / 0.6	-	38
WSe ₂ (bilayer)	635	0.0065	0.029 / 0.019	-	36
MoS ₂	636	0.05*	- / -	18	35
MoS ₂	635	0.05*	0.098 / 0.049	-	35
Intrinsic					
MoTe ₂ (25 nm)	780	2.5*	10	-	138
MoTe ₂ (4 nm)	780	0.23	223.5	-	138
WSe ₂ (25 nm)	780	-	426	-	31
MoS ₂ /WSe ₂	780	-	16.5	-	31
MoS ₂ (Mono)	452	EQE 0.001	3-5 (fast) 80-100 (slow)	300	30
Gr/WSe ₂ /Gr	759	-	10.3	50	414
Gr/40 nm WSe ₂ /Gr	759	IQE < 40 %	1×10^4	-	139
Gr/2.2 nm WSe ₂ /Gr	759	IQE > 70 %	5.5	100	139

List of Abbreviations & Symbols

α	polarizability
χ	electron affinity
δ	dimensionality
$\Delta\omega$	spectral width
Δf	offset frequency
Δk	change of momentum
Δt	delay time
$\epsilon(\omega)$	dielectric function
ϵ_0	vacuum permittivity
ϵ_m	dielectric constant of the surrounding medium
ϵ_r	dielectric constant
γ	damping
γ	non-resonant decay rate
\hbar	reduced Planck constant
κ	photon decay rate
μ	mobility
μ_{12}^2	transition dipole moment
ν	frequency
Ω	coupling strength
ω	angular frequency
Φ_M	work function of a metal
\Re	responsivity
$\rho_{\delta D}(E)$	density of states
τ_d	charge carrier drift time
τ_r	charge carrier recombination time
τ_s	charge carrier transfer time
τ_{RC}	RC time
ξ	dipole orientation factor

LIST OF ABBREVIATIONS & SYMBOLS

A	area
a_{exc}	Bohr exciton radius
C	capacitance
c	speed of light
C_{abs}	absorption cross section
C_{sca}	scattering cross section
D	diffusion coefficient
E	external electric field
e	elementary charge
E_B	exciton binding energy
E_F	Fermi energy
E_G	electrical band gap
E_{opt}	optical band gap
F_P	Purcell factor
f_{3dB}	3 dB bandwidth
f_{rep}	repetition rate
G	gain
g	channel length
$g(\omega)$	density of states inside a cavity
g_0	atom-photon coupling parameter
h	Planck constant
I_{dark}	dark current
I_{photo}	photocurrent
I_{SC}	short-circuit current
j_b	ballistic current
j_{sh}	shift current
$K(k)$	complete first order elliptical integral
k_B	Boltzmann constant
L	channel width

l	diffusion length
l_0	free path length
M	reduced exciton mass
m_e	effective electron mass
M_{12}	transition matrix element
N	number of electrode fingers
n	principal quantum number
n	refractive index
p	dipole moment
$P(\omega)$	power spectrum
P_1	steady state power
P_{laser}	laser power
Q	quality factor
q	electron charge
R	resistance
R_c	contact resistance
R_T	total resistance
R_{ch}	channel resistance
T	temperature
t_{life}	lifetime
V	mode volume
V_G	gate voltage
V_{OC}	open-circuit voltage
V_{SD}	applied bias
W	emission rate
w	electrode width
2DM	2D material
ASOPS	asynchronous optical sampling
BP	black phosphorous

LIST OF ABBREVIATIONS & SYMBOLS

BPVE	bulk photovoltaic effect
CB	conduction band
CdSe	cadmium selenide
CNL	charge neutrality level
CVD	chemical vapour deposition
DOS	density of states
EBL	electron beam lithography
EDT	1,2-ethanedithiol
EQE	external quantum efficiency
FFT	fast Fourier transform
FLP	Fermi level pinning
GBP	gain-bandwidth-product
GHz	gigahertz
hBN	hexagonal boron nitride
HMDS	hexamethyl disilazane
IDE	interdigitated electrodes
LED	light-emitting diode
LSPR	localized surface plasmon resonance
MSM	metal-semiconductor-metal
NA	numerical aperture
NEP	noise equivalent power
NIR	near-infrared
NP	nano particle
PbS	lead sulfide
PC	photoconductive
PDMS	polydimethylsiloxane
PDs	photodetectors
PG	photogating
PL	photoluminescence

PV	photovoltaic
QD	Quantum Dot
RIE	reactive ion etching
SC	semiconductor
SEM	scanning electron microscope
SHG	second harmonic generation
SLR	surface lattice resonance
SPP	surface plasmon polariton
SRH	Shockley-Read-Hall recombination
TIA	transimpedance amplifier
TMDCs	Transition metal dichalcogenides
VB	valence band
vdW	van-der-Waals
VLC	visible light communication

List of Figures

1.1	Graphical outline of this thesis	5
2.1	Concept of (in-)direct band gap	7
2.2	Schematic of the photoconductive effect	8
2.3	Different recombination mechanisms	9
2.4	Charging of a capacitor	10
2.5	Schematic of the photogating effect	11
2.6	Schematic of the photovoltaic effect	12
2.7	Formation of an Ohmic contact	13
2.8	Formation of a Schottky junction	14
2.9	Fermi level pinning and charge injection at a Schottky contact	16
2.10	Density of states from 3D to 0D	20
2.11	Quantum Confinement effect of nanocrystals	21
2.12	Number of publications per year of TMDC photodetectors	23
2.13	Literature overview responsivity vs. speed	27
2.14	Scheme of time-resolved photocurrent measurement setup	29
2.15	Scheme of square and impulse illumination	30
2.16	Scheme of intrinsic measurements	32
2.17	Lithographic scheme for EBL and OL	36
3.1	Photoresponse of a BPW 34 diode	42
3.2	Photoresponse of QDs and TMDCs	43
3.3	Bandwidth comparison among the different routes	44
4.1	Schematic of an edge contact	48
4.2	Edge contacts vs. Top contacts - square pulse	50
4.3	Bottom contacts vs. Top contacts - influence of the metal	51
4.4	Edge contacts vs. Top contacts - impulse	52
SI4.1	Light microscopy images and flake height	54
SI4.2	SEM-images of an etched flake	54
SI4.3	Lithographic process for fabricating edge contacts	55
SI4.4	Persistent photocurrents in MoS ₂ flakes	56
SI4.5	Edge contacts vs. Top contacts - I-V characteristics	56
SI4.6	Band diagram of an Au top and an Au edge contact	57
SI4.7	Rise / fall time vs. channel length	58
SI4.8	Rise / fall time vs. voltage	58
SI4.9	Bandwidth of fastest MoS ₂ PD	59
5.1	Square pulse & impulse measurements with and without focus	63
5.2	Fall time vs. resistance for (un-) focussed illumination	64
5.3	Bandwidth comparison of EBL and OL WSe ₂ and a diode	65
5.4	Characterisation and square pulse response of bilayer WSe ₂	67
SI5.1	Light microscopy images and height profile of the flakes 1 - 4	68
SI5.2	Dark current flake 1	69
SI5.3	ON/OFF ratio of flake 1	69
SI5.4	Square pulse measurements – current height	70
SI5.5	Scheme of geometrical terminology	70
SI5.6	Dark current flake 2	71
SI5.7	ON/OFF ratio of flake 2	71
SI5.8	ON/OFF ratio of flake 2 without bias	72

SI5.9	Variation of bias for flake 2 - bandwidth	72
SI5.10	Simulated capacity	73
SI5.11	Channel length and photo resistance vs. fall time for flake 3 and 4	74
SI5.12	Influence of channel length on the bandwidth	74
SI5.13	Cable reflections and influence on the bandwidth	75
SI5.14	Variation of the illumination intensity for flake 2	75
SI5.15	Scheme of the custom built confocal microscope	76
6.1	Image of a device with 350 nm channel length	77
6.2	Rise time vs. R_{illum} for CdSe on nm and μm devices on glass	78
6.3	Dark current of WSe ₂ on polyimide and glass	79
6.4	WSe ₂ rise times on polyimide and glass	80
6.5	Intrinsic and extrinsic response of PbS QDs	82
7.1	Overview bulk photovoltaic effect	86
7.2	Overview cavities	89
7.3	Overview plasmonics	93
8.1	Literature overview + this work responsivity vs. speed	100

List of Tables & Boxes

Box 1: Recombination Mechanisms	9
Box 2: Charging of a Capacitor	10
Table 1: Device Architectures	17
Box 3: Quantum Dots for photodetection	22
Box 4: Determination of the Speed Limiting Mechanism	31
Table 2: Responsivity vs. Speed Data	101

Bibliography

- [1] Burkacky, O., Dragon, J., and Lehmann, N. The semiconductor decade: A trillion-dollar industry (2022). <https://www.mckinsey.com/industries/semiconductors/our-insights/the-semiconductor-decade-a-trillion-dollar-industry>. Date accessed: 29.02.2024.
- [2] Andreani, L. C., Bozzola, A., Kowalczewski, P., Liscidini, M., and Redorici, L. Silicon solar cells: toward the efficiency limits. *Advances in Physics: X*, **4**, 1548305 (2019).
- [3] Keyes, R. W. Physical limits of silicon transistors and circuits. *Reports on Progress in Physics*, **68**, 2701–2746 (2005).
- [4] Chhowalla, M., Jena, D., and Zhang, H. Two-dimensional semiconductors for transistors. *Nature Reviews Materials*, **1**, 1–15 (2016).
- [5] Knobloch, T., Illarionov, Y. Y., Ducry, F., Schleich, C., Wachter, S., Watanabe, K., Taniguchi, T., Mueller, T., Walzl, M., Lanza, M., Vexler, M. I., Luisier, M., and Grasser, T. The performance limits of hexagonal boron nitride as an insulator for scaled CMOS devices based on two-dimensional materials. *Nature Electronics*, **4**, 98–108 (2021).
- [6] Mu, H., Yu, W., Yuan, J., Lin, S., and Zhang, G. Interface and surface engineering of black phosphorus: A review for optoelectronic and photonic applications. *Materials Futures*, **1**, 012301 (2022).
- [7] Buscema, M., Island, J. O., Groenendijk, D. J., Blanter, S. I., Steele, G. A., Zant, H. S. V. D., and Castellanos-Gomez, A. Photocurrent generation with two-dimensional van der Waals semiconductors. *Chemical Society Reviews*, **44**, 3691–3718 (2015).
- [8] Larki, F., Abdi, Y., Kameli, P., and Salamati, H. An Effort Towards Full Graphene Photodetectors. *Photonic Sensors*, **12**, 31–67 (2022).
- [9] Radisavljevic, B., Radenovic, A., Brivio, J., Giacometti, V., and Kis, A. Single-layer MoS₂ transistors. *Nature Nanotechnology*, **6**, 147–150 (2011).
- [10] Bernardi, M., Palumbo, M., and Grossman, J. C. Extraordinary sunlight absorption and one nanometer thick photovoltaics using two-dimensional monolayer materials. *Nano Letters*, **13**, 3664–3670 (2013).
- [11] Schedin, F., Geim, A. K., Morozov, S. V., Hill, E. W., Blake, P., Katsnelson, M. I., and Novoselov, K. S. Detection of individual gas molecules adsorbed on graphene. *Nature Materials*, **6**, 652–655 (2007).
- [12] Sundaram, R. S., Engel, M., Lombardo, A., Krupke, R., Ferrari, A. C., Avouris, P., and Steiner, M. Electroluminescence in single layer MoS₂. *Nano Letters*, **13**, 1416–1421 (2013).
- [13] Seo, J., Lee, J. H., Pak, J., Cho, K., Kim, J. K., Kim, J., Jang, J., Ahn, H., Lim, S. C., Chung, S., Kang, K., and Lee, T. Ultrasensitive Photodetection in MoS₂ Avalanche Phototransistors. *Advanced Science*, **8**, 2102437 (2021).

- [14] Qiu, Q. and Huang, Z. Photodetectors of 2D Materials from Ultraviolet to Terahertz Waves. *Advanced Materials*, **33**, 2008126 (2021).
- [15] Puttnam, B. J., Hout, M. V. D., Sciuillo, G. D., Luis, R. S., Rademacher, G., Sakaguchi, J., Antonelli, C., Okonkwo, C., and Furukawa, H. 22.9 Pb/s Data-Rate by Extreme Space-Wavelength Multiplexing. *International Conference: European Conference on Optical Communication (ECOC 2023)* (2023).
- [16] Chakraborty, P. S., Cardoso, A. S., Wier, B. R., Omprakash, A. P., Cressler, J. D., Kaynak, M., and Tillack, B. A 0.8 THz f_{MAX} SiGe HBT Operating at 4.3 K. *IEEE Electron Device Letters*, **35**, 151–153 (2014).
- [17] Wang, N., Xue, C., Wan, F., Zhao, Y., Xu, G., Liu, Z., Zheng, J., Zuo, Y., Cheng, B., and Wang, Q. High-Performance GeSn Photodetector Covering All Telecommunication Bands. *IEEE Photonics Journal*, **13**, 1–9 (2021).
- [18] Khalid, A. M., Cossu, G., Corsini, R., Choudhury, P., and Ciaramella, E. 1-Gb/s transmission over a phosphorescent white LED by using rate-adaptive discrete multitone modulation. *IEEE Photonics Journal*, **4**, 1465–1473 (2012).
- [19] Grobe, L., Paraskevopoulos, A., Hillt, J., Schulz, D., Lassak, F., Hartlieb, F., Kottke, C., Jungnickel, V., and Langer, K.-D. High-Speed Visible Light Communication systems. *IEEE Communications Magazine*, **51**, 60–66 (2013).
- [20] Khan, L. U. Visible light communication: Applications, architecture, standardization and research challenges. *Digital Communications and Networks*, **3**, 78–88 (2017).
- [21] Luo, Z., Lin, X., Lu, Z., Shi, J., Shen, C., Li, Z., Zhang, J., He, Z., Chen, H., Yu, S., and Chi, N. 113 Gbps Rainbow Visible Light Laser Communication System Based on 10λ Laser WDM Emitting Module in Fiber-Free Space-Fiber Link. *Optics Express*, **32**, 2561–2573 (2024).
- [22] Xia, F., Mueller, T., Lin, Y. M., Valdes-Garcia, A., and Avouris, P. Ultrafast graphene photodetector. *Nature Nanotechnology*, **4**, 839–843 (2009).
- [23] Mueller, T., Xia, F., and Avouris, P. Graphene photodetectors for high-speed optical communications. *Nature Photonics*, **4**, 297–301 (2010).
- [24] Long, M., Wang, P., Fang, H., and Hu, W. Progress, Challenges, and Opportunities for 2D Material Based Photodetectors. *Advanced Functional Materials*, **29**, 1803807 (2019).
- [25] Zhong, Q. Intrinsic and engineered properties of black phosphorus. *Materials Today Physics*, **28**, 100895 (2022).
- [26] Buscema, M., Groenendijk, D. J., Blanter, S. I., Steele, G. A., Zant, H. S. V. D., and Castellanos-Gomez, A. Fast and broadband photoresponse of few-layer black phosphorus field-effect transistors. *Nano Letters*, **14**, 3347–3352 (2014).
- [27] Youngblood, N., Chen, C., Koester, S. J., and Li, M. Waveguide-integrated black phosphorus photodetector with high responsivity and low dark current. *Nature Photonics*, **9**, 247–252 (2015).

- [28] Mueller, T. and Malic, E. Exciton physics and device application of two-dimensional transition metal dichalcogenide semiconductors. *npj 2D Materials and Applications*, **2**, 29 (2018).
- [29] Sorger, V. J. and Maiti, R. Roadmap for gain-bandwidth-product enhanced photodetectors: opinion. *Optical Materials Express*, **10**, 2192–2200 (2020).
- [30] Wang, H., Zhang, C., Chan, W., Tiwari, S., and Rana, F. Ultrafast response of monolayer molybdenum disulfide photodetectors. *Nature Communications*, **6**, 8831 (2015).
- [31] Zeng, Z., Ge, C., Braun, K., Eberle, M., Wang, Y., Zheng, B., Zhu, C., Sun, X., Huang, L., Luo, Z., Chen, Y., Duan, H., Wang, S., Li, D., Gao, F., Pan, A., and Wang, X. Manipulating Picosecond Photoresponse in van der Waals Heterostructure Photodetectors. *Advanced Functional Materials*, **32**, 2200973 (2022).
- [32] Intel Core i9 processor 14900K. <https://ark.intel.com/content/www/de/de/ark/products/236773/intel-core-i9-processor-14900k-36m-cache-up-to-6-00-ghz.html>. Date accessed: 29.02.2024.
- [33] Strauß, F., Zeng, Z., Braun, K., and Scheele, M. Toward GHz-Photodetection with Transition Metal Dichalcogenides. *ChemRxiv preprint* (2024). <https://doi.org/10.26434/chemrxiv-2024-d352b>.
- [34] Schedel, C., Strauß, F., and Scheele, M. Pitfalls in Determining the Electrical Bandwidth of Nonideal Nanomaterials for Photodetection. *Journal of Physical Chemistry C*, **126**, 14011–14016 (2022).
- [35] Strauß, F., Schedel, C., and Scheele, M. Edge contacts accelerate the response of MoS₂ photodetectors. *Nanoscale Advances*, **5**, 3494–3499 (2023).
- [36] Strauß, F., Kohlschreiber, P., Keck, J., Michel, P. M., Hiller, J., Meixner, A. J., and Scheele, M. A simple 230 MHz Photodetector Based on Exfoliated WSe₂ Multilayers. *RSC Applied Interfaces* (2024). <https://doi.org/10.1039/D4LF00019F>.
- [37] Schedel, C., Strauß, F., Kumar, K., Maier, A., Wurst, K. M., Michel, P., and Scheele, M. Substrate Effects on the Bandwidth of CdSe Quantum Dot Photodetectors. *ACS Applied Material & Interfaces*, **13**, 47954–47961 (2021).
- [38] Schedel, C., Strauß, F., Kohlschreiber, P., Geladari, O., Meixner, A. J., and Scheele, M. Substrate effects on the speed limiting factor of WSe₂ photodetectors. *Physical Chemistry Chemical Physics*, **24**, 25383–25390 (2022).
- [39] Maier, A., Strauß, F., Kohlschreiber, P., Schedel, C., Braun, K., and Scheele, M. Sub-nanosecond Intrinsic Response Time of PbS Nanocrystal IR-Photodetectors. *Nano Letters*, **22**, 2809–2816 (2022).
- [40] Saleh, B. E. A. and Teich, M. C. *Fundamentals of photonics*. John Wiley & Sons, (1991).
- [41] Sze, S. M. and Ng, K. K. *Physics of semiconductor devices*. John Wiley & Sons, (2007).

- [42] Wolfe, W. L. and Kruse, P. W. *Thermal Detectors. In Handbook of Optics.* McGraw Hill LLC, (2009).
- [43] Rogalski, A. *Progress in Quantum Dot Infrared Photodetectors, Quantum Dot Photodetectors.* Springer, Cham, (2021).
- [44] Einstein, A. Über einen die Erzeugung und Verwandlung des Lichtes betreffenden heuristischen Gesichtspunkt. *Annalen der Physik*, **4** (1905).
- [45] Ugeda, M. M., Bradley, A. J., Shi, S. F., Jornada, F. H. D., Zhang, Y., Qiu, D. Y., Ruan, W., Mo, S. K., Hussain, Z., Shen, Z. X., Wang, F., Louie, S. G., and Crommie, M. F. Giant bandgap renormalization and excitonic effects in a monolayer transition metal dichalcogenide semiconductor. *Nature Materials*, **13**, 1091–1095 (2014).
- [46] Demtröder, W. *Experimentalphysik 3: Atome, Moleküle und Festkörper.* Springer Spektrum Berlin, Heidelberg, (2016).
- [47] Göbel, H. *Einführung in die Halbleiter-Schaltungstechnik.* Springer Verlag Berlin, Heidelberg, (2014).
- [48] Czucholl, G. *Theoretische Festkörperphysik Band 1: Grundlagen: Phononen und Elektronen in Kristallen.* Springer Spektrum Berlin, Heidelberg, (2015).
- [49] Chernikov, A., Berkelbach, T. C., Hill, H. M., Rigosi, A., Li, Y., Aslan, O. B., Reichman, D. R., Hybertsen, M. S., and Heinz, T. F. Exciton binding energy and nonhydrogenic Rydberg series in monolayer WS₂. *Physical Review Letters*, **113**, 076802 (2014).
- [50] Stenzel, O. *The Hydrogen Atom. In Light-Matter Interaction.* Springer, Cham, (2022).
- [51] Ray, S. K., Mukherjee, S., Dey, T., Jana, S., and Koren, E. *Two-Dimensional Material-Based Quantum Dots for Wavelength-Selective Tunable, and Broadband Photodetector Devices. In Quantum Dot Photodetectors.* Springer, Cham, (2021).
- [52] Bowers, J. E. and Wey, Y. G. *High-Speed Photodetectors. In Handbook of Optics.* McGraw-Hill, Inc., (2009).
- [53] Wang, F., Zhang, T., Xie, R., Liu, A., Dai, F., Chen, Y., Xu, T., Wang, H., Wang, Z., Liao, L., Wang, J., Zhou, P., and Hu, W. Next-Generation Photodetectors beyond Van Der Waals Junctions. *Advanced Materials*, **36**, 2301197 (2024).
- [54] Decoster, D. and Harari, J., editors. *Optoelectronic sensors.* John Wiley & Sons, (2009).
- [55] Joshi, A. M. and Olsen, G. H. *Photodetection. In Handbook of Optics.* McGraw Hill LLC, (2009).
- [56] Bielecki, Z., Achtenberg, K., Kopytko, M., Mikołajczyk, J., Wojtas, J., and Rogalski, A. Review of photodetectors characterization methods. *Bulletin of the Polish Academy of Sciences. Technical Sciences*, **70** (2022).
- [57] Norton, P. R. *Photodetectors. In Handbook of Optics.* McGraw Hill LLC, (2009).
- [58] Fang, H. and Hu, W. Photogating in Low Dimensional Photodetectors. *Advanced Science*, **4**, 1700323 (2017).

- [59] Grundmann, M. *Recombination. In The Physics of Semiconductors. Graduate Texts in Physics.* Springer, Cham, (2016).
- [60] Danovich, M., Zólyomi, V., Fal’ko, V. I., and Aleiner, I. L. Auger recombination of dark excitons in WS₂ and WSe₂ monolayers. *2D Materials*, **3**, 035011 (2016).
- [61] Shockley, W. T. R. W. and Jr, W. T. R. Statistics of the Recombinations of Holes and Electrons. *Physical Review*, **87**, 835 (1952).
- [62] Wang, H., Zhang, C., and Rana, F. Surface Recombination Limited Lifetimes of Photoexcited Carriers in Few-Layer Transition Metal Dichalcogenide MoS₂. *Nano Lett.*, **15**, 8204–8210 (2015).
- [63] Rogalski, A. and Bielecki, Z. Detection of optical radiation. *Bulletin of the Polish Academy of Sciences. Technical Sciences*, **52**, 43–66 (2004).
- [64] Demtröder, W. *Electrodynamics and Optics.* Springer Cham, (2019).
- [65] Furchi, M. M., Polyushkin, D. K., Pospischil, A., and Mueller, T. Mechanisms of photoconductivity in atomically thin MoS₂. *Nano Letters*, **14**, 6165–6170 (2014).
- [66] Adinolfi, V. and Sargent, E. H. Photovoltage field-effect transistors. *Nature*, **542**, 324–327 (2017).
- [67] Li, Y., Chen, G., Zhao, S., Liu, C., and Zhao, N. Addressing gain-bandwidth trade-off by a monolithically integrated photovoltaic transistor. *Science Advances*, **8**, eabq0187 (2022).
- [68] Cremoux, B. *PIN Photodiodes for the Visible and Near-Infrared*, 15–56. John Wiley & Sons, (2010).
- [69] Schedel, C. A. *Dissertation: Substrate-Dependent Photodetection with Functional Nanomaterials.* University of Tübingen, (2022).
- [70] Mondal, A., Yadav, P. V., and Reddy, Y. A. K. A review on device architecture engineering on various 2-D materials toward high-performance photodetectors. *Materials Today Communications*, **34**, 105094 (2023).
- [71] Omnes, F. *Introduction to Semiconductor Photodetectors. In Optoelectronic Sensors.* John Wiley & Sons, (2009).
- [72] Allain, A., Kang, J., Banerjee, K., and Kis, A. Electrical contacts to two-dimensional semiconductors. *Nature Materials*, **14**, 1195–1205 (2015).
- [73] Averine, S. V., Chan, Y. C., and Lam, Y. L. Geometry optimization of interdigitated Schottky-barrier metal-semiconductor-metal photodiode structures. *Solid State Electronics*, **45**, 441–446 (2001).
- [74] Cloninger, J. A., Harris, R., Haley, K. L., Sterbentz, R. M., Taniguchi, T., Watanabe, K., and Island, J. O. A back-to-back diode model applied to MoS₂ van der Waals Schottky diodes. *arXiv preprint*, arXiv:2402.03611 (2024).
- [75] Harari, J. and Magnin, V. *Metal-Semiconductor-Metal Photodiodes. In Optoelectronic Sensors.* John Wiley & Sons, (2009).

-
- [76] Benelmekki, M. *Nanomaterials: The original product of nanotechnology*. Morgan & Claypool Publishers, (2019).
- [77] Kim, C., Moon, I., Lee, D., Choi, M. S., Ahmed, F., Nam, S., Cho, Y., Shin, H. J., Park, S., and Yoo, W. J. Fermi Level Pinning at Electrical Metal Contacts of Monolayer Molybdenum Dichalcogenides. *ACS Nano*, **11**, 1588–1596 (2017).
- [78] Liu, X., Choi, M. S., Hwang, E., Yoo, W. J., and Sun, J. Fermi Level Pinning Dependent 2D Semiconductor Devices: Challenges and Prospects. *Advanced Materials*, **34**, 2108425 (2022).
- [79] Roul, B., Kumar, M., Rajpalke, M. K., Bhat, T. N., and Krupanidhi, S. B. Binary group III-nitride based heterostructures: Band offsets and transport properties. *Journal of Physics D: Applied Physics*, **48**, 423001 (2015).
- [80] Li, W., Nomoto, K., Jena, D., and Xing, H. G. Thermionic emission or tunneling? The universal transition electric field for ideal Schottky reverse leakage current: A case study in β -Ga₂O₃. *Applied Physics Letters*, **117**, 222104 (2020).
- [81] Zhang, Y., He, S., Guo, W., Hu, Y., Huang, J., Mulcahy, J. R., and Wei, W. D. Surface-Plasmon-Driven Hot Electron Photochemistry. *Chemical Reviews*, **118**, 2927–2954 (2017).
- [82] Murphy, E. L. and Jr., R. H. G. Thermionic Emission, Field Emission, and the Transition Region. *Physical Review*, **102**, 1464–1473 (1956).
- [83] Tan, C., Yin, S., Chen, J., Lu, Y., Wei, W., Du, H., Liu, K., Wang, F., Zhai, T., and Li, L. Broken-Gap PtS₂/WSe₂ van der waals Heterojunction with Ultrahigh Reverse Rectification and Fast Photoresponse. *ACS Nano*, **15**, 8328–8337 (2021).
- [84] Ahn, J., Kang, J. H., Kyhm, J., Choi, H. T., Kim, M., Ahn, D. H., Kim, D. Y., Ahn, I. H., Park, J. B., Park, S., Yi, Y., Song, J. D., Park, M. C., Im, S., and Hwang, D. K. Self-Powered Visible-Invisible Multiband Detection and Imaging Achieved Using High-Performance 2D MoTe₂/MoS₂ Semivertical Heterojunction Photodiodes. *ACS Applied Materials and Interfaces*, **12**, 10858–10866 (2020).
- [85] Yang, H., Cai, S., Zhang, Y., Wu, D., and Fang, X. Enhanced Electrical Properties of Lithography-Free Fabricated MoS₂ Field Effect Transistors with Chromium Contacts. *The Journal of Physical Chemistry Letters*, **12**, 2705–2711 (2021).
- [86] Yao, J. D., Zheng, Z. Q., Shao, J. M., and Yang, G. W. Stable, highly-responsive and broadband photodetection based on large-area multilayered WS₂ films grown by pulsed-laser deposition. *Nanoscale*, **7**, 14974–14981 (2015).
- [87] Ye, L., Li, H., Chen, Z., and Xu, J. Near-Infrared Photodetector Based on MoS₂/Black Phosphorus Heterojunction. *ACS Photonics*, **3**, 692–699 (2016).
- [88] Wang, Z., Wang, P., Wang, F., Ye, J., He, T., Wu, F., Peng, M., Wu, P., Chen, Y., Zhong, F., Xie, R., Cui, Z., Shen, L., Zhang, Q., Gu, L., Luo, M., Wang, Y., Chen, H., Zhou, P., Pan, A., Zhou, X., Zhang, L., and Hu, W. A Noble Metal Dichalcogenide for High-Performance Field-Effect Transistors and Broadband Photodetectors. *Advanced Functional Materials*, **30**, 1907945 (2020).
-

- [89] Shin, G. H., Park, C., Lee, K. J., Jin, H. J., and Choi, S. Y. Ultrasensitive Phototransistor Based on WSe₂-MoS₂ van der Waals Heterojunction. *Nano Letters*, **20**, 5741–5748 (2020).
- [90] Maeso, D., Castellanos-Gomez, A., Agrait, N., and Rubio-Bollinger, G. Fast Yet Quantum-Efficient Few-Layer Vertical MoS₂ Photodetectors. *Advanced Electronic Materials*, **5**, 1900141 (2019).
- [91] Gong, F., Fang, H., Wang, P., Su, M., Li, Q., Ho, J. C., Chen, X., Lu, W., Liao, L., Wang, J., and Hu, W. Visible to near-infrared photodetectors based on MoS₂ vertical Schottky junctions. *Nanotechnology*, **28**, 484002 (2017).
- [92] Xu, Q., Meng, L., Sinha, K., Chowdhury, F. I., Hu, J., and Wang, X. Ultrafast Colloidal Quantum Dot Infrared Photodiode. *ACS Photonics*, **7**, 1297–1303 (2020).
- [93] Zhang, Q., Jie, J., Diao, S., Shao, Z., Zhang, Q., Wang, L., Deng, W., Hu, W., Xia, H., Yuan, X., and Lee, S. T. Solution-processed graphene quantum dot deep-UV photodetectors. *ACS Nano*, **9**, 1561–1570 (2015).
- [94] Tsai, D. S., Liu, K. K., Lien, D. H., Tsai, M. L., Kang, C. F., Lin, C. A., Li, L. J., and He, J. H. Few-layer MoS₂ with high broadband photogain and fast optical switching for use in harsh environments. *ACS Nano*, **7**, 3905–3911 (2013).
- [95] Li, X., Wu, J., Mao, N., Zhang, J., Lei, Z., Liu, Z., and Xu, H. A self-powered graphene-MoS₂ hybrid phototransistor with fast response rate and high on-off ratio. *Carbon*, **92**, 126–132 (2015).
- [96] Chen, Y., Wang, X., Wu, G., Wang, Z., Fang, H., Lin, T., Sun, S., Shen, H., Hu, W., Wang, J., Sun, J., Meng, X., and Chu, J. High-Performance Photovoltaic Detector Based on MoTe₂/MoS₂ Van der Waals Heterostructure. *Small*, **14**, 1703293 (2018).
- [97] Ahmed, A., Iqbal, M. Z., Dahshan, A., Aftab, S., Hegazy, H. H., and Yousef, E. S. Recent advances in 2D transition metal dichalcogenide-based photodetectors: a review. *Nanoscale* (2024).
- [98] Wadhwa, R., Agrawal, A. V., and Kumar, M. A strategic review of recent progress, prospects and challenges of MoS₂-based photodetectors. *Journal of Physics D: Applied Physics*, **55**, 063002 (2021).
- [99] Goushcha, A. O. and Tabbert, B. On response time of semiconductor photodiodes. *Optical Engineering*, **56**, 097101 (2017).
- [100] Willison, J. R. *Signal Detection and Analysis. In Handbook of Optics*. McGraw Hill LLC, (2009).
- [101] Wang, F., Zhang, T., Xie, R., Wang, Z., and Hu, W. How to characterize figures of merit of two-dimensional photodetectors. *Nature Communications*, **14**, 2224 (2023).
- [102] Zhang, Y., Ma, K., Zhao, C., Hong, W., Nie, C., Qiu, Z. J., and Wang, S. An Ultrafast WSe₂ Photodiode Based on a Lateral p-i-n Homojunction. *ACS Nano*, **15**, 4405–4415 (2021).

- [103] Mu, C., Xiang, J., and Liu, Z. Photodetectors based on sensitized two-dimensional transition metal dichalcogenides - A review. *Journal of Materials Research*, **32**, 4115–4131 (2017).
- [104] Rogalski, A. Commentary on the Record-Breaking Performance of Low-Dimensional Solid Photodetectors. *ACS Photonics*, **10**, 647–653 (2023).
- [105] Edvinsson, T. Optical quantum confinement and photocatalytic properties in two-, one- and zero-dimensional nanostructures. *Royal Society Open Science*, **5**, 180387 (2018).
- [106] Hunklinger, S. *Festkörperphysik*. De Gruyter Oldenbourg, (2014).
- [107] Kolobov, A. V. and Tominaga, J. *Two-Dimensional Transition-Metal Dichalcogenides*. Springer Cham, (2016).
- [108] Tang, C. S. and Yin, X. *Two-dimensional transition metal dichalcogenides: A general overview*. In *Two-Dimensional Transition-Metal Dichalcogenides: Phase Engineering and Applications in Electronics and Optoelectronics*. Wiley-VCH GmbH, (2023).
- [109] Hanbicki, A. T., Currie, M., Kioseoglou, G., Friedman, A. L., and Jonker, B. T. Measurement of high exciton binding energy in the monolayer transition-metal dichalcogenides WS₂ and WSe₂. *Solid State Communications*, **203**, 16–20 (2015).
- [110] Talapin, D. V. and Murray, C. B. PbSe Nanocrystal Solids for n- and p-Channel Thin Film Field-Effect Transistors. *Science*, **310**, 86–89 (2005).
- [111] Talapin, D. V., Lee, J.-S., Kovalenko, M. V., and Shevchenko, E. V. Prospects of Colloidal Nanocrystals for Electronic and Optoelectronic Applications. *Chemical Reviews*, **110**, 389–458 (2010).
- [112] Son, D., Chae, S. I., Kim, M., Choi, M. K., Yang, J., Park, K., Kale, V. S., Koo, J. H., Choi, C., Lee, M., Kim, J. H., Hyeon, T., and Kim, D. H. Colloidal Synthesis of Uniform-Sized Molybdenum Disulfide Nanosheets for Wafer-Scale Flexible Nonvolatile Memory. *Advanced Materials*, **28**, 9326–9332 (2016).
- [113] Luther, J. M., Law, M., Song, Q., Perkins, C. L., Beard, M. C., and Nozik, A. J. Structural, optical, and electrical properties of self-assembled films of PbSe nanocrystals treated with 1,2-ethanedithiol. *ACS Nano*, **2**, 271–280 (2008).
- [114] Kovalenko, M. V., Scheele, M., and Talapin, D. V. Colloidal Nanocrystals with Molecular Metal Chalcogenide Surface Ligands. *Science*, **324**, 1417–1420 (2009).
- [115] Lhuillier, E., Scarafagio, M., Hease, P., Nadal, B., Aubin, H., Xu, X. Z., Lequeux, N., Patriarche, G., Ithurria, S., and Dubertret, B. Infrared Photodetection Based on Colloidal Quantum-Dot Films with High Mobility and Optical Absorption up to THz. *Nano Letters*, **16**, 1282–1286 (2016).
- [116] Kagan, C. R., Lifshitz, E., Sargent, E. H., and Talapin, D. V. Building devices from colloidal quantum dots. *Science*, **353**, 5523 (2016).
- [117] Scheele, M., Brütting, W., and Schreiber, F. Coupled organic-inorganic nanostructures (COIN). *Physical Chemistry Chemical Physics*, **17**, 97–111 (2015).

- [118] Yin, X., Zhang, C., Guo, Y., Yang, Y., Xing, Y., and Que, W. PbS QD-based photodetectors: Future-oriented near-infrared detection technology. *Journal of Materials Chemistry C*, **9**, 417–438 (2021).
- [119] Gao, J., Nguyen, S. C., Bronstein, N. D., and Alivisatos, A. P. Solution-Processed, High-Speed, and High-Quantum-Efficiency Quantum Dot Infrared Photodetectors. *ACS Photonics*, **3**, 1217–1222 (2016).
- [120] Vafaie, M., Fan, J. Z., Najarian, A. M., Ouellette, O., Sagar, L. K., Bertens, K., Sun, B., Arquer, F. P. G., and Sargent, E. H. Colloidal quantum dot photodetectors with 10-ns response time and 80% quantum efficiency at 1,550 nm. *Matter*, **4**, 1042–1053 (2021).
- [121] Joensen, P., Frindt, R. F., and Morrison, S. R. Single-layer MoS₂. *Materials Research Bulletin*, **21**, 457–461 (1986).
- [122] Huang, H. H., Fan, X., Singh, D. J., and Zheng, W. T. Recent Progress of TMD Nanomaterials: Phase Transitions and Applications. *Nanoscale*, **12**, 1247–1268 (2020).
- [123] Duong, D. L., Yun, S. J., and Lee, Y. H. Van der Waals Layered Materials: Opportunities and Challenges. *ACS Nano*, **11**, 11803–11830 (2017).
- [124] Dai, Y., Huang, X., Han, X., Guo, J., Xu, X., Wang, L., Liu, L., Song, N., Wang, Y., and Huang, Y. *Recent progress of mechanical exfoliation and the application in the study of 2D materials. In Two-Dimensional Transition-Metal Dichalcogenides: Phase Engineering and Applications in Electronics and Optoelectronics.* Wiley-VCH GmbH, (2024).
- [125] Castellanos-Gomez, A., Buscema, M., Molenaar, R., Singh, V., Janssen, L., Zant, H. S. V. D., and Steele, G. A. Deterministic transfer of two-dimensional materials by all-dry viscoelastic stamping. *2D Materials*, **1**, 011002 (2014).
- [126] Kang, T., Tang, T. W., Pan, B., Liu, H., Zhang, K., and Luo, Z. Strategies for Controlled Growth of Transition Metal Dichalcogenides by Chemical Vapor Deposition for Integrated Electronics. *ACS Materials Au*, **2**, 665–685 (2022).
- [127] Yang, T., Wang, Z., Yuan, J., Zhou, J., and Yang, M. *Emerging electronic properties of polymorphic 2D-TMDs. In Two-Dimensional Transition-Metal Dichalcogenides: Phase Engineering and Applications in Electronics and Optoelectronics.* Wiley-VCH GmbH, (2023).
- [128] Mak, K. F., Lee, C., Hone, J., Shan, J., and Heinz, T. F. Atomically thin MoS₂: A New Direct-Gap Semiconductor. *Physical Review Letters*, **105**, 126805 (2010).
- [129] Zhao, W., Ghorannevis, Z., Chu, L., Toh, M., Kloc, C., Tan, P. H., and Eda, G. Evolution of Electronic Structure in Atomically Thin Sheets of WS₂ and WSe₂. *ACS Nano*, **7**, 791–797 (2013).
- [130] Huo, N., Yang, Y., and Li, J. Optoelectronics based on 2D TMDs and Heterostructures. *Journal of Semiconductors*, **38**, 031002 (2017).
- [131] Cunningham, P. D., Hanbicki, A. T., McCreary, K. M., and Jonker, B. T. Photoinduced Bandgap Renormalization and Exciton Binding Energy Reduction in WS₂. *ACS Nano*, **11**, 12601–12608 (2017).

- [132] Schaibley, J. R., Yu, H., Clark, G., Rivera, P., Ross, J. S., Seyler, K. L., Yao, W., and Xu, X. Valleytronics in 2D materials. *Nature Reviews Materials*, **1**, 1–15 (2016).
- [133] Manzeli, S., Ovchinnikov, D., Pasquier, D., Yazyev, O. V., and Kis, A. 2D transition metal dichalcogenides. *Nature Reviews Materials*, **2**, 1–15 (2017).
- [134] Vitale, S. A. *Valleytronics in 2D Materials*. In *Beyond-CMOS*. John Wiley & Sons, (2023).
- [135] Jamet, M., Vaz, D. C., Sierra, J. F., Svetlik, J., Valenzuela, S. O., Dlubak, B., Seneor, P., Bonell, F., and Guillet, T. *Two-Dimensional Spintronics*. In *Beyond-CMOS*. John Wiley & Sons, (2023).
- [136] Schwierz, F., Pezoldt, J., and Granzner, R. Two-dimensional materials and their prospects in transistor electronics. *Nanoscale*, **7**, 8261–8283 (2015).
- [137] Yao, Y., Li, S., Zha, J., Lai, Z., He, Q., Tan, C., and Zhang, H. *Applications of polymorphic two-dimensional transition metal dichalcogenides in electronics and optoelectronics*. In *Two-Dimensional Transition-Metal Dichalcogenides: Phase Engineering and Applications in Electronics and Optoelectronics*. Wiley-VCH GmbH, (2023).
- [138] Zeng, Z., Braun, K., Ge, C., Eberle, M., Zhu, C., Sun, X., Yang, X., Yi, J., Liang, D., Wang, Y., Huang, L., Luo, Z., Li, D., Pan, A., and Wang, X. Picosecond electrical response in graphene/MoTe₂ heterojunction with high responsivity in the near infrared region. *Fundamental Research*, **2**, 405–411 (2022).
- [139] Massicotte, M., Schmidt, P., Viialla, F., Schädler, K. G., Reserbat-Plantey, A., Watanabe, K., Taniguchi, T., Tielrooij, K. J., and Koppens, F. H. Picosecond photoresponse in van der Waals heterostructures. *Nature Nanotechnology*, **11**, 42–46 (2016).
- [140] Tang, W., Liu, C., Wang, L., Chen, X., Luo, M., Guo, W., Wang, S. W., and Lu, W. MoS₂ nanosheet photodetectors with ultrafast response. *Applied Physics Letters*, **111**, 153502 (2017).
- [141] Chandan, C., Sarkar, S., and Angadi, B. Defects induced persistent photoconductivity in monolayer MoS₂. *Applied Physics Letters*, **118** (2021).
- [142] Bartolomeo, A. D., Genovese, L., Foller, T., Giubileo, F., Luongo, G., Croin, L., Liang, S. J., Ang, L. K., and Schleberger, M. Electrical transport and persistent photoconductivity in monolayer MoS₂ phototransistors. *Nanotechnology*, **28**, 214002 (2017).
- [143] Dorodnyy, A., Salamin, Y., Ma, P., Plestina, J. V., Lassaline, N., Mikulik, D., Romero-Gomez, P., Morral, A. F. I., and Leuthold, J. Plasmonic Photodetectors. *IEEE Journal of Selected Topics in Quantum Electronics*, **24**, 1–13 (2018).
- [144] Ouyang, W., Teng, F., He, J. H., and Fang, X. Enhancing the Photoelectric Performance of Photodetectors Based on Metal Oxide Semiconductors by Charge-Carrier Engineering. *Advanced Functional Materials*, **29**, 1807672 (2019).

- [145] Zhang, W., Chiu, M. H., Chen, C. H., Chen, W., Li, L. J., and Wee, A. T. S. Role of metal contacts in high-performance phototransistors based on WSe₂ monolayers. *ACS Nano*, **8**, 8653–8661 (2014).
- [146] Kim, K., Choi, J. Y., Kim, T., Cho, S. H., and Chung, H. J. A role for graphene in silicon-based semiconductor devices. *Nature*, **479**, 338–344 (2011).
- [147] Somvanshi, D., Kallatt, S., Venkatesh, C., Nair, S., Gupta, G., Anthony, J. K., Karmakar, D., and Majumdar, K. Nature of carrier injection in metal/2D-semiconductor interface and its implications for the limits of contact resistance. *Physical Review B*, **96**, 205423 (2017).
- [148] Fan, Y., Zhou, Y., Wang, X., Tan, H., Rong, Y., and Warner, J. H. Photoinduced Schottky Barrier Lowering in 2D Monolayer WS₂ Photodetectors. *Advanced Optical Materials*, **4**, 1573–1581 (2016).
- [149] Miao, J., Zhang, S., Cai, L., and Wang, C. Black Phosphorus Schottky Diodes: Channel Length Scaling and Application as Photodetectors. *Advanced Electronic Materials*, **2**, 1500346 (2016).
- [150] Kawanago, T., Ikoma, R., Wanjing, D., and Oda, S. Adhesion lithography to fabricate MoS₂ FETs with self-assembled monolayer-based gate dielectrics. *2016 46th European Solid-State Device Research Conference (ESSDERC). IEEE*, 291–294 (2016).
- [151] Bie, Y. Q., Grosso, G., Heuck, M., Furchi, M. M., Cao, Y., Zheng, J., Bunandar, D., Navarro-Moratalla, E., Zhou, L., Efetov, D. K., Taniguchi, T., Watanabe, K., Kong, J., Englund, D., and Jarillo-Herrero, P. A MoTe₂-based light-emitting diode and photodetector for silicon photonic integrated circuits. *Nature Nanotechnology*, **12**, 1124–1129 (2017).
- [152] Ma, P., Flöry, N., Salamin, Y., Baeuerle, B., Emboras, A., Josten, A., Taniguchi, T., Watanabe, K., Novotny, L., and Leuthold, J. Fast MoTe₂ Waveguide Photodetector with High Sensitivity at Telecommunication Wavelengths. *ACS Photonics*, **5**, 1846–1852 (2018).
- [153] Huang, J. A. and Luo, L. B. Low-Dimensional Plasmonic Photodetectors: Recent Progress and Future Opportunities. *Advanced Optical Materials*, **6**, 1701282 (2018).
- [154] Ma, N. and Jena, D. Charge scattering and mobility in atomically thin semiconductors. *Physical Review X*, **4**, 011043 (2014).
- [155] Cui, Y., Xin, R., Yu, Z., Pan, Y., Ong, Z. Y., Wei, X., Wang, J., Nan, H., Ni, Z., Wu, Y., Chen, T., Shi, Y., Wang, B., Zhang, G., Zhang, Y. W., and Wang, X. High-Performance Monolayer WS₂ Field-Effect Transistors on High- κ Dielectrics. *Advanced Materials*, **27**, 5230–5234 (2015).
- [156] Yu, Z., Ong, Z. Y., Pan, Y., Cui, Y., Xin, R., Shi, Y., Wang, B., Wu, Y., Chen, T., Zhang, Y. W., Zhang, G., and Wang, X. Transistors: Realization of Room-Temperature Phonon-Limited Carrier Transport in Monolayer MoS₂ by Dielectric and Carrier Screening. *Advanced Materials*, **28**, 547–552 (2016).

-
- [157] Dean, C. R., Young, A. F., Meric, I., Lee, C., Wang, L., Sorgenfrei, S., Watanabe, K., Taniguchi, T., Kim, P., Shepard, K. L., and Hone, J. Boron nitride substrates for high-quality graphene electronics. *Nature Nanotechnology*, **5**, 722–726 (2010).
- [158] Jain, A., Szabó, Parzefall, M., Bonvin, E., Taniguchi, T., Watanabe, K., Bharadwaj, P., Luisier, M., and Novotny, L. One-Dimensional Edge Contacts to a Monolayer Semiconductor. *Nano Letters*, **19**, 6914–6923 (2019).
- [159] Wang, T., Andrews, K., Bowman, A., Hong, T., Koehler, M., Yan, J., Mandrus, D., Zhou, Z., and Xu, Y. Q. High-Performance WSe₂ Phototransistors with 2D/2D Ohmic Contacts. *Nano Letters*, **18**, 2766–2771 (2018).
- [160] Ghosh, S., Varghese, A., Thakar, K., Dhara, S., and Lodha, S. Enhanced responsivity and detectivity of fast WSe₂ phototransistor using electrostatically tunable in-plane lateral p-n homojunction. *Nature Communications*, **12**, 3336 (2021).
- [161] Lee, C. H., Lee, G. H., Zande, A. M. V. D., Chen, W., Li, Y., Han, M., Cui, X., Arefe, G., Nuckolls, C., Heinz, T. F., Guo, J., Hone, J., and Kim, P. Atomically thin p-n junctions with van der Waals heterointerfaces. *Nature Nanotechnology*, **9**, 676–681 (2014).
- [162] Li, X., Aftab, S., Hussain, S., Kabir, F., Al-Sehemi, A. G., Aslam, M., Kim, J. H., and Goud, B. S. Progress in Photodetector Devices Utilizing Transition Metal Dichalcogenides. *Journal of Materials Chemistry C*, **12**, 1211–1232 (2024).
- [163] Varghese, A., Saha, D., Thakar, K., Jindal, V., Ghosh, S., Medhekar, N. V., Ghosh, S., and Lodha, S. Near-Direct Bandgap WSe₂/ReS₂ Type-II pn Heterojunction for Enhanced Ultrafast Photodetection and High-Performance Photovoltaics. *Nano Letters*, **20**, 1707–1717 (2020).
- [164] Kufer, D., Nikitskiy, I., Lasanta, T., Navickaite, G., Koppens, F. H., and Konstantatos, G. Hybrid 2D-0D MoS₂-PbS Quantum Dot Photodetectors. *Advanced Materials*, **27**, 176–180 (2015).
- [165] Huo, N. and Konstantatos, G. Ultrasensitive all-2D MoS₂ Phototransistors enabled by an out-of-plane MoS₂ PN Homojunction. *Nature Communications*, **8**, 572 (2017).
- [166] Zhang, W., Huang, J. K., Chen, C. H., Chang, Y. H., Cheng, Y. J., and Li, L. J. High-gain phototransistors based on a CVD MoS₂ monolayer. *Advanced Materials*, **25**, 3456–3461 (2013).
- [167] Wang, H., Wang, X., Chen, Y., Zhang, S., Jiang, W., Zhang, X., Qin, J., Wang, J., Li, X., Pan, Y., Liu, F., Shi, Z., Zhang, H., Tu, L., Wang, H., Long, H., Li, D., Lin, T., Wang, J., Zhan, Y., Shen, H., Meng, X., and Chu, J. Extremely Low Dark Current MoS₂ Photodetector via 2D Halide Perovskite as the Electron Reservoir. *Advanced Optical Materials*, **8**, 1901402 (2020).
- [168] Huang, Y., Zhou, X., Luo, L., Zou, J., Liu, H., Li, X., Ren, A., Shen, K., and Wu, J. High-Performance Broadband Visible-Near Infrared Photodetector Enabled by Atomic Capping Layer. *Advanced Optical Materials*, **10**, 2200539 (2022).
- [169] Huo, N. and Konstantatos, G. Recent Progress and Future Prospects of 2D-based Photodetectors. *Advanced Materials*, **30**, 1801164 (2018).
-

- [170] Zha, J., Luo, M., Ye, M., Ahmed, T., Yu, X., Lien, D. H., He, Q., Lei, D., Ho, J. C., Bullock, J., Crozier, K. B., and Tan, C. Infrared Photodetectors Based on 2D Materials and Nanophotonics. *Advanced Functional Materials*, **32**, 2111970 (2022).
- [171] Zhang, Y., Shen, W., Wu, S., Tang, W., Shu, Y., Ma, K., Zhang, B., Zhou, P., and Wang, S. High-Speed Transition-Metal Dichalcogenides Based Schottky Photodiodes for Visible and Infrared Light Communication. *ACS Nano*, **16**, 19187–19198 (2022).
- [172] Taffelli, A., Dirè, S., Quaranta, A., and Pancheri, L. MoS₂ Based Photodetectors: A Review. *Sensors*, **21**, 2758 (2021).
- [173] George, A., Fistul, M. V., Gruenewald, M., Kaiser, D., Lehnert, T., Mupparapu, R., Neumann, C., Hübner, U., Schaal, M., Masurkar, N., Arava, L. M., Staude, I., Kaiser, U., Fritz, T., and Turchanin, A. Giant persistent photoconductivity in monolayer MoS₂ field-effect transistors. *npj 2D Materials and Applications*, **5**, 15 (2021).
- [174] Zeng, Z., Wang, Y., Pan, A., and Wang, X. Ultrafast Photocurrent Detection in Low-Dimensional Materials. *Physica Status Solidi Rapid Research Letters*, **18**, 2300120 (2024).
- [175] Yin, J., Tan, Z., Hong, H., Wu, J., Yuan, H., Liu, Y., Chen, C., Tan, C., Yao, F., Li, T., Chen, Y., Liu, Z., Liu, K., and Peng, H. Ultrafast and highly sensitive infrared photodetectors based on two-dimensional oxyselenide crystals. *Nature Communications*, **9**, 3311 (2018).
- [176] Youngblood, N. and Li, M. Ultrafast photocurrent measurements of a black phosphorus photodetector. *Applied Physics Letters*, **110**, 051102 (2017).
- [177] Yan, J., Kim, M. H., Elle, J. A., Sushkov, A. B., Jenkins, G. S., Milchberg, H. M., Fuhrer, M. S., and Drew, H. D. Dual-gated bilayer graphene hot-electron bolometer. *Nature Nanotechnology*, **7**, 472–478 (2012).
- [178] Elliott, A. D. Confocal Microscopy: Principles and Modern Practices. *Current Protocols in Cytometry*, **92**, e68 (2020).
- [179] Paddock, S. W., editor. *Confocal Microscopy: Methods and Protocols*. Humana Totowa, NJ, (2014).
- [180] Abbe, E. Beiträge zur Theorie des Mikroskops und der mikroskopischen Wahrnehmung. *Archiv für mikroskopische Anatomie*, **9**, 413–468 (1873).
- [181] Franssila, S. *Introduction to Microfabrication*. John Wiley & Sons, (2010).
- [182] Mohammad, M. A., Muhammad, M., Stepanova, M., and Dew, S. K. *Fundamentals of Electron Beam Exposure and Development*. In *Nanofabrication: Techniques and Principles*. Springer, Vienna, (2012).
- [183] Landis, S., editor. *Nano-lithography*. John Wiley & Sons, (2011).
- [184] Madou, M. J. *Fundamentals of Microfabrication: The Science of Miniaturization*. CRC press, (2002).
- [185] Chen, Y. Nanofabrication by electron beam lithography and its applications: A review. *Microelectronic Engineering*, **135**, 57–72 (2015).

- [186] Heidelberg Instruments, Datasheet μ MLA tabletop Maskless Aligner. <https://heidelberg-instruments.com/wp-content/uploads/2022/11/Fact-sheet-uMLA-V5.0.pdf>. Date accessed: 29.02.2024.
- [187] Bennett, J. M. *Characterization of Surface Roughness. In Light Scattering and Nanoscale Surface Roughness*. Springer New York, NY, (2007).
- [188] Küpfmüller, K. *Die Systemtheorie der elektrischen Nachrichtenübertragung*. Hirzel Verlag Stuttgart, (1968).
- [189] Saran, R. and Curry, R. J. Lead sulphide nanocrystal photodetector technologies. *Nature Photonics*, **10**, 81–92 (2016).
- [190] Jie, J. S., Zhang, W. J., Jiang, Y., Meng, X. M., Li, Y. Q., and Lee, S. T. Photoconductive characteristics of single-crystal CdS nanoribbons. *Nano Letters*, **6**, 1887–1892 (2006).
- [191] Shen, C., Liu, Y., Wu, J., Xu, C., Cui, D., Li, Z., Liu, Q., Li, Y., Wang, Y., Cao, X., Kumazoe, H., Shimojo, F., Krishnamoorthy, A., Kalia, R. K., Nakano, A., Vashishta, P. D., Amer, M. R., Abbas, A. N., Wang, H., Wu, W., and Zhou, C. Tellurene Photodetector with High Gain and Wide Bandwidth. *ACS Nano*, **14**, 303–310 (2020).
- [192] Nikitskiy, I., Goossens, S., Kufer, D., Lasanta, T., Navickaite, G., Koppens, F. H., and Konstantatos, G. Integrating an electrically active colloidal quantum dot photodiode with a graphene phototransistor. *Nature Communications*, **7**, 11954 (2016).
- [193] Jagtap, A., Goubet, N., Livache, C., Chu, A., Martinez, B., Gréboval, C., Qu, J., Dandeu, E., Becerra, L., Witkowski, N., Ithurria, S., Mathevet, F., Silly, M. G., Dubertret, B., and Lhuillier, E. Short Wave Infrared Devices Based on HgTe Nanocrystals with Air Stable Performances. *Journal of Physical Chemistry C*, **122**, 14979–14985 (2018).
- [194] Gallo, E. M., Cola, A., Quaranta, F., and Spanier, J. E. High speed photodetectors based on a two-dimensional electron/hole gas heterostructure. *Applied Physics Letters*, **102** (2013).
- [195] Soole, J. B., Schumacher, H., LeBlanc, H. P., Bhat, R., and Koza, M. A. High-frequency performance of InGaAs metal-semiconductor-metal photodetectors at 1.55 and 1.3 μ m wavelengths. *Applied Physics Letters*, **55**, 729–731 (1989).
- [196] Peumans, P., Bulović, V., and Forrest, S. R. Efficient, high-bandwidth organic multilayer photodetectors. *Applied Physics Letters*, **76**, 3855–3857 (2000).
- [197] Chen, X., Nabet, B., Quaranta, F., Cola, A., and Currie, M. Resonant-cavity-enhanced heterostructure metal-semiconductor-metal photodetector. *Applied Physics Letters*, **80**, 3222–3224 (2002).
- [198] Punke, M., Valouch, S., Kettlitz, S. W., Christ, N., Gärtner, C., Gerken, M., and Lemmer, U. Dynamic characterization of organic bulk heterojunction photodetectors. *Applied Physics Letters*, **91**, 071118 (2007).

- [199] Moglestue, C., Rosenzweig, J., Kuhl, J., Klingenstein, M., Lambsdorff, M., Axmann, A., Schneider, J., and Hülsmann, A. Picosecond pulse response characteristics of GaAs metal-semiconductor-metal photodetectors. *Journal of Applied Physics*, **70**, 2435–2448 (1991).
- [200] Shimizu, N., Watanabe, N., Furuta, T., and Ishibashi, T. InP-InGaAs uni-traveling-carrier photodiode with improved 3-dB bandwidth of over 150 GHz. *IEEE Photonics Technology Letters*, **10**, 412–414 (1998).
- [201] Chou, S. Y. and Liu, M. Y. Nanoscale Tera-Hertz Metal-Semiconductor-Metal Photodetectors. *IEEE Journal of Quantum Electronics*, **28**, 2358 – 2368 (1992).
- [202] Pospischil, A., Humer, M., Furchi, M. M., Bachmann, D., Guider, R., Fromherz, T., and Mueller, T. CMOS-compatible graphene photodetector covering all optical communication bands. *Nature Photonics*, **7**, 892–896 (2013).
- [203] Pradhan, N. R., Ludwig, J., Lu, Z., Rhodes, D., Bishop, M. M., Thirunavukkuarasu, K., McGill, S. A., Smirnov, D., and Balicas, L. High Photoresponsivity and Short Photoresponse Times in Few-Layered WSe₂ Transistors. *ACS Applied Materials & Interfaces*, **7**, 12080–12088 (2015).
- [204] Oertel, D. C., Bawendi, M. G., Arango, A. C., and Bulović, V. Photodetectors based on treated CdSe quantum-dot films. *Applied Physics Letters*, **87**, 213505 (2005).
- [205] Hoogland, S., Sukhovatkin, V., Shukla, H., Clifford, J., Levina, L., and Sargent, E. H. Megahertz-frequency large-area optical modulators at 1.55 μm based on solution-cast colloidal quantum dots. *Optics Express*, **16**, 6683–6691 (2008).
- [206] Perrais, G., Derelle, S., Mollard, L., Chamonal, J. P., Destefanis, G., Vincent, G., Bernhardt, S., and Rothman, J. Study of the transit-time limitations of the impulse response in Mid-Wave infrared HgCdTe avalanche photodiodes. *Journal of Electronic Materials*, **38**, 1790–1799 (2009).
- [207] Sedghi, M., Gholami, A., Jahangard, F., and Zabolian, H. Bandwidth and transient analysis of bilayer organic photodetectors. *Organic Electronics*, **49**, 262–268 (2017).
- [208] Portnoi, M., Haigh, P. A., Macdonald, T. J., Ambroz, F., Parkin, I. P., Darwazeh, I., and Papakonstantinou, I. Bandwidth limits of luminescent solar concentrators as detectors in free-space optical communication systems. *Light: Science & Applications*, **10** (2021).
- [209] Geng, X., Wang, F., Tian, H., Feng, Q., Zhang, H., Liang, R., Shen, Y., Ju, Z., Gou, G. Y., Deng, N., Li, Y., Ren, J., Xie, D., Yang, Y., and Ren, T. L. Ultrafast Photodetector by Integrating Perovskite Directly on Silicon Wafer. *ACS Nano*, **14**, 2860–2868 (2020).
- [210] Han, S. G., Lee, H., Choi, W., Lee, D., Kim, S., Sung, Y., Kim, S., and Cho, K. Photomultiplication-Type Organic Photodetectors with Fast Response Enabled by the Controlled Charge Trapping Dynamics of Quantum Dot Interlayer. *Advanced Functional Materials*, **31**, 2102087 (2021).

-
- [211] Kumar, M., Kim, H. S., Park, D. Y., Jeong, M. S., and Kim, J. Wide channel broadband $\text{CH}_3\text{NH}_3\text{PbI}_3/\text{SnS}$ hybrid photodetector: breaking the limit of bandgap energy operation. *RSC Advances*, **8**, 23206–23212 (2018).
- [212] Bogatin, E. *Signal Integrity: Simplified*. Prentice Hall Professional, (2003).
- [213] Schall, D., Neumaier, D., Mohsin, M., Chmielak, B., Bolten, J., Porschatis, C., Prinzen, A., Matheisen, C., Kuebart, W., Junginger, B., Templ, W., Giesecke, A. L., and Kurz, H. 50 GBit/s Photodetectors Based on Wafer-Scale Graphene for Integrated Silicon Photonic Communication Systems. *ACS Photonics*, **1**, 781–784 (2014).
- [214] Mittermayer, C. On the determination of dynamic errors for rise time measurement with an oscilloscope. *IEEE Transactions on Instrumentation and Measurement*, **48**, 1103–1107 (1999).
- [215] Konstantatos, G., Clifford, J., Levina, L., and Sargent, E. H. Sensitive solution-processed visible-wavelength photodetectors. *Nature Photonics*, **1**, 531–534 (2007).
- [216] Konstantatos, G., Howard, I., Fischer, A., Hoogland, S., Clifford, J., Klem, E., Levina, L., and Sargent, E. H. Ultrasensitive solution-cast quantum dot photodetectors. *Nature*, **442**, 180–183 (2006).
- [217] Cao, G., Chen, G., and Li, X. Core Shell Single-Nanowire Photodetector with Radial Carrier Transport: an Opportunity to Break the Responsivity-Speed Trade-off. *Advanced Electronic Materials*, **7**, 2000920 (2021).
- [218] Osedach, T. P., Zhao, N., Geyer, S. M., Chang, L. Y., Wanger, D. D., Arango, A. C., Bawendi, M. C., and Bulović, V. Interfacial recombination for fast operation of a planar organic/QD infrared photodetector. *Advanced Materials*, **22**, 5250–5254 (2010).
- [219] Gréboval, C., Dabard, C., Konstantinov, N., Cavallo, M., Chee, S. S., Chu, A., Dang, T. H., Khalili, A., Izquierdo, E., Prado, Y., Majjad, H., Xu, X. Z., Dayen, J. F., and Lhuillier, E. Split-Gate Photodiode Based on Graphene/HgTe Heterostructures with a Few Nanosecond Photoresponse. *ACS Applied Electronic Materials*, **3**, 4681–4688 (2021).
- [220] Li, Z., Xu, K., and Wei, F. Recent progress in photodetectors based on low-dimensional nanomaterials. *Nanotechnology Reviews*, **7**, 393–411 (2018).
- [221] Yadav, P. V. K., Ajitha, B., Reddy, Y. A. K., and Sreedhar, A. Recent advances in development of nanostructured photodetectors from ultraviolet to infrared region: A review. *Chemosphere*, **279**, 130473 (2021).
- [222] OSRAM Opto Semiconductors, Silicon PIN Photodiode BPW34; Version 1.1 (2014). <https://asset.conrad.com/media10/add/160267/c1/-/g1/000153005DS01/datenblatt-153005-osram-fotodiode-dil-1100-nm-60-bpw-34.pdf>. Date accessed: 29.02.2024.
- [223] Weidman, M. C., Beck, M. E., Hoffman, R. S., Prins, F., and Tisdale, W. A. Monodisperse, Air-Stable PbS Nanocrystals via Precursor Stoichiometry Control. *ACS Nano*, **8**, 6363–6371 (2014).
-

- [224] Sayevich, V., Guhrenz, C., Dzhagan, V. M., Sin, M., Werheid, M., Cai, B., Borchardt, L., Widmer, J., Zahn, D. R., Brunner, E., Lesnyak, V., Gaponik, N., and Eychmüller, A. Hybrid N-Butylamine-Based Ligands for Switching the Colloidal Solubility and Regeneration of Inorganic-Capped Nanocrystals. *ACS Nano*, **11**, 1559–1571 (2017).
- [225] Kumar, K., Liu, Q., Hiller, J., Schedel, C., Maier, A., Meixner, A., Braun, K., Lauth, J., and Scheele, M. Fast, Infrared-Active Optical Transistors Based on Dye-Sensitized CdSe Nanocrystals. *ACS Applied Materials & Interfaces*, **11**, 48271–48280 (2019).
- [226] Yue, D. W., Ra, C. H., Liu, X. C., Lee, D. Y., and Yoo, W. J. Edge contacts of graphene formed by using a controlled plasma treatment. *Nanoscale*, **7**, 825–831 (2015).
- [227] Chai, Y., Ionescu, R., Su, S., Lake, R., Ozkan, M., and Ozkan, C. S. Making one-dimensional electrical contacts to molybdenum disulfide-based heterostructures through plasma etching. *Physica Status Solidi (A)*, **213**, 1358–1364 (2016).
- [228] Clifford, J. P., Konstantatos, G., Johnston, K. W., Hoogland, S., Levina, L., and Sargent, E. H. Fast, sensitive and spectrally tuneable colloidal-quantum-dot photodetectors. *Nature Nanotechnology*, **4**, 40–44 (2009).
- [229] Yin, Z., Li, H., Li, H., Jiang, L., Shi, Y., Sun, Y., Lu, G., Zhang, Q., Chen, X., and Zhang, H. Single-layer MoS₂ phototransistors. *ACS Nano*, **6**, 74–80 (2012).
- [230] Brar, V. W., Sherrott, M. C., and Jariwala, D. Emerging photonic architectures in two-dimensional opto-electronics. *Chemical Society Reviews*, **47**, 6824–6844 (2018).
- [231] Lopez-Sanchez, O., Lembke, D., Kayci, M., Radenovic, A., and Kis, A. Ultrasensitive photodetectors based on monolayer MoS₂. *Nature Nanotechnology*, **8**, 497–501 (2013).
- [232] Hu, Z., Wu, Z., Han, C., He, J., Ni, Z., and Chen, W. Two-dimensional transition metal dichalcogenides: Interface and defect engineering. *Chemical Society Reviews*, **47**, 3100–3128 (2018).
- [233] Pham, P. V., Bodepudi, S. C., Shehzad, K., Liu, Y., Xu, Y., Yu, B., and Duan, X. 2D Heterostructures for Ubiquitous Electronics and Optoelectronics: Principles, Opportunities, and Challenges. *Chemical Reviews*, **122**, 6514–6613 (2022).
- [234] Sagar, S., Sanderson, S., Gedefaw, D., Pan, X., Philippa, B., Andersson, M. R., Lo, S. C., and Namdas, E. B. Toward Faster Organic Photodiodes: Tuning of Blend Composition Ratio. *Advanced Functional Materials*, **31**, 2010661 (2021).
- [235] Marin, J. F. G., Unuchek, D., Watanabe, K., Taniguchi, T., and Kis, A. MoS₂ photodetectors integrated with photonic circuits. *npj 2D Materials and Applications*, **3**, 14 (2019).
- [236] Li, M., Lan, F., Yang, W., Ji, Z., Zhang, Y., Xi, N., Xin, X., Jin, X., and Li, G. Influence of MoS₂-metal interface on charge injection: A comparison between various metal contacts. *Nanotechnology*, **31**, 395713 (2020).
- [237] Burm, J., Litvin, K. I., Schaff, W. J., and Eastman, L. F. Optimization of High-speed Metal-Semiconductor-Metal Photodetectors. *IEEE Photonics Technology Letters*, **6**, 722–724 (1994).

-
- [238] Averine, S. V., Chan, Y. C., and Lam, Y. L. Optimization of high-speed MSM-photodiode structures. *COMMAD 2000 Proceedings. Conference on Optoelectronic and Microelectronic Materials and Devices. IEEE*, 515–518 (2000).
- [239] Li, Z., Wu, J., Wang, C., Zhang, H., Yu, W., Lu, Y., and Liu, X. High-performance monolayer MoS₂ photodetector enabled by oxide stress liner using scalable chemical vapor growth method. *Nanophotonics*, **9**, 1981–1991 (2020).
- [240] Wang, L., Meric, I., Huang, P. Y., Gao, Q., Gao, Y., Tran, H., Taniguchi, T., Watanabe, K., Campos, L. M., Muller, D. A., Guo, J., Kim, P., Hone, J., Shepard, K. L., and Dean, C. R. One-Dimensional Electrical Contact to a two-dimensional material. *Science*, **342**, 614–617 (2013).
- [241] Yang, Z., Kim, C., Lee, K. Y., Lee, M., Appalakondaiah, S., Ra, C. H., Watanabe, K., Taniguchi, T., Cho, K., Hwang, E., Hone, J., and Yoo, W. J. A Fermi-Level-Pinning-Free 1D Electrical Contact at the Intrinsic 2D MoS₂-Metal Junction. *Advanced Materials*, **31**, 1808231 (2019).
- [242] Cheng, Z., Yu, Y., Singh, S., Price, K., Noyce, S. G., Lin, Y. C., Cao, L., and Franklin, A. D. Immunity to Contact Scaling in MoS₂ Transistors Using in Situ Edge Contacts. *Nano Lett.*, **19**, 5077–5085 (2019).
- [243] Schulman, D. S., Arnold, A. J., and Das, S. Contact engineering for 2D materials and devices. *Chemical Society Reviews*, **47**, 3037–3058 (2018).
- [244] Guimarães, M. H., Gao, H., Han, Y., Kang, K., Xie, S., Kim, C. J., Muller, D. A., Ralph, D. C., and Park, J. Atomically Thin Ohmic Edge Contacts between Two-Dimensional Materials. *ACS Nano*, **10**, 6392–6399 (2016).
- [245] Choi, H., Moon, B. H., Kim, J. H., Yun, S. J., Han, G. H., Lee, S. G., Gul, H. Z., and Lee, Y. H. Edge Contact for Carrier Injection and Transport in MoS₂ Field-Effect Transistors. *ACS Nano*, **13**, 13169–13175 (2019).
- [246] Wong, L. W., Huang, L., Zheng, F., Thi, Q. H., Zhao, J., Deng, Q., and Ly, T. H. Site-specific electrical contacts with the two-dimensional materials. *Nature Communications*, **11**, 3982 (2020).
- [247] Liu, K., Luo, P., Han, W., Yang, S., Zhou, S., Li, H., and Zhai, T. Approaching ohmic contact to two-dimensional semiconductors. *Science Bulletin*, **64**, 1426–1435 (2019).
- [248] Liao, W., Zhao, S., Li, F., Wang, C., Ge, Y., Wang, H., Wang, S., and Zhang, H. Interface engineering of two-dimensional transition metal dichalcogenides towards next-generation electronic devices: Recent advances and challenges. *Nanoscale Horizons*, **5**, 787–807 (2020).
- [249] Kang, J., Liu, W., Sarkar, D., Jena, D., and Banerjee, K. Computational study of metal contacts to monolayer transition-metal dichalcogenide semiconductors. *Physical Review X*, **4**, 031005 (2014).
- [250] Kong, L., Zhang, X., Tao, Q., Zhang, M., Dang, W., Li, Z., Feng, L., Liao, L., Duan, X., and Liu, Y. Doping-free complementary WSe₂ circuit via van der Waals metal integration. *Nature Communications*, **11**, 1866 (2020).
-

- [251] Fivaz, R. and Mooser, E. Mobility of charge carriers in semiconducting layer structures. *Physical Review*, **163**, 743–755 (1967).
- [252] Jain, S. K., Aggarwal, N., Krishna, S., Kumar, R., Husale, S., Gupta, V., and Gupta, G. GaN-UV Photodetector integrated with asymmetric Metal Semiconductor Metal Structure for enhanced Responsivity. *Journal of Material Science: Materials in Electronics*, **29**, 8958–8963 (2018).
- [253] Uda, M., Nakamura, A., Yamamoto, T., and Fujirnoto, Y. Work function of polycrystalline Ag, Au and Al. *Journal of Electron Spectroscopy and. Related Phenomena*, **91**, 643–648 (1998).
- [254] Baik, S. S., Im, S., and Choi, H. J. Work Function Tuning in Two-Dimensional MoS₂ Field-Effect-Transistors with Graphene and Titanium Source-Drain Contacts. *Scientific Reports*, **7**, 45546 (2017).
- [255] Asadi, M., Kumar, B., Behranginia, A., Rosen, B. A., Baskin, A., Repnin, N., Pisasale, D., Phillips, P., Zhu, W., Haasch, R., Klie, R. F., Král, P., Abiade, J., and Salehi-Khojin, A. Robust carbon dioxide reduction on molybdenum disulphide edges. *Nature Communications*, **5**, 4470 (2014).
- [256] Greulich, K., Belser, A., Bölke, S., Grüninger, P., Karstens, R., Sättele, M. S., Ovsyannikov, R., Giangrisostomi, E., Basova, T. V., Klyamer, D., Chassé, T., and Peisert, H. Charge Transfer from Organic Molecules to Molybdenum Disulfide: Influence of the Fluorination of Iron Phthalocyanine. *Journal of Physical Chemistry C*, **124**, 16990–16999 (2020).
- [257] Konstantatos, G. Current status and technological prospect of photodetectors based on two-dimensional materials. *Nature Communications*, **9**, 5266 (2018).
- [258] Huang, C. C., Wang, H., Cao, Y., Weatherby, E., Richheimer, F., Wood, S., Jiang, S., Wei, D., Dong, Y., Lu, X., Wang, P., Polcar, T., and Hewak, D. W. Facilitating Uniform Large-Scale MoS₂, WS₂ Monolayers, and Their Heterostructures through van der Waals Epitaxy. *ACS Applied Materials & Interfaces*, **14**, 42365–42373 (2022).
- [259] Zhou, H., Wang, C., Shaw, J. C., Cheng, R., Chen, Y., Huang, X., Liu, Y., Weiss, N. O., Lin, Z., Huang, Y., and Duan, X. Large area growth and electrical properties of p-type WSe₂ atomic layers. *Nano Letters*, **15**, 709–713 (2015).
- [260] George, A., Neumann, C., Kaiser, D., Mupparapu, R., Lehnert, T., Hübner, U., Tang, Z., Winter, A., Kaiser, U., Staude, I., and Turchanin, A. Controlled growth of transition metal dichalcogenide monolayers using Knudsen-type effusion cells for the precursors. *J. Phys. Mater.*, **2**, 016001 (2019).
- [261] Wu, G., Wang, X., Chen, Y., Wang, Z., Shen, H., Lin, T., Hu, W., Wang, J., Zhang, S., Meng, X., and Chu, J. Ultrahigh photoresponsivity MoS₂ photodetector with tunable photocurrent generation mechanism. *Nanotechnology*, **29**, 485204 (2018).
- [262] Tan, C., Wang, H., Zhu, X., Gao, W., Li, H., Chen, J., Li, G., Chen, L., Xu, J., Hu, X., Li, L., and Zhai, T. A Self-Powered Photovoltaic Photodetector Based on a Lateral WSe₂-WSe₂ Homojunction. *ACS Applied Materials & Interfaces*, **12**, 44934–44942 (2020).

-
- [263] Zhang, M., Liu, X., Duan, X., Zhang, S., Liu, C., Wan, D., Li, G., Xia, Z., Fan, Z., and Liao, L. Schottky-Contacted WSe₂ Hot-Electron Photodetectors with Fast Response and High Sensitivity. *ACS Photonics*, **9**, 132–137 (2021).
- [264] Luo, M., Wu, F., Long, M., and Chen, X. WSe₂/Au vertical Schottky junction photodetector with low dark current and fast photoresponse. *Nanotechnology*, **29**, 444001 (2018).
- [265] Lei, T., Tu, H., Lv, W., Ma, H., Wang, J., Hu, R., Wang, Q., Zhang, L., Fang, B., Liu, Z., Shi, W., and Zeng, Z. Ambipolar Photoresponsivity in an Ultrasensitive Photodetector Based on a WSe₂/InSe Heterostructure by a Photogating Effect. *ACS Applied Materials & Interfaces*, **13**, 50213–50219 (2021).
- [266] Zhou, C., Zhang, S., Lv, Z., Ma, Z., Yu, C., Feng, Z., and Chan, M. Self-driven WSe₂ photodetectors enabled with asymmetrical van der Waals contact interfaces. *npj 2D Materials and Applications*, **4**, 46 (2020).
- [267] You, C., Deng, W., Chen, X., Zhou, W., Zheng, Z., An, B., Li, S., Wang, B., and Zhang, Y. Enhanced Photodetection Performance in Graphene-Assisted Tunneling Photodetector. *IEEE Transactions on Electron Devices*, **68**, 1702–1709 (2021).
- [268] Wu, J., Ma, H., Zhong, C., Wei, M., Sun, C., Ye, Y., Xu, Y., Tang, B., Luo, Y., Sun, B., Jian, J., Dai, H., Lin, H., and Li, L. Waveguide-Integrated PdSe₂ Photodetector over a Broad Infrared Wavelength Range. *Nano Letters*, **22**, 6816–6824 (2022).
- [269] Li, C., Tian, R., Chen, X., Gu, L., Luo, Z., Zhang, Q., Yi, R., Li, Z., Jiang, B., Liu, Y., Castellanos-Gomez, A., Chua, S. J., Wang, X., Sun, Z., Zhao, J., and Gan, X. Waveguide-Integrated MoTe₂ p-i-n Homojunction Photodetector. *ACS Nano*, **16**, 20946–20955 (2022).
- [270] Flöry, N., Ma, P., Salamin, Y., Emboras, A., Taniguchi, T., Watanabe, K., Leuthold, J., and Novotny, L. Waveguide-integrated van der Waals heterostructure photodetector at telecom wavelengths with high speed and high responsivity. *Nature Nanotechnology*, **15**, 118–124 (2020).
- [271] Xue, H., Dai, Y., Kim, W., Wang, Y., Bai, X., Qi, M., Halonen, K., Lipsanen, H., and Sun, Z. High photoresponsivity and broadband photodetection with a band-engineered WSe₂/SnSe₂ heterostructure. *Nanoscale*, **11**, 3240–3247 (2019).
- [272] Liu, B., Tang, B., Lv, F., Zeng, Y., Liao, J., Wang, S., and Chen, Q. Photodetector based on heterostructure of two-dimensional WSe₂/In₂Se₃. *Nanotechnology*, **31**, 065203 (2020).
- [273] Kang, D. H., Pae, S. R., Shim, J., Yoo, G., Jeon, J., Leem, J. W., Yu, J. S., Lee, S., Shin, B., and Park, J. H. An Ultrahigh-Performance Photodetector based on a Perovskite–Transition-Metal-Dichalcogenide Hybrid Structure. *Advanced Materials*, **28**, 7799–7806 (2016).
- [274] Yu, Y., Zhang, Y., Song, X., Zhang, H., Cao, M., Che, Y., Dai, H., Yang, J., Zhang, H., and Yao, J. PbS-Decorated WS₂ Phototransistors with Fast Response. *ACS Photonics*, **4**, 950–956 (2017).
-

- [275] Wackenhut, F., Failla, A. V., and Meixner, A. J. Multicolor microscopy and spectroscopy reveals the physics of the one-photon luminescence in gold nanorods. *Journal of Physical Chemistry C*, **117**, 17870–17877 (2013).
- [276] Octon, T. J., Nagareddy, V. K., Russo, S., Craciun, M. F., and Wright, C. D. Fast High-Responsivity Few-Layer MoTe₂ Photodetectors. *Advanced Optical Materials*, **4**, 1750–1754 (2016).
- [277] Lee, C. H., Park, Y., Youn, S., Yeom, M. J., Kum, H. S., Chang, J., Heo, J., and Yoo, G. Design of p-WSe₂/n-Ge Heterojunctions for High-Speed Broadband Photodetectors. *Advanced Functional Materials*, **32**, 2107992 (2022).
- [278] Nabetl, B., Lioul, L., and Paoella, A. Transit Time and RC Time Constant Trade-offs in MSM Photodetectors. *IEEE Princeton Section Sarnoff Symposium.*, 187–191 (1993).
- [279] Gao, W., Zhang, S., Zhang, F., Wen, P., Zhang, L., Sun, Y., Chen, H., Zheng, Z., Yang, M., Luo, D., Huo, N., and Li, J. 2D WS₂ Based Asymmetric Schottky Photodetector with High Performance. *Advanced Electronic Materials*, **7**, 2000964 (2021).
- [280] Bartolomeo, A. D., Grillo, A., Urban, F., Iemmo, L., Giubileo, F., Luongo, G., Amato, G., Croin, L., Sun, L., Liang, S. J., and Ang, L. K. Asymmetric Schottky Contacts in Bilayer MoS₂ Field Effect Transistors. *Adv. Funct. Mater.*, **28**, 1800657 (2018).
- [281] Schott AG, Technical Glasses - Physical and Technical Properties. Mainz (2014).
- [282] DETAKTA, KAPTON[®] HN-Polyimid-Folie. Isolier- und Messtechnik GmbH & Co KG: KAPTON[®] HN-Polyimid-Folie (2015).
- [283] Biondi, M., Choi, M. J., Wang, Z., Wei, M., Lee, S., Choubisa, H., Sagar, L. K., Sun, B., Baek, S. W., Chen, B., Todorović, P., Najarian, A. M., Rasouli, A. S., Nam, D. H., Vafaie, M., Li, Y. C., Bertens, K., Hoogland, S., Voznyy, O., Arquer, F. P. G., and Sargent, E. H. Facet-Oriented Coupling Enables Fast and Sensitive Colloidal Quantum Dot Photodetectors. *Advanced Materials*, **33**, 2101056 (2021).
- [284] Tao, L., Chen, Z., Li, Z., Wang, J., Xu, X., and Xu, J. B. Enhancing light-matter interaction in 2D materials by optical micro/nano architectures for high-performance optoelectronic devices. *InfoMat*, **3**, 36–60 (2021).
- [285] Gan, X., Shiue, R. J., Gao, Y., Meric, I., Heinz, T. F., Shepard, K., Hone, J., Assefa, S., and Englund, D. Chip-integrated ultrafast graphene photodetector with high responsivity. *Nature Photonics*, **7**, 883–887 (2013).
- [286] Schall, D., Pallecchi, E., Ducournau, G., Avramovic, V., Otto, M., and Neumaier, D. Record high bandwidth integrated graphene photodetectors for communication beyond 180 Gb/s. *Optical Fiber Communication Conference*, **M2I.4** (2018).
- [287] Salamin, Y., Ma, P., Baeuerle, B., Emboras, A., Fedoryshyn, Y., Heni, W., Cheng, B., Josten, A., and Leuthold, J. 100 GHz Plasmonic Photodetector. *ACS Photonics*, **5**, 3291–3297 (2018).
- [288] Pomona Model 5299 Adapter 3 Lug Triaxial (F) to BNC (M). https://www.mouser.de/datasheet/2/159/d5299_1_04-1513638.pdf. Date accessed: 29.02.2024.

-
- [289] Zurich Instruments, UHF User Manual. https://docs.zhinst.com/uhf_user_manual/.
- [290] FEMTO, Datasheet HSA-Y-1-60 1 GHz High-Speed Amplifier. <https://www.femto.de/images/pdf-dokumente/de-hsa-y-1-60.pdf>.
- [291] Lampen, S. Six-Gigahertz Coaxial Cable. *38th SMPTE Advanced Motion Imaging Conference*, 1–12 (2004).
- [292] Thorlabs, Datasheet SMA-to-SMA Microwave Cables. <https://www.thorlabs.com/drawings/b6f5dc45ec899a17-8CA85995-0440-B55A-E845021D8463D8B1/SMM24-SpecSheet.pdf>. Date accessed: 29.02.2024.
- [293] NKT Photonics, Datasheet SuperK FIANIUM Pulsed white light fiber laser. <https://contentnktphotonics.s3.eu-central-1.amazonaws.com/SuperK-FIANIUM/SuperK%20FIANIUM%20Datasheet.pdf>.
- [294] Jiang, J., Chen, Z., Hu, Y., Xiang, Y., Zhang, L., Wang, Y., Wang, G. C., and Shi, J. Flexo-photovoltaic effect in MoS₂. *Nature Nanotechnology*, **16**, 894–901 (2021).
- [295] Dai, Z. and Rappe, A. M. Recent progress in the theory of bulk photovoltaic effect. *Chemical Physics Reviews*, **4** (2023).
- [296] Glass, A. M., Linde, D. V. D., and Negran, T. J. High-voltage bulk photovoltaic effect and the photorefractive process in LiNbO₃. *Applied Physics Letters*, **25**, 233–235 (1974).
- [297] Belinicher, V. I., Ivchenko, E. L., and Sturman, B. I. Kinetic theory of the displacement photovoltaic effect in piezoelectrics. *Zh. Eksp. Teor. Fiz.*, **83**, 649 (1992).
- [298] Sturman, B. I. Ballistic and shift currents in the bulk photovoltaic effect theory. *Physics-Uspekhi*, **63**, 407–411 (2020).
- [299] Spanier, J. E., Fridkin, V. M., Rappe, A. M., Akbashev, A. R., Polemi, A., Qi, Y., Gu, Z., Young, S. M., Hawley, C. J., Imbrenda, D., Xiao, G., Bennett-Jackson, A. L., and Johnson, C. L. Power conversion efficiency exceeding the Shockley-Queisser limit in a ferroelectric insulator. *Nature Photonics*, **10**, 611–616 (2016).
- [300] Barik, T. and Sau, J. D. Nonequilibrium nature of nonlinear optical response: Application to the bulk photovoltaic effect. *Physical Review B*, **101**, 045201 (2020).
- [301] Li, Y., Fu, J., Mao, X., Chen, C., Liu, H., Gong, M., and Zeng, H. Enhanced bulk photovoltaic effect in two-dimensional ferroelectric CuInP₂S₆. *Nature Communications*, **12**, 5896 (2021).
- [302] Shockley, W. and Queisser, H. J. Detailed Balance Limit of Efficiency of p-n Junction Solar Cells. *Journal of Applied Physics*, **32**, 510–519 (1961).
- [303] Guillemoles, J. F., Kirchartz, T., Cahen, D., and Rau, U. Guide for the perplexed to the Shockley–Queisser model for solar cells. *Nature Photonics*, **13**, 501–505 (2019).
- [304] Wang, L., Huang, L., Tan, W. C., Feng, X., Chen, L., Huang, X., and Ang, K. W. 2D Photovoltaic Devices: Progress and Prospects. *Small Methods*, **2**, 1700294 (2018).
-

- [305] Yang, D., Wu, J., Zhou, B. T., Liang, J., Ideue, T., Siu, T., Awan, K. M., Watanabe, K., Taniguchi, T., Iwasa, Y., Franz, M., and Ye, Z. Spontaneous-polarization-induced photovoltaic effect in rhombohedrally stacked MoS₂. *Nature Photonics*, **16**, 469–474 (2022).
- [306] Liu, Q., Cui, S., Bian, R., Pan, E., Cao, G., Li, W., and Liu, F. The Integration of Two-Dimensional Materials and Ferroelectrics for Device Applications. *ACS Nano*, **18**, 1778–1819 (2024).
- [307] Wang, Q., Zheng, J., He, Y., Cao, J., Liu, X., Wang, M., Ma, J., Lai, J., Lu, H., Jia, S., Yan, D., Shi, Y., Duan, J., Han, J., Xiao, W., Chen, J. H., Sun, K., Yao, Y., and Sun, D. Robust edge photocurrent response on layered type II Weyl semimetal WTe₂. *Nature Communications*, **10**, 5736 (2019).
- [308] Zhou, Y., Zhou, X., Yu, X. L., Liang, Z., Zhao, X., Wang, T., Miao, J., and Chen, X. Giant intrinsic photovoltaic effect in one-dimensional van der Waals grain boundaries. *Nature Communications*, **15**, 501 (2024).
- [309] Aftab, S., Shehzad, M. A., Ajmal, H. M. S., Kabir, F., Iqbal, M. Z., and Al-Kahtani, A. A. Bulk Photovoltaic Effect in Two-Dimensional Distorted MoTe₂. *ACS Nano*, **17**, 17884–17896 (2023).
- [310] Wang, X., Yasuda, K., Zhang, Y., Liu, S., Watanabe, K., Taniguchi, T., Hone, J., Fu, L., and Jarillo-Herrero, P. Interfacial ferroelectricity in rhombohedral-stacked bilayer transition metal dichalcogenides. *Nature Nanotechnology*, **17**, 367–371 (2022).
- [311] Wu, J., Yang, D., Liang, J., Werner, M., Ostroumov, E., Xiao, Y., Watanabe, K., Taniguchi, T., Dadap, J. I., Jones, D., and Ye, Z. Ultrafast response of spontaneous photovoltaic effect in 3R-MoS₂-based heterostructures. *Science Advances*, **8**, 3759 (2022).
- [312] Cook, A. M., Fregoso, B. M., Juan, F. D., Coh, S., and Moore, J. E. Design principles for shift current photovoltaics. *Nature Communications*, **8**, 14176 (2017).
- [313] Guan, Z., Hu, H., Shen, X., Xiang, P., Zhong, N., Chu, J., and Duan, C. Recent Progress in Two-Dimensional Ferroelectric Materials. *Advanced Electronic Materials*, **6**, 1900818 (2020).
- [314] Cheon, C. Y., Sun, Z., Cao, J., Marin, J. F. G., Tripathi, M., Watanabe, K., Taniguchi, T., Luisier, M., and Kis, A. Disorder-induced bulk photovoltaic effect in a centrosymmetric van der Waals material. *npj 2D Materials and Applications*, **7**, 74 (2023).
- [315] Zhang, D., Schoenherr, P., Sharma, P., and Seidel, J. Ferroelectric order in van der Waals layered materials. *Nature Reviews Materials*, **8**, 25–40 (2023).
- [316] Mennel, L., Paur, M., and Mueller, T. Second harmonic generation in strained transition metal dichalcogenide monolayers: MoS₂, MoSe₂, WS₂, and WSe₂. *APL Photonics*, **4**, 034404 (2019).
- [317] Autere, A., Jussila, H., Marini, A., Saavedra, J. R., Dai, Y., Säynätjoki, A., Karvonen, L., Yang, H., Amirsolaimani, B., Norwood, R. A., Peyghambarian, N., Lipsanen, H.,

- Kieu, K., Abajo, F. J. G. D., and Sun, Z. Optical harmonic generation in monolayer group-VI transition metal dichalcogenides. *Physical Review B*, **98**, 115426 (2018).
- [318] Yu, H., Talukdar, D., Xu, W., Khurgin, J. B., and Xiong, Q. Charge-Induced Second-Harmonic Generation in Bilayer WSe₂. *Nano Letters*, **15**, 5653–5657 (2015).
- [319] Wen, X., Xu, W., Zhao, W., Khurgin, J. B., and Xiong, Q. Plasmonic Hot Carriers-Controlled Second Harmonic Generation in WSe₂ Bilayers. *Nano Letters*, **18**, 1686–1692 (2018).
- [320] Huang, W., Xiao, Y., Xia, F., Chen, X., and Zhai, T. Second Harmonic Generation Control in 2D Layered Materials: Status and Outlook. *Advanced Functional Materials*, 2310726 (2024).
- [321] Akamatsu, T., Ideue, T., Zhou, L., Dong, Y., Kitamura, S., Yoshii, M., Yang, D., Onga, M., Nakagawa, Y., Watanabe, K., Taniguchi, T., Laurienzo, J., Huang, J., Ye, Z., Morimoto, T., Yuan, H., and Iwasa, Y. A van der Waals interface that creates in-plane polarization and a spontaneous photovoltaic effect. *Science*, **372**, 68–72 (2021).
- [322] Dong, Y., Yang, M. M., Yoshii, M., Matsuoka, S., Kitamura, S., Hasegawa, T., Ogawa, N., Morimoto, T., Ideue, T., and Iwasa, Y. Giant bulk piezophotovoltaic effect in 3R-MoS₂. *Nature Nanotechnology*, **18**, 36–41 (2023).
- [323] Simo, P. C., Laible, F., Horneber, A., Burkhardt, C. J., and Fleischer, M. Hexagonal arrays of plasmonic gold nanopillars on flexible substrates for surface-enhanced Raman scattering. *Nanotechnology*, **33**, 095303 (2022).
- [324] Schneider, C., Glazov, M. M., Korn, T., Höfling, S., and Urbaszek, B. Two-dimensional semiconductors in the regime of strong light-matter coupling. *Nature Communications*, **9**, 2695 (2018).
- [325] Fox, A. M. *Quantum Optics: An Introduction*. Oxford University Press, (2006).
- [326] Vahala, K. J. Optical microcavities. *Nature*, **424**, 839–846 (2003).
- [327] Hertzog, M., Wang, M., Mony, J., and Börjesson, K. Strong light-matter interactions: A new direction within chemistry. *Chemical Society Reviews*, **48**, 937–961 (2019).
- [328] Purcell, E. M. *Spontaneous Emission Probabilities at Radio Frequencies*. In *Confined Electrons and Photons*. Springer, Boston, MA, (1995).
- [329] Ribeiro, R. F., Martínez-Martínez, L. A., Du, M., Campos-Gonzalez-Angulo, J., and Yuen-Zhou, J. Polariton chemistry: controlling molecular dynamics with optical cavities. *Chemical Science*, **9**, 6325–6339 (2018).
- [330] Jaynes, E. T. and Cummings, F. W. Comparison of quantum and semiclassical radiation theories with application to the beam maser. *Proceedings of the IEEE*, **51**, 89–109 (1963).
- [331] Baranov, D. G., Wersäll, M., Cuadra, J., Antosiewicz, T. J., and Shegai, T. Novel Nanostructures and Materials for Strong Light-Matter Interactions. *ACS Photonics*, **5**, 24–42 (2018).

- [332] Janisch, C., Song, H., Zhou, C., Lin, Z., as, A. L. E., Ji, D., Terrones, M., Gan, Q., and Liu, Z. MoS₂ Monolayers on Nanocavities: Enhancement in Light-Matter Interaction. *2D Materials*, **3**, 025017 (2016).
- [333] Gan, X., Gao, Y., Mak, K. F., Yao, X., Shiue, R. J., Zande, A. V. D., Trusheim, M. E., Hatami, F., Heinz, T. F., Hone, J., and Englund, D. Controlling the spontaneous emission rate of monolayer MoS₂ in a photonic crystal nanocavity. *Applied Physics Letters*, **103** (2013).
- [334] Wu, S., Buckley, S., Jones, A. M., Ross, J. S., Ghimire, N. J., Yan, J., Mandrus, D. G., Yao, W., Hatami, F., Vučković, J., Majumdar, A., and Xu, X. Control of Two-Dimensional Excitonic Light Emission via Photonic Crystal. *2D Materials*, **1**, 011001 (2014).
- [335] Reed, J. C., Zhu, A. Y., Zhu, H., Yi, F., and Cubukcu, E. Wavelength tunable microdisk cavity light source with a chemically enhanced MoS₂ emitter. *Nano Letters*, **15**, 1967–1971 (2015).
- [336] Furchi, M., Urich, A., Pospischil, A., Lilley, G., Unterrainer, K., Detz, H., Klang, P., Andrews, A. M., Schrenk, W., Strasser, G., and Mueller, T. Microcavity-integrated graphene photodetector. *Nano Letters*, **12**, 2773–2777 (2012).
- [337] Törmä, P. and Barnes, W. L. Strong coupling between surface plasmon polaritons and emitters: A review. *Reports on Progress in Physics*, **78**, 013901 (2015).
- [338] Tian, R., Gu, L., Ji, Y., Li, C., Chen, Y., Hu, S., Li, Z., Gan, X., and Zhao, J. Black Phosphorus Photodetector Enhanced by a Planar Photonic Crystal Cavity. *ACS Photonics*, **8**, 3104–3110 (2021).
- [339] Al-Ani, I. A., As’Ham, K., Klochan, O., Hattori, H. T., Huang, L., and Miroshnichenko, A. E. Recent advances on strong light-matter coupling in atomically thin TMDC semiconductor materials. *Journal of Optics*, **24**, 053001 (2022).
- [340] Liu, X., Galfsky, T., Sun, Z., Xia, F., Lin, E. C., Lee, Y. H., Kéna-Cohen, S., and Menon, V. M. Strong light-matter coupling in two-dimensional atomic crystals. *Nature Photonics*, **9**, 30–34 (2015).
- [341] Flatten, L. C., He, Z., Coles, D. M., Trichet, A. A., Powell, A. W., Taylor, R. A., Warner, J. H., and Smith, J. M. Room-Temperature exciton-polaritons with two-dimensional WS₂. *Scientific Reports*, **6**, 33134 (2016).
- [342] Li, B. W., Zu, S., Zhang, Z. P., Zheng, L. H., Jiang, Q., Du, B. W., Luo, Y., Gong, Y. J., Zhang, Y. F., Lin, F., Shen, B., Zhu, X., Ajayan, P. M., and Fang, Z. Y. Large rabi splitting obtained in Ag-WS₂ strong-coupling heterostructure with optical microcavity at room temperature. *Opto-Electronic Advances*, **2**, 190008 (2019).
- [343] Schäfer, C., Ruggenthaler, M., Appel, H., and Rubio, A. Modification of excitation and charge transfer in cavity quantum-electrodynamical chemistry. *Proceedings of the National Academy of Sciences*, **116**, 4883–4892 (2019).
- [344] Schachenmayer, J., Genes, C., Tignone, E., and Pupillo, G. Cavity-enhanced transport of excitons. *Physical Review Letters*, **114**, 196403 (2015).

- [345] Feist, J. and Garcia-Vidal, F. J. Extraordinary exciton conductance induced by strong coupling. *Physical Review Letters*, **114**, 196402 (2015).
- [346] Orgiu, E., George, J., Hutchison, J. A., Devaux, E., Dayen, J. F., Doudin, B., Stellacci, F., Genet, C., Schachenmayer, J., Genes, C., Pupillo, G., Samorì, P., and Ebbesen, T. W. Conductivity in organic semiconductors hybridized with the vacuum field. *Nature Materials*, **14**, 1123–1129 (2015).
- [347] Bhatt, P., Kaur, K., and George, J. Enhanced Charge Transport in Two-Dimensional Materials through Light–Matter Strong Coupling. *ACS Nano*, **15**(8), 13616–13622 (2021).
- [348] Kavokin, A. and Lagoudakis, P. Exciton-mediated superconductivity. *Nature Materials*, **15**, 599–600 (2016).
- [349] Lidzey, D. G., Bradley, D. D. C., Skolnick, M. S., Virgili, T., Walker, S., and Whittaker, D. M. Strong exciton-photon coupling in an organic semiconductor microcavity. *Nature*, **395**, 53–55 (1998).
- [350] Rammler, T., Wackenhut, F., Oven-Krockhaus, S., Rapp, J., Forchhammer, K., Harter, K., and Meixner, A. J. Strong coupling between an optical microcavity and photosystems in single living cyanobacteria. *Journal of Biophotonics*, **15**, e202100136 (2022).
- [351] Ledos, N., Dang, T. H., Cavallo, M., Zhang, H., Bossavit, E., Khalili, A., Do, L. N., Gréboval, C., Ithurria, S., Utterback, J. K., Pierucci, D., Vincent, G., Vasanelli, A., and Lhuillier, E. Stop Blaming Hopping Conduction in Nanocrystal Arrays, Use it for Active Photonics! *Advanced Materials Technologies*, 2301463 (2024).
- [352] Munkhbat, B., Baranov, D. G., Stührenberg, M., Wersäll, M., Bisht, A., and Shegai, T. Self-Hybridized Exciton-Polaritons in Multilayers of Transition Metal Dichalcogenides for Efficient Light Absorption. *ACS Photonics*, **6**, 139–147 (2019).
- [353] Niehues, I., Marauhn, P., Deilmann, T., Wigger, D., Schmidt, R., Arora, A., Vasconcellos, S. M. D., Rohlfing, M., and Bratschitsch, R. Strain tuning of the Stokes shift in atomically thin semiconductors. *Nanoscale*, **12**, 20786–20796 (2020).
- [354] Ritala, M., Kukli, K., Rahtu, A., Räisänen, P. I., Leskelä, M., Sajavaara, T., and Keinonen, J. Atomic Layer Deposition of Oxide Thin Films with Metal Alkoxides as Oxygen Sources. *Science*, **288**, 319–321 (2000).
- [355] Chikkaraddy, R., Nijs, B. D., Benz, F., Barrow, S. J., Scherman, O. A., Rosta, E., Demetriadou, A., Fox, P., Hess, O., and Baumberg, J. J. Single-molecule strong coupling at room temperature in plasmonic nanocavities. *Nature*, **535**, 127–130 (2016).
- [356] Liu, J. and Tan, J. *Confocal Microscopy*. Morgan & Claypool Publishers, (2016).
- [357] Cao, E., Lin, W., Sun, M., Liang, W., and Song, Y. Exciton-plasmon coupling interactions: From principle to applications. *Nanophotonics*, **7**, 145–167 (2018).
- [358] Brongersma, M. L. and Shalaev, V. M. The Case for Plasmonics. *Science*, **328**, 440–441 (2010).

- [359] Maier, S. A. *Plasmonics: Fundamentals and Applications*. Springer New York, NY, (2007).
- [360] Hecht, B. and Novotny, L. *Principles of Nano-Optics*. Cambridge University Press, (2006).
- [361] Otto, A. Excitation of Nonradiative Surface Plasma Waves in Silver by the Method of Frustrated Total Reflection. *Zeitschrift für Physik A Hadrons and Nuclei*, **216**, 398–410 (1968).
- [362] Kretschmann, E. and Raether, H. Radiative Decay of Non Radiative Surface Plasmons Excited by Light. *Zeitschrift für Naturforschung*, **23**, 2135–2136 (1968).
- [363] Bhattarai, J. K., Maruf, M. H. U., and Stine, K. J. Plasmonic-active nanostructured thin films. *Processes*, **8**, 115 (2020).
- [364] Wang, H., Li, S., Ai, R., Huang, H., Shao, L., and Wang, J. Plasmonically enabled two-dimensional material-based optoelectronic devices. *Nanoscale*, **12**, 8095–8108 (2020).
- [365] Jain, P. K. and El-Sayed, M. A. Plasmonic coupling in noble Metal Nanostructures. *Chemical Physics Letters*, **487**, 153–164 (2010).
- [366] Kravets, V. G., Kabashin, A. V., Barnes, W. L., and Grigorenko, A. N. Plasmonic Surface Lattice Resonances: A Review of Properties and Applications. *Chemical Reviews*, **118**, 5912–5951 (2018).
- [367] Khurgin, J. B. How to deal with the loss in plasmonics and metamaterials. *Nature Nanotechnology*, **10**, 2–6 (2015).
- [368] Brown, A. M., Sundararaman, R., Narang, P., Goddard, W. A., and Atwater, H. A. Nonradiative plasmon decay and hot carrier dynamics: Effects of phonons, surfaces, and geometry. *ACS Nano*, **10**, 957–966 (2016).
- [369] Steiner, A. M., Lissel, F., Fery, A., Lauth, J., and Scheele, M. Prospects of Coupled Organic–Inorganic Nanostructures for Charge and Energy Transfer Applications. *Angewandte Chemie International Edition*, **60**, 1152–1175 (2021).
- [370] Zhu, Y., Xu, H., Yu, P., and Wang, Z. Engineering plasmonic hot carrier dynamics toward efficient photodetection. *Applied Physics Reviews*, **8**, 021305 (2021).
- [371] Koya, A. N., Romanelli, M., Kuttruff, J., Henriksson, N., Stefancu, A., Grinblat, G., Andres, A. D., Schnur, F., Vanzan, M., Marsili, M., Rahaman, M., Rodríguez, A. V., Tapani, T., Lin, H., Dana, B. D., Lin, J., Barbillon, G., Zaccaria, R. P., Brida, D., Jariwala, D., Veisz, L., Cortés, E., Corni, S., Garoli, D., and Maccaferri, N. Advances in ultrafast plasmonics. *Applied Physics Reviews*, **10**, 021318 (2023).
- [372] Brongersma, M. L., Halas, N. J., and Nordlander, P. Plasmon-induced hot carrier science and technology. *Nature Nanotechnology*, **10**, 25–34 (2015).
- [373] Yu, Y., Sun, Y., Hu, Z., An, X., Zhou, D., Zhou, H., Wang, W., Liu, K., Jiang, J., Yang, D., Zafar, Z., Zeng, H., Wang, F., Zhu, H., Lu, J., and Ni, Z. Fast Photoelectric Conversion in the Near-Infrared Enabled by Plasmon-Induced Hot-Electron Transfer. *Advanced Materials*, **31**, 1903829 (2019).

-
- [374] Wang, W., Klots, A., Prasai, D., Yang, Y., Bolotin, K. I., and Valentine, J. Hot Electron-Based Near-Infrared Photodetection Using Bilayer MoS₂. *Nano Letters*, **15**, 7440–7444 (2015).
- [375] Besteiro, L. V., Yu, P., Wang, Z., Holleitner, A. W., Hartland, G. V., Wiederrecht, G. P., and Govorov, A. O. The fast and the furious: Ultrafast hot electrons in plasmonic metastructures. Size and structure matter. *Nano Today*, **27**, 120–145 (2019).
- [376] Kumar, R., Sharma, A., Kaur, M., and Husale, S. Pt-Nanostrip-Enabled Plasmonically Enhanced Broad Spectral Photodetection in Bilayer MoS₂. *Advanced Optical Materials*, **5**, 1700009 (2017).
- [377] Zhang, J., Wang, Y., Li, D., Sun, Y., and Jiang, L. Engineering Surface Plasmons in Metal/Nonmetal Structures for Highly Desirable Plasmonic Photodetectors. *ACS Materials Letters*, **4**, 343–355 (2022).
- [378] Sobhani, A., Lauchner, A., Najmaei, S., Ayala-Orozco, C., Wen, F., Lou, J., and Halas, N. J. Enhancing the photocurrent and photoluminescence of single crystal monolayer MoS₂ with resonant plasmonic nanoshells. *Applied Physics Letters*, **104**, 031112 (2014).
- [379] Desiatov, B., Goykhman, I., Mazurski, N., Shappir, J., Khurgin, J. B., and Levy, U. Plasmonic enhanced silicon pyramids for internal photoemission Schottky detectors in the near-infrared regime. *Optica*, **2**, 335–338 (2015).
- [380] Qi, Z., Zhai, Y., Wen, L., Wang, Q., Chen, Q., Iqbal, S., Chen, G., Xu, J., and Tu, Y. Au nanoparticle-decorated silicon pyramids for plasmon-enhanced hot electron near-infrared photodetection. *Nanotechnology*, **28**, 275202 (2017).
- [381] Kurt, H. F., Atabey, T. N., Dereli, O. C., Salmanoglu, A., and Gecim, H. S. Photodetector Engineering with Plasmonic Properties. *International Journal of Electronics and Communication Engineering*, **15**, 94–98 (2021).
- [382] Wang, B., Zou, Y., Lu, H., Kong, W., Singh, S. C., Zhao, C., Yao, C., Xing, J., Zheng, X., Yu, Z., Tong, C., Xin, W., Yu, W., Zhao, B., and Guo, C. Boosting Perovskite Photodetector Performance in NIR Using Plasmonic Bowtie Nanoantenna Arrays. *Small*, **16**, 2001417 (2020).
- [383] Chu, A., Gréboval, C., Goubet, N., Martinez, B., Livache, C., Qu, J., Rastogi, P., Bresciani, F. A., Prado, Y., Suffit, S., Ithurria, S., Vincent, G., and Lhuillier, E. Near Unity Absorption in Nanocrystal Based Short Wave Infrared Photodetectors Using Guided Mode Resonators. *ACS Photonics*, **6**, 2553–2561 (2019).
- [384] Ge, J., Luo, M., Zou, W., Peng, W., and Duan, H. Plasmonic photodetectors based on asymmetric nanogap electrodes. *Applied Physics Express*, **9**, 084101 (2016).
- [385] Kumar, P. V., Rossi, T. P., Marti-Dafcik, D., Reichmuth, D., Kuisma, M., Erhart, P., Puska, M. J., and Norris, D. J. Plasmon-Induced Direct Hot-Carrier Transfer at Metal-Acceptor Interfaces. *ACS Nano*, **13**, 3188–3195 (2019).
- [386] Hong, C., Jang, S. G., Yu, Y. J., and Kim, J. H. Hot Electron Dynamics in MoS₂/Pt Van Der Waals Electrode Interface for Self-Powered Hot Electron Photodetection. *Advanced Materials Interfaces*, **10**, 2300140 (2023).
-

- [387] Liu, Y., Chen, Q., Chen, Q., Cullen, D. A., Xie, Z., and Lian, T. Efficient Hot Electron Transfer from Small Au Nanoparticles. *Nano Letters*, **20**, 4322–4329 (2020).
- [388] Shan, H., Yu, Y., Wang, X., Luo, Y., Zu, S., Du, B., Han, T., Li, B., Li, Y., Wu, J., Lin, F., Shi, K., Tay, B. K., Liu, Z., Zhu, X., and Fang, Z. Direct observation of ultrafast plasmonic hot electron transfer in the strong coupling regime. *Light: Science and Applications*, **8**, 9 (2019).
- [389] Du, W., Zhao, J., Zhao, W., Zhang, S., Xu, H., and Xiong, Q. Ultrafast Modulation of Exciton-Plasmon Coupling in a Monolayer WS₂-Ag Nanodisk Hybrid System. *ACS Photonics*, **6**, 2832–2840 (2019).
- [390] Li, Z., Hu, S., Zhang, Q., Tian, R., Gu, L., Zhu, Y., Yuan, Q., Yi, R., Li, C., Liu, Y., Hao, Y., Gan, X., and Zhao, J. Telecom-Band Waveguide-Integrated MoS₂ Photodetector Assisted by Hot Electrons. *ACS Photonics*, **9**, 282–289 (2022).
- [391] Geladari, O., Eberle, M., Maier, A., Fetzer, F., Chassé, T., Meixner, A. J., Scheele, M., Schnepf, A., and Braun, K. Nanometer Sized Direct Laser-Induced Gold Printing for Precise 2D-Electronic Device Fabrication. *Small Methods*, **7**, 2201221 (2023).
- [392] Geladari, O., Haizmann, P., Maier, A., Strienz, M., Eberle, M., Scheele, M., Peisert, H., Schnepf, A., Chassé, T., Braun, K., and Meixner, A. J. Direct laser induced writing of high precision gold nanosphere SERS patterns. *Nanoscale Advances* (2024).
- [393] Wadhwa, R., Ghosh, A., Kumar, D., Kumar, P., and Kumar, M. Platinum nanoparticle sensitized plasmonic-enhanced broad spectral photodetection in large area vertical-aligned MoS₂ flakes. *Nanotechnology*, **33**, 255702 (2022).
- [394] Hans, E. A. D. and Regulacio, M. D. Dual Plasmonic Au-Cu_{2-x}S Nanocomposites: Design Strategies and Photothermal Properties. *Chemistry - A European Journal*, **27**, 11030–11040 (2021).
- [395] Bessel, P., Niebur, A., Kranz, D., Lauth, J., and Dorfs, D. Probing Bidirectional Plasmon-Plasmon Coupling-Induced Hot Charge Carriers in Dual Plasmonic Au/CuS Nanocrystals. *Small*, **19**, 2206379 (2023).
- [396] Galarreta, B. C., Harté, E., Marquestaut, N., Norton, P. R., and Lagugné-Labarthe, F. Plasmonic properties of Fischer’s patterns: Polarization effects. *Physical Chemistry Chemical Physics*, **12**, 6810–6816 (2010).
- [397] You, Y. G., Shin, D. H., Ryu, J. H., Campbell, E. E., Chung, H. J., and Jhang, S. H. Atomic layer deposited Al₂O₃ passivation layer for few-layer WS₂ field effect transistors. *Nanotechnology*, **32**, 505702 (2021).
- [398] Borghardt, S., Tu, J. S., Winkler, F., Schubert, J., Zander, W., Leosson, K., and Kardynał, B. E. Engineering of optical and electronic band gaps in transition metal dichalcogenide monolayers through external dielectric screening. *Physical Review Materials*, **1**, 054001 (2017).
- [399] Lu, J., Deng, Z., Ye, Q., Zheng, Z., Yao, J., and Yang, G. Promoting the Performance of 2D Material Photodetectors by Dielectric Engineering. *Small Methods*, **6**, 2101046 (2022).

-
- [400] Zhou, X., Zhou, N., Li, C., Song, H., Zhang, Q., Hu, X., Gan, L., Li, H., Lü, J., Luo, J., Xiong, J., and Zhai, T. Vertical heterostructures based on SnSe₂/MoS₂ for high performance photodetectors. *2D Materials*, **4**, 025048 (2017).
- [401] Mitta, S. B., Ali, F., Yang, Z., Moon, I., Ahmed, F., Yoo, T. J., Lee, B. H., and Yoo, W. J. Gate-Modulated Ultrasensitive Visible and Near-Infrared Photodetection of Oxygen Plasma-Treated WSe₂ Lateral pn-Homojunctions. *ACS Applied Materials & Interfaces*, **12**, 23261–23271 (2020).
- [402] Huang, Y., Zhuge, F., Hou, J., Lv, L., Luo, P., Zhou, N., Gan, L., and Zhai, T. Van der Waals Coupled Organic Molecules with Monolayer MoS₂ for Fast Response Photodetectors with Gate-Tunable Responsivity. *ACS Nano*, **12**, 4062–4073 (2018).
- [403] Ornelas, C. D., Bowman, A., Walmsley, T. S., Wang, T., Andrews, K., Zhou, Z., and Xu, Y. Q. Ultrafast Photocurrent Response and High Detectivity in Two-Dimensional MoSe₂-based Heterojunctions. *ACS applied materials & interfaces*, **12**, 46476–46482 (2020).
- [404] He, J., Yang, Y., He, Y., Ge, C., Zhao, Y., Gao, L., and Tang, J. Low Noise and Fast Photoresponse of Few-Layered MoS₂ Passivated by MA₃Bi₂Br₉. *ACS Photonics*, **5**, 1877–1884 (2018).
- [405] Ye, K., Liu, L., Liu, Y., Nie, A., Zhai, K., Xiang, J., Wang, B., Wen, F., Mu, C., Zhao, Z., Gong, Y., Liu, Z., and Tian, Y. Lateral Bilayer MoS₂-WS₂ Heterostructure Photodetectors with High Responsivity and Detectivity. *Advanced Optical Materials*, **7**, 1900815 (2019).
- [406] Tsai, D. S., Lien, D. H., Tsai, M. L., Su, S. H., Chen, K. M., Ke, J. J., Yu, Y. C., Li, L. J., and He, J. H. Trilayered MoS₂ Metal-Semiconductor-Metal Photodetectors: Photogain and Radiation Resistance. *IEEE Journal of Selected Topics in Quantum Electronics*, **20**, 30–35 (2014).
- [407] Chen, J., Wang, Q., Sheng, Y., Cao, G., Yang, P., Shan, Y., Liao, F., Muhammad, Z., Bao, W., Hu, L., Liu, R., Cong, C., and Qiu, Z. J. High-Performance WSe₂ Photodetector Based on a Laser-Induced p-n Junction. *ACS Applied Materials & Interfaces*, **11**, 43330–43336 (2019).
- [408] Wu, D., Wang, Y., Zeng, L., Jia, C., Wu, E., Xu, T., Shi, Z., Tian, Y., Li, X., and Tsang, Y. H. Design of 2D Layered PtSe₂ Heterojunction for the High-Performance, Room-Temperature, Broadband, Infrared Photodetector. *ACS Photonics*, **5**, 3820–3827 (2018).
- [409] Long, M., Liu, E., Wang, P., Gao, A., Xia, H., Luo, W., Wang, B., Zeng, J., Fu, Y., Xu, K., Zhou, W., Lv, Y., Yao, S., Lu, M., Chen, Y., Ni, Z., You, Y., Zhang, X., Qin, S., Shi, Y., Hu, W., Xing, D., and Miao, F. Broadband Photovoltaic Detectors Based on an Atomically Thin Heterostructure. *Nano Letters*, **16**, 2254–2259 (2016).
- [410] Zhang, S., Hao, Y., Gao, F., Wu, X., Hao, S., Qiu, M., Zheng, X., Wei, Y., and Hao, G. Controllable growth of wafer-scale two-dimensional WS₂ with outstanding optoelectronic properties. *2D Materials*, **11**, 015007 (2023).
-

- [411] Wang, Z., Chen, Y., Wu, P., Ye, J., Peng, M., Yan, Y., Zhong, F., He, T., Wang, Y., Xu, M., Zhang, K., Hu, Z., Li, Q., Zhang, L., Wang, F., and Wang, P. High-performance MoSe₂ homojunction infrared photodetector. *Infrared Physics & Technology*, **106**, 103272 (2020).
- [412] Zhang, Z. X., Long-Hui, Z., Tong, X. W., Gao, Y., Xie, C., Tsang, Y. H., Luo, L. B., and Wu, Y. C. Ultrafast, Self-Driven, and Air-Stable Photodetectors Based on Multilayer PtSe₂/Perovskite Heterojunctions. *The Journal of Physical Chemistry Letters*, **9**, 1185–1194 (2018).
- [413] Thorlabs, FDS015 Si Photodiode (2017). <https://www.thorlabs.com/drawings/b6f5dc45ec899a17-8CA85995-0440-B55A-E845021D8463D8B1/FDS015-SpecSheet.pdf>. Date accessed: 29.02.2024.
- [414] Massicotte, M., Vialla, F., Schmidt, P., Lundeberg, M. B., Latini, S., Hastrup, S., Danovich, M., Davydovskaya, D., Watanabe, K., Taniguchi, T., Fal'ko, V. I., Thygesen, K. S., Pedersen, T. G., and Koppens, F. H. Dissociation of two-dimensional excitons in monolayer WSe₂. *Nature Communications*, **9**, 1633 (2018).

List of Publications & Scholarly Contributions

Peer-reviewed publications

This thesis is based on the following publications:

1. Christine Schedel*, **Fabian Strauß*** & Marcus Scheele.
Pitfalls in Determining the Electrical Bandwidth of Nonideal Nanomaterials for Photodetection.
The Journal of Physical Chemistry C, **126**, 14011-14016 (2022).
<https://doi.org/10.1021/acs.jpcc.2c04584>
(* Equal contribution.)
2. **Fabian Strauß**, Christine Schedel & Marcus Scheele.
Edge Contacts accelerate the Response of MoS₂ Photodetectors.
Nanoscale Advances, **5**, 3494 (2023).
<https://doi.org/10.1039/d3na00223c>
3. **Fabian Strauß***, Pia Kohlschreiber*, Jakob Keck, Patrick Michel, Jonas Hiller, Alfred J. Meixner & Marcus Scheele.
A simple 230 MHz Photodetector Based on Exfoliated WSe₂ Multilayers.
RSC Applied Interfaces, **1**, 728-733 (2024).
<https://doi.org/10.1039/D4LF00019F>
(* Equal contribution.)

The thesis also includes the following publications to a lesser extent.

4. Christine Schedel, **Fabian Strauß**, Krishan Kumar, Andre Maier, Kai M. Wurst, Patrick Michel & Marcus Scheele.
Substrate Effects on the Bandwidth of CdSe Quantum Dot Photodetectors.
ACS Applied Materials & Interfaces, **13**, 47954-47961 (2021).
<https://doi.org/10.1021/acsami.1c13581>
5. Christine Schedel, **Fabian Strauß**, Pia Kohlschreiber, Olympia Geladari, Alfred J. Meixner & Marcus Scheele.
Substrate effects on the speed limiting factor of WSe₂ photodetectors.
Physical Chemistry Chemical Physics, **24**, 25383-25390 (2022).
<https://doi.org/10.1039/d2cp03364j>
6. Andre Maier, **Fabian Strauß**, Pia Kohlschreiber, Christine Schedel, Kai Braun & Marcus Scheele.
Sub-nanosecond Intrinsic Response Time of PbS Nanocrystal IR-Photodetectors.
Nano Letters, **22**, 2809-2816 (2022).
<https://doi.org/10.1021/acs.nanolett.1c04938>

Other scholarly publications with the author of this work:

1. **Fabian Strauß**, Zhouxiaosong Zeng, Kai Braun & Marcus Scheele.
Towards GHz-photodetection with Transition Metal Dichalcogenides.
Accounts of Chemical Research, **57**, 1488-1499 (2024).
<https://doi.org/10.1021/acs.accounts.4c00088>
2. Zhouxiaosong Zeng, Zhiqiang Tian, Yufan Wang, Cuihuan Ge, **Fabian Strauß**, Kai Braun, Patrick Michel, Lanyu Huang, Guixian Liu, Dong Li, Marcus Scheele, Mingxing Chen, Anlian Pan & Xiao Wang.
Dual polarization-enabled ultrafast bulk photovoltaic response in van der Waals heterostructures.
Nature Communications, **15**, 5355 (2024).
<https://doi.org/10.1038/s41467-024-49760-6>
3. Fabian Grahlow, **Fabian Strauß**, Marcus Scheele, Markus Ströbele, Alberto Carta, Sophie F. Weber, Scott Kroeger, Carl P. Romao & H.-Jürgen Meyer.
Electronic Structure and Transport in the Potential Luttinger Liquids CsNb₃Br₇S and RbNb₃Br₇S.
Physical Chemistry Chemical Physics, **26**, 11789-11797 (2024).
<https://doi.org/10.1039/D4CP00293H>
4. Fabian Grahlow, **Fabian Strauß**, Patrick Schmidt, Jaroslav Valenta, Markus Ströbele, Marcus Scheele, Carl P. Romao & H.-Jürgen Meyer.
Ta₄SBr₁₁: A Cluster Mott Insulator with a Corrugated, Van der Waals Layered Structure.
Inorganic Chemistry, accepted manuscript (2024).
<https://doi.org/10.1021/acs.inorgchem.4c02896>

Conference Contributions During the thesis, the following contributions to summer schools and conferences were made in the form of a poster presentation:

1. Bad Honnef Physics School ‘Exciting nanostructures’ 2021
2. 763. WE-Heraeus Seminar on ‘Optoelectronic Processes at Nanostructured Interfaces’ 2022 - *Price for best poster*.
3. 122nd Bunsen-Tagung 2023 in Berlin

Supervision of theses and practical courses

The following students were supervised during this thesis:

1. Jasmin Moser, Practical Course, Teaching Chemistry (2022)
'Beeinflussung der Schnelligkeit von WSe₂-Photodetektoren mithilfe von Edge-On Kontaktierung im Vergleich zu Face-On Kontaktierung'
2. Catharina Brand, Practical Course, Chemistry (2023)
'Übergangsmetallchalkogenide als elektronische und optoelektronische Bauelemente'
3. Pia Kohlschreiber, Master Thesis, Nano-Science (2023)
'Exploring the speed limits of neat WSe₂ photodetectors'

Contribution to other theses

During this thesis, the author contributed to the following other theses, mainly by performing lithography, exfoliation or teaching fabrication and measurement procedures:

1. Christine Schedel, Ph.D. Thesis
2. Patrick Michel, Ph.D. Thesis
3. Jonas Hiller, Ph.D. Thesis
4. Jakob Keck, Ph.D. Thesis
5. Robert Thalwitzer, Ph.D. Thesis
6. Philipp Haizmann, Ph.D. Thesis
7. Eric Juriatti, Ph.D. Thesis
8. William Roberts, Ph.D. Thesis
9. Mario Martin, Ph.D. Thesis
10. Melanie Sommer, Ph.D. Thesis
11. Ata Bozkurt, Master Thesis

Declaration of Contribution

In this chapter the authors contribution and those of collaboration partners to the publications of this cumulative thesis are declared.

Publication I

‘Pitfalls in Determining the Electrical Bandwidth of Nonideal Nanomaterials for Photodetection’, published in *The Journal of Physical Chemistry C*:

Herein, the concept of the paper, design of the figures and writing of the manuscript was equally split among Christine Schedel and me. The manuscript and process was critically reviewed by Marcus Scheele.

Estimated contribution of my own: ~50 %

Publication II

‘Edge Contacts accelerate the Response of MoS₂ Photodetectors’, published in *Nanoscale Advances*:

Within this publication, I performed the fabrication, measurements and data evaluation. The initial manuscript was entirely written by me. Christine Schedel and Marcus Scheele supported with critical questions and in discussion throughout the whole experimental phase and within reviewing the manuscript.

Estimated contribution of my own: ~90 %

Publication III

‘A simple 230 MHz Photodetector Based on Exfoliated WSe₂ Multilayers’, published in *RSC Applied Interfaces*:

Pia Kohlschreiber and I performed the device fabrication as well as recording of the data. Pia Kohlschreiber and me evaluated the data. Jakob Keck helped establishing and explaining the home-built confocal microscope as well as constant support throughout the whole experimental phase with the optics and home-built solutions. Patrick Michel built the focussing for measurements of the sample inside the probe station. Jonas Hiller, Jakob Keck and me conceived the project and its feasibility. I wrote the initial version of the manuscript which was revised by all authors, especially Alfred Meixner and Marcus Scheele. Furthermore, Marcus Scheele provided critical supervision throughout the whole project.

Estimated contribution of my own: ~50 %

Publication IV

‘Substrate Effects on the Bandwidth of CdSe Quantum Dot Photodetectors’, published in *ACS Applied Materials & Interfaces*:

Christine Schedel conceived the project and performed the majority of experiments as well as analysis and writing of the manuscript. I performed electron beam lithography and helped with experiments as well as I contributed to the discussion and interpretation of results. Krishan Kumar and Patrick Michel synthesised and provided the nanoparticles. Andre Maier contributed the electrode structures on polyimide substrates. Marcus Scheele supervised the whole project and supported the manuscript as well as enriched the discussion of progress.

Estimated contribution of my own: ~15 %

Publication V

‘Substrate effects on the speed limiting factor of WSe₂ photodetectors’, published in *Physical Chemistry Chemical Physics*:

Christine performed the measurements, exfoliation of the TMDCs and analysis of data. I provided the lithographically patterned substrates on glass and polyimide as well as critical discussion throughout the process. Pia Kohlschreiber performed AFM measurements. Olympia Geladari trained Christine Schedel and me in the exfoliation and stamping process. Alfred J. Meixner provided the TMDC material and laboratory space for fabrication of the detectors. Marcus Scheele assisted the project with fruitful discussions. Christine Schedel wrote the manuscript with support of Marcus Scheele and me.

Estimated contribution of my own: ~15 %

Publication VI

‘Sub-nanosecond Intrinsic Response Time of PbS Nanocrystal IR-Photodetectors’, published in *Nano Letters*:

Andre Maier, Kai Braun and Marcus Scheele conceived the project. Andre Maier performed device fabrication and characterization as well as developing the ASOPS setup and performing and analysing the measurements. I designed the device layout and supported device fabrication as well as the setup development. Furthermore, I performed the extrinsic measurements of the devices. Pia Kohlschreiber supported thin film fabrication and performed profilometry and optical microscopy. Christine Schedel supported the probe station setup. Marcus Scheele supervised the manuscript. Andre Maier wrote the manuscript with contributions and rich discussions of all the other authors.

Estimated contribution of my own: ~20 %

Publication VII

‘Towards GHz-photodetection with Transition Metal Dichalcogenides’, published in *Accounts of Chemical Research*:

Within this review, I coordinated and structured the manuscript as well as allocated the graphics. Zhouxiaosong Zeng wrote the chapter about the intrinsic measurements and provided the data. Kai Braun provided the data of the gold printing section. Marcus Scheele conceived the idea, unified the graphics and revised the manuscript.

Estimated contribution of my own: ~70 %

Acknowledgements

‘Find a group of people who challenge and inspire you, spend a lot of time with them, and it will change your life.’ This quote from Amy Poehler sums up my Ph.D. time pretty good. Without all the wonderful people surrounding me, this work would never have finished, let alone begun. Accordingly, it is time to express my deep gratitude to all the people who accompanied and influenced my Ph.D. time.

First of all, I am grateful for Marcus Scheele, my supervisor and head of the workgroup. Your time and constant support have been invaluable for me. I appreciate the freedom you gave me to develop the projects into the direction I wanted and for always keeping things in perspective, especially when I was about to lose track in the many projects. Thank you for your optimism and taking time for me, even when you were busy yourself. Beyond the scientific input I learned so much more from you on how to promote myself in talks, on delivering a clear message in written texts and inspiration on great birthday cards.

Secondly, I want to thank my second supervisor Monika Fleischer for continually willing to listen to my research, as well as for critically question the process and providing ideas to improve it. Moreover, thank you very much for not only the access to your lab, but welcoming me within the group all those years ago for my first scientific work, the bachelor thesis. Starting from there, the plasmons caught my attention and never left me again.

I want to acknowledge Alfred J. Meixner for the access to his laboratory which enabled me to work with the TMDCs. Far beyond that, I want to thank you for the fruitful discussions about cavity experiments and the support of measuring at your home-built confocal setup.

My deepest thanks belong to Christine Schedel who supervised my practical course in January 2020, followed by my master thesis. Within this time and even afterwards you became my role model for the lab and pushed my inner aspirations. I cannot imagine anyone else to recover better from the low blows of academic life than with you. But beyond the shared work and scientific goals, it was wonderful sharing an office with you, which was especially on rough days a big motivation to go to university, because I knew it was going to be a fun day with you there.

My special thanks go to Jakob Keck and Jonas Hiller for sharing a seemingly endless motivation and enthusiasm about science. Without your brilliant ideas, optical know-how, or baking muffins in creative ways at nine o’clock, this work would have ended halfway.

Being part of the Scheele group has been a real pleasure because of the wonderful people there. I want to say thank you to Theresa Hettiger, Andre Maier, and Robert Thalwitzer for being great partners in the office, having fun and supporting each other. I appreciate Patrick Michel, Sophia Westendorf, Kai Wurst and Zhouxiaosong Zeng for sharing the ‘New Glovebox Lab’ in the most supportive manner possible. I enjoyed working alongside you as it provided me with opportunities to learn. We could share the highs and lows of the job and laugh about them now and then. I appreciate my practical students Jasmin Moser, Catharina Brand and Nikola Kohlschreiber as well as my two successors William Roberts and Mario Martin - You made teaching an enriching experience. Your

enthusiasm and fresh ideas taught me a lot. Furthermore, I want to thank Philipp Haizmann, Eric Juriatti, Philipp Frech, Yongju Kwon and Ata Bozkurt for completing the wonderful AK experience with experimental ideas and strategies for XPS measurements, InSb nanoparticles, support for moving the exfoliation setups in the TA room and much more. My sincere gratitude belongs to Kai Braun, Heike Alexa, Elke Nadler, Karsten Stampke and Jochen Mehne for fruitful discussions, for handling all the bureaucracy which allowed me to focus on my work, for taking magnificent images of my samples with the SEM and for dealing with all the broken parts around us.

Thanks to all of you, the atmosphere in our workgroup is unique and enabling us to produce good work.

Collaborations with other groups provide us with a look into another world of interesting science. Thus, I am very thankful to have such lovely, motivated, and proficient partners within the university. Temperature-dependant conductivity measurements of crystals synthesised by the group of H.-Jürgen Meyer, were never dull due to their sometimes surprising properties, but even more, because measurements with Fabian Grahlow were always in good company.

Searching for guidance in EBL and plasmonics matter, I could always stop by the office of Melanie Sommer, Lukas Lang and Christian Simo or Florian Laible. You and the entire AG Fleischer team not only assisted me in the fabrication process, but also provided simulations for my structures and listened to my plans and failures. Moreover, you welcomed me as a member of your group and we always enjoyed spending time together, whether working side by side in the lab or after work playing cards or bowling.

Some groups do not really feel like other groups, because they are on the same floors. I want to thank the whole groups of Alfred Meixner, Heiko Peisert and Jannika Lauth for having a great ‘extended’ work group in which we could have fun playing games, eating cake, sharing lunch or discuss experiments together.

I want to also thank all my external cooperation partners, Volodymyr Shamraienko (Eychmüller group, university of Dresden) and the team around Antony George and Andrey Turchanin (university of Jena). You provided me with interesting samples of highest quality to analyse.

I thank Heidi Potts from Zurich Instruments for engaging in productive discussions regarding high-speed detection and the measurement setup.

Although not related to my research, I had the opportunity to improve my proficiency with gloveboxes and at this point I want to thank Niklas Auer and the team of GS Glovebox Systems for having so much patience with me - I’m pretty sure, only my supervisor received more emails from me than you over the last three years.

This work would have been nothing without Ronny Löffler and Markus Turad providing constant support for every kind of question related to problems or opportunities in the VG. Thank you two for creating a great shared space, where every machine works at its best, thanks to you.

Furthermore, I would like to thank my experts for the outlook of this work, Christian Simo, Jakob Keck and Zhouxiaosong Zeng for critically reviewing the manuscript. Jasmin Breitel for taking up the fight with my English grammar and Christine Schedel for diligently reading and improving the complete work.

ACKNOWLEDGMENTS

Although some phases may suggest otherwise, a life outside of the lab has completed my journey over the last years. I want to express my sincere gratitude to all the wonderful people of the Ph.D. initiative sustainAbility who welcomed me in the group and showed me different perspectives on mental health, city transformation and ideas for change.

A special thanks to all my Nanos, my fellow students, especially my roommates Nicolas Previdi, Amelie Spazierer, Markus Strienz and Aylin Balmes who have grown into my Tübingen family over the years and made the studies over the last eight and a half to a memorable time I will cherish forever.

I appreciate all my other friends who supported me each in their own way, with long walks, intense volleyball games, cooking together or late game nights.

Last but not least I want to thank my family and above all my partner Jasmin Breitel for the constant support and love, although we were far apart for a long part of our journey.

Without all of you this work would not have been possible.